

Influences of Reaction Parameters on the Product of a Geothermite Reaction:
A Multi-Component Oxidation-Reduction Reaction Study

Eric J. Faierson

Thesis submitted to the faculty of the Virginia Polytechnic Institute and State University in
partial fulfillment of the requirements for the degree of

Master of Science
In
Materials Science and Engineering

Kathryn Logan, Chair
David Clark
Gary Pickrell
Norman Dowling

April 29, 2009
Blacksburg, VA

Copyright 2009, Eric J. Faierson

Influences of Reaction Parameters on the Product of a Geothermite Reaction: A Multi-Component Oxidation-Reduction Reaction Study

Eric J. Faierson

ABSTRACT

This study investigated an oxidation-reduction reaction involving a mixture of minerals, glass, and aluminum that exhibited thermite-type reaction behavior. Thermite reactions are a class of Self-propagating High-temperature Synthesis (SHS) reactions. Chemical reactions between raw minerals and a reducing agent, which exhibit thermite-type reaction behavior, are termed geothermite reactions by the author. Geothermite reactions have the potential for use in In-Situ Resource Utilization (ISRU) applications on the Earth, the Moon, Mars, and beyond.

A geothermite reaction was shown to occur between two particle size distributions of lunar regolith simulant. Regolith simulant is a naturally occurring mixture of minerals and glass mined from a volcanic ash deposit. The chemical composition of the simulant is similar to actual lunar regolith found on the Moon. The product of the reaction was a ceramic-composite material. The effect of reactant stoichiometry, regolith simulant particle size, and reaction environment on phase formation, microstructure, and compressive strength of the reaction product was investigated. Reaction environments used in this study included a standard atmosphere and a vacuum environment of 0.600 Torr. In addition, the energy required to initiate each reaction using various reaction parameters was measured.

X-ray diffraction (XRD) analysis of reaction products synthesized in a standard atmosphere and in vacuum typically indicated the presence of the chemical species: silicon, corundum (α - Al_2O_3), spinel (MgAl_2O_4), and grossite (CaAl_4O_7). Many additional chemical species were present; their occurrence depended on reaction parameters used during synthesis. Diffraction peaks were observed for phases of aluminum nitride within all reaction products formed in a standard atmosphere. Scanning Electron Microscopy (SEM) showed the presence of whisker networks throughout the microstructure for all reactions conducted in a standard atmosphere. Energy Dispersive Spectroscopy (EDS) indicated the presence of aluminum and nitrogen within many of the whiskers. It was hypothesized that many of the whisker networks were composed of phases of aluminum nitride. No whisker networks were observed in the vacuum synthesized reaction products. Maximum mean compressive strengths were found to be ~ 18 MPa and occurred in the coarse particle size distribution of simulant using the smallest quantity of aluminum. Reactant mixtures using a coarse particle size distribution of regolith simulant were found to require substantially more energy to initiate the reaction than the simulant with the fine particle size distribution.



A Geothermite Reaction Utilizing Lunar Regolith Simulant

This work is dedicated to my parents and grandparents who always supported me in my endeavors and taught me to reach for the stars.

ACKNOWLEDGMENTS

Dr. Kathryn Logan, my advisor, for advice, guidance, and the opportunities I have had at Virginia Tech, the National Institute of Aerospace, and NASA Langley Research Center (LaRC)

Dr. Gary Pickrell, Dr. Norman Dowling, and Dr. David Clark for being on my committee, and offering advice with respect to this work

The National Institute of Aerospace for funding this work

NASA LaRC for the use of laboratory facilities

Jim Baughman, at LaRC, and Steve McCartney, at ICTAS for assistance and training with SEM

David Hartman, for assistance with XRD at LaRC

Mac McCord at Virginia Tech for assistance with compressive strength testing

Dr. Wallace Vaughn and Craig Leggette for assistance with compressive strength testing at LaRC

Michael Hunt, Brian Stewart, Sharon Jefferies, and Susan Holt for research advice during my graduate study

TABLE OF CONTENTS

ACKNOWLEDGMENTS	v
LIST OF FIGURES	x
LIST OF TABLES	xvi
I. INTRODUCTION	1
RESEARCH OBJECTIVE	1
JUSTIFICATION	1
RESEARCH OVERVIEW	1
SIGNIFICANCE	2
II. BACKGROUND	3
A. Chemical Reactions	3
<i>Oxidation-Reduction Reactions</i>	3
<i>Self-propagating High-temperature Synthesis</i>	4
<i>Particle Surface Area</i>	5
<i>Thermodynamics and Kinetics</i>	5
B. Intergranular Growth and Binding	7
<i>Sintering</i>	7
<i>Ceramics and Glasses</i>	8
<i>Mechanical Properties</i>	9
C. SHS Systems	11
<i>Aluminum-Iron Oxide SHS Systems</i>	11
<i>Other SHS Systems</i>	13
<i>Formation of Aluminum Nitrides in SHS Systems</i>	14
<i>Geothermite Systems</i>	17
<i>Nanoparticle SHS</i>	17
<i>Vacuum SHS</i>	17
D. Lunar Environment, Resource Utilization, and Simulation	18
<i>Lunar Regolith and Environment</i>	18
<i>In-Situ Resource Utilization (ISRU)</i>	21
<i>Regolith Simulant</i>	22
<i>Simplified Thermodynamics of a Geothermite Reaction Using Bulk Oxides</i>	23
<i>Volatization and Melting Studies</i>	25
E. Identification and Material Properties of Chemical Species Produced in this Study	25
<i>X-ray Diffraction</i>	26
<i>Material Properties of Chemical Species Produced in this Study</i>	26
F. Statistical Methods Using a T-test	27
III. EXPERIMENTAL METHODS	29
A. Reactant Stoichiometry Selection	29
B. Preliminary Crucible Experiments	30
C. Sample Preparation and Reaction Environments	31
<i>Standard Atmosphere SHS Reactions</i>	32
<i>Preliminary Variac Settings and Nickel-Chromium Wire Placements</i>	32
<i>Standard Atmosphere SHS Reaction Initiation</i>	32
<i>Vacuum SHS Reactions</i>	33
<i>Vacuum Chamber Setup</i>	33

<i>Preliminary Nickel-Chromium Wire Vacuum Reaction Initiation</i>	35
<i>Vacuum SHS Reaction Initiation</i>	35
D. Identification of Chemical Species	36
E. Characterization of Microstructures and Elemental Analysis	37
F. Density Measurements	38
G. Mechanical Strength Measurements	38
<i>Sample Preparation and Testing</i>	38
H. Energy Required to Initiate the SHS Reaction	39
IV. RESULTS AND DISCUSSION	40
A. Reaction Environments	40
<i>Standard Atmosphere SHS Reactions</i>	40
<i>Preliminary Experiment Results</i>	40
<i>Experimental Results</i>	41
<i>Vacuum SHS Reactions</i>	48
<i>Preliminary Experiment Results</i>	48
<i>Experimental Results</i>	48
B. Identification of Chemical Species	56
<i>Chemical Species Present in Unreacted JSC-1AF Regolith Simulant</i>	56
<i>Chemical Species Present in Unreacted JSC-1A Regolith Simulant</i>	59
<i>Comparison of Unreacted JSC-1AF and JSC-1A Regolith Simulant Samples</i>	61
<i>Chemical Species Present in Standard Atmosphere SHS Reaction Products Utilizing JSC-1AF Regolith Simulant</i>	62
19.44% Al by weight.....	62
24.45% Al by weight.....	65
28.85% Al by weight.....	66
33.33% Al by weight.....	70
Comparison of Chemical species Formed in JSC-1AF Reactant Stoichiometries.....	73
<i>Chemical Species Present in Standard Atmosphere SHS Reaction Products Utilizing JSC-1A Regolith Simulant</i>	76
19.44% Al by weight.....	76
24.45% Al by weight.....	78
28.85% Al by weight.....	81
Comparison of Chemical species Formed in JSC-1A Reactant Stoichiometries	85
<i>Chemical Species Present in Vacuum SHS Reaction Products Utilizing JSC-1AF Regolith Simulant</i>	91
19.44% Al by weight.....	91
24.45% Al by weight.....	92
28.85% Al by weight.....	94
33.33% Al by weight.....	96
Comparison of Chemical Species Formed in JSC-1AF Vacuum Products.....	98
<i>Chemical Species Present in Vacuum SHS Reaction Products Utilizing JSC-1A Regolith Simulant</i>	101
19.44% Al by weight.....	101
24.45% Al by weight.....	103
28.85% Al by weight.....	105
Comparison of Chemical Species Formed in JSC-1A Vacuum Products	106

C. Characterization of Microstructures and Elemental Analysis	112
<i>Micrographs of Unreacted JSC-IAF Simulant</i>	112
<i>Elemental Analysis of Unreacted JSC-IAF Simulant</i>	113
<i>Micrographs of Unreacted JSC-IA Simulant</i>	114
<i>Elemental Analysis of Unreacted JSC-IA Simulant</i>	115
<i>Comparison of Elemental Analyses for Unreacted JSC-IAF and JSC-IA Simulant</i>	116
<i>Microstructures within the Reaction Products of a Standard Atmosphere SHS Reaction</i>	117
500x Magnification.....	117
2kx Magnification	119
10kx Magnification	121
<i>Nanostructures and Elemental Analysis within the Reaction Products of a Standard Atmosphere SHS Reaction Utilizing JSC-IAF Regolith Simulant</i>	124
19.44% Al by weight.....	124
24.45% Al by weight.....	133
28.85% Al by weight.....	137
33.33% Al by weight.....	140
<i>Nanostructures and Elemental Analysis within the Reaction Product of a Standard Atmosphere SHS Reaction Utilizing JSC-IA Regolith Simulant</i>	147
19.44% Al by weight.....	147
24.45% Al by weight.....	152
28.85% Al by weight.....	155
<i>Microstructures within the Reaction Products of a Vacuum SHS Reaction</i>	159
500x Magnification.....	159
2kx Magnification	161
10kx Magnification	164
<i>Elemental Analysis for Vacuum Synthesized Reaction Products Utilizing JSC-IAF Regolith Simulant</i>	167
19.44% Al by weight.....	167
24.45% Al by weight.....	170
28.85% Al by weight.....	173
33.33% Al by weight.....	176
<i>Elemental Analysis for Vacuum Synthesized Reaction Products Utilizing JSC-IA Regolith Simulant</i>	180
19.44% Al by weight.....	180
24.45% Al by weight.....	183
28.85% Al by weight.....	186
D. Density Measurements	191
E. Mechanical Strength Measurements	193
<i>Preliminary Experiment Results</i>	193
<i>Experimental Results</i>	193
F. Energy Required to Initiate SHS Reactions	199
<i>Mean Energy Required to Initiate JSC-IAF Reactions</i>	199
<i>Mean Energy Required to Initiate JSC-IA Reactions</i>	201
<i>Mean Energy Required to Initiate JSC-IA & JSC-IAF Reactions</i>	203
<i>Energy Required to Initiate SHS Reactions in a Vacuum</i>	205

G. Reaction Thermodynamics	205
Standard Atmosphere	205
Vacuum	219
V. CONCLUSIONS	230
A. Reaction Environment	230
B. Identification of Chemical Species	230
<i>Standard Atmosphere Synthesis</i>	230
<i>Vacuum Synthesis</i>	231
C. Microstructural Characterization and Elemental Analysis	232
D. Density Measurements	233
E. Mechanical Strength Measurements	234
F. Measurements of Energy Required to Initiate Reactions	235
G. Reaction Thermodynamics	235
VI. FUTURE WORK	237
<i>Appendix 1: Calculations for Reactant Stoichiometries</i>	239
<i>Appendix 2: Images of Standard Atmosphere Reaction Products</i>	242
<i>Appendix 3: Images of Vacuum Reaction Products</i>	244
VII. REFERENCES	246

LIST OF FIGURES

FIGURE I: VACUUM CHAMBER AND VARIAC SETUP	33
FIGURE II: DIAGRAM OF THE SAMPLE REGION USED FOR XRD ANALYSIS.....	37
FIGURE III: A DIAGRAM OF THE PLANAR COMBUSTION WAVE PROPAGATING THROUGH A SAMPLE.	41
FIGURE IV: HEAT IS APPLIED TO A MIXTURE OF JSC-1AF REGOLITH SIMULANT AND ALUMINUM POWDER.....	42
FIGURE V: REACTION PROPAGATION BEGINS, NO FURTHER EXTERNAL ENERGY IS APPLIED.	42
FIGURE VI: ~20 SEC AFTER INITIATION.....	42
FIGURE VII: ~40 SEC AFTER INITIATION.	42
FIGURE VIII: ~1 MIN AFTER INITIATION.....	42
FIGURE IX: ~1 MIN 20 SEC AFTER INITIATION.	42
FIGURE X: ~2 MIN AFTER INITIATION.....	43
FIGURE XI: ~2 MIN 30 SEC AFTER INITIATION.	43
FIGURE XII: REACTION PROPAGATION HAS COMPLETED. (~3 MIN 10 SEC AFTER INITIATION)	43
FIGURE XIII: REACTION PRODUCT AFTER COOLING. (~ 5MIN 40 SEC AFTER INITIATION).....	43
FIGURE XIV: A REACTION PRODUCT DEFORMED DURING SYNTHESIS USING A STOICHIOMETRY OF 53.33% JSC-1AF AND 46.67% ALUMINUM.....	44
FIGURE XV: CRACKS IN THE REACTION PRODUCT OF THE 19.44% ALUMINUM STOICHIOMETRY.....	45
FIGURE XVI: THE REACTION PRODUCT USING A STOICHIOMETRY OF 80.56% JSC-1A AND 19.44% ALUMINUM WITH A SMALL UNREACTED PORTION AT FAR LEFT.....	46
FIGURE XVII: A GREEN-WHITE COATING ON THE REACTION PRODUCT USING JSC-1AF AND 33.33% ALUMINUM.	47
FIGURE XVIII: INTERIOR OF JSC-1AF SAMPLE	47
FIGURE XIX: REACTANT MIXTURE IN ALUMINUM CRUCIBLE WITHIN VACUUM CHAMBER.....	49
FIGURE XX: HEAT IS APPLIED TO REACTANT MIXTURE.	49
FIGURE XXI: ENERGETIC EMISSION OF PARTICLES, PROPAGATION BEGINS.....	49
FIGURE XXII: ~20 SEC AFTER INITIATION.....	49
FIGURE XXIII: ~40 SEC AFTER INITIATION.	49
FIGURE XXIV: ~ 1 MIN 30 SEC AFTER INITIATION.	49
FIGURE XXV: ~ 3 MIN AFTER INITIATION.	50
FIGURE XXVI: ~4 MIN AFTER INITIATION.....	50
FIGURE XXVII: ~6 MIN AFTER INITIATION.	50
FIGURE XXVIII: THE VACUUM REACTION PRODUCT AFTER COOLING. (~7 MIN 30 SEC AFTER INITIATION)	50
FIGURE XXIX: VACUUM CHAMBER PRESSURE AS A FUNCTION OF TIME DURING REACTION SYNTHESIS.	52
FIGURE XXX: SECONDARY REACTION UPON PRESSURIZING THE VACUUM CHAMBER TO AMBIENT CONDITIONS ABRUPTLY. (~9 MIN AFTER INITIATION)	53
FIGURE XXXI: ~9 MIN 15 SEC AFTER INITIATION.	53
FIGURE XXXII: ~9 MIN 30 SEC AFTER INITIATION.....	53
FIGURE XXXIII: A WHITE COATING IS PRODUCED FROM THE SECONDARY REACTION, WHICH IS CONFINED TO THE SAMPLE SURFACE.....	53
FIGURE XXXIV: SEM MICROGRAPH OF THE WHITE SUBSTANCE FORMED IN THE SECONDARY REACTION.	54
FIGURE XXXV: SEM MICROGRAPH OF THE WHITE SUBSTANCE FORMED IN THE SECONDARY REACTION.....	55
FIGURE XXXVI: DENDRITIC DEPOSITION OBSERVED WITHIN VACUUM CHAMBER.	56
FIGURE XXXVII: ENLARGED VIEW OF DENDRITIC DEPOSITION WITHIN VACUUM CHAMBER.....	56
FIGURE XXXVIII: XRD PATTERN FOR UNREACTED JSC-1AF SIMULANT WITH DIFFRACTION PEAKS LABELED.	57
FIGURE XXXIX: STACKED XRD PATTERNS FOR THREE SAMPLES OF JSC-1AF REGOLITH SIMULANT	59
FIGURE XL: STACKED XRD PATTERNS FOR THREE SAMPLES OF JSC-1A REGOLITH SIMULANT	60
FIGURE XLI: STACKED XRD PATTERNS OF UNREACTED JSC-1AF AND JSC-1A SIMULANT	61
FIGURE XLII: XRD PATTERN FOR THE REACTION PRODUCT OF THE 80.56% JSC-1AF AND 19.44% ALUMINUM STOICHIOMETRY.....	62
FIGURE XLIII: XRD PATTERNS OF TWO REACTED SAMPLES OF 80.56% JSC-1AF AND 19.44% AL BY WEIGHT	64
FIGURE XLIV: XRD PATTERN FOR THE REACTION PRODUCT OF THE 75.55% JSC-1AF AND 24.45% ALUMINUM STOICHIOMETRY.....	65
FIGURE XLV: XRD PATTERN FOR THE REACTION PRODUCT OF THE 71.15% JSC-1AF AND 28.85% ALUMINUM STOICHIOMETRY.....	67
FIGURE XLVI: XRD PATTERNS OF TWO REACTED SAMPLES OF 71.15% JSC-1AF AND 28.85% AL BY WEIGHT	69

FIGURE XLVII: XRD PATTERN FOR THE REACTION PRODUCT OF THE 66.67% JSC-1AF AND 33.33% ALUMINUM STOICHIOMETRY.....	70
FIGURE XLVIII: XRD PATTERNS OF TWO REACTED SAMPLES OF 66.67% JSC-1AF AND 33.33% AL BY WEIGHT	72
FIGURE XLIX: STACKED XRD PATTERNS OF FOUR REACTED STOICHIOMETRIES OF AL AND JSC-1AF SIMULANT	73
FIGURE L: XRD PATTERN FOR THE REACTION PRODUCT OF THE 80.56% JSC-1A AND 19.44% ALUMINUM STOICHIOMETRY.....	76
FIGURE LI: XRD PATTERNS OF TWO REACTED SAMPLES OF 80.56% JSC-1A AND 19.44% AL BY WEIGHT	78
FIGURE LII: XRD PATTERN FOR THE REACTION PRODUCT OF THE 75.55% JSC-1A AND 24.45% ALUMINUM STOICHIOMETRY.....	79
FIGURE LIII: XRD PATTERNS OF TWO REACTED SAMPLES OF 75.55% JSC-1A AND 24.45% AL BY WEIGHT	81
FIGURE LIV: XRD PATTERN FOR THE REACTION PRODUCT OF THE 71.15% JSC-1A AND 28.85% ALUMINUM STOICHIOMETRY.....	82
FIGURE LV: XRD PATTERNS OF TWO REACTED SAMPLES OF 71.15% JSC-1A AND 28.85% AL BY WEIGHT.....	84
FIGURE LVI: STACKED XRD PATTERNS OF THREE REACTED STOICHIOMETRIES OF AL AND JSC-1A SIMULANT.....	85
FIGURE LVII: RELATIVE DIFFRACTION INTENSITIES FOR SELECTED CHEMICAL SPECIES IN THE STANDARD ATMOSPHERE REACTION PRODUCT.....	89
FIGURE LVIII: XRD PATTERN FOR THE REACTION PRODUCT OF THE 80.56% JSC-1AF AND 19.44% ALUMINUM STOICHIOMETRY.....	91
FIGURE LIX: XRD PATTERN FOR THE REACTION PRODUCT OF THE 75.55% JSC-1AF AND 24.45% ALUMINUM STOICHIOMETRY.....	93
FIGURE LX: XRD PATTERN FOR THE REACTION PRODUCT OF THE 71.15% JSC-1AF AND 28.85% ALUMINUM STOICHIOMETRY.....	95
FIGURE LXI: XRD PATTERN FOR THE REACTION PRODUCT OF THE 66.67% JSC-1AF AND 33.33% ALUMINUM STOICHIOMETRY.....	97
FIGURE LXII: STACKED XRD PATTERNS OF FOUR REACTED STOICHIOMETRIES OF AL AND JSC-1AF SIMULANT.....	99
FIGURE LXIII: XRD PATTERN FOR THE REACTION PRODUCT OF THE 80.56% JSC-1A AND 19.44% ALUMINUM STOICHIOMETRY.....	102
FIGURE LXIV: XRD PATTERN FOR THE REACTION PRODUCT OF THE 75.55% JSC-1A AND 24.45% ALUMINUM STOICHIOMETRY.....	104
FIGURE LXV: XRD PATTERN FOR THE REACTION PRODUCT OF THE 71.15% JSC-1A AND 28.85% ALUMINUM STOICHIOMETRY.....	105
FIGURE LXVI: STACKED XRD PATTERNS OF THREE REACTED STOICHIOMETRIES OF AL AND JSC-1A SIMULANT....	107
FIGURE LXVII: RELATIVE DIFFRACTION INTENSITIES FOR SELECTED CHEMICAL SPECIES IN THE VACUUM REACTION PRODUCT.....	111
FIGURE LXVIII: SEM MICROGRAPH OF UNREACTED JSC-1AF SIMULANT AT 500X.....	113
FIGURE LXIX: SEM MICROGRAPH OF UNREACTED JSC-1AF SIMULANT AT 1KX.....	113
FIGURE LXX: SEM MICROGRAPH OF UNREACTED JSC-1AF SIMULANT AT 2.5KX.....	113
FIGURE LXXI: SEM MICROGRAPH OF UNREACTED JSC-1A SIMULANT AT 100X.....	115
FIGURE LXXII: SEM MICROGRAPH OF UNREACTED JSC-1A SIMULANT AT 250X.....	115
FIGURE LXXIII: SEM MICROGRAPH OF UNREACTED JSC-1A SIMULANT AT 500X.....	115
FIGURE LXXIV: STANDARD ATMOSPHERE SYNTHESIZED 19.44% ALUMINUM STOICHIOMETRY UTILIZING JSC-1AF.	117
FIGURE LXXV: STANDARD ATMOSPHERE SYNTHESIZED 24.45% ALUMINUM STOICHIOMETRY UTILIZING JSC-1AF.	117
FIGURE LXXVI: STANDARD ATMOSPHERE SYNTHESIZED 28.85% ALUMINUM STOICHIOMETRY UTILIZING JSC-1AF.	117
FIGURE LXXVII: STANDARD ATMOSPHERE SYNTHESIZED 33.33% ALUMINUM STOICHIOMETRY UTILIZING JSC-1AF.	117
FIGURE LXXVIII: STANDARD ATMOSPHERE SYNTHESIZED 19.44% ALUMINUM STOICHIOMETRY UTILIZING JSC-1A.	118
FIGURE LXXIX: STANDARD ATMOSPHERE SYNTHESIZED 24.45% ALUMINUM STOICHIOMETRY UTILIZING JSC-1A.	118
FIGURE LXXX: STANDARD ATMOSPHERE SYNTHESIZED 24.45% ALUMINUM STOICHIOMETRY UTILIZING JSC-1A.	118
FIGURE LXXXI: STANDARD ATMOSPHERE SYNTHESIZED 28.85% ALUMINUM STOICHIOMETRY UTILIZING JSC-1A.	119
FIGURE LXXXII: STANDARD ATMOSPHERE SYNTHESIZED 19.44% ALUMINUM STOICHIOMETRY UTILIZING JSC-1AF.	119

FIGURE LXXXIII: STANDARD ATMOSPHERE SYNTHESIZED 24.45% ALUMINUM STOICHIOMETRY UTILIZING JSC-1AF.	119
FIGURE LXXXIV: STANDARD ATMOSPHERE SYNTHESIZED 28.85% ALUMINUM STOICHIOMETRY UTILIZING JSC-1AF.	120
FIGURE LXXXV: STANDARD ATMOSPHERE SYNTHESIZED 33.33% ALUMINUM STOICHIOMETRY UTILIZING JSC-1AF.	120
FIGURE LXXXVI: STANDARD ATMOSPHERE SYNTHESIZED 19.44% ALUMINUM STOICHIOMETRY UTILIZING JSC-1A.	120
FIGURE LXXXVII: STANDARD ATMOSPHERE SYNTHESIZED 24.45% ALUMINUM STOICHIOMETRY UTILIZING JSC-1A.	120
FIGURE LXXXVIII: STANDARD ATMOSPHERE SYNTHESIZED 28.85% ALUMINUM STOICHIOMETRY UTILIZING JSC-1A.	121
FIGURE LXXXIX: STANDARD ATMOSPHERE SYNTHESIZED 19.44% ALUMINUM STOICHIOMETRY UTILIZING JSC-1AF.	122
FIGURE XC: STANDARD ATMOSPHERE SYNTHESIZED 24.45% ALUMINUM STOICHIOMETRY UTILIZING JSC-1AF.	122
FIGURE XCI: STANDARD ATMOSPHERE SYNTHESIZED 28.85% ALUMINUM STOICHIOMETRY UTILIZING JSC-1AF.	122
FIGURE XCII: STANDARD ATMOSPHERE SYNTHESIZED 33.33% ALUMINUM STOICHIOMETRY UTILIZING JSC-1AF.	122
FIGURE XCIII: STANDARD ATMOSPHERE SYNTHESIZED 19.44% ALUMINUM STOICHIOMETRY UTILIZING JSC-1A.	123
FIGURE XCIV: STANDARD ATMOSPHERE SYNTHESIZED 24.45% ALUMINUM STOICHIOMETRY UTILIZING JSC-1A.	123
FIGURE XCV: STANDARD ATMOSPHERE SYNTHESIZED 28.85% ALUMINUM STOICHIOMETRY UTILIZING JSC-1A.	123
FIGURE XCVI: STANDARD ATMOSPHERE SYNTHESIZED 19.44% ALUMINUM STOICHIOMETRY UTILIZING JSC-1AF.	124
FIGURE XCVII: STANDARD ATMOSPHERE SYNTHESIZED 19.44% ALUMINUM STOICHIOMETRY UTILIZING JSC-1AF.	125
FIGURE XCVIII: SEM MICROGRAPH FOR REGION A OF THE STANDARD ATMOSPHERE SYNTHESIZED 19.44% ALUMINUM STOICHIOMETRY UTILIZING JSC-1AF SIMULANT WITH THE REGION OF EDS HIGHLIGHTED.	126
FIGURE XCIX: SEM MICROGRAPH FOR REGION B OF THE STANDARD ATMOSPHERE SYNTHESIZED 19.44% ALUMINUM STOICHIOMETRY UTILIZING JSC-1AF SIMULANT WITH THE REGION OF EDS HIGHLIGHTED.	127
FIGURE C: SEM MICROGRAPH FOR REGION B OF THE STANDARD ATMOSPHERE SYNTHESIZED 19.44% ALUMINUM STOICHIOMETRY UTILIZING JSC-1AF SIMULANT WITH THE REGION OF EDS HIGHLIGHTED.	128
FIGURE CI: SEM MICROGRAPH FOR REGION C OF THE STANDARD ATMOSPHERE SYNTHESIZED 19.44% ALUMINUM STOICHIOMETRY UTILIZING JSC-1AF SIMULANT WITH THE REGION OF EDS HIGHLIGHTED.	129
FIGURE CII: SEM MICROGRAPH FOR REGION D OF THE STANDARD ATMOSPHERE SYNTHESIZED 19.44% ALUMINUM STOICHIOMETRY UTILIZING JSC-1AF SIMULANT WITH THE REGION OF EDS HIGHLIGHTED.	130
FIGURE CIII: SEM MICROGRAPH FOR REGION E OF THE STANDARD ATMOSPHERE SYNTHESIZED 19.44% ALUMINUM STOICHIOMETRY UTILIZING JSC-1AF SIMULANT WITH THE REGION OF EDS HIGHLIGHTED.	131
FIGURE CIV: SEM MICROGRAPH FOR REGION F OF THE STANDARD ATMOSPHERE SYNTHESIZED 19.44% ALUMINUM STOICHIOMETRY UTILIZING JSC-1AF SIMULANT WITH THE REGION OF EDS HIGHLIGHTED.	132
FIGURE CV: SEM MICROGRAPH FOR REGION G OF THE STANDARD ATMOSPHERE SYNTHESIZED 19.44% ALUMINUM STOICHIOMETRY UTILIZING JSC-1AF SIMULANT WITH THE REGION OF EDS HIGHLIGHTED.	133
FIGURE CVI: SEM MICROGRAPH OF THE STANDARD ATMOSPHERE SYNTHESIZED 24.45% ALUMINUM STOICHIOMETRY UTILIZING JSC-1AF SIMULANT AT 50KX.	134
FIGURE CVII: SEM MICROGRAPH OF THE MICROSTRUCTURE IN REGION A FOR THE 24.45% ALUMINUM STOICHIOMETRY WITH THE REGIONS OF EDS HIGHLIGHTED.	135
FIGURE CVIII: SEM MICROGRAPH OF THE MICROSTRUCTURE IN REGION B FOR THE 24.45% ALUMINUM STOICHIOMETRY WITH THE REGIONS OF EDS HIGHLIGHTED.	136
FIGURE CIX: SEM MICROGRAPH OF THE STANDARD ATMOSPHERE SYNTHESIZED 28.85% ALUMINUM STOICHIOMETRY UTILIZING JSC-1AF SIMULANT AT 50KX.	137
FIGURE CX: SEM MICROGRAPH OF THE STANDARD ATMOSPHERE SYNTHESIZED 28.85% ALUMINUM STOICHIOMETRY UTILIZING JSC-1AF SIMULANT AT 200KX.	138
FIGURE CXI: SEM MICROGRAPH OF THE MICROSTRUCTURE IN REGION A FOR THE 28.85% ALUMINUM STOICHIOMETRY WITH THE REGIONS OF EDS HIGHLIGHTED.	139
FIGURE CXII: SEM MICROGRAPH OF THE MICROSTRUCTURE IN REGION B FOR THE 28.85% ALUMINUM STOICHIOMETRY WITH THE REGION OF EDS HIGHLIGHTED.	140
FIGURE CXIII: SEM MICROGRAPH OF THE STANDARD ATMOSPHERE SYNTHESIZED 33.33% ALUMINUM STOICHIOMETRY UTILIZING JSC-1AF SIMULANT AT 50KX.	141

FIGURE CXIV: SEM MICROGRAPH OF THE STANDARD ATMOSPHERE SYNTHESIZED 33.33% ALUMINUM STOICHIOMETRY UTILIZING JSC-1AF SIMULANT AT 200KX.....	141
FIGURE CXV: SEM MICROGRAPH OF THE MICROSTRUCTURE IN REGION A FOR THE 33.33% ALUMINUM STOICHIOMETRY WITH THE REGION OF EDS HIGHLIGHTED.....	142
FIGURE CXVI: SEM MICROGRAPH OF REGION B FOR THE STANDARD ATMOSPHERE SYNTHESIZED 33.33% ALUMINUM STOICHIOMETRY UTILIZING JSC-1AF SIMULANT WITH THE REGION OF EDS HIGHLIGHTED.....	143
FIGURE CXVII: SEM MICROGRAPH OF REGION C FOR THE STANDARD ATMOSPHERE SYNTHESIZED 33.33% ALUMINUM STOICHIOMETRY UTILIZING JSC-1AF SIMULANT WITH THE REGION OF EDS HIGHLIGHTED.....	144
FIGURE CXVIII: SEM MICROGRAPH OF REGION D FOR THE STANDARD ATMOSPHERE SYNTHESIZED 33.33% ALUMINUM STOICHIOMETRY UTILIZING JSC-1AF SIMULANT WITH THE REGIONS OF EDS HIGHLIGHTED.....	145
FIGURE CXIX: SEM MICROGRAPH OF REGION E FOR THE STANDARD ATMOSPHERE SYNTHESIZED 33.33% ALUMINUM STOICHIOMETRY UTILIZING JSC-1AF SIMULANT WITH THE REGIONS OF EDS HIGHLIGHTED.....	146
FIGURE CXX: SEM MICROGRAPH OF THE STANDARD ATMOSPHERE SYNTHESIZED 19.44% ALUMINUM STOICHIOMETRY UTILIZING JSC-1A SIMULANT AT 50KX.....	148
FIGURE CXXI: SEM MICROGRAPH OF THE STANDARD ATMOSPHERE SYNTHESIZED 19.44% ALUMINUM STOICHIOMETRY UTILIZING JSC-1A SIMULANT AT 200KX.....	148
FIGURE CXXII: SEM MICROGRAPH OF THE MICROSTRUCTURE IN REGION A FOR THE 19.44% ALUMINUM STOICHIOMETRY, WITH THE REGIONS OF EDS HIGHLIGHTED.....	150
FIGURE CXXIII: SEM MICROGRAPH OF THE MICROSTRUCTURE IN REGION B FOR THE 19.44% ALUMINUM STOICHIOMETRY WITH THE REGIONS OF EDS HIGHLIGHTED.....	151
FIGURE CXXIV: SEM MICROGRAPH OF THE STANDARD ATMOSPHERE SYNTHESIZED 24.45% ALUMINUM STOICHIOMETRY UTILIZING JSC-1A SIMULANT AT 50KX.....	152
FIGURE CXXV: SEM MICROGRAPH OF THE STANDARD ATMOSPHERE SYNTHESIZED 24.45% ALUMINUM STOICHIOMETRY UTILIZING JSC-1A SIMULANT AT 200KX.....	153
FIGURE CXXVI: SEM MICROGRAPH OF THE MICROSTRUCTURE IN REGION A FOR THE 24.45% ALUMINUM STOICHIOMETRY, WITH THE REGIONS OF EDS HIGHLIGHTED.....	154
FIGURE CXXVII: SEM MICROGRAPH OF THE MICROSTRUCTURE IN REGION B FOR THE 24.45% ALUMINUM STOICHIOMETRY WITH THE REGIONS OF EDS HIGHLIGHTED.....	155
FIGURE CXXVIII: SEM MICROGRAPH OF THE STANDARD ATMOSPHERE SYNTHESIZED 28.85% ALUMINUM STOICHIOMETRY UTILIZING JSC-1A SIMULANT AT 50KX.....	156
FIGURE CXXIX: SEM MICROGRAPH OF THE STANDARD ATMOSPHERE SYNTHESIZED 28.85% ALUMINUM STOICHIOMETRY UTILIZING JSC-1A SIMULANT AT 200KX.....	156
FIGURE CXXX: SEM MICROGRAPH OF THE MICROSTRUCTURE IN REGION A FOR THE 28.85% ALUMINUM STOICHIOMETRY WITH THE REGIONS OF EDS HIGHLIGHTED.....	157
FIGURE CXXXI: VACUUM SYNTHESIZED 19.44% ALUMINUM STOICHIOMETRY UTILIZING JSC-1AF.....	159
FIGURE CXXXII: VACUUM SYNTHESIZED 24.45% ALUMINUM STOICHIOMETRY UTILIZING JSC-1AF.....	159
FIGURE CXXXIII: VACUUM SYNTHESIZED 28.85% ALUMINUM STOICHIOMETRY UTILIZING JSC-1AF.....	159
FIGURE CXXXIV: VACUUM SYNTHESIZED 33.33% ALUMINUM STOICHIOMETRY UTILIZING JSC-1AF.....	159
FIGURE CXXXV: VACUUM SYNTHESIZED 19.44% ALUMINUM STOICHIOMETRY UTILIZING JSC-1A.....	160
FIGURE CXXXVI: VACUUM SYNTHESIZED 24.45% ALUMINUM STOICHIOMETRY UTILIZING JSC-1A.....	160
FIGURE CXXXVII: VACUUM SYNTHESIZED 28.85% ALUMINUM STOICHIOMETRY UTILIZING JSC-1A.....	160
FIGURE CXXXVIII: VACUUM SYNTHESIZED 19.44% ALUMINUM STOICHIOMETRY UTILIZING JSC-1AF.....	161
FIGURE CXXXIX: VACUUM SYNTHESIZED 24.45% ALUMINUM STOICHIOMETRY UTILIZING JSC-1AF.....	161
FIGURE CXL: VACUUM SYNTHESIZED 28.85% ALUMINUM STOICHIOMETRY UTILIZING JSC-1AF.....	162
FIGURE CXLI: VACUUM SYNTHESIZED 33.33% ALUMINUM STOICHIOMETRY UTILIZING JSC-1AF.....	162
FIGURE CXLII: VACUUM SYNTHESIZED 19.44% ALUMINUM STOICHIOMETRY UTILIZING JSC-1A.....	163
FIGURE CXLIII: VACUUM SYNTHESIZED 24.45% ALUMINUM STOICHIOMETRY UTILIZING JSC-1A.....	163
FIGURE CXLIV: VACUUM SYNTHESIZED 28.85% ALUMINUM STOICHIOMETRY UTILIZING JSC-1A.....	163
FIGURE CXLV: VACUUM SYNTHESIZED 19.44% ALUMINUM STOICHIOMETRY UTILIZING JSC-1AF.....	164
FIGURE CXLVI: VACUUM SYNTHESIZED 19.44% ALUMINUM STOICHIOMETRY UTILIZING JSC-1AF.....	164
FIGURE CXLVII: VACUUM SYNTHESIZED 24.45% ALUMINUM STOICHIOMETRY UTILIZING JSC-1AF.....	164
FIGURE CXLVIII: VACUUM SYNTHESIZED 28.85% ALUMINUM STOICHIOMETRY UTILIZING JSC-1AF.....	165
FIGURE CXLIX: VACUUM SYNTHESIZED 28.85% ALUMINUM STOICHIOMETRY UTILIZING JSC-1AF.....	165
FIGURE CL: VACUUM SYNTHESIZED 33.33% ALUMINUM STOICHIOMETRY UTILIZING JSC-1AF.....	165
FIGURE CLI: VACUUM SYNTHESIZED 33.33% ALUMINUM STOICHIOMETRY UTILIZING JSC-1AF.....	165
FIGURE CLII: VACUUM SYNTHESIZED 19.44% ALUMINUM STOICHIOMETRY UTILIZING JSC-1A.....	166

FIGURE CLIII: VACUUM SYNTHESIZED 24.45% ALUMINUM STOICHIOMETRY UTILIZING JSC-1A	166
FIGURE CLIV: VACUUM SYNTHESIZED 28.85% ALUMINUM STOICHIOMETRY UTILIZING JSC-1A	166
FIGURE CLV: VACUUM SYNTHESIZED 28.85% ALUMINUM STOICHIOMETRY UTILIZING JSC-1A	166
FIGURE CLVI: SEM MICROGRAPH OF THE MICROSTRUCTURE IN REGION A FOR THE 19.44% ALUMINUM STOICHIOMETRY WITH THE REGIONS OF EDS HIGHLIGHTED.	168
FIGURE CLVII: SEM MICROGRAPH OF THE MICROSTRUCTURE IN REGION B FOR THE 19.44% ALUMINUM STOICHIOMETRY WITH THE REGIONS OF EDS HIGHLIGHTED.	169
FIGURE CLVIII: SEM MICROGRAPH OF THE MICROSTRUCTURE IN REGION A FOR THE 24.45% ALUMINUM STOICHIOMETRY WITH THE REGIONS OF EDS HIGHLIGHTED.	171
FIGURE CLIX: SEM MICROGRAPH OF THE MICROSTRUCTURE IN REGION B FOR THE 24.45% ALUMINUM STOICHIOMETRY WITH THE REGIONS OF EDS HIGHLIGHTED.	172
FIGURE CLX: SEM MICROGRAPH OF THE MICROSTRUCTURE IN REGION A FOR THE 28.85% ALUMINUM STOICHIOMETRY WITH THE REGIONS OF EDS HIGHLIGHTED.	174
FIGURE CLXI: SEM MICROGRAPH OF THE MICROSTRUCTURE IN REGION B FOR THE 28.85% ALUMINUM STOICHIOMETRY, WITH THE REGIONS OF EDS HIGHLIGHTED.	175
FIGURE CLXII: SEM MICROGRAPH OF THE MICROSTRUCTURE IN REGION A FOR THE 33.33% ALUMINUM STOICHIOMETRY WITH EDS REGIONS HIGHLIGHTED.	176
FIGURE CLXIII: SEM MICROGRAPH OF THE MICROSTRUCTURE IN REGION B FOR THE 33.33% ALUMINUM STOICHIOMETRY WITH EDS REGIONS HIGHLIGHTED.	178
FIGURE CLXIV: SEM MICROGRAPH OF THE MICROSTRUCTURE IN REGION C FOR THE 33.33% ALUMINUM STOICHIOMETRY WITH EDS REGIONS HIGHLIGHTED.	179
FIGURE CLXV: SEM MICROGRAPH OF THE MICROSTRUCTURE IN REGION A FOR THE 19.44% ALUMINUM STOICHIOMETRY WITH EDS REGIONS HIGHLIGHTED.	181
FIGURE CLXVI: SEM MICROGRAPH OF THE MICROSTRUCTURE IN REGION B FOR THE 19.44% ALUMINUM STOICHIOMETRY WITH EDS REGIONS HIGHLIGHTED.	182
FIGURE CLXVII: SEM MICROGRAPH OF THE MICROSTRUCTURE IN REGION A FOR THE 24.45% ALUMINUM STOICHIOMETRY WITH EDS REGIONS HIGHLIGHTED.	184
FIGURE CLXVIII: SEM MICROGRAPH OF THE MICROSTRUCTURE IN REGION B FOR THE 24.45% ALUMINUM STOICHIOMETRY WITH EDS REGIONS HIGHLIGHTED.	185
FIGURE CLXIX: SEM MICROGRAPH OF THE MICROSTRUCTURE IN REGION A FOR THE 28.85% ALUMINUM STOICHIOMETRY WITH EDS REGIONS HIGHLIGHTED.	186
FIGURE CLXX: SEM MICROGRAPH OF THE MICROSTRUCTURE IN REGION B FOR THE 28.85% ALUMINUM STOICHIOMETRY WITH EDS REGIONS HIGHLIGHTED.	188
FIGURE CLXXI: SEM MICROGRAPH OF THE MICROSTRUCTURE IN REGION C FOR THE 28.85% ALUMINUM STOICHIOMETRY WITH EDS REGION HIGHLIGHTED.	189
FIGURE CLXXII: SEM MICROGRAPH OF THE MICROSTRUCTURE IN REGION D FOR THE 28.85% ALUMINUM STOICHIOMETRY WITH EDS REGIONS HIGHLIGHTED.	190
FIGURE CLXXIII: MEAN DENSITY OF REACTION PRODUCTS UTILIZING JSC-1A AND JSC-1AF SIMULANTS	191
FIGURE CLXXIV: FRACTURE OF A JSC-1AF, 33.33% AL STOICHIOMETRY SYNTHESIZED IN A STANDARD ATMOSPHERE.	194
FIGURE CLXXV: FRACTURE OF A JSC-1A, 28.85% AL STOICHIOMETRY SYNTHESIZED IN A STANDARD ATMOSPHERE.	194
FIGURE CLXXVI: FRACTURE OF A JSC-1AF, 46.67% AL STOICHIOMETRY SYNTHESIZED IN A STANDARD ATMOSPHERE.	194
FIGURE CLXXVII: FRACTURE OF A JSC-1A, 28.85% AL STOICHIOMETRY SYNTHESIZED IN A STANDARD ATMOSPHERE.	194
FIGURE CLXXVIII: MEAN COMPRESSIVE STRENGTH OF JSC-1A AND JSC-1AF STANDARD ATMOSPHERE REACTION PRODUCTS	195
FIGURE CLXXIX: STRESS-STRAIN CURVES FOR STANDARD ATMOSPHERE REACTION PRODUCTS USING JSC-1AF. ...	198
FIGURE CLXXX: STRESS-STRAIN CURVES FOR STANDARD ATMOSPHERE REACTION PRODUCTS USING JSC-1A.	199
FIGURE CLXXXI: A GRAPH OF THE MEAN ENERGY REQUIRED TO INITIATE AN SHS REACTION VS THE ALUMINUM COMPOSITION FOR THE JSC-1AF SIMULANT.	200
FIGURE CLXXXII: A GRAPH OF THE MEAN ENERGY REQUIRED TO INITIATE AN SHS REACTION VS THE ALUMINUM COMPOSITION FOR THE JSC-1A SIMULANT.	202
FIGURE CLXXXIII: A GRAPH OF THE MEAN ENERGY REQUIRED TO INITIATE AN SHS REACTION VS THE ALUMINUM COMPOSITION AND TYPE OF REGOLITH SIMULANT.	204

FIGURE CLXXXIV: ENTHALPY AND GIBBS FREE ENERGY PLOT FOR $20\text{Al}+5\text{CaAl}_2\text{Si}_2\text{O}_8\rightarrow 5\text{CaAl}_4\text{O}_7+10\text{Si}+5\text{Al}_2\text{O}$	206
FIGURE CLXXXV: ENTHALPY AND GIBBS FREE ENERGY PLOT FOR $6\text{Al}_2\text{O}+6\text{N}_2\rightarrow 12\text{AlN}+3\text{O}_2$	207
FIGURE CLXXXVI: ENTHALPY AND GIBBS FREE ENERGY PLOT FOR $\text{Al}_2\text{O}+\text{O}_2\rightarrow \text{Al}_2\text{O}_3$	208
FIGURE CLXXXVII: ENTHALPY AND GIBBS FREE ENERGY PLOT FOR $4\text{Al}+3\text{O}_2\rightarrow 2\text{Al}_2\text{O}_3$	209
FIGURE CLXXXVIII: ENTHALPY AND GIBBS FREE ENERGY PLOT FOR $8\text{Al}+2\text{NaAlSi}_3\text{O}_8\rightarrow \text{Na}_2\text{O}+6\text{Si}+5\text{Al}_2\text{O}_3$	210
FIGURE CLXXXIX: ENTHALPY AND GIBBS FREE ENERGY PLOT FOR $8\text{Al}+2\text{NaAlSi}_3\text{O}_8\rightarrow \text{Na}_2\text{O}+6\text{Si}+5\text{Al}_2\text{O}_3$	211
FIGURE CXC: ENTHALPY AND GIBBS FREE ENERGY PLOT FOR $8\text{Al}+3\text{CaMgSi}_2\text{O}_6\rightarrow \text{Ca}_3\text{Mg}(\text{SiO}_4)_2+2\text{MgAl}_2\text{O}_4+4\text{Si}+2\text{Al}_2\text{O}$	212
FIGURE CXCI: ENTHALPY AND GIBBS FREE ENERGY PLOT FOR $8\text{Al}+3\text{CaMgSi}_2\text{O}_6\rightarrow \text{Ca}_3\text{Al}_2\text{O}_6+3\text{MgAl}_2\text{O}_4+6\text{Si}+2\text{Al}_2\text{O}$	213
FIGURE CXCI: ENTHALPY AND GIBBS FREE ENERGY PLOT FOR $10\text{Al}+3\text{CaFeSi}_2\text{O}_6\rightarrow \text{Ca}_3\text{Al}_2\text{O}_6+3\text{FeSi}_2+4\text{Al}_2\text{O}_3$	214
FIGURE CXCIII: ENTHALPY AND GIBBS FREE ENERGY PLOT FOR $\text{Fe}+\text{Si}\rightarrow \text{FeSi}$	215
FIGURE CXCIV: ENTHALPY AND GIBBS FREE ENERGY PLOT FOR $8\text{Al}+2\text{CaFeSi}_2\text{O}_6\rightarrow \text{Ca}_2\text{Al}_2\text{Si}_2\text{O}_7+\text{Al}_2\text{O}_3+2\text{FeSi}+\text{Si}+2\text{Al}_2\text{O}$	216
FIGURE CXCV: ENTHALPY AND GIBBS FREE ENERGY PLOT FOR $\text{Fe}+2\text{Si}\rightarrow \text{FeSi}_2$	217
FIGURE CXCVI: ENTHALPY AND GIBBS FREE ENERGY PLOT FOR $8\text{Al}+3\text{CaAl}_2\text{Si}_2\text{O}_8\rightarrow 3\text{CaAl}_4\text{O}_7+6\text{Si}+\text{Al}_2\text{O}_3$	218
FIGURE CXCVII: ENTHALPY AND GIBBS FREE ENERGY PLOT FOR $12\text{Al}+2\text{CaMgSi}_2\text{O}_6+2\text{CaAl}_2\text{Si}_2\text{O}_8\rightarrow 4\text{CaAl}_4\text{O}_7+8\text{Si}+2\text{Mg}$	219
FIGURE CXCVIII: ENTHALPY AND GIBBS FREE ENERGY PLOT FOR $20\text{Al}+5\text{CaAl}_2\text{Si}_2\text{O}_8\rightarrow 5\text{CaAl}_4\text{O}_7+10\text{Si}+5\text{Al}_2\text{O}$	220
FIGURE CXCIX: ENTHALPY AND GIBBS FREE ENERGY PLOT FOR $\text{Fe}+2\text{Si}\rightarrow \text{FeSi}_2$	221
FIGURE CC: ENTHALPY AND GIBBS FREE ENERGY PLOT FOR $\text{Fe}+\text{Si}\rightarrow \text{FeSi}$	222
FIGURE CCI: ENTHALPY AND GIBBS FREE ENERGY PLOT FOR $8\text{Al}+2\text{CaFeSi}_2\text{O}_6\rightarrow \text{Ca}_2\text{Al}_2\text{SiO}_7+\text{Al}_2\text{O}_3+2\text{FeSi}+\text{Si}+2\text{Al}_2\text{O}$	223
FIGURE CCII: ENTHALPY AND GIBBS FREE ENERGY PLOT FOR $8\text{Al}+2\text{NaAlSi}_3\text{O}_8\rightarrow \text{Na}_2\text{O}+6\text{Si}+5\text{Al}_2\text{O}_3$ USING LOW-ALBITE	224
FIGURE CCIII: ENTHALPY AND GIBBS FREE ENERGY PLOT FOR $8\text{Al}+2\text{NaAlSi}_3\text{O}_8\rightarrow \text{Na}_2\text{O}+6\text{Si}+5\text{Al}_2\text{O}_3$ USING HIGH-ALBITE	225
FIGURE CCIV: ENTHALPY AND GIBBS FREE ENERGY PLOT FOR $2\text{Al}+\text{Fe}_2\text{O}_3\rightarrow 2\text{Fe}+\text{Al}_2\text{O}_3$	226
FIGURE CCV: ENTHALPY AND GIBBS FREE ENERGY PLOT FOR $4\text{Al}_2\text{O}+\text{Mg}\rightarrow \text{MgAl}_2\text{O}_4+6\text{Al}$	227
FIGURE CCVI: ENTHALPY AND GIBBS FREE ENERGY PLOT FOR $8\text{Al}+3\text{CaAl}_2\text{Si}_2\text{O}_8\rightarrow 3\text{CaAl}_4\text{O}_7+6\text{Si}+\text{Al}_2\text{O}_3$	228
FIGURE CCVII: ENTHALPY AND GIBBS FREE ENERGY PLOT FOR $12\text{Al}+2\text{CaMgSi}_2\text{O}_6+2\text{CaAl}_2\text{Si}_2\text{O}_8\rightarrow 4\text{CaAl}_4\text{O}_7+8\text{Si}+2\text{Mg}$	229
FIGURE CCVIII: IMAGE OF A REACTION PRODUCT USING JSC-1AF SIMULANT AND 19.44% ALUMINUM	242
FIGURE CCIX: IMAGE OF A REACTION PRODUCT USING JSC-1AF SIMULANT AND 24.45% ALUMINUM	242
FIGURE CCX: IMAGE OF A REACTION PRODUCT USING JSC-1AF SIMULANT AND 28.85% ALUMINUM	242
FIGURE CCXI: IMAGE OF A REACTION PRODUCT USING JSC-1AF SIMULANT AND 33.33% ALUMINUM	242
FIGURE CCXII: IMAGE OF A REACTION PRODUCT USING JSC-1A SIMULANT AND 19.44% ALUMINUM	242
FIGURE CCXIII: IMAGE OF A REACTION PRODUCT USING JSC-1A SIMULANT AND 24.45% ALUMINUM	242
FIGURE CCXIV: IMAGE OF A REACTION PRODUCT USING JSC-1A SIMULANT AND 28.85% ALUMINUM	243
FIGURE CCXV: IMAGE OF A REACTION PRODUCT USING JSC-1AF SIMULANT AND 19.44% ALUMINUM	244
FIGURE CCXVI: IMAGE OF A REACTION PRODUCT USING JSC-1AF SIMULANT AND 24.45% ALUMINUM	244
FIGURE CCXVII: IMAGE OF A REACTION PRODUCT USING JSC-1AF SIMULANT AND 28.85% ALUMINUM	244
FIGURE CCXVIII: IMAGE OF A REACTION PRODUCT USING JSC-1AF SIMULANT AND 33.33% ALUMINUM	244
FIGURE CCXIX: IMAGE OF A REACTION PRODUCT USING JSC-1A SIMULANT AND 19.44% ALUMINUM	244
FIGURE CCXX: IMAGE OF A REACTION PRODUCT USING JSC-1A SIMULANT AND 24.45% ALUMINUM	244
FIGURE CCXXI: IMAGE OF A REACTION PRODUCT USING JSC-1A SIMULANT AND 28.85% ALUMINUM	245

LIST OF TABLES

TABLE I: STANDARD ATMOSPHERE MELTING POINTS FOR VARIOUS ENDMEMBER MINERALS WITHIN LUNAR REGOLITH.....	20
TABLE II: MEAN BULK COMPOSITION OF LUNAR REGOLITH AND SIMULANT JSC-1AF ^{45, 47}	23
TABLE III- STANDARD MOLAR ENTHALPIES, ENTROPIES, AND GIBBS FREE ENERGIES OF FORMATION OF SELECTED SPECIES ⁴⁸	24
TABLE IV: EXPERIMENTAL MATRIX OF REACTION PARAMETERS.....	31
TABLE V: POWER APPLICATION RATE FOR JOULE HEATING OF A SAMPLE IN A STANDARD ATMOSPHERE.....	33
TABLE VI: POWER APPLICATION RATE FOR JOULE HEATING OF A SAMPLE IN A VACUUM ENVIRONMENT.....	36
TABLE VII: EDS ANALYSIS OF SPECTRUM 1 SHOWN IN FIGURE XXXIV.....	54
TABLE VIII: EDS ANALYSIS OF SPECTRUM 1 SHOWN IN FIGURE XXXV.....	55
TABLE IX: LEGEND OF IDENTIFIED CHEMICAL SPECIES IN THE DIFFRACTION PATTERN SHOWN IN FIGURE XXXVIII.....	58
TABLE X: LEGEND OF IDENTIFIED CHEMICAL SPECIES IN THE DIFFRACTION PATTERN SHOWN IN FIGURE XXXVIII.....	63
TABLE XI: LEGEND OF IDENTIFIED CHEMICAL SPECIES IN THE DIFFRACTION PATTERN SHOWN IN FIGURE XLIV.....	66
TABLE XII: LEGEND OF IDENTIFIED CHEMICAL SPECIES IN THE DIFFRACTION PATTERN SHOWN IN FIGURE XLV.....	68
TABLE XIII: LEGEND OF IDENTIFIED CHEMICAL SPECIES IN THE DIFFRACTION PATTERN SHOWN IN FIGURE XLVII.....	71
TABLE XIV: IDENTIFIED CHEMICAL SPECIES IN THE DIFFRACTION PATTERNS IN FIGURE XLIX.....	74
TABLE XV: LEGEND OF IDENTIFIED CHEMICAL SPECIES IN THE DIFFRACTION PATTERN SHOWN IN FIGURE L.....	77
TABLE XVI: LEGEND OF IDENTIFIED CHEMICAL SPECIES IN THE DIFFRACTION PATTERN SHOWN IN FIGURE LII.....	80
TABLE XVII: LEGEND OF IDENTIFIED CHEMICAL SPECIES IN THE DIFFRACTION PATTERN SHOWN IN FIGURE LIV.....	83
TABLE XVIII: IDENTIFIED CHEMICAL SPECIES IN THE DIFFRACTION PATTERNS IN FIGURE LVI.....	86
TABLE XIX: IDENTIFIED CHEMICAL SPECIES IN THE REACTION PRODUCTS USING JSC-1AF AND JSC-1A SIMULANTS.....	88
TABLE XX: LEGEND OF IDENTIFIED CHEMICAL SPECIES IN THE DIFFRACTION PATTERN SHOWN IN FIGURE LVIII.....	92
TABLE XXI: LEGEND OF IDENTIFIED CHEMICAL SPECIES IN THE DIFFRACTION PATTERN SHOWN IN FIGURE LIX.....	94
TABLE XXII: LEGEND OF IDENTIFIED CHEMICAL SPECIES IN THE DIFFRACTION PATTERN SHOWN IN FIGURE LX.....	96
TABLE XXIII: LEGEND OF IDENTIFIED CHEMICAL SPECIES IN THE DIFFRACTION PATTERN SHOWN IN FIGURE LXI.....	98
TABLE XXIV: IDENTIFIED CHEMICAL SPECIES IN THE DIFFRACTION PATTERNS IN FIGURE LXII.....	100
TABLE XXV: LEGEND OF IDENTIFIED CHEMICAL SPECIES IN THE DIFFRACTION PATTERN SHOWN IN FIGURE LXIII.....	103
TABLE XXVI: LEGEND OF IDENTIFIED CHEMICAL SPECIES IN THE DIFFRACTION PATTERN SHOWN IN FIGURE LXIV.....	104
TABLE XXVII: LEGEND OF IDENTIFIED CHEMICAL SPECIES IN THE DIFFRACTION PATTERN SHOWN IN FIGURE LXV.....	106
TABLE XXVIII: IDENTIFIED CHEMICAL SPECIES IN THE REACTION PRODUCTS USING JSC-1A SIMULANT.....	108
TABLE XXIX: IDENTIFIED CHEMICAL SPECIES IN THE REACTION PRODUCTS USING JSC-1AF AND JSC-1A SIMULANTS.....	110
TABLE XXX: EDS ANALYSIS OF JSC-1AF REGIONS (VALUES IN ATOMIC %).....	114
TABLE XXXI: EDS ANALYSIS OF JSC-1A REGIONS (VALUES IN ATOMIC %).....	116
TABLE XXXII: MEAN EDS ANALYSIS OF JSC-1AF AND JSC-1A REGIONS (VALUES IN ATOMIC %).....	116
TABLE XXXIII: EDS ANALYSIS OF SPECTRUM 2 SHOWN IN FIGURE XCVIII.....	126
TABLE XXXIV: EDS ANALYSIS OF SPECTRUM 1 SHOWN IN FIGURE XCIX.....	127
TABLE XXXV: EDS ANALYSIS OF SPECTRUM 2 SHOWN IN FIGURE C.....	128
TABLE XXXVI: EDS ANALYSIS OF SPECTRUM 3 SHOWN IN FIGURE CI.....	129
TABLE XXXVII: EDS ANALYSIS OF SPECTRUM 1 SHOWN IN FIGURE CII.....	130
TABLE XXXVIII: EDS ANALYSIS OF SPECTRUM 2 SHOWN IN FIGURE CIII.....	131
TABLE XXXIX: EDS ANALYSIS OF SPECTRUM 1 SHOWN IN FIGURE CIV.....	132
TABLE XL: EDS ANALYSIS OF SPECTRUM 2 SHOWN IN FIGURE CV.....	133
TABLE XLI: EDS ANALYSIS OF SPECTRA 1, 2, AND 3 SHOWN IN FIGURE CVII.....	135
TABLE XLII: EDS ANALYSIS OF SPECTRA 1 AND 2 SHOWN IN FIGURE CVIII.....	137
TABLE XLIII: EDS ANALYSIS OF SPECTRA 2 AND 3 SHOWN IN FIGURE CXI.....	139
TABLE XLIV: EDS ANALYSIS OF SPECTRUM 2 SHOWN IN FIGURE CXII.....	140
TABLE XLV: EDS ANALYSIS OF SPECTRUM 1 SHOWN IN FIGURE CXV.....	143
TABLE XLVI: EDS ANALYSIS OF SPECTRUM 1 SHOWN IN FIGURE CXVI.....	144
TABLE XLVII: EDS ANALYSIS OF SPECTRUM 1 SHOWN IN FIGURE CXVII.....	144

TABLE XLVIII: EDS ANALYSIS OF SPECTRA 2 AND 3 SHOWN IN FIGURE CXVIII	146
TABLE XLIX: EDS ANALYSIS OF SPECTRA 1 AND 2 SHOWN IN FIGURE CXIX.....	147
TABLE L: EDS ANALYSIS OF SPECTRA 1, 2, AND 3 SHOWN IN FIGURE CXXII.....	150
TABLE LI: EDS ANALYSIS OF SPECTRA 1 AND 2 SHOWN IN FIGURE CXXIII.....	152
TABLE LII: EDS ANALYSIS OF SPECTRA 1 AND 3 SHOWN IN FIGURE CXXVI	154
TABLE LIII: EDS ANALYSIS OF SPECTRA 1 AND 2 SHOWN IN FIGURE CXXVII.....	155
TABLE LIV: EDS ANALYSIS OF SPECTRA 1, 2, AND 3 SHOWN IN FIGURE CXXX	158
TABLE LV: EDS ANALYSIS OF SPECTRA 1, 2, AND 3 SHOWN IN FIGURE CLVI.....	168
TABLE LVI: EDS ANALYSIS OF SPECTRA 1, 2, 3, AND 4 SHOWN IN FIGURE CLVII	170
TABLE LVII: EDS ANALYSIS OF SPECTRA 1 AND 2 SHOWN IN FIGURE CLVIII	171
TABLE LVIII: EDS ANALYSIS OF SPECTRA 1, 2, AND 3 SHOWN IN FIGURE CLIX.....	173
TABLE LIX: EDS ANALYSIS OF SPECTRA 1, 2, AND 3 SHOWN IN FIGURE CLX.....	174
TABLE LX: EDS ANALYSIS OF SPECTRA 1, 2, AND 3 SHOWN IN FIGURE CLXI.....	175
TABLE LXI: EDS ANALYSIS OF SPECTRUM 1 SHOWN IN FIGURE CLXII	177
TABLE LXII: EDS ANALYSIS OF SPECTRA 1, 2, AND 3 SHOWN IN FIGURE CLXIII	178
TABLE LXIII: EDS ANALYSIS OF SPECTRA 1, 2, AND 3 SHOWN IN FIGURE CLXIV	180
TABLE LXIV: EDS ANALYSIS OF SPECTRA 1, 2, AND 3 SHOWN IN FIGURE CLXV	181
TABLE LXV: EDS ANALYSIS OF SPECTRA 1, 2, AND 3 SHOWN IN FIGURE CLXVI.....	183
TABLE LXVI: EDS ANALYSIS OF SPECTRA 1, 2, AND 3 SHOWN IN FIGURE CLXVII	184
TABLE LXVII: EDS ANALYSIS OF SPECTRA 1, 2, AND 3 SHOWN IN FIGURE CLXVIII.....	185
TABLE LXVIII: EDS ANALYSIS OF SPECTRA 1, 2, AND 3 SHOWN IN FIGURE CLXIX.....	187
TABLE LXIX: EDS ANALYSIS OF SPECTRA 1, 2, AND 3 SHOWN IN FIGURE CLXX.....	188
TABLE LXX: EDS ANALYSIS OF SPECTRA 1 AND 3 SHOWN IN FIGURE CLXXI.....	189
TABLE LXXI: EDS ANALYSIS OF SPECTRA 1 AND 2 SHOWN IN FIGURE CLXXII.....	190
TABLE LXXII: T-TEST RESULTS FOR MEAN DENSITY DATASETS SHOWN IN FIGURE CLXXIII	192
TABLE LXXIII: T-TEST RESULTS FOR COMPRESSIVE STRENGTH DATASETS SHOWN IN FIGURE CLXXVIII	196
TABLE LXXIV: T-TEST RESULTS FOR REACTION INITIATION ENERGY DATASETS SHOWN IN FIGURE CLXXXI.....	201
TABLE LXXV: T-TEST RESULTS FOR REACTION INITIATION ENERGY DATASETS SHOWN IN FIGURE CLXXXII.....	203
TABLE LXXVI: T-TEST RESULTS FOR REACTION INITIATION ENERGY DATASETS SHOWN IN FIGURE CLXXXIII	204
TABLE LXXVII: BULK COMPOSITION OF MARS REGOLITH (VALUES IN WT.%) ⁵⁸	238
TABLE LXXVIII: STANDARDIZED WT.% FOR BULK COMPONENTS IN JSC-1AF.....	239
TABLE LXXIX: GRAMS PER MOLE FOR BULK COMPONENTS IN JSC-1AF	239
TABLE LXXX: MOLES OF EACH BULK COMPONENT PRESENT IN A 100 G SAMPLE OF JSC-1AF	240
TABLE LXXXI: MOLES OF ALUMINUM REQUIRED TO REDUCE ONE MOLE OF THE RESPECTIVE BULK COMPONENTS	240
TABLE LXXXII: MOLES OF ALUMINUM REQUIRED TO REDUCE TOTAL MOLES OF EACH BULK COMPONENT PRESENT IN A 100G SAMPLE OF REGOLITH	240
TABLE LXXXIII: MOLES OF ALUMINUM REQUIRED TO REDUCE TOTAL MOLES OF EACH THERMODYNAMICALLY FAVORABLE BULK COMPONENT PRESENT IN A 100G SAMPLE OF REGOLITH	241

I. INTRODUCTION

The following section discusses the objective, justification, research overview and significance of this study. The research overview briefly describes oxidation-reduction, thermite, and SHS reactions. A description of reactants used in this study is also provided.

RESEARCH OBJECTIVE

The objective of this study was to conduct an investigation into complex oxidation-reduction reaction behavior by determining the role of reactant stoichiometry, reactant particle size, and reaction environment on the chemical species, microstructure, and compressive strength of the reaction product.

JUSTIFICATION

The bulk of knowledge concerning oxidation-reduction reactions pertains to single, binary, and ternary component systems. This study examined the oxidation-reduction process in a complex mineral and glass assemblage.

RESEARCH OVERVIEW

This study investigated a class of reactions, which are termed geothermite by the author. The term geothermite refers to a thermite-type chemical reaction performed with unrefined minerals and glass that react with a reducing agent. Thermite reactions are exothermic chemical reactions between a metal and metallic oxide.¹ The reaction leads to the formation of a more stable metal oxide and the reduced metal that was initially bound in oxide form.

Thermite reactions are a type of Self-propagating High-temperature Synthesis (SHS) reaction. Many studies have been conducted using SHS reactions; however, prior studies have generally been confined to single, binary, and ternary SHS systems. This study utilized a raw material that had not been chemically refined. The material consisted of naturally occurring minerals and glass obtained from a deposit of volcanic ash. While the particular deposit of volcanic ash was selected due to its similar composition to lunar regolith; theoretically, the reaction could be initiated using most types of particulate derived from rock.

This study examined oxidation-reduction reactions between lunar regolith simulant and powdered aluminum in both a standard atmosphere and a vacuum environment. Two particle

size distributions of regolith simulant were used in this study: JSC-1A (coarse particles), and JSC-1AF (fine particles). The oxidation-reduction reaction used in study exhibited SHS behavior. Reactions exhibiting the SHS phenomenon are capable of producing sufficient heat to continue to react and propagate after the external energy source used to initiate the reaction has been removed.

SIGNIFICANCE

The Constellation program of NASA intends to return humans to the Moon by 2020.² Methods to utilize in-situ lunar resources will allow a more efficient, less costly, and thus a more sustainable human presence on the Moon to be achieved. The knowledge gained in this study could lead to the ability to fabricate useful products from in-situ raw materials on Earth, the Moon, and Mars.

II. BACKGROUND

This section provides a background in several areas related to the present study. Topics related to chemical reactions, intergranular growth and binding, SHS systems, the lunar environment and its simulation, characterization methods and material properties, and statistical analysis are discussed.

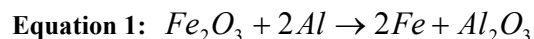
A. Chemical Reactions

The following section discusses oxidation-reduction reactions, Self-propagating High-temperature Synthesis (SHS), particle surface area, and thermodynamics and kinetics of reactions. The defining characteristics of oxidation-reduction reactions, transfer of electrons and charge state, are discussed. Parameters that affect propagation of SHS reactions, and thermodynamic quantities such as enthalpy and Gibbs free energy are also discussed.

Oxidation-Reduction Reactions

Oxidation-reduction reactions involve transfer of one or more electrons between reactants.³ Of the non-metallic elements, fluorine has the greatest affinity for shared electrons, followed by oxygen and nitrogen.

An example of an oxidation-reduction reaction is given in Equation 1.



Equation 1 is a thermite reaction and is capable of producing very high temperatures. In regards to the reactants in Equation 1, each atom of iron in Fe_2O_3 carries a charge of +3, and each atom of oxygen has a charge of -2. Each atom of aluminum in elemental aluminum has a charge of 0. After the reaction completes, elemental iron has a charge of 0. Each aluminum atom has a charge of +3 and each atom of oxygen has a charge of -2. Equation 1 is referred to as an oxidation-reduction reaction due to the transfer of charge or electrons between atoms during the reaction.

When heat generated by a thermite reaction is sufficient to melt at least one reactant, differences between the specific gravity of the metal and metal oxide can allow their segregation.⁴

Self-propagating High-temperature Synthesis

Self-propagating High-temperature Synthesis (SHS) can be achieved in chemical systems that are able to sustain a combustion wave during exothermic reactions.⁵ Products of SHS reactions generally exhibit a high porosity: theoretical densities are generally around 50%. Porous ceramic-composite materials can be used to filter particulate from liquids and gases.⁶ SHS processes can also produce non-equilibrium, metastable phases.⁷ Several variables influence the SHS process, some of which include stoichiometry of the reactants, particle size, green density, gas pressure, reactant volume, and method of ignition.⁵ A deviation in one of the variables can result in incomplete reaction propagation.

Multi-component SHS systems incorporate reaction steps that occur either simultaneously or sequentially.⁷ When reaction steps occur sequentially, the products of the prior reaction step can be incorporated into the reactants of the subsequent reaction step.

The reactant particle size can influence the degree of reaction self-propagation, the amount of time necessary for the reaction to complete, along with the temperature gradient and velocity of the combustion wave.⁵

A higher degree of compaction can be obtained with particles which are not very hard and which have a large distribution of particle sizes.⁵ It has been observed that it is difficult to initiate reactions within green compacts having either extremely high or extremely low densities. It is theorized that a moderate density is needed to provide adequate particle contact and at the same time not to lose excessive heat from increased thermal conductivities induced by a higher density green compact. The porosity of the compact also defines the amount of void space available for molten metal to fill. When the pore volume is approximately equal to the volume of molten metal, an optimum density can be achieved. The density of the reaction product is influenced by the reactant compact density, the molar density difference between reactants and products, and release of gases during the reaction.

Reactant compacts having small volumes are more difficult to ignite due to an increase in radial heat loss.⁵ Combustion rates have been shown to be dependent on the thickness of the reactant compact.

No processes currently exist to solely use the heat produced from an SHS reaction to allow rapid, low-cost, densification to over 97% theoretical values.⁴ However, a study by *Horvitz and Gotman* achieved theoretical densities up to 98% fabricating MgAl₂O₄-TiAl

composites using pressure-assisted SHS.⁸ Degassing during the reaction and changes in volume between reactants and products are two main factors preventing full densification of the product.⁴

Particle Surface Area

The available surface area for reactions to occur depends on particle size.⁹ As particle size decreases, the surface area available for reactions increases. Reaction rate is largely influenced by available surface area and more specifically by the amount of actual contact between particles. Pressing reactant mixtures can provide increased surface contact between particles, but typical cold-pressed pellets still have 20-40% porosity. Heating the pellet while pressing can further increase the surface contact between particles, in a process known as hot pressing.

Thermodynamics and Kinetics

The field of thermodynamics involves the study of whether physical and chemical reactions can occur; while kinetics involves determining how quickly the reactions will occur.¹⁰ In order for a reaction to occur, it must cause the total energy of the system to decrease. However, just because a reaction decreases the total energy of the system does not mean it will occur. In most cases the rate a reaction occurs is dependent exponentially on temperature given by the equation:

$$\text{Equation 2: } \text{Rate} = C \exp\left(\frac{-Q}{RT}\right)$$

In the above equation, C is a constant, Q is the activation energy of the process, R is the gas constant, and T is absolute temperature.

Equilibrium within a system can only be maintained if heating and cooling are performed at extremely slow rates, which are often unpractical.¹¹ When non-equilibrium cooling occurs, referred to as supercooling, phase transformations occur at lower than the equilibrium temperatures. Non-equilibrium heating is referred to as superheating, which causes phase transformations to occur at higher temperatures.

The difference between the enthalpy of the products of a chemical reaction and the reactants is referred to as a change in enthalpy, or ΔH .¹² Reactions that produce heat are referred to as exothermic and have a negative ΔH . Reactions that absorb heat have a positive ΔH and are referred to as endothermic. Stable elements at 298 K are assigned a value of zero for their enthalpy.

The difference between the amount of order present within the products and the reactant in a reaction is referred to as the change in entropy, or ΔS .¹² Entropy is the measure of disorder in a substance on an atomic scale. For example, the atoms in a crystalline solid have more order than a liquid. Since the liquid has less atomic order, it would have greater entropy.

For a closed system, the change in Gibbs free energy is given by Equation 3.

$$\text{Equation 3: } \Delta G = \Delta H - T\Delta S$$

The change in Gibbs free energy, ΔG in a given reaction, determines whether the reaction is thermodynamically favorable.¹² Reactions that have a negative ΔG are favorable by thermodynamics; while reactions with a positive ΔG are unfavorable thermodynamically.

Heat can be transferred by conduction, convection, and radiation.¹³ Thermal conduction involves the transfer of heat through collision of atoms vibrating quickly with those vibrating more slowly. Convection involves the transfer of heat by the migration of molecules. Heat is radiated by the emission of electromagnetic waves. The rate that energy is being radiated by an object is described by Stefan's law using the equation:

$$\text{Equation 4: } P = T^4 \sigma A e$$

In Equation 4, P refers to the power in watts, T is the temperature of the surface in Kelvin, e is the emissivity, A is the object's surface area, and σ is the constant $5.6695 \cdot 10^{-8}$ $\text{W/m}^2 \cdot \text{K}^4$.

Heat capacity refers to the ratio of heat applied or withdrawn from a system compared with the temperature change of the system.¹²

$$\text{Equation 5: } C = \frac{q}{\Delta T}$$

In Equation 5, C is the heat capacity, q is heat, and ΔT is the change in temperature. Specific heat is the heat capacity per unit quantity, typically a gram. Chemical species within a mixture that have different heat capacities can cause gradients in temperature within the mixture during uniform heating. Materials with large heat capacities are good thermal insulators, while those with low heat capacity are good thermal conductors.

B. Intergranular Growth and Binding

The following section discusses the processes of sintering and diffusion, properties of ceramics and glasses, and mechanical properties of materials. Stages of sintering, formation of glasses, nucleation of crystals, and relationships between particle size and porosity to the strength and elastic modulus of materials are discussed.

Sintering

Sintering is a processing method that uses high-temperature self-diffusion that removes voids between particles.¹⁴ Generally, the higher the porosity in a ceramic material, the lower its strength. Bonding will begin to occur between powders when heated to a temperature over half the melting point.¹⁵ During the sintering process, a decrease in surface area occurs and the strength of the powder compact is increased. Liquid phase sintering involves coexistence of a liquid phase with the compact particles at sintering temperatures. Generally the presence of a liquid will increase the rate of bonding between particles. The presence of liquid during sintering also induces an internal force between particles through capillary action, which creates a denser product and often eliminates the need for pressing. The presence of liquid between particles allows easier rearrangement of particles with non-uniform shapes and promotes more efficient particle packing. Many times the phase that liquefies during sintering will have a lower hardness than the phase with a higher melting point, which allows a more ductile material to be formed. Some disadvantages of liquid phase sintering include distortion of the compact shape due to formation of excess liquid. Liquid phase sintering is less predictable due to the higher

reaction rates and presence of multiple phases (solid, liquid, and/or gas). Activated sintering uses an additional solid state component to increase the rate of inter-particle bonding.

The first stage of liquid phase sintering is referred to as rearrangement.¹⁵ Once temperatures are high enough to form a liquid phase, the liquid phase wets the solid phase particles. Capillary force decreases the porosity of the compact and the interfacial energy. The viscosity of the compact increases as the porosity decreases, which decreases the densification rate. The quantity of liquid, particle sizes, and solid phase solubility dictates the densification that can occur through rearrangement. High green densities and irregular particle shape can inhibit particle rearrangement.

During the second phase of liquid sintering (solution-reprecipitation) smaller grains go into solution with the liquid.¹⁵ The process creates a concentration gradient in the liquid and causes the coarse grains to grow by means of diffusion. The solution-reprecipitation process also further densifies the compact.

The third phase is solid state controlled sintering.¹⁵ A solid framework exists in the material and further slows the densification process. The framework prevents further rearrangement of particles; however, grain growth still occurs through diffusion. Trapped gases will cause pores to enlarge and thereby lower the pressure within them. Solid state sintering occurs at grain boundaries and growth will occur through solution re-precipitation, coalescence of grains, or solid state diffusion.

Ceramics and Glasses

The inability of ceramics to plastically deform at room temperature prevents ceramics from being used in many applications where metals and polymers can be used.¹⁴ Machinability problems, along with high melting points that inhibit casting, further reduce industrial applications for ceramics. However, ceramics are good candidates for materials used in extreme conditions.

Glasses are formed by cooling a liquid fast enough to avoid crystallization and are generally considered metastable.¹⁴ Glasses have a thermodynamic driving force to crystallize, however the kinetics are generally so slow that there is no observable crystallization. SiO₂ is a primary glass forming compound due to its suitable structure and slow crystallization rate from liquid. Al₂O₃ will form glasses under some circumstances. Al₂O₃ and TiO₂ are considered

intermediate oxides, which do not form glasses on their own but will form glasses in the presence of glass formers such as SiO₂. Network modifiers are compounds that do not form glasses, but modify properties such as the softening point of the glass or its hardness. MgO, CaO, Na₂O, and K₂O are examples of network modifiers. Vitrification is a process that binds particles together with glasses.¹⁴

Crystallization from liquid to solid does not occur simultaneously through a phase.¹⁶ The term, phase, refers to a defined volume in a system that has uniform properties.¹² A homogeneous system contains only one phase; while heterogeneous systems contain two or more phases. Crystallization begins from distinct locations and proceeds outward from regions referred to as nuclei.¹⁶ The process of forming regions of longer range atomic order than is usually found in the liquid phase is termed nucleation. Nucleation occurs in two types: homogeneous and heterogeneous. Homogeneous nucleation involves formation of nuclei of the same composition as the material that will crystallize. Heterogeneous nucleation involves formation of nuclei that are chemically different than the material that will crystallize. Homogeneous nucleation tends to occur when a liquid phase is highly supersaturated or supercooled. Heterogeneous nucleation generally depends on the similarity between the structure of the nuclei and the phase being crystallized.

The growth of crystals depends on the rate that a glass structure can be re-arranged into a crystal lattice and the rate at which energy from the phase transformation can be eliminated.¹⁶ The crystal structure of a material can greatly influence properties such as hardness.¹⁴

Mechanical Properties

The grain size of a sample affects the mechanical properties.¹¹ In polycrystalline metals, increasing the surface area of grain boundaries impedes dislocations, increasing material strength. Grain boundaries act as barriers to dislocations due to a difference in orientation of grain boundaries with respect to each other. The yield strength of many materials is described by the Hall-Petch equation shown in Equation 6.

$$\text{Equation 6: } \sigma_y = \sigma_0 + k_y d^{-1/2}$$

In the above equation d is the average grain size, and σ_0 and k_y are constants for a given material. The two basic types of material failure are deformation and fracture.¹⁷ Deformation involves a change in size or shape of a material that degrades or destroys its functionality. Fracture involves the breaking of a material into two or more pieces. Deformation can occur in two manners: elastic and plastic. A material deforming in an elastic manner will recover as soon as the load is removed. The modulus of elasticity defines a region of constant proportion between stress and strain. When a material deforms plastically, the deformation is permanent and the material does not recover. Generally, during plastic deformation, a small increase in stress will cause a significant deformation or yield. The yield strength, σ_0 , of a material defines where the region of plastic deformation begins. A material that can withstand large amounts of plastic deformation has a ductile behavior; while materials that cannot, exhibit brittle behavior. A fracture that occurs rapidly with little plastic deformation is called brittle fracture. Ductile fracture occurs more gradually and has a larger amount of plastic deformation. During elastic deformation, chemical bonds are stretched but not broken.¹⁷

The elastic modulus of a material is the slope of the stress-strain curve within the linear region of stress-strain proportionality, and is given by Equation 7.¹⁸

$$\text{Equation 7: } E = \frac{\sigma}{\epsilon}$$

In Equation 7, E is the elastic modulus, σ is the stress, and ϵ is the strain. A material that exhibits elastic deformation will revert to an unstrained state when the load on the material is removed.¹⁸ The elastic limit occurs at the greatest stress that the material behaves elastically. Strain is derived by dividing the elongation measured between two points on the material by the original distance between the points.

The elastic modulus of a ceramic material decreases with increasing porosity. As porosity increases, the rate of change in the elastic modulus decreases. An equation that can be used to relate the porosity of a material to the elastic modulus is shown in Equation 8.

$$\text{Equation 8: } E = E_0(1 - f_1p + f_2p^2)$$

In Equation 8, E_0 is the elastic modulus of the fully dense material, f_1 and f_2 are constants, and p is the fraction of porosity for the material. The shape of the pores dictates the constants f_1 and f_2

When performing compressive strength testing, the ratio of the length, L to the diameter, d of a specimen is generally between 1 and 3.¹⁷ If a specimen has a larger length, buckling can occur due to imperfections in geometry of the specimen, such as ends that are not completely parallel. If the length of the specimen is too small, the specimen can deform into a barrel shape. The compression induces an increase in diameter of specimen perpendicular to the applied force. Friction holds the ends of the sample in place, but the center region can deform. The end result is that specimens that are too short or too long can alter the measurement of the actual compressive strength of the material. Ductile materials generally use an L/d ratio of 3, while brittle materials use an L/d ratio between 1.5 and 2.

The compressive strength, S , (MPa) of a material is given by Equation 9.¹⁹

$$\text{Equation 9: } S = \frac{P_{\max}}{A}$$

In Equation 9, P_{\max} (N) refers to the maximum load, and A is the original cross-sectional area (mm^2).

C. SHS Systems

This section discusses various SHS systems utilizing aluminum in the reactants. SHS systems involving iron oxide, titanium oxide, silicon oxide, and magnesium oxide are discussed. Formation of aluminum nitride, geothermite reactions, nanoparticle SHS, and SHS in a vacuum environment will also be discussed.

Aluminum-Iron Oxide SHS Systems

A thermite reaction involving aluminum and iron oxide can achieve temperatures near 3000 °C.²⁰ The temperature required to initiate the reaction is 1000 °C. A thin Al_2O_3 coating forms over aluminum particles in oxidizing environments.²¹ The oxide coating cracks when exposed to elevated temperatures due to the differences in thermal expansion coefficients

between aluminum and Al_2O_3 . The cracking of the shell allows molten aluminum to interact with other reactants. Several methods can be used to initiate a thermite reaction: two of which are joule heating of a wire, and the use of an oxyacetylene torch.²⁰ The addition of Al_2O_3 to thermite reactions utilizing aluminum as a reducing agent slows the reaction rate and can lower reaction temperatures allowing better control of the reaction.

A prior study performed by *Duraes, et.al*, utilizing a thermite reaction between Fe_2O_3 and aluminum, analyzed the chemical species produced during reactions involving different reactant stoichiometries of iron oxide and aluminum.²² Two chemical species in the products that were common to all the stoichiometries used in the study were $\alpha\text{-Al}_2\text{O}_3$ and Fe. Fe_3Al was present in larger quantities in mixtures with greater aluminum content, while FeAl_2O_4 , was present in mixtures with more available oxygen from Fe_2O_3 . Order-disorder phase transformations occur near the Fe_3Al composition in the Fe-Al system, which result in non-uniform placement of Al atoms within the lattice. Partially disordered chemical species result in a decrease in peak intensity and an increase in peak width of X-ray diffraction patterns.

The study by *Duraes, et.al* proposed a mechanism for the reaction, which involved the reduction of Fe_2O_3 to Fe_3O_4 and FeO, along with oxygen being released at a high temperature. Oxygen reacted with melted or vaporized Al, forming alumina and releasing heat.²²

Another study, performed by *Mei, et. al* investigated reaction mechanisms of an aluminum-iron oxide thermite reaction. The interface between liquid aluminum and sintered Fe_2O_3 was studied using SEM.¹ Two phases of FeO_x were found, which were termed phase I and phase II since precise identification was not possible using EDX. A layer of phase I of FeO_x was observed adjacent to aluminum, followed by a composite of Al_2O_3 and FeAl_x . Another layer of phase I of FeO_x was on the other side of the Al_2O_3 and FeAl_x layer. A layer of phase II of FeO_x followed the layer of phase I of FeO_x . The layer of phase II of FeO_x was adjacent to Fe_2O_3 .

DTA was used for analysis of reaction temperatures in both a powdered and pressed sample.¹ There was an endothermic reaction peak observed at 660 °C and two exothermic reaction peaks observed at 960 °C and 1060 °C. The peak at 660 °C was observed in both powdered and pressed samples, and was formed due to the melting of aluminum. The exothermic peaks were observed at lower temperatures in the pressed sample. It is thought that a larger surface area of contact between the aluminum and Fe_2O_3 in the pressed sample allows easier reaction initiation. Crystalline needles, identified as aluminum were found at the top

center of the specimen, but not at the edges indicating that aluminum vapor was generated during the reaction and deposited on the surface. Since reaction heat was more easily lost along the edges, the crystalline needles were not observed.

XRD analysis of a powdered sample synthesized at 960 °C showed diffraction peaks for Fe₃O₄ and aluminum.¹ Diffraction peaks for Al₂O₃, Fe, and FeAl₂O₄ were found in the sample synthesized at 1060 °C. A sample taken from the top surface of the sample synthesized at 1060 °C showed diffraction peaks for Fe₂O₃ and Fe₃O₄.

Other SHS Systems

Research by *Logan and Walton* investigated the affects of particle size (-100 and -300 mesh) and compaction (loose powder and pressed at 66 MPa) in several systems.²⁰ All reactions were performed in a preheated furnace. Reactions were performed in slip cast fused silica crucibles, and thermocouples were placed within the samples to monitor temperatures. Reactant mixtures in the TiO₂ and Al system could only be initiated in loose powders using -300 mesh aluminum. Reaction mixtures using both -100 and -300 mesh TiO₂ particle sizes achieved reaction initiation. The combustion wave traveled from the surface to the base of the specimen, at an approximate rate of 0.4 mm/s. High intensity diffraction peaks for TiN and α-Al₂O₃, and low intensity diffraction peaks for TiO₂ were observed in XRD patterns. Reaction mixtures having loose particles initiated between 540-650 °C, had a heating rate of 28 °C/min. Pressed samples exhibited a faster heating rate, near 42 °C/min. Initiation of the reaction occurred around 870-980 °C. Reactions using a finer particle size of aluminum initiated at lower temperatures than reactions using coarse grained aluminum regardless of TiO₂ particle size.

Prior work performed by *Cutler, et.al* investigated SHS synthesis processes in several alumina-metal carbide systems. One result of their study indicated that the reaction initiation temperature is affected by both particle size and reactant stoichiometry. Reaction initiation temperatures were observed to increase with carbon content in the formation of SiC and MgO. Temperatures of reaction initiation also increased with an increase in reactant particle size.⁴

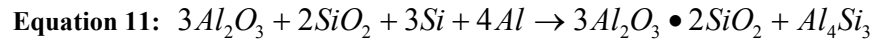
Spinel was produced by *Ping, et.al* using powdered Al and MgO as reactants.²³ The mixtures were milled and then uniaxially pressed at ~30 MPa. Synthesis was conducted by heating the samples slowly to 700 °C in an argon atmosphere. The temperature was held at 700 °C for two hours, then increased to 1000 °C for four hours while changing the atmosphere from

argon to air. The temperature was decreased to 1200 °C for eight hours. Quantitative analysis indicated that around ~55% MgAl₂O₄, ~25%Al₂O₃, and ~20% MgO were formed. Other samples were heated to 1300 °C for two hours following the temperature hold at 1200 °C. Quantitative analysis indicated that ~90% of the chemical species present were MgAl₂O₄, after the further processing at 1300 °C.

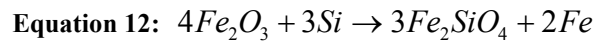
More complex SHS reactions, utilizing either aluminum or magnesium as reducing agents, were discussed by Karpukhin, et. Al. In reactions utilizing aluminum, the first reaction step involved Equation 10.⁷



The second reaction step used both the products and reactants of the first reaction step to produce mullite and an intermetallic aluminum-silicide given by Equation 11.⁷



The second reaction step was preheated in order to sustain the reaction. SHS reactions also have the potential to be used to bind radioactive wastes into structures that are highly insoluble.⁵ One investigation used the reaction,



The reaction in described in Equation 12 created a polysilicate framework in order to incorporate the radioactive wastes.

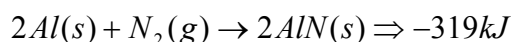
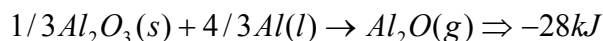
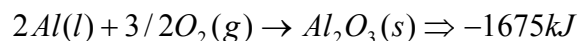
Formation of Aluminum Nitrides in SHS Systems

The vast majority of literature dealing with the synthesis of aluminum nitrides and oxynitrides use nitrogen pressures well in excess of those found in ambient conditions. A study by *Gromov and Vereshchagin*, however, was performed under ambient pressures using an SHS reaction to synthesize aluminum nitride. The ignition temperature range for an aluminum powder with a mean particle diameter of .1µm ranged from 750± 100 K to 820± 100 K.²⁴ The samples were ignited by means of joule heating of a NiCr wire. The reaction proceeded in two

stages. In the first stage a red combustion wave migrated through the sample. Pyrometer measurements for temperatures in the first stage did not exceed 1400 ± 100 K. The second stage occurred more quickly than the first, and began in the interior and propagated through the sample. Thermocouple measurements indicated temperatures ranging from 2500 ± 50 K to 2800 ± 50 K. Bright white radiation was observed during the second stage. Analysis of an argon quenched first stage product indicated a bound nitrogen content of $.5 \pm .3$ mass%, and an Al metal content of 70 ± 1.4 mass%. Primary products included unreacted aluminum, amorphous aluminum oxides, and traces of AlN. Analysis of the second stage indicated an Al metal content of 11.0 ± 1.4 mass%, with $18.2 \pm .3$ mass% bound nitrogen. The aluminum powder consisted of spherical particles prior to the reaction. After the reaction, the microstructure was an acicular network. It is hypothesized that Al_2O_3 surrounded AlN and prevented oxidation of the nitride. Thermodynamics do not favor the formation of AlN. Lower temperatures, such as those seen in the first stage of combustion, allow diffusion of oxygen and the oxidation of the nitride. The proposed reaction steps of *Gromov and Vereshchagin* are listed below:

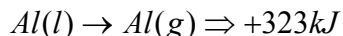
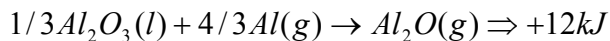
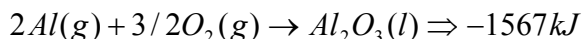
Equation Set 13

First Combustion Stage: ²⁴



Equation Set 14

Second Combustion Stage: ²⁴



Three methods which can produce AlN using SHS reactions include the reaction of an Al and AlN mixture in a nitrogen atmosphere; the reaction of Al, AlN, and salt in a nitrogen atmosphere; and the reaction of an Al and NaN_3 mixture in a nitrogen atmosphere.²⁵

A study performed by *Zakorzhevskii, et. al* used a nitrogen pressure of seven MPa for AlN synthesis.²⁵ AlN was found to take on different colors depending on the amount of aluminum used in the reaction. From low to high aluminum contents, the colors ranged from

white, to greenish-white, to pale yellow. The temperatures of reaction ranged from 1570° C to 3030° C. At high combustion temperatures, AlN fibers were formed having a thickness around 0.1 μm and up to 20 μm in length. Crystallites were also formed having a thickness of 1-2 μm and lengths up to 20 μm. The thin fibers were likely the result of AlN deposition from the vapor phase, as was the growth of crystallites occurs during cooling. The high speed of the combustion wave created a nitrogen pressure gradient across the combustion wave. The nitrogen pressure dropped after passage of the combustion wave, which allowed partial dissociation of AlN. When the nitrogen pressure reached equilibrium, deposition of AlN occurred and growth of crystallites occurred.

A study conducted by *Guojian, et. al* investigated the synthesis of AlN whiskers by an SHS method.²⁶ Aluminum powder with an average particle size of ~25 μm was ball milled with AlN powder having an average particle size of ~6 μm. The mixture was placed into a graphite vessel under a nitrogen pressure of 1 to 10 MPa. An SHS reaction was initiated using a titanium powder compact. Several different whisker morphologies were observed, including hexagonal, branched, dendritic, layered, and star-like. Some whiskers had a stacked structure of AlN single crystals. The whiskers had diameters between 0.01-20 μm. XRD analysis identified the presence of hexagonal AlN, PDF# 25-1133.

Several mechanisms can be used to explain AlN whisker growth. Whisker growth by the VS (Vapor-Solid) mechanism involves super-saturation of vapor phase atoms.²⁷ Low super-saturation conditions result in good whisker growth, high super-saturation conditions results in nucleation of powders, and medium super-saturation results in dendritic growth and/or spherical particle nucleation. Growth by the VLS (Vapor feed gases, Liquid catalyst, and Solid whisker) mechanism involves a liquid catalyst. Vapor is deposited on the catalyst since it is a preferred deposition site. Growth occurs by precipitation from the super-saturated liquid. Impurities play an important role in growth by the VLS mechanism. Upon cooling, a spherical shape formed to terminate whiskers formed by the VLS mechanism. High temperatures can result in evaporation of the droplet terminating an AlN whisker, resulting in a change in growth mechanism from VLS to VS. AlN whiskers can also be formed by a VTR (Vapor Transaction Reaction) mechanism using CVD (Chemical Vapor Deposition). One VTR mechanism involves vaporization of aluminum powder, reaction with N₂, and nucleation. Growth of the whiskers then occurs by the VLS or VS mechanisms within the VTR process.

Geothermite Systems

Minimal literature exists for reactions using thermite-type reactions with a mixture of minerals and glass. A study by *Maltsev, et.al* was conducted using SHS reactions for mixtures of sand, kaolin, and ash with aluminum as the reducing agent.²⁸ The temperature of reaction initiation was found to occur between 650-850 °C. Reactions were performed in a muffle furnace and the samples press-packed to dimensions of 40x40x10 mm. Temperatures up to 1800 °C were measured by thermocouple. An increase in particle size was shown to decrease the velocity of combustion wave propagation. Discussion of experimental procedures and results were minimal.

An unpublished work by *Urakaev, et.al* referenced the use of pyrrhotite, manganese, and chromite ores in thermite reactions; However, no details were provided with respect to experimental procedures or results.²⁹

Nanoparticle SHS

The rate of reactions involving mixtures of solid fuels and oxidizers was controlled by mass diffusion.³⁰ Decreasing the distance between the fuel and the oxidizer increased the rate of reaction. The distance was decreased through the use of nano-particles in the reaction.

Research by *Prentice, et. al* was conducted using nano-particles of Fe₂O₃ and SiO₂ in a nano-thermite reaction with aluminum.³⁰ The use of SiO₂ in reactions, which was less energetic than Fe₂O₃, allowed the rate of energy release to be controlled. The optimum ratio of Al:Fe₂O₃ was shown to be 1.2 in a prior study. Velocity of the combustion wave was reduced as weight percent SiO₂ increased. SiO₂ has a lower thermal conductivity (1.38 W/m K) than Fe₂O₃ (20.0 W/m K), which meant that SiO₂ acted as a heat sink. The addition of Al₂O₃ in quantities of less than 2 wt.% increased the strength of metallic alloys synthesized by SHS. Larger quantities of Al₂O₃ significantly decreased wave propagation speed.

Vacuum SHS

Conducting SHS reactions in vacuum using reactants that underwent volatilization with the intent on producing a low-porosity, coherent product, required degassing of the reactants prior to reaction initiation.³¹ If degassing was not performed, large quantities of gas were emitted during

the reaction forming cracks and porosity. A study performed by *Chernyshev, et. al* utilizing an SHS process in the Ti-Al system in vacuum found that temperatures of propagation in the vacuum were 130-160 °C higher than in air. It was also found that the temperature of propagation was 50-60 °C lower than the melting temperature of aluminum when conducted in air, and 70-100 °C higher than the aluminum melting temperature in vacuum.

Research involving SHS processes in vacuum was conducted by *Shabalin, et. al* investigating reactions between titanium, zirconium, and hafnium with carbon, boron, and silicon.³² The chamber was pumped down to 1-5 pascals prior to the reaction. Reaction initiation was accomplished using a 0.5 mm diameter wire composed of tungsten or molybdenum, and a 50 Hz alternating current ranging between 5 and 30 amps. Intensive degassing was observed during the process, which was induced by the high temperatures. Degassing of the sample caused chamber pressures to increase to 0.1 MPa and higher.

D. Lunar Environment, Resource Utilization, and Simulation

This section will discuss aspects of the lunar environment, potential methods to utilize lunar resources, simulation of the lunar environment, and properties of lunar regolith simulant. Formation and composition of lunar regolith, characteristics of the lunar surface environment, composition of lunar regolith simulant, fabrication of materials from lunar regolith simulant, and simplified thermodynamics of oxidation-reduction reactions between aluminum and lunar regolith simulant bulk components are discussed.

Lunar Regolith and Environment

The mass of the Moon is smaller than the Earth, which results in a smaller escape velocity.³³ The small escape velocity does not allow the Moon to maintain an appreciable atmosphere. The lunar atmosphere is extremely small, exerting a pressure of less than 10^{-7} Torr. In comparison, the standard pressure on Earth is 760 Torr. The negligible atmosphere prevents retention of solar energy and allows the full intensity of solar wind, cosmic rays, and meteoroids to bombard the lunar surface. Particles from the solar wind including hydrogen, helium, and carbon accumulate in the lunar regolith. In addition, large changes in temperature ranging from 135 °C to -130 °C occur due to the absence of insulating atmospheric gases. The only significant

process of weathering and erosion that occurs on the Moon is due to meteoroid impact, since no liquid water can exist at the surface.

Over 380 kg of lunar samples were brought to Earth from the Apollo and Luna missions.³³ Typical lunar regolith is composed of over 95% particles that are smaller than 1 mm.³⁴ For the particles less than 1 mm, about 50% are smaller than 60 μm , and 10-20% are smaller than 20 μm . The particles that compose the regolith are very irregularly shaped, which gives them a large surface area. The large surface area and non-uniform particle shapes prevent efficient packing. After thorough compression and packing, porosity still ranges from 40-50%.

Lunar regolith contains five types of particles, breccia fragments, glasses, mineral fragments, crystalline rock fragments, and agglutinates.³⁵ The density of a lunar sample taken from a maria region retrieved on Apollo 12, had a density of $3.10 \pm .01 \text{ g/cm}^3$. The density of a sample taken from a highland region on Apollo 16 had a density of $2.79 \pm .01 \text{ g/cm}^3$.

A study of sorption properties of actual lunar regolith conducted by Robens, et.al found no significant differences of sorption between mare and highland regions.³⁵ The study found that regolith does not store water well due to having a low specific surface area, surface properties between hydrophobic and hydrophilic in character, and little porosity at the nano-scale. Since the regolith can not support liquid water, features such as permafrost will not occur.

Lunar regolith contains nanophase Fe^0 that is not found naturally on Earth.³⁴ The low fugacity of oxygen present at the lunar surface allowed native iron to form during initial crystallization. The majority of Fe^0 was formed by a reduction process that is induced by meteoroid impact. The high hydrogen concentration found at the lunar surface, which is deposited by the solar wind, provides a reducing environment conducive to the formation of nanophase Fe^0 . The iron particles are typically 3-33 nm in size. Microwave energy has been shown to couple with the nanophase iron, which could allow a more efficient means of melting and sintering lunar regolith.

Igneous rocks are the predominant rock type found on the Moon. Igneous rocks are formed through the crystallization of silicate melts.³³ The formation of igneous rocks on the Moon differs from those formed on Earth in both formation temperatures and partial pressures of oxygen present during formation. The crystallization temperatures are 100-150 $^{\circ}\text{C}$ higher on the Moon than Earth due to the lack of water. In addition, iron does not exist in the 3^+ valence, but can exist in elemental state on the surface due to the low fugacity of oxygen.

Breccias are another rock type common at the lunar surface. Breccias are a mixture of regolith and rock that are cemented together by a process of shock-metamorphism, induced by the impact of meteoroids. The majority of minerals within lunar rocks are silicates. Lunar basalts contain approximately 50% pyroxenes, 20-30% plagioclase, and 0-20% olivine by volume.

Pyroxenes are minerals which display a large solid solution, and have Ca, Fe, and Mg as major constituents.³³ The endmembers of said solid solutions include diopside ($\text{CaMgSi}_2\text{O}_6$), hedenbergite ($\text{CaFeSi}_2\text{O}_6$), ferrosilite ($\text{Fe}_2\text{Si}_2\text{O}_6$), and enstatite ($\text{Mg}_2\text{Si}_2\text{O}_6$).

Calcium-rich plagioclase is the predominant feldspar on the moon.³³ The endmembers of the plagioclase feldspar solid solution are anorthite ($\text{CaAl}_2\text{Si}_2\text{O}_8$), and albite ($\text{NaAlSi}_3\text{O}_8$). Anorthite has a high degree of ordering in its structure due to having an equivalent ratio of aluminum and silicon atoms.³⁶ The structure consists of alternating aluminum and silicon tetrahedra. Albite exists in both high and low ordered states. The aluminum and silicon atoms are disordered in high albite and ordered in low albite. The mare basalts have compositions ranging from 98-74 mole % anorthite.³³ Highland rocks range from 90-99 mole % anorthite.

The endmembers of the olivine solid solution series are forsterite (Mg_2SiO_4) and fayalite (Fe_2SiO_4).³³ In the mare basalts there are a wide range of compositions, ranging from 20-70 mole % fayalite, which translates to 30-80 mole % forsterite. The composition of the highland regions have a narrower range of 7-18 mole % fayalite, which corresponds to 82-93 mole % forsterite.

Most lunar regolith compositions have a liquidus around 1200° C.³⁷ A low viscosity melt can be formed with most lunar regolith compositions at temperatures around 1400° C.

Table I: Standard Atmosphere Melting Points for Various Endmember Minerals within Lunar Regolith

	Melting Point (° C)
Anorthite	1553 ³⁶
Albite	1118 ³⁶
Forsterite	1890 ³⁶
Fayalite	1205 ³⁶
Diopside	1391.5 ³⁸
Hedenbergite	965 ³⁹
Ferrosilite	960 ⁴⁰
Enstatite	1557-1600 ⁴¹ Incongruent

The mineral enstatite exhibits incongruent melting.⁴¹ At 1557 °C a liquid slightly silica rich coexists with forsterite crystals. Forsterite dissolves fully into liquid silicate melt, and yields the original enstatite composition at 1600 °C.

In-Situ Resource Utilization (ISRU)

There have been many studies performed with respect to lunar In-Situ Resource Utilization (ISRU). Brief discussions on other studies that are most pertinent to the subjects covered in this study are provided.

Devices that concentrate solar energy can be useful for ISRU purposes. The use of solar concentrators on the Moon would require less infrastructure than photovoltaic or nuclear energy generation.⁴² In addition, solar concentrators do not require the transformation of thermal energy into electricity, followed by subsequent conversion back into thermal energy, making solar concentrators more efficient. McDonnell Douglas built a 75 kW solar concentrator on Earth in the early 1980's, which was able to produce 25 kW of electricity using a Stirling engine. Around 1340 J/m² enters the top of Earth's atmosphere each second.¹³ Much of this energy is absorbed by the atmosphere before it reaches Earth's surface. The lack of an atmosphere on the Moon will allow the majority of incoming solar energy to be harvested utilizing a solar concentrator.

A study performed by Magoffin and Garvey was able to convert a layer of regolith simulant contained within a 25 cm diameter alumina crucible into glass by means of a solar concentrator.⁴² The glass produced was 0.64 cm and measured 8 cm x 12 cm. Temperatures as high as 1090 °C were achieved within the regolith inside the crucible, however the temperatures were not high enough to form glass. A layer of glass did form in the regolith at the crucible lip, which was able to reach temperatures of at least 1200 °C, adequate to melt the simulant.

A study by *Fabes, et.al* investigated the use of solar heating in order to melt and volatilize samples of regolith simulant less than three grams in mass.³⁷ Larger samples were found to be difficult to melt utilizing solar heating. High iron concentrations made the melt opaque, which caused the melt to act as a thermal insulator at high temperatures. Heat transfer occurred primarily through radiation at higher temperatures. The center of the solar beam reached temperatures of 2500 °C, but the temperature rapidly dropped off away from the focal spot. Moving the beam across the sample could melt the entire surface, but the opacity of the melt inhibited the transfer of heat from the surface into the sample, preventing the interior from

melting. A crucible with a high heat capacity was shown to allow better heat transfer through the sample.

The melting of regolith simulant was investigated by Tucker, et.al for the purpose of drawing the melt and making fiberglass.⁴³ The drawn glass fibers and rods would be used to reinforce lunar concrete that was made without using water, from sulfur and regolith simulant. Fibers were synthesized with diameters as small as 3 μm , and rods synthesized as large as 3/8" in diameter. The glass fibers and rods were shown to increase the strength of the concrete, provided that the glass fibers were isolated from the moisture found in Earth's atmosphere.

Allen, et.al investigated sintering of regolith simulant using radiant and microwave heating at temperatures of 1100 °C.⁴⁴ Two different simulants were used, MLS-1 and JSC-1. The MLS-1 simulant is a titanium-rich crystalline basalt, which was processed to a particle size ranging from 1mm to <10 μm . JSC-1 is basaltic ash that has high concentrations of glass and is similar in composition to lunar mare regions. Particles able to pass through a 1.168 mm sieve were used in the experiments. Hand tamping, uniaxial compaction (45, 000 psi), and vibrational methods (80 Hz, 3g max acceleration, over 5 minutes) were used to densify the MLS-1 mixture. The prior mentioned densification methods yielded sample porosities of 30-31%, 23-24%, and 30% respectively. Unprocessed MLS-1 had porosity of around 40%. Inconel and porous fused silica were used as crucibles during the heating process. Thermal cracking, induced by uneven heating caused by the insulating characteristics of the simulants was observed. It was found that the glass content of the JSC-1 assisted in allowing more uniform sintering when compared with the MLS-1 which is crystalline. Microwave heating was found to be more difficult to control than radiant heating in controlled sintering applications due to the difficulty in maintaining the temperature of the sample just below its melting point.

Regolith Simulant

The JSC-1A lunar regolith simulant was commissioned by NASA for use in experiments as a substitute for actual lunar regolith.⁴⁵ The fine particle size distribution of the simulant is referred to as JSC-1AF. The term regolith refers to the layer of loose, unconsolidated rock of all sizes overlying bedrock. The average particle size of the JSC-1AF regolith simulant is 24.89 μm .⁴⁵ The median particle size is 23.72 μm . Around 80% of the JSC-1AF particles are between 5 and 46 μm . The average particle sizes for three samples of JSC-1A simulant were 196.8 μm ,

184.7 μm , and 181.6 μm .⁴⁶ The median particle sizes were 105 μm , 103.5 μm , and 99.85 μm , respectively. Around 80% of the JSC-1A particles are between 19 μm and 550 μm .

JSC-1A and JSC-1AF simulants are an assemblage of minerals and glass consisting primarily of components of the plagioclase solid solution series and basaltic glass.⁴⁵ The simulants also contains components of the pyroxene and olivine solid solution series, along with various trace minerals. Table 1 shows the results of bulk composition analyses for JSC-1AF simulant and lunar samples from the Apollo and Luna missions.

Table II: Mean Bulk Composition of Lunar Regolith and Simulant JSC-1AF^{45, 47}
(Values in Wt. %)

Constituents	Maria		Highlands		Simulant
	Apollo 14	Luna 16	Luna 20	Apollo 16	JSC-1AF
SiO ₂	47.93	41.70	45.40	44.94	47.1
Al ₂ O ₃	17.6	15.33	23.44	26.71	17.1
CaO	11.19	12.50	13.38	15.57	10.3
FeO	10.37	16.64	7.37	5.49	7.57
MgO	9.24	8.78	9.19	5.96	6.9
Fe ₂ O ₃	-	-	-	-	3.41
TiO ₂	1.74	3.38	.47	.58	1.87

The presence of Fe₂O₃ in the simulant is one of the primary differences in bulk composition between actual lunar regolith and the JSC-1AF simulant. Substantial compositional variations occur in lunar regolith samples obtained from different regions of the Moon. Bulk composition represents elemental abundance using simple oxide compounds; it does not represent the actual chemical species present. Various minerals and glasses, not listed in Table II, make up actual lunar regolith and the JSC-1A and JSC-1AF simulants.

The average plagioclase content of the simulant is 70% anorthite, 29% albite, and 1% orthoclase (KAlSi₃O₈).⁴⁵ The Ca-pyroxene content averages 45% wollastonite (CaSiO₃), 38% enstatite, and 22% ferrosilite. Olivine chemical species have an average content of 73% forsterite and 27% fayalite.

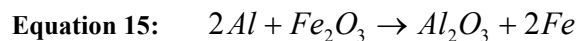
Simplified Thermodynamics of a Geothermite Reaction Using Bulk Oxides

Thermodynamic data for the bulk components (from Table II) of the lunar regolith simulant are shown in Table III.

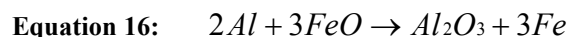
Table III- Standard Molar Enthalpies, Entropies, and Gibbs Free Energies of Formation of Selected Species⁴⁸

	ΔH_f^0 solid kJ/mol	$T\Delta S_f^0$ solid J/mol·K	ΔG_f at 298 K kJ/mol
SiO ₂	-910.7	41.46	-952.16
TiO ₂	-938.72	50.62	-989.34
Al ₂ O ₃	-1675.69	50.92	-1726.61
FeO	-272.04	60.75	-332.79
Fe ₂ O ₃	-825.50	87.40	-912.90
MgO	-601.24	26.85	-628.09
CaO	-635.09	38.19	-673.28

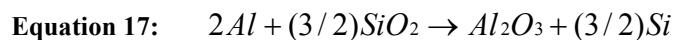
Thermodynamic reaction data were calculated using aluminum as a reducing agent with the data from Table III. The enthalpies and Gibbs free energies (kJ/mol) of the following oxidation-reduction reactions were calculated at standard temperature and pressure: ⁴⁸



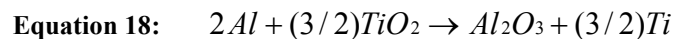
$$\Delta H = -850.19, \Delta G_{298K} = -813.71$$



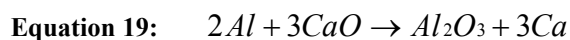
$$\Delta H = -859.57, \Delta G_{298K} = -728.24$$



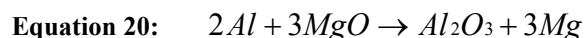
$$\Delta H = -309.64, \Delta G_{298K} = -298.37$$



$$\Delta H = -267.61, \Delta G_{298K} = -242.60$$



$$\Delta H = 229.58, \Delta G_{298K} = 157.66$$



$$\Delta H = 128.03, \Delta G_{298K} = 293.23$$

All the chemical reactions except Equation 19 and Equation 20 were thermodynamically favorable and exothermic at 298 K.

Volatization and Melting Studies

The low pressures present in a vacuum environment allow the vaporization of volatiles at lower temperatures than in a standard atmosphere. Prior research by *Y. Yu and R. Hewins* has shown substantial vaporization of sodium and potassium when exposed to heat in a vacuum environment.⁴⁹ Their experiments utilized a synthetic silicate glass specimen that was enriched with 3.3% K₂O and 2.8% Na₂O. Experiments were conducted in a standard atmosphere and a vacuum with pressure range in the vicinity of $\sim 10^{-2}$ - 10^{-3} Torr. The sample was heated to a temperature of 1450 °C. Their study showed that significantly more sodium and potassium is vaporized at low pressures than in a standard atmosphere. Sodium was shown to vaporize easier than potassium in both a standard atmosphere and a vacuum.

A study was performed by *Matović, et.al* using raw materials that have similar bulk composition to that of the regolith simulant. Their study involved melting and casting basaltic rock. The study found that basaltic rocks with silica content below 50% and a high content of Fe₂O₃, MgO, and CaO have a low viscosity when melted.⁵⁰ High alkali content caused a significant decrease in the melting points of the samples. A homogenous melt was obtained in a temperature range between 1140 °C and 1160 °C.

Knowledge of the behavior of elements in a low pressure environment is of value when performing reactions in a vacuum environment. At a pressure of ~ 0.600 Torr the temperature of vaporization for aluminum, magnesium, and sodium are ~ 1500 °C, ~ 560 °C, and ~ 420 °C, respectively.⁵¹

E. Identification and Material Properties of Chemical Species Produced in this Study

The following section discusses aspects of X-ray diffraction analysis, material properties of selected chemical species produced in this study, and statistical methods utilizing a t-test. Powder characteristics that can affect X-ray diffraction peaks, material properties for chemical species such as AlN, MgAl₂O₄, and CaAl₄O₇, and a method to determine the certainty of statistical significance between two datasets are discussed.

X-ray Diffraction

X-ray diffraction (XRD) is a common method of characterizing crystalline chemical species. Two factors that can influence XRD patterns include the size of particles and the strain within the particles. Crystals that are very small can cause peak broadening within the diffraction pattern.⁵² The broadening can be described by Equation 21:

$$\text{Equation 21: } t = \frac{\lambda}{B \cos(\theta_B)}$$

In Equation 21, t is the thickness of the crystal, θ_B is the angle that satisfies a given set of parameters for Bragg's law, B is the peak broadening measured in radians, and λ is the X-ray wavelength. Uniform strain can cause a shift in the observed diffraction peaks, while non-uniform strain can result in a decrease in peak intensity and a broadening of the peak width.⁵²

Material Properties of Chemical Species Produced in this Study

Some of the major chemical species produced in this study include CaAl_4O_7 , AlN, MgAl_2O_4 , and Al_2O_3 . Compounds within the CaO- Al_2O_3 system are widely used in ceramic materials, metallurgical slags, and cements due to their desirable refractory properties.⁵³ Two values for the melting point of CaAl_4O_7 (CA_2) exist in the literature, 1745 °C and 1775 °C. This compound melts congruently, and is also known as calcium di-aluminate. It is preferred for use over other high-alumina cements.

The unique properties of AlN make it useful in electronic applications.²⁵ AlN has a high thermal conductivity of 280 W/m K in ceramic form and 320 W/m·K in crystals. The electrical resistivity of AlN is high, greater than 10^{13} Ω cm. AlN has a low thermal expansion coefficient of 4.3×10^{-6} K^{-1} . AlN ceramics are resistant to oxidation at temperatures up to 1400 °C in air, they are also non-reactive in many molten metals and salts. The non-reactivity of AlN allows it to be used in crucible fabrication.

AlN is both a refractory and semi-conducting material.⁵⁴ AlN has been observed to form in tabular crystals, blade-shaped crystals, platy crystals, blade-shaped filaments, whisker and needle, and whisker morphologies. Single crystal growth has been observed to occur at temperatures between 1700 °C and 2000 °C, terminating in a black spherical shape. Oxygen has

high solubility within the AlN structure and can substitute for nitrogen. Magnesium and silicon also have high solubility within the AlN structure and can substitute for aluminum. Single crystal whiskers have potential for use as reinforcement within materials.

High-purity single crystals can have significantly different optical, electrical, magnetic, and superconducting characteristics than polycrystalline materials.⁵⁵ In addition, as the diameter of whiskers is reduced, the strength increases due to the whisker having a more perfect structure. Whiskers can withstand strains as high as 3% without permanent deformation while bulk ceramics can generally withstand less than 0.1% strain. Whisker growth can occur by basal or tip processes. Basal growth occurs by atomic migration to the base of the whisker, followed by extrusion from the substrate. Growth from the tip requires high temperatures in order for the vapor pressure of the whisker material to be significant enough for atoms to attach to the whisker tip. The melting point of aluminum nitride whiskers is 2198 °C. The tensile strength of aluminum nitride whiskers range from 14-21 GPa.

Spinel (MgAl_2O_4) is a refractory oxide that has applications as a structural ceramic.²³ The melting point of spinel is 2135 °C. It exhibits low electrical losses, and high resistance to attack by acids and alkalis. It has many uses within chemical, structural, optical, and electrical industries. Spinel also has a high resistance to neutron radiation damage.⁵⁶ When radiation induces point defects in the structure of spinel, most of the point defects are eliminated by means by an interstitial vacancy recombination mechanism. In many other materials, radiation induced point defects form dislocation loops and voids, which can be significantly detrimental to the material properties.

Several phases of aluminum oxide exist, $\alpha\text{-Al}_2\text{O}_3$ is known as corundum and has a hexagonal structure.¹⁴ Alumina has a compressive strength of 2620 MPa and retains significant strength at higher temperatures. Corundum is one of the hardest materials known besides diamond. The melting point of aluminum oxide whiskers is 2198 °C.⁵⁵ The tensile strength of aluminum oxide whiskers range from 14-28 GPa.

F. Statistical Methods Using a T-test

An independent sample t-test can be used to compare the means of two datasets that are not dependent on each other.⁵⁷ A t-test is used to determine if there is a statistical difference between two datasets. The equation used to calculate the t-value is shown in Equation 22.

$$\text{Equation 22: } t = \frac{\bar{Y}_1 - \bar{Y}_2}{\sigma_{diff}}$$

In Equation 22, Y_1 and Y_2 are the means of two datasets and σ_{diff} is the standard error of the difference between two means. The value σ_{diff} is calculated using Equation 23:

$$\text{Equation 23: } \sigma_{diff} = \sqrt{\left(\frac{S_1^2}{n_1}\right) + \left(\frac{S_2^2}{n_2}\right)}$$

In Equation 23, S_1^2 and S_2^2 are the variances of the two datasets, and n_1 and n_2 are the number of samples in the respective dataset.⁵⁷ The value of t is compared with a statistical table that lists values for significance, known as α , and values for the degrees of freedom. Significance values determine the degree of statistical certainty that a difference exists between the values of the dataset means. The total number of degrees of freedom are determined by subtracting two from the total number of samples in the datasets.

III. EXPERIMENTAL METHODS

The experimental methods section describes the experimental approach used in this study. Multiple experimental approaches were used either to find an experimental method that would work, and/or to find an experimental method that would provide repeatable results. Selection of reactant stoichiometries, selection of crucible shape and composition, sample preparation, and experimental procedures in ambient and vacuum conditions are discussed. Material characterization procedures using X-ray diffraction, scanning electron microscopy, energy dispersive spectroscopy, and compressive strength testing are also described. In addition, methods used to determine densities of the reaction product and energy required to initiate an SHS reaction are discussed.

A. Reactant Stoichiometry Selection

Lunar regolith simulant and aluminum powder were used as reactants in this study. Two particle size distributions of lunar regolith simulant were used: the JSC-1AF had fine particles, and the JSC-1A had coarse particles. The core investigation of this study utilized four different reaction stoichiometries chosen both theoretically and experimentally. However, data from reactions that were performed using reactant stoichiometries other than the main four are included in certain instances to expand the available data set. Two of the four reactant stoichiometries were determined experimentally to set an upper and lower boundary of aluminum required to achieve repeatable SHS reactions using JSC-1AF simulant that propagated completely through a sample. It is emphasized that the upper and lower boundaries used in this study are not discrete limits on reaction propagation. The boundaries represent constraints needed to achieve adequate reaction repeatability desired for this study. Reactions have been performed and have propagated to completion outside the highest and lowest quantities of aluminum used in this study.

The other two stoichiometries were calculated using the bulk composition of oxides found within the JSC-1AF regolith simulant. The 28.85 wt.% aluminum stoichiometry represents the proportion of aluminum required to reduce all oxides found within the regolith simulant, regardless of thermodynamic favorability. The 24.45 wt.% aluminum stoichiometry represents the proportion of aluminum required to reduce the selected thermodynamically

favorable oxides, consisting of SiO_2 , TiO_2 , Fe_2O_3 , and FeO . The methods used to calculate the stoichiometries are described in Appendix 1.

Reactants were mixed in quantities of 80 grams. The aluminum used in the reactions had a -325 mesh particle size. The four primary reactant stoichiometries consisted of 80.56% simulant and 19.44% aluminum; 75.55% simulant and 24.45% aluminum; 71.15% regolith and 28.85% aluminum; and 66.67% regolith and 33.33% aluminum by weight. All reactant stoichiometries were measured in wt.%. Each of the stoichiometries was used for both JSC-1AF and JSC-1A simulants, with the exception of the 33.33% aluminum stoichiometry. The 33.33% aluminum stoichiometry would not support the repeatability requirements of this study using the JSC-1A simulant.

B. Preliminary Crucible Experiments

Initial SHS reactions were performed with a simulant-aluminum mixture contained in a rectangular crucible of aluminum foil fabricated by hand. Since one of the objectives of this study was to conduct compressive strength tests on the synthesized samples, samples were fabricated in the shape of cylinders, which is a common shape used for compressive testing.

Initial forming of reaction products in the shape of cylinders was attempted using a fused quartz crucible. The crucible had inner dimensions of 3.4925 cm (1- 3/8") diameter and 9.2075 cm (3- 5/8") length and was available commercially. A fused silica crucible was desired since successful reactions had been performed with silica crucibles having a low aspect ratio (height: diameter). However, one could not be located in the dimensional range desired. No reactions ran to completion in the quartz crucible. Two experimental setups were used: one with the crucible on top of a refractory brick, and one with the crucible on top of a sand bed on top of a refractory brick. The sand bed was used in an attempt to lower heat loss through conduction. Reaction propagation was always begun at the top of these mixtures and propagated downwards. The propagation would stop between 1.905 cm (3/4") and 2.54 cm (1") from the bottom of the crucible. It was decided that cylindrical crucibles would be manually fabricated from aluminum foil for this study. The fabrication process will be discussed subsequently.

C. Sample Preparation and Reaction Environments

Reactions were performed in both a standard atmosphere and a vacuum environment. The experimental matrix used in this study is shown in Table IV. At least three samples were fabricated for each set of reaction parameters in ambient conditions. At least one sample was fabricated for each set of reaction parameters under vacuum conditions.

Table IV: Experimental Matrix of Reaction Parameters

Environment	Reactants (Weight Percent Aluminum and Simulant Type)			
	19.44%	24.45%	28.85%	33.33%
Ambient	JSC-1AF	JSC-1AF	JSC-1AF	JSC-1AF
	JSC-1A	JSC-1A	JSC-1A	*
Vacuum (0.600 Torr)	JSC-1AF	JSC-1AF	JSC-1AF	JSC-1AF
	JSC-1A	JSC-1A	JSC-1A	*

**JSC-1A did not support the reaction propagation repeatability required for this study*

Sample preparation was the same for both ambient and vacuum environments. The mass of each constituent was determined using an Ohaus Adventurer Pro AU313 Scale. The powders were manually mixed until a uniform dispersion of reactant particles was achieved.

The fabrication of aluminum foil crucibles was accomplished by cutting sheets of 0.01 mm aluminum foil with dimensions of 19.685 cm (7 3/4") x 10.16 cm (4"). The cut sheet of aluminum foil was rolled tightly over a cylinder mandrel with a 2.8575 cm (1- 1/8") outer diameter. A length of 1.905 cm (3/4") of the rolled aluminum foil was slid off the cylinder then folded over on itself to form the crucible bottom. While the aluminum foil did not provide as uniform a shape as the quartz crucible did, it did however allow the reaction to complete and a near net cylindrical shape to be produced.

The mass of the aluminum foil crucible was measured following the shaping process. The typical crucible mass was ~1.5 grams. Mixed reactants were poured into the crucible in volumetric fifths. After each fifth the crucible and mixture were dropped on the counter from a height of 2.54 cm (1") above the counter surface for a total of four times in order to promote powder densification. The next volumetric fifth was poured into the crucible and the densification process was repeated. Once all the mixture was contained in the crucible, a straight piece of 18 awg wire was pushed into the mixture from the top to the bottom of the crucible ten times. Pushing the wire into the mixture broke up graded density layers formed by the

intermittent densification process. The breaking up of the graded density layers allowed formation of a more uniform product.

Standard Atmosphere SHS Reactions

Preliminary Variac Settings and Nickel-Chromium Wire Placements

Numerous experiments were conducted using different power outputs and power rates from the Variac to determine the necessary voltage to cause reaction initiation. A constant heating rate for each sample was desired, so the Variac voltage was increased a set amount for each passage of time. The NiCr wire was composed of 60% nickel, 16% chromium, and 24% iron and had a resistance of 0.4219 ohms per 30.48 cm (12"). Multiple experiments were performed using various NiCr wire configurations and placements within the sample mixture.

Standard Atmosphere SHS Reaction Initiation

For uniformity, a 30.48 cm (12") length of 18 awg NiCr wire was pushed into the sample mixture stopping just above the crucible bottom. The NiCr wire was bent into the shape of a "U" and had a 1.27 cm (1/2") space between each side of the "U".

Standard atmosphere reactions were performed in a 121.92 cm (4 ft.) x 121.92 cm (4 ft.) plexiglass chamber lined with refractory bricks and insulation. The aluminum foil crucible was placed on a 1.27 cm (1/2") bed of sand to reduce conduction of heat to the adjacent bottom surface during the reaction. The chamber was continuously purged of airborne particulate by means of an air filter and fan assembly. The ends of the NiCr wire were connected to a 30 ampere Variac power supply to induce joule heating. In order to minimize the creation of voids in the mixture, the crucible was tamped down twice after connection to the Variac terminals. The power supplied by the Variac was controlled manually, and was increased at approximately the same rate for each of the samples. The power application rate is shown in Table V. The time of each amperage increase was recorded as was the time of reaction initiation. The amperage and time data were used to calculate the energy required to initiate each reaction, the details of which are discussed later. When the reaction initiated, the Variac was turned off. The time of reaction completion, and the time where visible radiation ceased to be emitted from the sample was also noted.

Table V: Power Application Rate for Joule Heating of a Sample in a Standard Atmosphere

Minutes:Seconds	Variac Output (%)	Amps*
0:10	2	2.5
0:20	4	7.5
0:30	6	10.5
1:30	7	13.5
2:30	8	16.0
3:30	9	18.5
4:30	10+ **	22.5

*General approximation of amperage.

** Power setting until reaction initiation occurred.

Vacuum SHS Reactions

Vacuum Chamber Setup

A vacuum chamber was designed in order to perform SHS reactions in a vacuum environment. The vacuum chamber setup is shown in Figure I.



Figure I: Vacuum Chamber and Variac Setup

The chamber was made from Type 304 Stainless Steel, and was a horizontally oriented cylinder with a diameter of 45.72 cm (18") and a length of 50.80 cm (20"). A 15.24 cm (6") glass viewport was installed on the chamber door, and a 10.16 cm (4") quartz viewport was installed at the top center of the chamber. The chamber had a Type 304 stainless steel shelf installed 10.16 cm (4") from the bottom of the chamber. A two conductor, 30 amp electrical feedthrough, was centered on the left side of the chamber. A feedthrough to accommodate four thermocouples was centered on the right side of the chamber. Three type-K thermocouples and one type-C thermocouple could be connected to the feedthrough. An exhaust port with a manual valve was located at the top rear of the vacuum chamber. The vacuum chamber was manufactured by Laco Technologies.

A y-adaptor was attached to the exhaust valve on the chamber with additional valves attached to each side of the adaptor. One valve allowed air to enter the chamber for re-pressurization and the other side was connected to an exhaust fan and air filter. The exhaust fan and air filter were used to remove any airborne contaminants within the chamber after re-pressurization.

A manual valve was attached to the vacuum port on the chamber to allow separation of the vacuum chamber from the vacuum pump. Three vacuum traps were attached in series between the valve and the vacuum pump in order to prevent fine particulate from the SHS reactions from entering the vacuum pump. The trap nearest the chamber used a stainless steel gauze filter, which was followed by a sodasorb filter and a five micron polypro filter. A Leybold D8B dual-stage vacuum pump was attached to the output of the five micron polypro filter using vacuum hose. An oil mist eliminator was attached to the output port on the vacuum pump, which prevented oil mist from the vacuum pump from being expelled into the air.

A digital vacuum gauge was connected to a thermocouple-type sensor installed at the top of the chamber. The range of the gauge was from 0.001-760 Torr. Readings from 0.001 to 1 Torr were highly accurate, whereas readings above 1 Torr were only for general reference. The gauge had an RS-232 port to allow data to be recorded to a computer.

A 30 amp variable AC power supply was one method used to initiate SHS reactions. A modified extension cable with two test clips instead of a connection plug was used to connect the variable AC power supply to the two conductor 30 amp electrical feedthrough on the vacuum chamber. Two additional test clips were connected to the feedthrough on the interior of the

chamber, which were attached to nickel-chromium wire. Nickel-chromium wire was used for resistance heating of the sample mixture, which allowed initiation of the SHS reaction.

Preliminary Nickel-Chromium Wire Vacuum Reaction Initiation

Several challenges were encountered during initial attempts at initiating the SHS Regolith reaction in a vacuum. The Variac power supply was used to induce 22 amperes of current to flow through the braided wires for a period of two minutes in a standard atmosphere. The shape of the NiCr wire used in vacuum was the same shape and spacing used in the standard atmosphere tests. Repeatable reaction propagation was achieved in vacuum using double braided 18 awg NiCr wire. Using the double-braided NiCr wire decreased the resistance in the Variac circuit, allowing a larger number of amps to flow at lower Variac settings than in a standard atmosphere. After some experimentation, it was decided that the same Variac settings used in a standard atmosphere would be used in a vacuum, despite reaching the desired amperage more quickly.

Vacuum SHS Reaction Initiation

After sample preparation was accomplished, the “U” shaped 30.48 cm (12”) length of heat-treated, double-braided 18 awg NiCr wire was pushed into the sample mixture. The tip of the NiCr wire was pushed to a depth just above the crucible bottom. The ends of the NiCr wire were connected to terminals on the electrical feedthrough within the vacuum chamber. In order to minimize creation of voids in the mixture, the crucible was tamped down twice after connection to the Variac terminals. The vacuum chamber door was closed, and all valves leading to the chamber were closed. Labview software was then initialized and used to record the pressures within the vacuum chamber. The vacuum pump was turned on, and the valve located between the vacuum traps and the vacuum chamber was opened to allow evacuation of the chamber to begin. When the pressure in the chamber reached 0.600 Torr, the Variac power supply was turned on and the Joule heating process began. The approximate power application rates are shown in Table VI. The increase in resistance caused by the double-braided NiCr wire increased the current delivered to the sample at each given voltage interval when compared to the standard atmosphere reactions.

Table VI: Power Application Rate for Joule Heating of a Sample in a Vacuum Environment

Minutes:Seconds	Variac Output (%)	Amps*
0:10	2	5.0
0:20	4	14.0
0:30	6+ **	23.0

*General approximation of amperage.

** Power setting until reaction initiation occurred.

The pressure of 0.600 Torr is roughly 0.08% of a standard Earth atmosphere (760 Torr). The pressure was selected to avoid substantially longer vacuum chamber pump down times, while eliminating the vast majority of atmospheric gases, and reaching a significantly lower pressure than exists in ambient conditions. The vacuum pump continuously evacuated the chamber throughout the entire reaction process. The time of reaction completion, and the time where visible radiation ceased to be emitted from the sample was also noted. Once visible radiation ceased to be observed from the sample, the valve to the vacuum pump was closed, and the chamber pressure was allowed to increase to 0.600 Torr. The chamber was then re-pressurized to ambient conditions while transferring air from the chamber to an air filter assembly through another valve.

D. Identification of Chemical Species

A portion of each sample, located near the center lengthwise, was used for X-ray diffraction (XRD) analysis. It was desirable to have a full cross-section of the sample analyzed by XRD due to the potential of heat gradients altering the formation of chemical species. Figure II shows a diagram of the sample region used for XRD analysis.

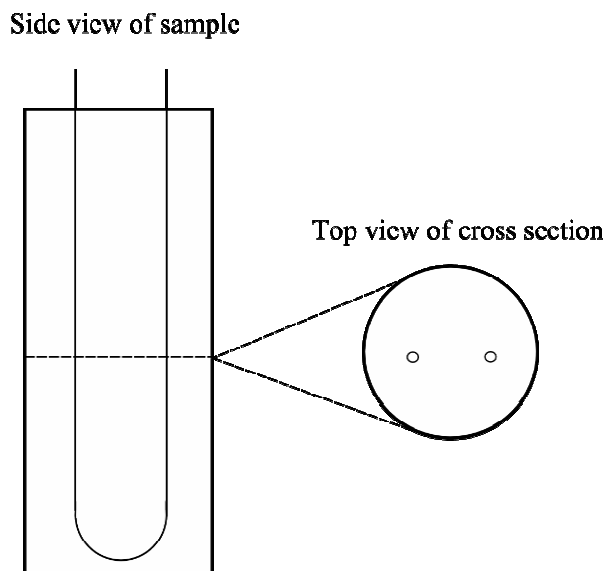


Figure II: Diagram of the sample region used for XRD analysis

Each sample was ground with a mortar and pestle, and sieved to -200 mesh in order to obtain particle sizes suitable for XRD analysis. XRD analysis was also performed on unreacted JSC-1AF and JSC-1A regolith simulant. XRD analysis for standard atmosphere reaction products was conducted using a Panalytical X-Pert Pro diffractometer. A continuous goniometer scan was conducted from 10° to 120° , with a goniometer radius of 240 mm. A current of 40 mA was used with an accelerating voltage of 45 kV. The copper anode used for the analysis had a $K_{\alpha 1}$ wavelength of 1.5406 \AA . The sample tray was rotated during the scan in order to decrease effects of preferred orientation of particles. Due to equipment availability issues, XRD scans for vacuum synthesized products were conducted on a Siemens D5000 X-ray diffractometer. An analysis of the diffraction patterns generated by each of the diffractometers using the same sample indicated suitable correlation between diffraction peaks generated by the diffractometers. A 2-theta / theta locked scan was conducted on the Siemens D5000 from 10° to 120° , with a step of 0.01° and a step interval of 2.5 seconds. A $K_{\alpha 1}$ wavelength of 1.5406 \AA was used.

E. Characterization of Microstructures and Elemental Analysis

The microstructure and element composition of each reaction product were examined using Scanning Electron Microscopy (SEM) and Energy Dispersive Spectroscopy (EDS). As with XRD, samples located near the center lengthwise were used for SEM analysis. SEM analysis was performed on regions of the sample between the outer edge of the NiCr wire and

the outer edge of the sample radius. In addition, analyses were performed on unreacted JSC-1AF and JSC-1A simulant. A Hitachi 3700SN SEM and a LEO 1550 SEM were used to perform the analyses. An Oxford Energy Dispersive Spectroscopy (EDS) system was used to obtain chemical compositions of selected microstructures. Samples were coated with a 15 nm 60/40 gold/palladium coating using a Cressington 208HR sputter coater. Samples synthesized in vacuum were cleaned with compressed air to eliminate any loose powder on the sample surface before applying the coating.

F. Density Measurements

Density measurements were conducted on reaction products synthesized in a standard atmosphere. An Ohaus Adventurer Pro AU313 Scale was used to obtain the mass of each reaction product. A Marathon digital caliper was used to make three measurements of sample diameter and three measurements of sample length. The mean values of diameter and sample length were used to calculate sample volume. The mass of each sample was then divided by the volume to determine an approximate density.

G. Mechanical Strength Measurements

Sample Preparation and Testing

In order to conduct compressive strength testing, the ends of each reacted sample needed to be leveled. A ceramic tile saw utilizing a diamond blade was used to machine the samples, without use of a lubricating medium. A Marathon digital caliper was used to make three measurements of sample diameter and three measurements of sample length after each sample was cut. The mean diameter for each sample was used to calculate the surface area, used in the calculation of the compressive strength of the material.

Compression testing was performed on samples using ASTM standards as general guides. Two standards were utilized: C 773-88: Standard Test Method for Compressive (Crushing) Strength of Fired Whiteware Materials; and C 1424-99: Standard Test Method for Monotonic Compressive Strength of Advanced Ceramics at Ambient Temperature.

An Instron 4468 with a 50kN load cell was used to perform compressive strength testing. Strain measurements were made with a MTS model 632.11B-20 extensometer. Platen

displacement was set to a rate of 1mm per minute for the compressive strength measurements. Stress and strain measurements were recorded.

H. Energy Required to Initiate the SHS Reaction

Measurements of current applied to the NiCr wire were obtained using an ammeter built into the Variac power supply. As Variac power was increased, the time and the amperage were recorded manually. The resistance of the nickel-chromium wire was 0.4219 ohm per 30.48 cm (12"). The terminal connections were made approximately 1.27 cm (1/2") beyond each wire end. The terminal connections decreased the total wire length, and therefore the total wire resistance to 0.3867 ohms. Ohm's law was used to calculate the power using Equation 24.

$$\text{Equation 24: } P = I^2 R$$

In Equation 24, P is the power, I is current, and R is the resistance. The power was multiplied by the time it was applied to calculate energy in units of watt-hours. The energy was calculated for each interval of time that the Variac was held at a particular current setting. The energy at each setting was added together to calculate total energy. The total energy was converted from watt-hours to joules. The total energy was divided by the mass of the reactants to give a quantity of joules/gram in order to create a standardized unit to accurately compare energy required to initiate reactions in different samples. The energy quantities calculated were meant to be used to compare various reaction parameters within this study. The energy quantities were not meant to be used for comparison outside this study since factors such as the influence of temperature on resistance within the NiCr wire were not incorporated into the calculations.

IV. RESULTS AND DISCUSSION

The results and discussion section will describe the reaction process in ambient and vacuum conditions. Results of XRD characterization, SEM/EDS characterization, compressive strength testing, density measurements, and reaction initiation energy requirements will be discussed.

A. Reaction Environments

This section discusses the reaction process that occurs in standard atmosphere and vacuum reaction environments. Images of the reaction process in both environments are provided. The results of preliminary experiments are discussed in order to demonstrate the process that was used to define the experimental procedures used for this study.

Standard Atmosphere SHS Reactions

Preliminary Experiment Results

During initial experiments to determine suitable Variac settings for reaction initiation, it was discovered that increasing the amperage over 24 amps without allowing sufficient time to heat the specimen often caused incomplete reaction propagation. The incomplete reaction propagation was hypothesized to be a result of premature local reaction initiation, followed by an open (a break) circuit in the nickel-chromium (NiCr) wire, and loss of external heat. The ideal amperage range to initiate the reaction on a repeatable basis was observed to occur between 21 and 23 amperes. Initial experiments also indicated that the NiCr wire configuration and placement could greatly influence whether the reaction went to completion, as well as the time it took to initiate the reaction. If the NiCr wire was placed too close to the sides of the aluminum foil crucible, the reaction often failed to initiate or failed to go to completion. A larger spacing of the NiCr wire would likely have decreased the temperature in the region between the wires, where reaction initiation is likely to begin. If the wires were placed too close together, the reaction generally started too quickly and caused an open circuit in the NiCr wire before enough heat could be transferred through the sample. The faster reaction initiation was likely caused by higher temperatures induced by the closer proximity of the NiCr wires. The faster reaction initiation would have led to a decrease in total external heat applied to the sample and could have caused incomplete reaction propagation.

Experimental Results

In a standard atmosphere, reaction propagation typically began at the uppermost surface of the cylinder. A horizontal planar combustion wave propagated from the top of the cylinder to the bottom, shown in Figure III.

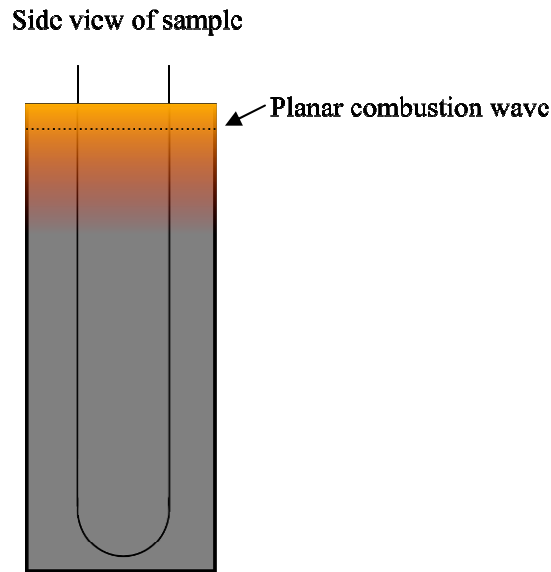


Figure III: A diagram of the planar combustion wave propagating through a sample.

Generally the rate of combustion wave propagation slowed towards the bottom of the specimen. It is hypothesized that the slower rate of combustion wave propagation was a result of heat loss by conduction to the surface on which the cylinder rested. In a reaction conducted in a standard atmosphere, heat is lost from the sample by conduction to the sand bed, convection to the surrounding air, and various wavelengths of electromagnetic radiation, some of which are visible. Slowing of the combustion wave is also likely to be a result of melting of the aluminum crucible, which will be discussed later. Images of the standard atmosphere reaction process using JSC-1AF simulant and 28.85 wt.% aluminum are shown in Figure IV-Figure XIII.



Figure IV: Heat is applied to a mixture of JSC-1AF regolith simulant and aluminum powder.



Figure V: Reaction propagation begins, no further external energy is applied.



Figure VI: ~20 sec after initiation.



Figure VII: ~40 sec after initiation.



Figure VIII: ~1 min after initiation.



Figure IX: ~1 min 20 sec after initiation.



Figure X: ~2 min after initiation.



Figure XI: ~2 min 30 sec after initiation.



Figure XII: Reaction propagation has completed. (~3 min 10 sec after initiation)



Figure XIII: Reaction product after cooling. (~5min 40 sec after initiation)

It was observed that reactions conducted with mixtures having a larger quantity of aluminum in the reactants tended to evolve more gas than those with lower quantities of aluminum. Reactions utilizing JSC-1AF simulant evolved more gas than those using JSC-1A simulant. It is possible that formation of larger quantities of Al_2O gas, a chemical species which will be discussed later, were induced by the larger aluminum quantities.

As the combustion wave passed through a portion of the reactant mixture, slight expansion of that portion of the cylinder was observed. After the wave passed, the region returned to approximately the initial size. Occasionally cylinders deformed during the reaction and formed a bent cylinder. The phenomenon seemed to be confined to stoichiometries with large aluminum quantities. Deformation likely occurred due to flow of liquid aluminum combined with thermal expansion of reacting species during the reaction, which would likely

indicate liquid phase sintering. Deformation was observed during synthesis using a 46.67% aluminum stoichiometry with JSC-1AF, shown in Figure XIV. (The stoichiometry was not selected for vigorous investigation due to reaction repeatability issues.)

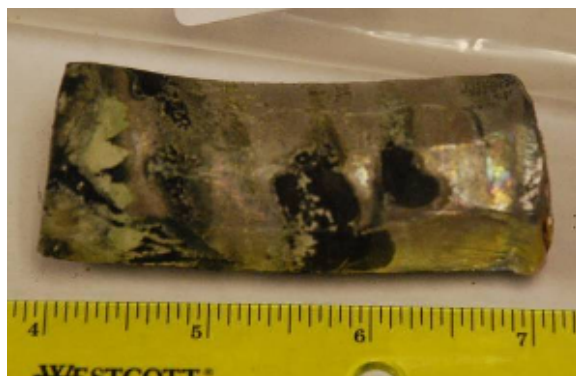


Figure XIV: A reaction product deformed during synthesis using a stoichiometry of 53.33% JSC-1AF and 46.67% aluminum.

It was rare to synthesize a sample using JSC-1AF with a 19.44% aluminum stoichiometry without cracks occurring during synthesis (See Figure XV). No cracks were observed using the same reactant stoichiometry with JSC-1A simulant. The cracks were apparent immediately after the propagation wave passed, and always occurred in the top half of the sample. It is hypothesized that the low amount of aluminum present prohibited uniform propagation of the combustion wave at a speed sufficient to accommodate thermal expansion and contraction of the reacting species. Thus an uncracked surface could not be maintained. It is also possible the degassing of the mixture caused the cracking. Another possibility is that stoichiometries with larger quantities of aluminum produce sufficient heat to allow liquid phase sintering of some of the reacting species, which prevents macroscopic cracking.

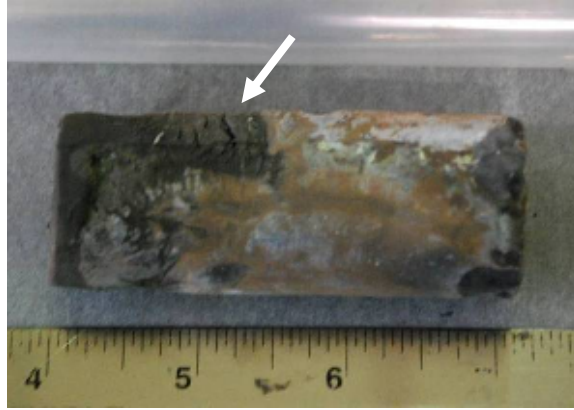


Figure XV: Cracks in the reaction product of the 19.44% aluminum stoichiometry.

It was frequently observed in reactions using either simulant that excess aluminum from the crucible would melt down the side of the sample and accumulate. The accumulation of aluminum was observed to slow reaction propagation as the combustion wave reached the bottom of the sample. All but one reactant stoichiometry produced enough heat to complete the reaction at the bottom of the sample. An example of reaction completion was shown in Figure XII. Upon cooling, some of the residual aluminum can be seen at the bottom of the reaction product identified with an arrow in Figure XIII.

The reactant stoichiometry with the least aluminum utilizing JSC-1A simulant frequently left a small unreacted portion of mixture (1/4-1/2 cm) at the bottom of the unreacted product. It is likely that a combination of thermal conduction at the sample base and production of less heat by the 19.44% aluminum stoichiometry during the reaction caused the unreacted region in the sample. The unreacted portion is observed at the farthest left portion of the specimen shown in Figure XVI. Prior to compressive strength testing, the ends were leveled, and the unreacted area cut off.

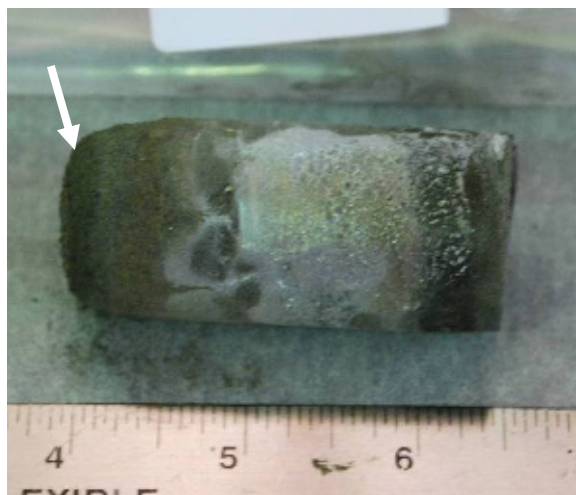


Figure XVI: The reaction product using a stoichiometry of 80.56% JSC-1A and 19.44% aluminum with a small unreacted portion at far left.

Another notable phenomenon was the formation of a green-white coating that was often observed on the sides and surface of reaction products synthesized using JSC-1AF simulant. The coating was not predominant in reactions using JSC-1A. The green-white surface coating was observed to increase in predominance as the amount of aluminum used in the reaction increased. The 19.44% aluminum stoichiometry utilizing JSC-1AF did not produce the white-green exterior surface coating (see Figure XV). The green-white coating on the product using JSC-1AF with the 33.33% aluminum stoichiometry is shown in Figure XVII. Various studies on aluminum nitrides mention that certain phases exhibit green-white coloration. Aluminum nitride formation will be discussed later on.



Figure XVII: A green-white coating on the reaction product using JSC-1AF and 33.33% aluminum.

The interior of a sample synthesized using JSC-1AF simulant is shown in Figure XVIII. Coloration differences can be observed from the interior to the exterior of the cross-section. The region around the NiCr wire is light gray, while the regions further away are darker gray. The coloring phenomenon may be a result of temperature gradients (higher near NiCr wire and lower near exterior surface) and variations in formation of chemical species. Gradients in temperature could be induced by differences in values for thermal conductivity and specific heat for the different chemical species within the sample.



Figure XVIII: Interior of JSC-1AF sample

Images of standard atmosphere reaction products for all reactant stoichiometries and both simulant types can be found in Appendix 2.

Vacuum SHS Reactions

Preliminary Experiment Results

Initial experiments utilized a single NiCr wire for reaction initiation in vacuum, the same configuration that was used in a standard atmosphere. It was observed that an open circuit occurred in the NiCr wire far quicker in vacuum than occurred in a standard atmosphere. In addition, reaction initiation was not observed when the open condition occurred in vacuum. Examination of the wire after attempting a reaction revealed significant pitting. It was hypothesized that the reducing conditions found in the vacuum would allow chemical bonding between a component in the NiCr wire and component(s) in the reactant mixture. In particular, it was hypothesized that elemental silicon produced from aluminum oxidation during heating was interacting with a component in the NiCr wire and causing the degradation of the wire. In order to slow the degradation process, the NiCr wire was heated in a standard atmosphere for a given amount of time prior to use in the vacuum environment, allowing an oxide layer to form on the exterior of the NiCr wire, which slowed the pitting process. Sufficient repeatability was not achieved using a single strand of NiCr wire; it was thought that better repeatability would be achieved by using two pieces of 30.48 cm (12") NiCr wire braided together.

Experimental Results

Visual observations during the reaction process were far more difficult to make for vacuum reactions due to the limited size and location of the viewport on the vacuum chamber. From the vantage point of the viewport, reactions were observed to begin near the midpoint between the upper and lower surface of the cylinder. Combustion wave propagation did not occur in a horizontal, planar manner as it did in a standard atmosphere. Combustion wave propagation could be described as radiative spreading from a point source. Images of the reaction process in a vacuum environment are shown in Figure XIX-Figure XXVIII.



Figure XIX: Reactant mixture in aluminum crucible within vacuum chamber.



Figure XX: Heat is applied to reactant mixture.



Figure XXI: Energetic emission of particles, propagation begins.



Figure XXII: ~20 sec after initiation.



Figure XXIII: ~40 sec after initiation.



Figure XXIV: ~1 min 30 sec after initiation.



Figure XXV: ~3 min after initiation.



Figure XXVI: ~4 min after initiation.



Figure XXVII: ~6 min after initiation.



Figure XXVIII: The vacuum reaction product after cooling. (~7 min 30 sec after initiation)

In a reaction conducted in a vacuum, heat is lost by conduction to the sand bed (no sand bed was used in the reaction shown in the images above), and electromagnetic radiation emitted. In the vacuum synthesis process, the intensity of visible radiation was lower than that observed in standard atmosphere synthesis. White and yellow wavelengths are present at the reaction maximum in a standard atmosphere, while red, orange, and some yellow are present at the maximum in vacuum. The differences in wavelengths of light emitted by the reaction in different environments could indicate that temperatures are not as high in the vacuum environment. Significantly lower quantities of heat were predicted to be lost by convection in a vacuum environment due to the low partial pressures of gases present at 0.600 Torr. Reaction products produced in vacuum generally had regions of loose powder at the upper and lower surfaces of the cylinder. The lower surface was most likely unreacted simulant and aluminum.

The uppermost surface was generally a white to brown-grey color, distinctly different from the lower surface. It is thought that the upper surface may be composed of elements that are easily volatilized in vacuum, such as magnesium and sodium. The region just below the uppermost surface was likely to be unreacted simulant and aluminum. Images of vacuum reaction products for all reactant stoichiometries and both simulant types can be found in Appendix 3.

Pressure within the vacuum chamber was generally observed to increase over two intervals during the synthesis process, even with continuous chamber evacuation using a vacuum pump. Without continuous evacuation, pressure within the chamber increased substantially due to outgassing of volatiles from the sample mixture. The first increase in chamber pressure occurred shortly after heating commenced. The second increase occurred when reaction propagation began, the time of which was dependent on the reaction parameters. The upper limit of measured chamber pressures was ~ 2.5 Torr. The 19.44% and 28.85% aluminum stoichiometries using JSC-1A, and the 24.45% aluminum stoichiometry using JSC-1AF exhibited significantly longer reaction times. A comparison of chamber pressures measured during synthesis is shown in Figure XXIX.



**Figure XXX: Secondary reaction upon pressurizing the vacuum chamber to ambient conditions abruptly.
(~9 min after initiation)**

Figure XXXI: ~9 min 15 sec after initiation.

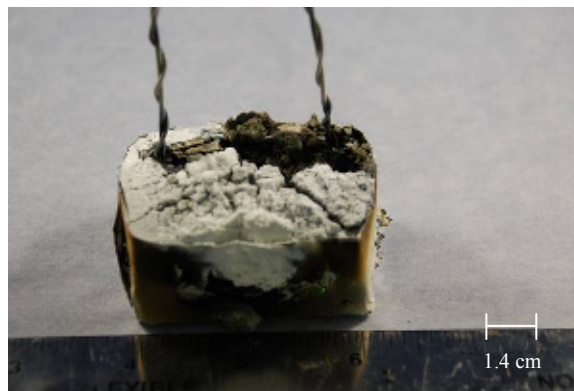


Figure XXXII: ~9 min 30 sec after initiation.

Figure XXXIII: A white coating is produced from the secondary reaction, which is confined to the sample surface.

SEM and EDS analysis were conducted on a portion of the white coating. The microstructure of the white coating is shown in Figure XXXIV and Figure XXXV. Chemical analysis of the regions in Figure XXXIV and Figure XXXV are shown in Table VII and Table VIII. Data from the chemical analysis likely indicates that the white substance is magnesium oxide.

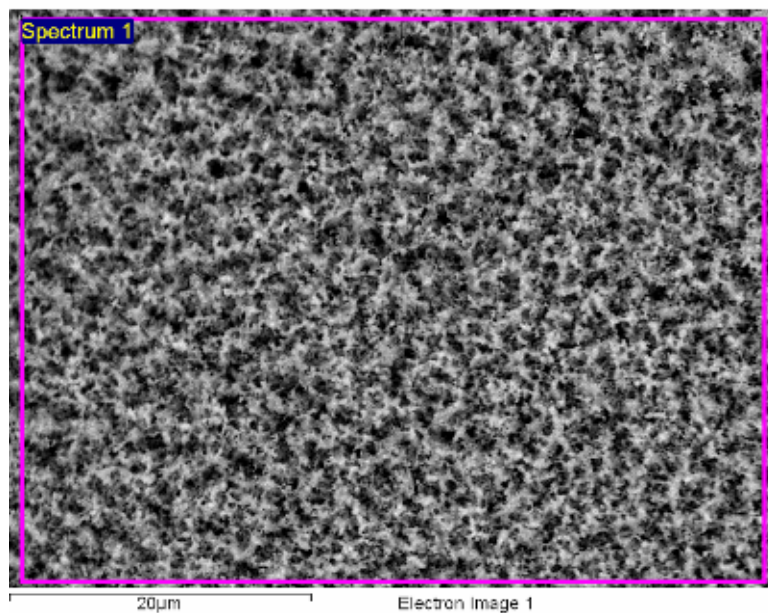


Figure XXXIV: SEM micrograph of the white substance formed in the secondary reaction.

Table VII: EDS Analysis of Spectrum 1 shown in Figure XXXIV

Element	Weight%	Atomic%
C	2.23	3.64
O	41.83	51.28
Na	0.88	0.75
Mg	54.57	44.02
P	0.49	0.31

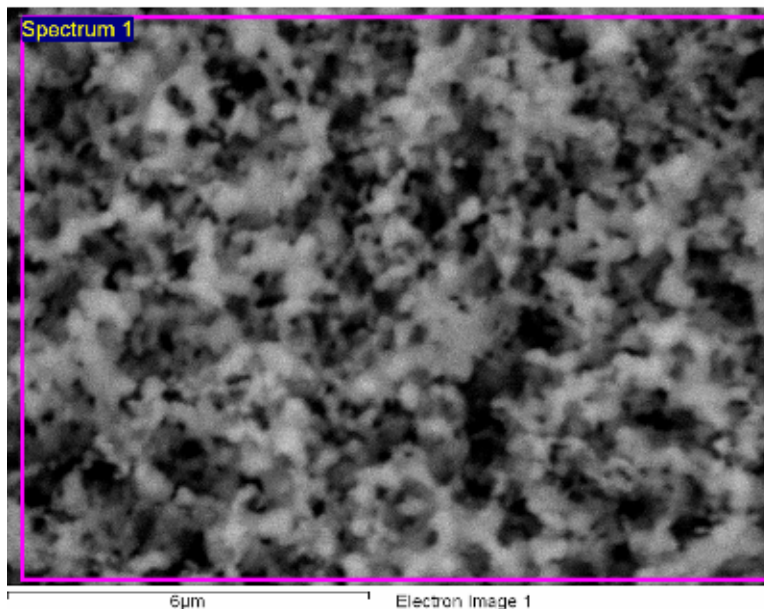


Figure XXXV: SEM micrograph of the white substance formed in the secondary reaction.

Table VIII: EDS Analysis of Spectrum 1 shown in Figure XXXV

Element	Weight%	Atomic%
C	1.89	3.10
O	41.47	51.04
Na	1.00	0.86
Mg	55.27	44.76
P	0.37	0.23

In addition to the white coating observed on the samples, dendritic growth, shown in Figure XXXVI and Figure XXXVII, was observed on the vacuum chamber walls after performing reactions. It is possible that the chemical species underwent heterogeneous nucleation on the stainless steel walls of the vacuum chamber.



Figure XXXVI: Dendritic deposition observed within vacuum chamber.



Figure XXXVII: Enlarged view of dendritic deposition within vacuum chamber.

During the heating of the mixture in vacuum, a silver-grey metallic liquid was observed to coalesce in droplets on the crucible used to contain the sand that supported the aluminum foil crucible. After re-pressurization of the chamber, the liquid metal had solidified into a white substance. The metal was hypothesized to be magnesium and the white substance was presumed to be magnesium oxide.

B. Identification of Chemical Species

This section will cover identification of chemical species present in both unreacted regolith simulant, and products of the reaction utilizing different stoichiometries, particle sizes, and reaction environments. XRD was used to identify the crystalline species present within the samples. A region from 1.3 Å to 7 Å in size was chosen for XRD analysis presentation since it contained all significant diffraction peaks found within the unreacted simulants and the reaction products of various stoichiometries and simulant types. The powder diffraction file (PDF) associated with each identified chemical species is listed in the subsequent data analysis tables. High quality PDF files are indicated by a (*) following the number and good quality PDF files are indicated by an (I) following the number.

Chemical Species Present in Unreacted JSC-1AF Regolith Simulant

XRD scans were performed on unreacted JSC-1AF samples in order to identify the chemical species present. A representative XRD pattern of unreacted JSC-1AF simulant is

shown in Figure XXXVIII. The legend for the identified chemical species is contained in Table IX.

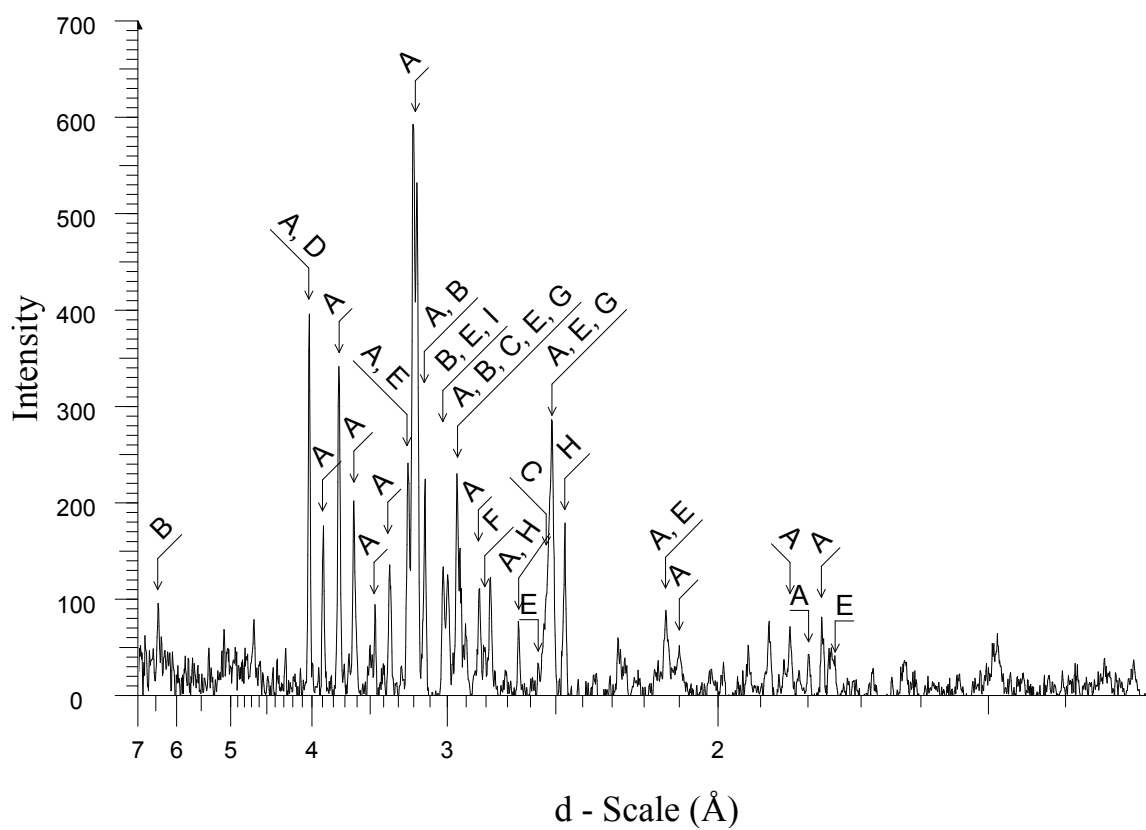


Figure XXXVIII: XRD pattern for unreacted JSC-1AF simulant with diffraction peaks labeled.

Table IX: Legend of Identified Chemical species in the Diffraction Pattern Shown in Figure XXXVIII

	Compound Name	Formula	Y-Scale	PDF #
A	Anorthite, sodian, disordered	$(\text{Ca},\text{Na})(\text{Si},\text{Al})_4\text{O}_8$	88.8	41-1481 (I)
A	Anorthite, ordered	$\text{CaAl}_2\text{Si}_2\text{O}_8$	76.74	41-1486 (*)
A	Albite, disordered	$\text{Na}(\text{Si}_3\text{Al})\text{O}_8$	36.89	10-0393 (*)
A	Anorthite, sodian, intermediate	$(\text{Ca},\text{Na})(\text{Si},\text{Al})_4\text{O}_8$	26.59	18-1202 (I)
A	Albite, calcian, ordered	$(\text{Na},\text{Ca})\text{Al}(\text{Si},\text{Al})_3\text{O}_8$	25.83	41-1480 (I)
E	Augite, aluminian	$\text{Ca}(\text{Mg},\text{Fe},\text{Al})(\text{Si},\text{Al})_2\text{O}_6$	16.67	41-1483 (I)
B	Potassium Silicate	$\text{K}_6\text{Si}_3\text{O}_9$	16.66	35-0394 (I)
C	Magnesioferrite, disordered, syn	$\text{MgFe}_2^{+3}\text{O}_4$	14.58	36-0398 (*)
D	Cristobalite, syn	SiO_2	12.7	39-1425 (*)
E	Augite	$\text{Ca}(\text{Fe},\text{Mg})\text{Si}_2\text{O}_6$	12.5	24-0201 (I)
F	Potassium Iron Oxide	KFeO_2	8.33	26-1319 (I)
G	Maghemite-C, syn	Fe_2O_3	5.73	39-1346 (*)
H	Calcium Magnesium Aluminum Oxide	$\text{Ca}_2\text{Mg}_2\text{Al}_{28}\text{O}_{46}$	4.17	50-0033 (I)
I	Hedenbergite	$\text{CaFe}^{+2}\text{Si}_2\text{O}_6$	5.73	41-1372 (*)

The presence of the two endmembers of the plagioclase solid solution series, albite and anorthite, are indicated by diffraction peaks in Figure XXXVIII and are identified in Table IX. Figure XXXIX contains XRD diffraction patterns from three unreacted samples of JSC-1AF regolith simulant. The composition of the simulant is somewhat uniform. A full representative XRD pattern is shown in Figure XXXVIII and a representative analysis is shown in Table IX. There is some variability in the simulant; however, the crystalline chemical species appear to be fairly uniform throughout as evidenced by the closely matching diffraction patterns.

XRD Patterns for Three JSC-1AF Samples

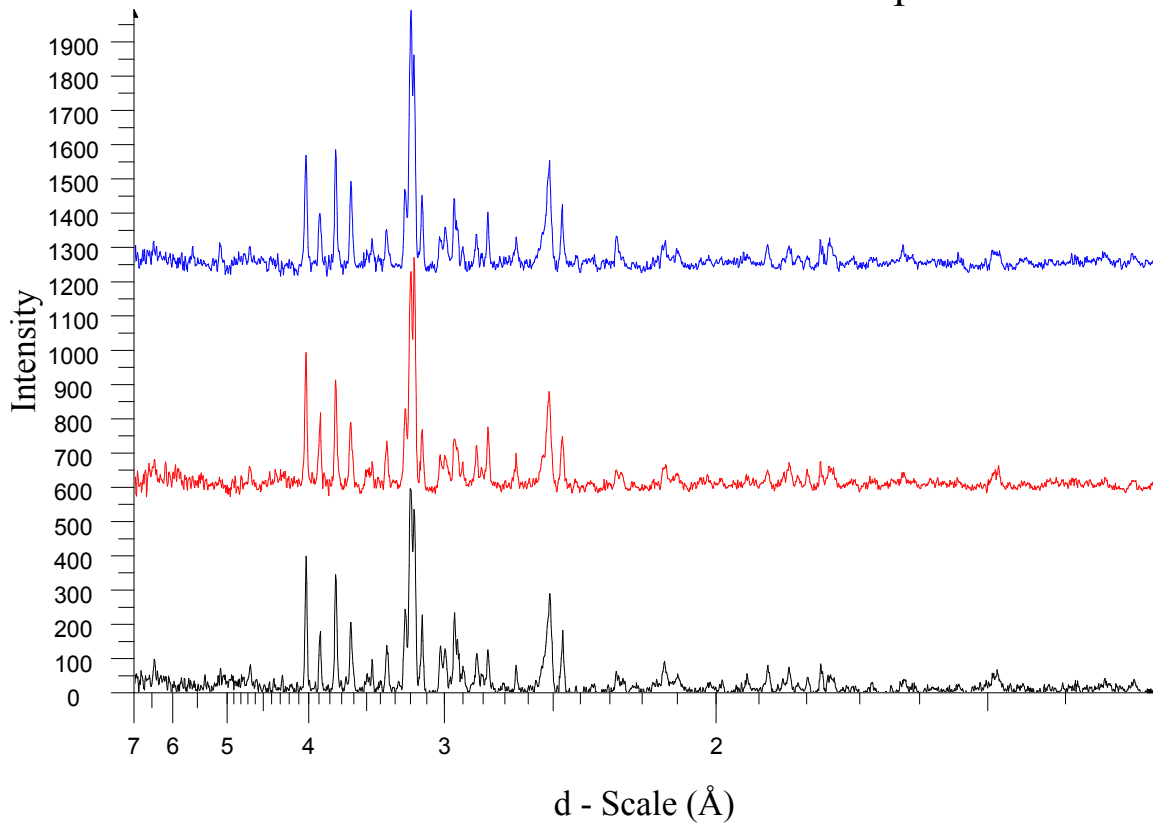


Figure XXXIX: Stacked XRD patterns for three samples of JSC-1AF regolith simulant

Chemical Species Present in Unreacted JSC-1A Regolith Simulant

Figure XL contains XRD diffraction patterns for three unreacted samples of JSC-1A regolith simulant. There seems to be more variability in the JSC-1A simulant than the JSC-1AF. However, there is still a large degree of uniformity between the XRD patterns.

XRD Patterns for Three JSC-1A Samples

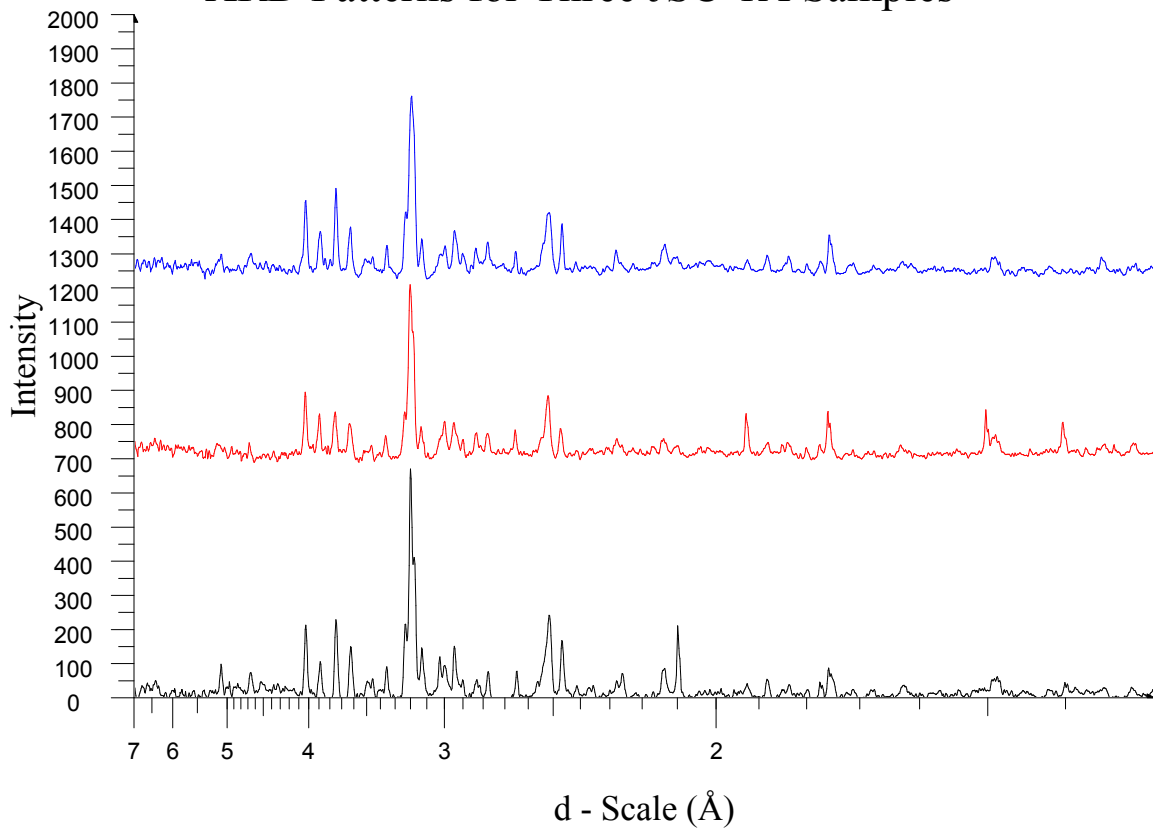


Figure XL: Stacked XRD patterns for three samples of JSC-1A regolith simulant

Legend for Color Coding in Figure XL:

Black: Unreacted JSC-1A regolith simulant sample

Red: Unreacted JSC-1A regolith simulant sample

Blue: Unreacted JSC-1A regolith simulant sample

The black pattern in Figure XL has a small defined peak at 2.26 Å, which does not appear in the other patterns. A defined peak of medium size is present in the black pattern at 2.10 Å, whereas in the other two patterns a small broad region is found at 2.10 Å. The red pattern has a defined medium size peak at 1.93 Å, while the other two patterns have a small broad region at 1.93 Å. Broadness and intensity of diffraction vary between all three patterns from 1.76-1.74 Å. Defined peaks exist in the red pattern at 1.50 Å and 1.40 Å which are not present in the other patterns. The likely reason for slight variability in the diffraction patterns is natural variability in the volcanic ash deposit in which the regolith simulant was mined.

Comparison of Unreacted JSC-1AF and JSC-1A Regolith Simulant Samples

Stacked diffraction patterns for unreacted JSC-1AF and JSC-1A simulants are shown in Figure XLI.

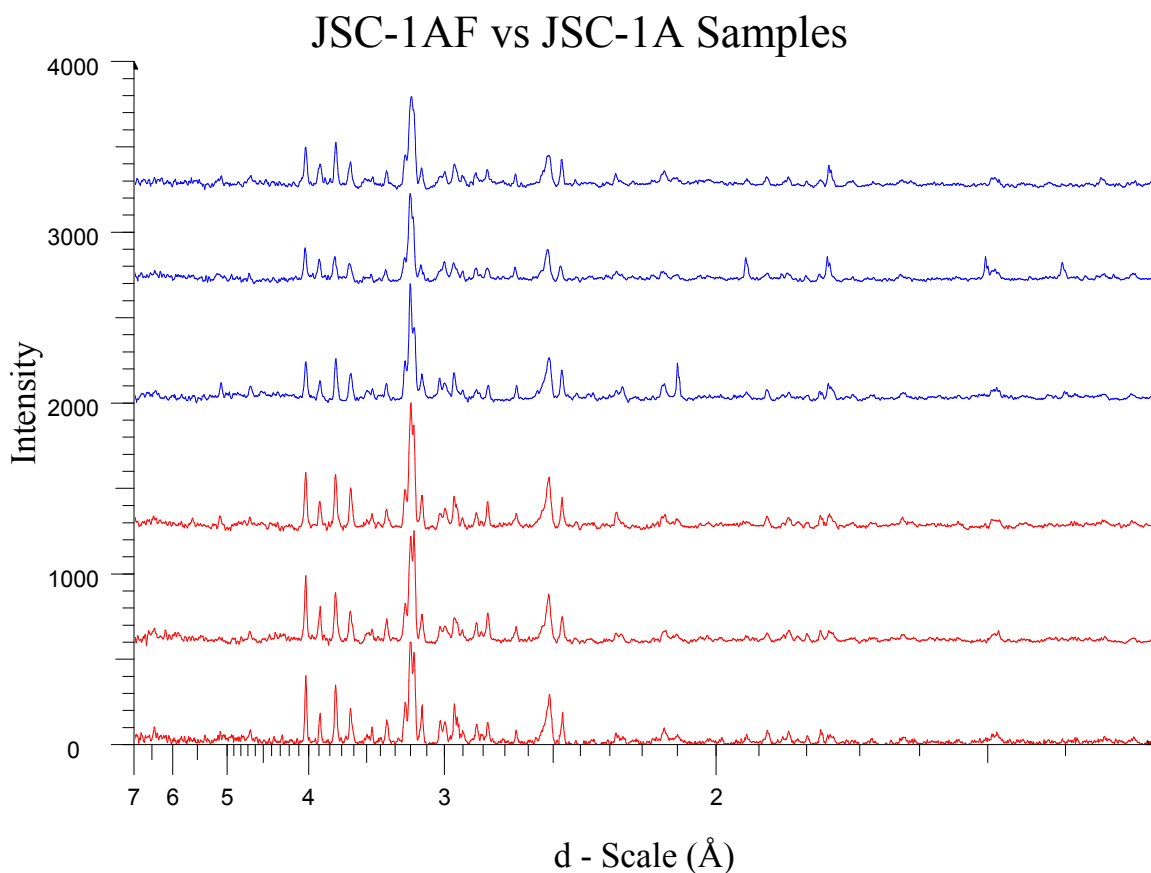


Figure XLI: Stacked XRD patterns of unreacted JSC-1AF and JSC-1A simulant

Legend for Color Coding in Figure XLI:

Blue: Unreacted JSC-1A regolith simulant samples

Red: Unreacted JSC-1AF regolith simulant samples

The diffraction patterns for the JSC-1A simulant and the JSC-1AF simulant in Figure XLI were found to be very similar. It was of interest to compare the patterns to determine whether processing the simulant to a smaller particle size resulted in preferential elimination of harder crystalline chemical species from the end product. A few differences have been noted when comparing the diffraction patterns of the two simulants. The JSC-1AF simulant has a more

defined shoulder peak at 3.18 Å. One pattern of the JSC-1A simulant has a defined peak at 2.10 Å, another JSC-1A pattern has a defined peak at 1.93 Å, and all JSC-1A patterns have a defined peak at 1.76 Å, not present in the JSC-1AF patterns. Two potential reasons for the variations observed in the diffraction patterns include natural variation in the volcanic ash deposit that the simulant was mined from, and preferential elimination of chemical species with a high hardness during the particle size refining process.

Chemical Species Present in Standard Atmosphere SHS Reaction Products Utilizing JSC-1AF Regolith Simulant

19.44% Al by weight

The XRD pattern for the reaction product utilizing a 19.44% aluminum stoichiometry, with identified chemical species labeled, is shown in Figure XLII. The legend for the identified chemical species is shown in Table X.

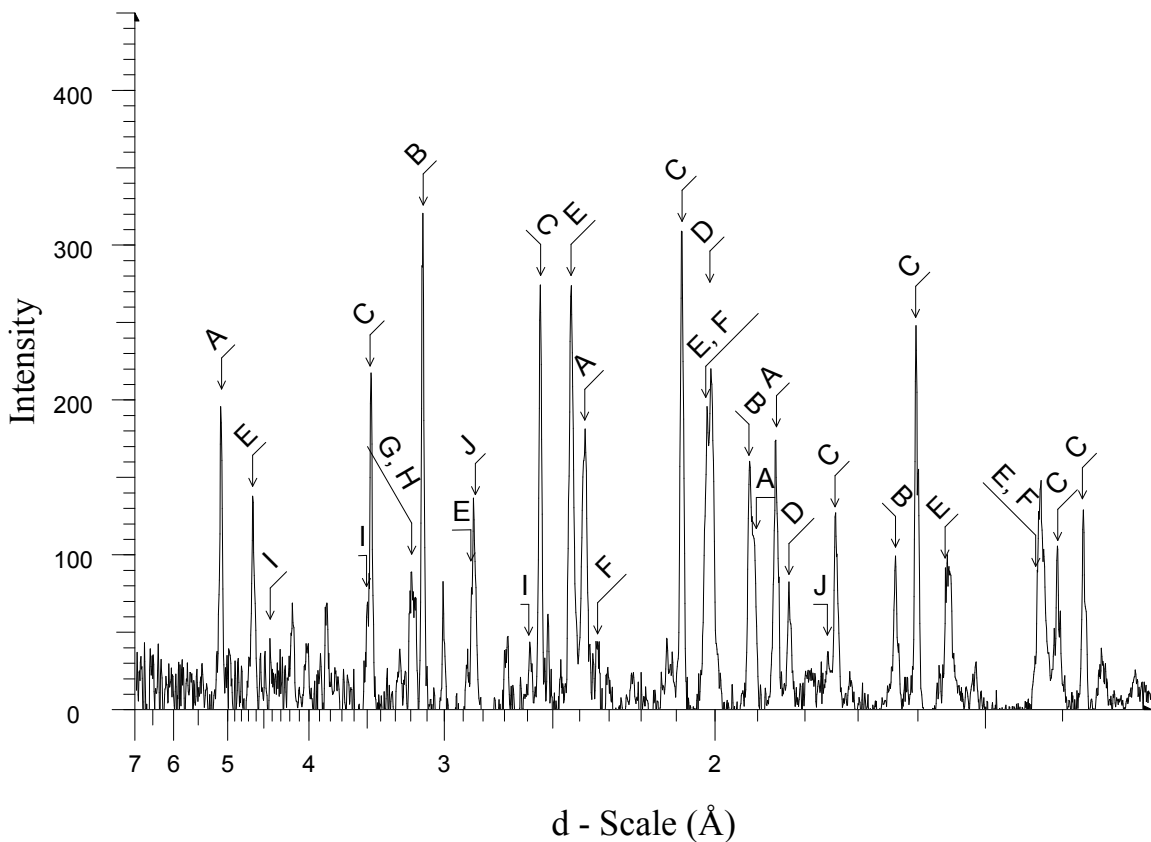


Figure XLII: XRD pattern for the reaction product of the 80.56% JSC-1AF and 19.44% aluminum stoichiometry.

Table X: Legend of Identified Chemical species in the Diffraction Pattern Shown in Figure XXXVIII

	Compound Name	Formula	Y-Scale	PDF #
B	Silicon, syn	Si	95.71	27-1402 (*)
C	Corundum, syn	Al ₂ O ₃	85.63	46-1212 (*)
C	Corundum, syn	Al ₂ O ₃	81.01	10-0173 (I)
E	Spinel, syn	MgAl ₂ O ₄	67.58	21-1152 (*)
A	Ferdisilicite, syn [NR]	FeSi ₂	55.56	35-0822 (*)
D	Fersilicite, syn [NR]	FeSi	53.42	38-1397 (*)
J	Gehlenite, syn	Ca ₂ Al ₂ SiO ₇	31.66	35-0755 (*)
F	Aluminum Nitride (FCC)	AlN	28.86	46-1200 (*)
G	Albite, disordered	Na(Si ₃ Al)O ₈	21.36	10-0393 (*)
H	Anorthite, ordered	CaAl ₂ Si ₂ O ₈	19.23	41-1486 (*)
I	Grossite, syn	CaAl ₄ O ₇ /CaO·2Al ₂ O ₃	18.75	23-1037 (*)
I	Grossite	CaAl ₄ O ₇	8.33	46-1475 (I)
	Aluminum Oxide	Al ₂ O ₃	19.23	50-1496 (I)
	Sodium Aluminum Silicate	Na _{1.65} Al _{1.65} Si _{0.35} O ₄	14.95	49-0005 (*)
	Aluminum, syn	Al	14.95	04-0787 (*)
	Potassium Aluminum Silicate	K _{1.25} Al _{1.25} Si _{0.75} O ₄	12.82	32-0731 (I)
	Diaoyudaoite, syn	NaAl ₁₁ O ₁₇ /0.5(Na ₂ O·11Al ₂ O ₃)	12.5	21-1096 (I)
	Iron, syn	Fe	10.69	06-0696 (*)
	Iron Nitride	Fe ₂ N	9.3	50-0957 (I)
	Magnesium Aluminum Oxide	Mg _{0.388} Al _{2.408} O ₄	8.54	48-0528 (I)
	Potassium Aluminum Oxide	K ₂ Al ₂ O ₃₄ /K ₂ O·11Al ₂ O ₃	6.25	31-0960 (I)

Figure XLIII shows two stacked XRD patterns from two different reaction products, synthesized using a 19.44% aluminum stoichiometry. The similarity of the diffraction patterns illustrates that the formation of specific crystalline chemical species in the reaction product is repeatable.

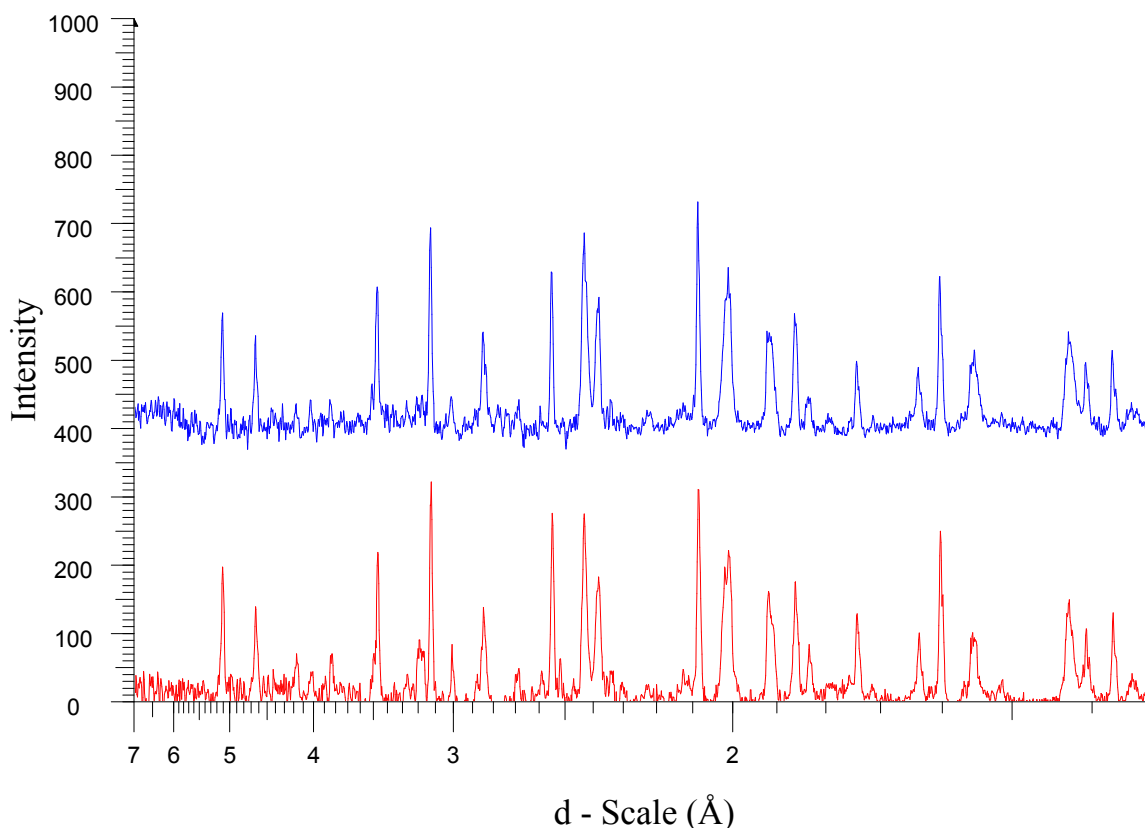


Figure XLIII: XRD patterns of two reacted samples of 80.56% JSC-1AF and 19.44% Al by weight

Legend for Color Coding in Figure XLIII:

Blue: JSC-1AF reaction product utilizing 19.44% aluminum

Red: JSC-1AF reaction product utilizing 19.44% aluminum

Analysis of the peaks found within the XRD patterns of the 19.44% aluminum stoichiometry in Figure XLIII show several regions where broad peak areas are observed, which can indicate multiple chemical species, solid solutions, or both. Broad areas of intensity are observed between 1.395-1.435 Å, 1.536-1.569 Å, 1.895-1.926 Å, 1.985-2.037 Å, 2.330-2.446 Å, 3.154-3.217 Å, and 3.450-3.533 Å.

24.45% Al by weight

The XRD pattern for the reaction product utilizing a 24.45% aluminum stoichiometry, with identified chemical species labeled, is shown in Figure XLIV. The legend for the identified chemical species is shown in Table XI.

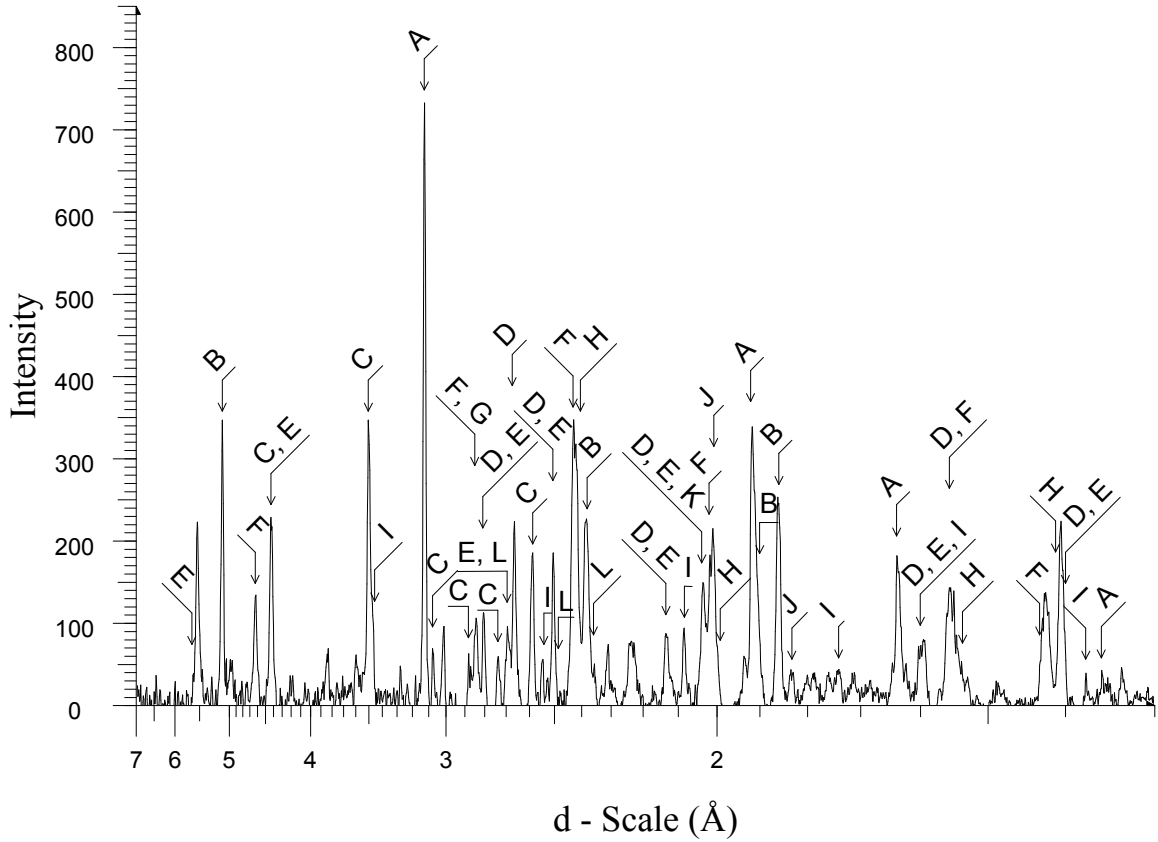


Figure XLIV: XRD pattern for the reaction product of the 75.55% JSC-1AF and 24.45% aluminum stoichiometry.

Table XI: Legend of Identified Chemical species in the Diffraction Pattern Shown in Figure XLIV

	Compound Name	Formula	Y-Scale	PDF #
A	Silicon, syn	Si	87.78	27-1402 (*)
B	Ferdisilicite, syn [NR]	FeSi ₂	33.44	35-0822 (*)
C	Grossite, syn	CaAl ₄ O ₇ /CaO·2Al ₂ O ₃	41.1	23-1037 (*)
D	Hibonite-5H, ferroan	Ca(Al,Fe) ₁₂ O ₁₉	18.81	38-0469 (*)
C	Grossite	CaAl ₄ O ₇	18.78	46-1475 (I)
E	Nitrosyl Aluminum Oxide	(NO) ₂ Al ₂₂ O ₃₄ /(NO) ₂ O·11Al ₂ O ₃	16.98	23-0457 (I)
F	Spinel, syn	MgAl ₂ O ₄	15.33	21-1152 (*)
G	Gehlenite, syn	Ca ₂ Al ₂ SiO ₇	14.14	35-0755 (*)
H	Magnesium Aluminum Oxide	Mg _{0.388} Al _{2.408} O ₄	10.45	48-0528 (I)
I	Corundum, syn	Al ₂ O ₃	8.36	10-0173 (I)
J	Fersilicite, syn [NR]	FeSi	8.36	38-1397 (*)
I	Corundum, syn	Al ₂ O ₃	8.36	46-1212 (*)
K	Iron, syn	Fe	4.6	06-0696 (*)
L	Aluminum Nitride (Hex)	AlN	4.18	25-1133 (*)
	Diaoyudaoite, syn	NaAl ₁₁ O ₁₇ /0.5(Na ₂ O·11Al ₂ O ₃)	28.21	21-1096 (I)
	Calcium Aluminum Oxide	(CaO) _x (Al ₂ O ₃) ₁₁	24.99	41-0358 (*)
	Potassium Aluminum Oxide	K ₂ Al ₂₂ O ₃₄ /K ₂ O·11Al ₂ O ₃	18.81	31-0960 (I)
	Potassium Iron Oxide	KFeO ₂	14.63	26-1319 (I)
	Potassium Aluminum Silicate	K _{1.25} Al _{1.25} Si _{0.75} O ₄	12.54	32-0731 (I)
	Diaoyudaoite, syn	NaAl ₁₁ O ₁₇ /0.5(Na ₂ O·11Al ₂ O ₃)	12.5	21-1096 (I)
	Sodium Aluminum Oxide	Na ₂ Al ₂₂ O ₃₄ /Na ₂ O·11Al ₂ O ₃	10.45	31-1263 (I)
	Potassium Titanium Oxide	K ₃ Ti ₈ O ₁₇	6.27	24-0901 (I)
	Aluminum Oxide Nitride	Al ₈ O ₃ N ₆	6.27	48-1581 (I)
	Aluminum Nitride (FCC)	AlN	6.25	46-1200 (*)
	Aluminum Oxide	Al ₂ O ₃	3.83	47-1292 (I)
	Aluminum, syn	Al	2.09	04-0787 (*)

28.85% Al by weight

The XRD pattern for the reaction product utilizing a 28.85% aluminum stoichiometry, with identified chemical species labeled, is shown in Figure XLV. The legend for the identified chemical species is shown in Table XII.

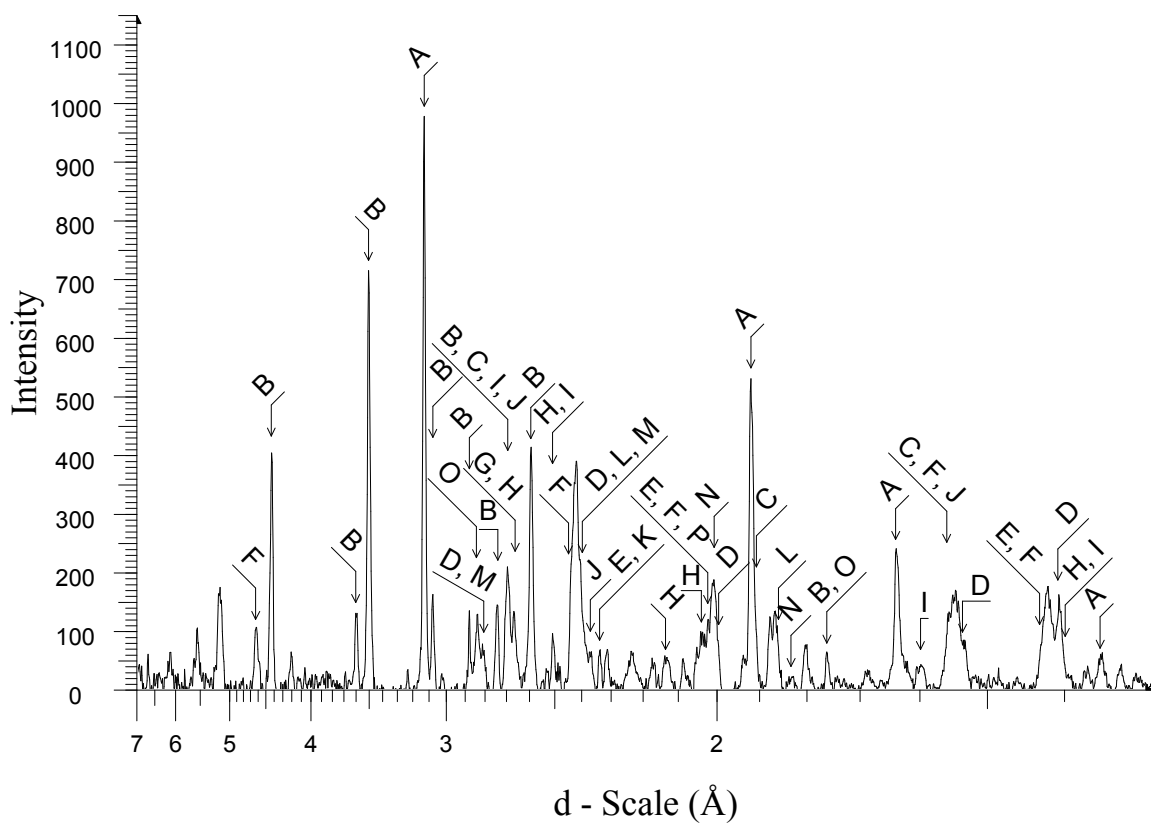


Figure XLV: XRD pattern for the reaction product of the 71.15% JSC-1AF and 28.85% aluminum stoichiometry.

Table XII: Legend of Identified Chemical species in the Diffraction Pattern Shown in Figure XLV

	Compound Name	Formula	Y-Scale	PDF #
A	Silicon, syn	Si	97.07	27-1402 (*)
B	Grossite, syn	CaAl ₄ O ₇ /CaO·2Al ₂ O ₃	64.61	23-1037 (*)
B	Grossite	CaAl ₄ O ₇	45.08	46-1475 (I)
C	Calcium Aluminum Oxide tricalcium aluminate	Ca ₃ Al ₂ O ₆	21.05	38-1429 (*)
F	Spinel, syn	MgAl ₂ O ₄	14.61	21-1152 (*)
D	Magnesium Aluminum Oxide	Mg _{0.388} Al _{2.408} O ₄	12.73	48-0528 (I)
O	Gehlenite, syn	Ca ₂ Al ₂ SiO ₇	12.5	35-0755 (*)
E	Aluminum Nitride (FCC)	AlN	12.38	46-1200 (*)
G	Merwinite, syn	Ca ₃ Mg(SiO ₄) ₂	9.39	35-0591 (*)
H	Hibonite-5H, ferroan	Ca(Al,Fe) ₁₂ O ₁₉	8.48	38-0469 (*)
I	Nitrosyl Aluminum Oxide	(NO) ₂ Al ₂₂ O ₃₄ /(NO) ₂ O·11Al ₂ O ₃	8.48	23-0457 (I)
P	Iron, syn	Fe	8.33	06-0696 (*)
J	Aluminum Nitride (Hex)	AlN	7.7	25-1133 (*)
C	Calcium Aluminum Oxide	Ca ₃ Al ₂ O ₆	7.29	32-0148 (I)
K	Aluminum, syn	Al	7.09	04-0787 (*)
L	Ferdisilicite, syn [NR]	FeSi ₂	6.45	35-0822 (*)
M	Aluminum Oxide	Al ₂ O ₃	6.36	47-1292 (I)
N	Fersilicite, syn [NR]	FeSi	4.25	38-1397 (*)
	Potassium Aluminum Silicate	K _{1.25} Al _{1.25} Si _{0.75} O ₄	14.58	32-0731 (I)
	Diaoyudaoite, syn	NaAl ₁₁ O ₁₇ /0.5(Na ₂ O·11Al ₂ O ₃)	11.67	21-1096 (I)
	Sodium Aluminum Oxide	Na ₂ Al ₂₂ O ₃₄ /Na ₂ O·11Al ₂ O ₃	8.48	31-1263 (I)
	Potassium Aluminum Oxide	K ₂ Al ₂₂ O ₃₄ /K ₂ O·11Al ₂ O ₃	6.25	31-0960 (I)
	Potassium Iron Oxide	KFeO ₂	5.54	26-1319 (I)
	Calcium Aluminum Oxide	(CaO) _x (Al ₂ O ₃) ₁₁	4.25	41-0358 (*)
	Aluminum Oxide Nitride	Al ₈ O ₃ N ₆	3.98	48-1581 (I)
	Hibonite-5H, syn	CaAl ₁₂ O ₁₉	1.68	38-0470 (I)

Figure XLVI shows two stacked XRD patterns from two different reaction products, synthesized using a 28.85% aluminum stoichiometry. The similarity of the diffraction patterns illustrates that the formation of specific crystalline chemical species in the reaction product is repeatable.

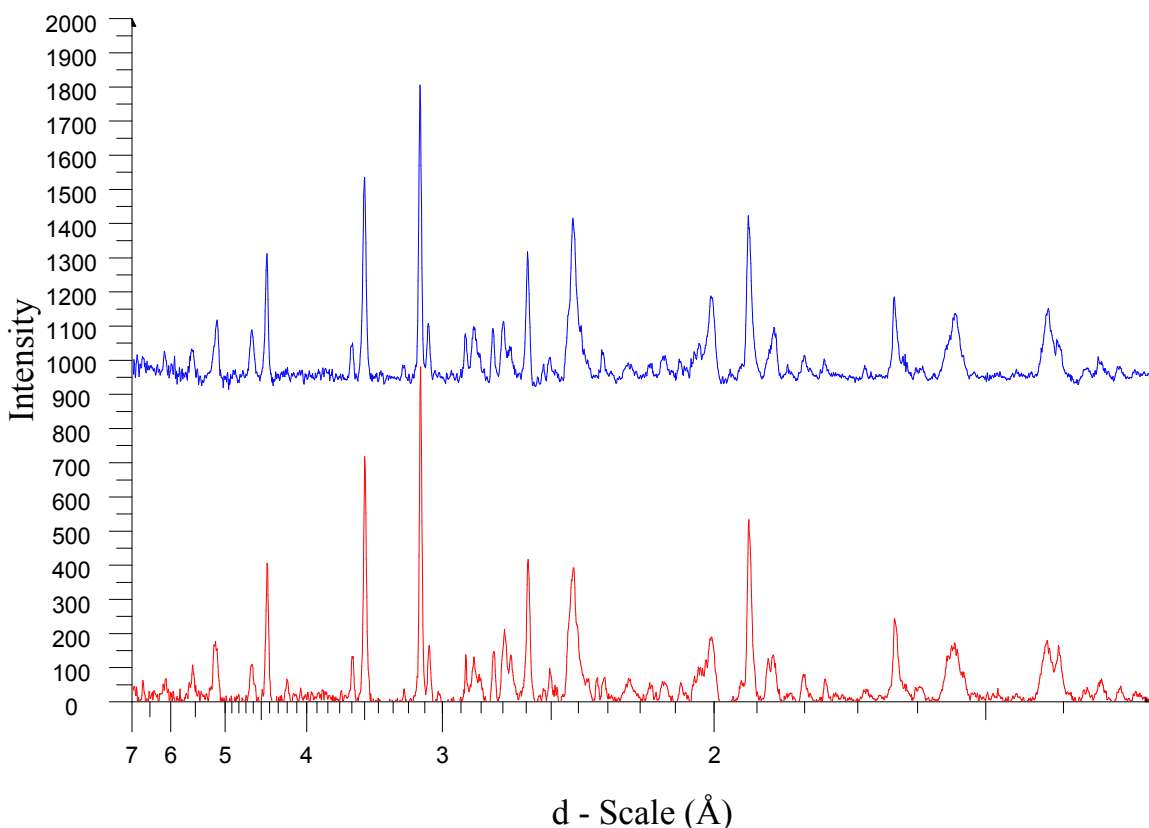


Figure XLVI: XRD patterns of two reacted samples of 71.15% JSC-1AF and 28.85% Al by weight

Legend for Color Coding in Figure XLVI:

Blue: JSC-1AF reaction product utilizing 28.85% aluminum

Red: JSC-1AF reaction product utilizing 28.85% aluminum

Analysis of the peaks found within the XRD patterns of the 28.85% aluminum stoichiometry in Figure XLVI show several regions where broad peak areas are observed, which indicate multiple chemical species, solid solutions, or both. Broad areas of intensity are observed between 1.395-1.431 Å, 1.524-1.566 Å, 1.850-1.882 Å, 1.992-2.057 Å, 2.356-2.451 Å, 2.646-2.719 Å, and 2.793-2.893 Å.

The patterns in Figure XLVI are very similar, having only a few differences. The red pattern has a small peak at 2.33 Å, which does not appear in the blue pattern. There are peaks at 1.88 Å and 1.86 Å combined in a broad peak in the red pattern, while the blue pattern only has a defined peak at 1.86 Å and has a broad region encompassing the 1.88 Å position. Shoulder

peaks are present at 1.62 Å in the blue pattern, but not the red. A well defined peak exists at 1.40 Å in the red pattern, but not the blue. The differences in the diffraction patterns could be a result of slight differences in the composition of the simulat. Slight changes in the preferential ordering of grains within the XRD sample holder are another possibility.

33.33% Al by weight

The XRD pattern for the reaction product utilizing a 33.33% aluminum stoichiometry, with identified chemical species labeled, is shown in Figure XLVII. The legend for the identified chemical species is shown in Table XIII.

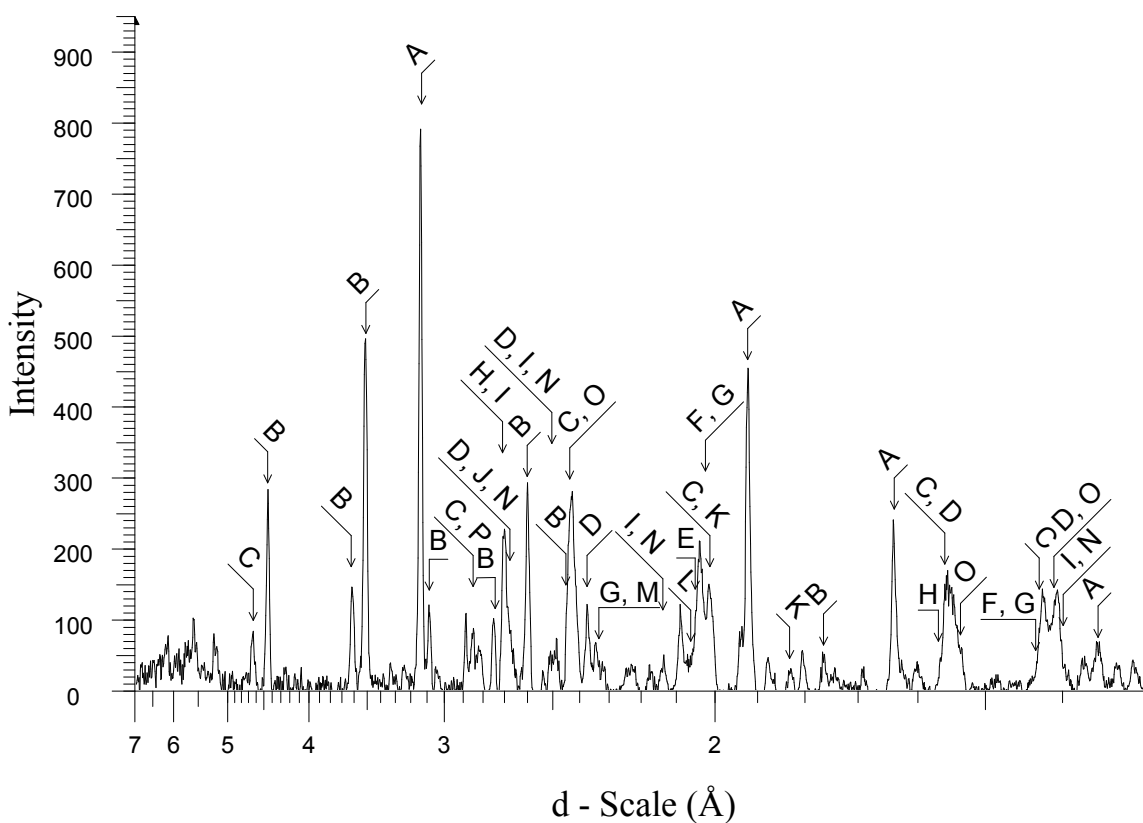


Figure XLVII: XRD pattern for the reaction product of the 66.67% JSC-1AF and 33.33% aluminum stoichiometry.

Table XIII: Legend of Identified Chemical species in the Diffraction Pattern Shown in Figure XLVII

	Compound Name	Formula	Y-Scale	PDF #
A	Silicon, syn	Si	103.82	27-1402 (*)
B	Grossite	CaAl ₄ O ₇	61.1	46-1475 (I)
C	Spinel, syn	MgAl ₂ O ₄	27.09	21-1152 (*)
B	Grossite, syn	CaAl ₄ O ₇ /CaO·2Al ₂ O ₃	22.92	23-1037 (*)
D	Aluminum Nitride (Hex)	AlN	16.4	25-1133 (*)
E	Aluminum Iron	AlFe	14.58	33-0020 (*)
F	Iron, syn	Fe	12.5	06-0696 (*)
G	Aluminum Nitride (FCC)	AlN	12.5	46-1200 (*)
H	Calcium Aluminum Oxide	Ca ₃ Al ₂ O ₆	12.5	33-0251 (*)
P	Gehlenite, syn	Ca ₂ Al ₂ SiO ₇	10.42	35-0755 (*)
I	Nitrosyl Aluminum Oxide	(NO) ₂ Al ₂₂ O ₃₄ /(NO) ₂ O·1 1Al ₂ O ₃	10.42	23-0457 (I)
J	Merwinite, syn	Ca ₃ Mg(SiO ₄) ₂	8.33	35-0591 (*)
K	Fersilicite, syn [NR]	FeSi	7.29	38-1397 (*)
L	Aluminum Iron	AlFe ₃	6.25	50-0955 (*)
M	Aluminum, syn	Al	6.25	04-0787 (*)
N	Hibonite-5H, ferroan	Ca(Al,Fe) ₁₂ O ₁₉	6.25	38-0469 (*)
O	Magnesium Aluminum Oxide	Mg _{0.388} Al _{2.408} O ₄	6.25	48-0528 (I)
	Diaoyudaoite, syn	NaAl ₁₁ O ₁₇ /0.5(Na ₂ O·11 Al ₂ O ₃)	27.08	21-1096 (I)
	Sodium Magnesium Aluminum Oxide	NaMg ₂ Al ₁₅ O ₂₅ /Na ₂ O·4M gO·15Al ₂ O ₃	16.67	27-0730 (I)
	Potassium Magnesium Silicate	K ₂ MgSiO ₄	12.5	48-0900 (I)
	Potassium Magnesium Aluminum Oxide K-beta"-alumina	KMg ₂ Al ₁₅ O ₂₅	10.42	42-0204 (I)
	Sodium Aluminum Oxide	Na ₂ Al ₂₂ O ₃₄ /Na ₂ O·11Al ₂ O ₃	8.33	31-1263 (I)
	Potassium Iron Oxide	KFeO ₂	4.56	26-1319 (I)

Figure XLVIII shows two stacked XRD patterns from two different reaction products, synthesized using a 33.33% aluminum stoichiometry. The similarity of the diffraction patterns illustrates that the formation of specific crystalline chemical species in the reaction product is repeatable. Analysis of the XRD patterns of the 33.33% aluminum stoichiometry in Figure XLVIII show several regions where broad peak areas are observed, which indicate multiple chemical species, solid solutions, or both.

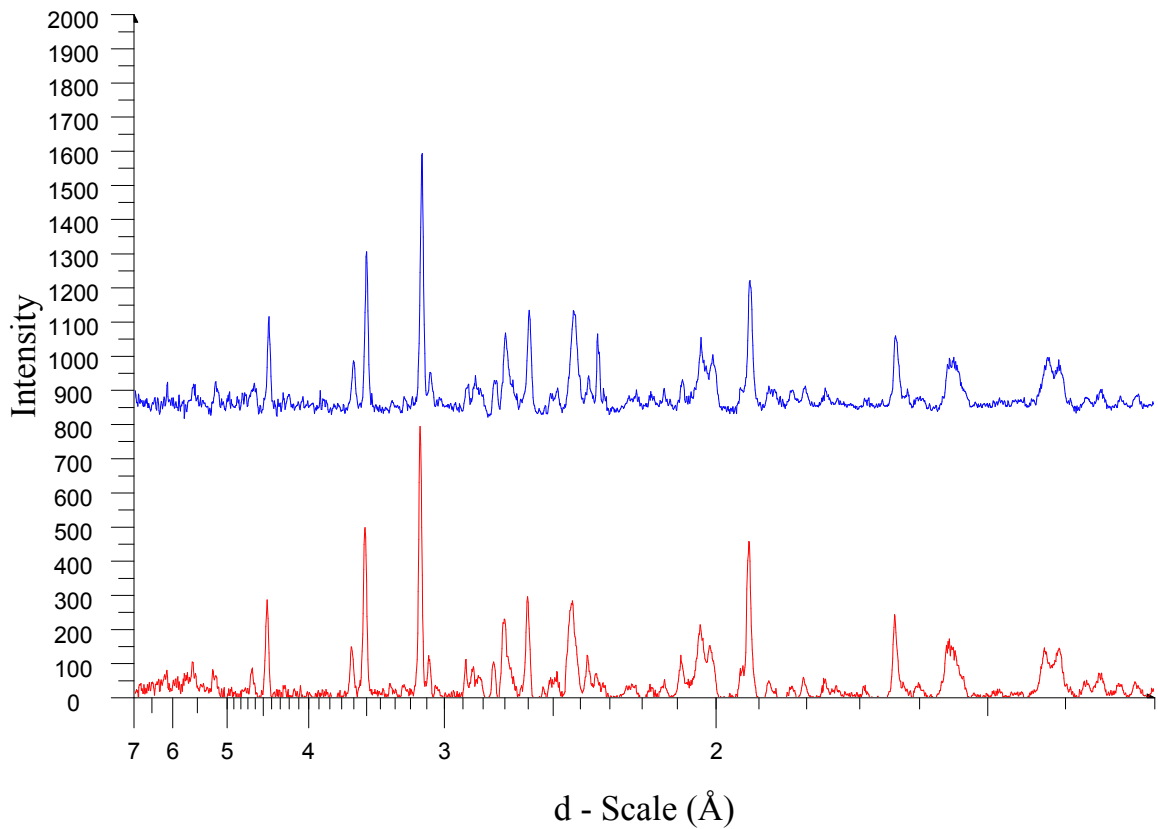


Figure XLVIII: XRD patterns of two reacted samples of 66.67% JSC-1AF and 33.33% Al by weight

Legend for Color Coding in Figure XLVIII:

Blue: JSC-1AF reaction product utilizing 33.33% aluminum

Red: JSC-1AF reaction product utilizing 33.33% aluminum

Comparison of Chemical species Formed in JSC-1AF Reactant Stoichiometries

XRD patterns of the four JSC-1AF reactant stoichiometries in Figure XLII, Figure XLIV, Figure XLV, and Figure XLVII are stacked and shown in Figure XLIX in order to illustrate the differences in chemical species present within reaction products synthesized using different stoichiometries of aluminum. Table XIV compares relative diffraction intensities for chemical species present in the various reaction stoichiometries that were identified in Table X, Table XI, Table XII, and Table XIII.

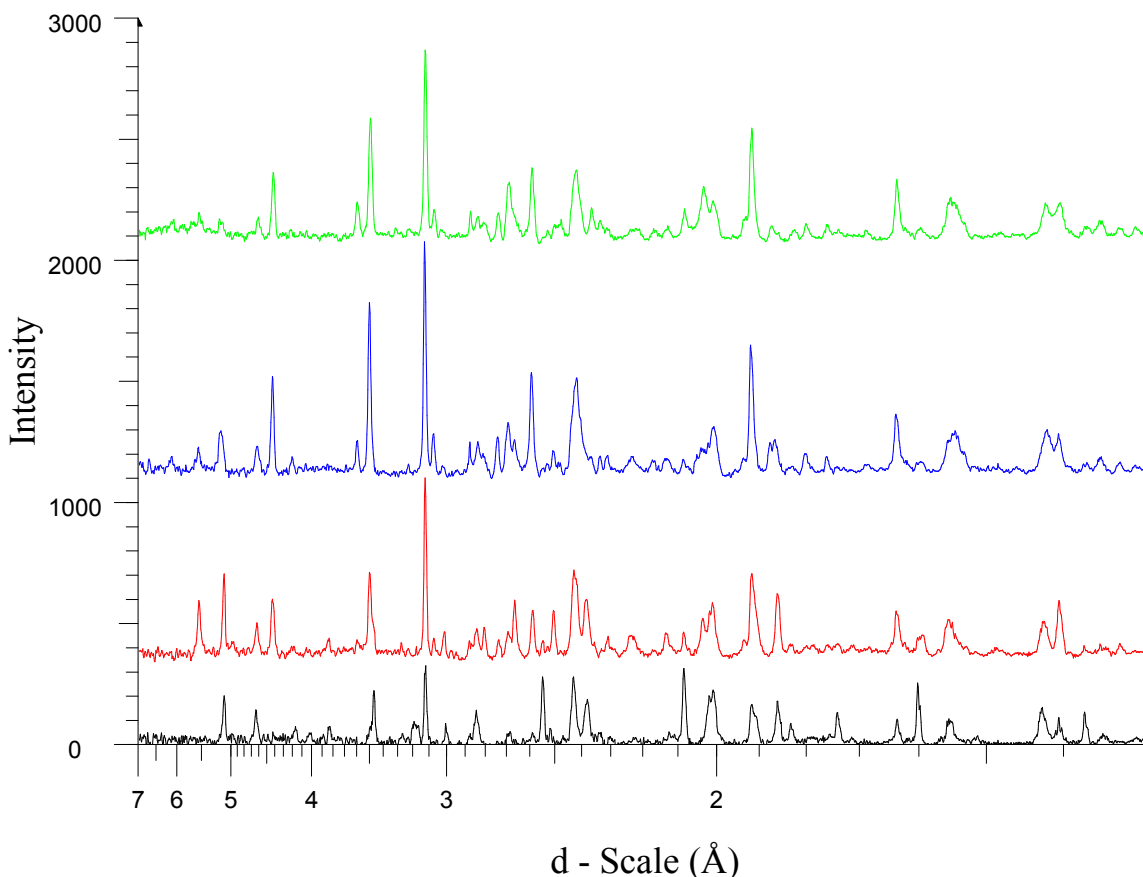


Figure XLIX: Stacked XRD patterns of four reacted stoichiometries of Al and JSC-1AF simulant

Legend for Color Coding in Figure XLIX and Table XIV:

Black: 80.56% JSC-1AF and 19.44% Al by weight

Red: 75.55% JSC-1AF and 24.45% Al by weight

Blue: 71.15% JSC-1AF and 28.85% Al by weight

Green: 66.67% JSC-1AF and 33.33% Al by weight

Table XIV: Identified Chemical species in the Diffraction Patterns in Figure XLIX

Formula	Intensity				PDF #
	19.44AF	24.45AF	28.85AF	33.33AF	
Si	307	644	955	826	27-1402 (*)
MgAl ₂ O ₄	217	113	144	216	21-1152 (*)
Al ₂ O ₃ (α)	275	61	0	0	46-1212 (*)
Al ₂ O ₃ (α)	260	61	0	0	10-0173 (I)
FeSi	171	61	42	58	38-1397 (*)
FeSi ₂	178	245	63	0	35-0822 (*)
AlN (FCC)	93	46	122	100	46-1200 (*)
AlN (Hex)	0	31	76	131	25-1133 (*)
CaAl ₄ O ₇	27	138	444	486	46-1475 (I)
CaAl ₄ O ₇ /CaO·2Al ₂ O ₃	60	302	636	182	23-1037 (*)
Mg _{0.388} Al _{2.408} O ₄	27	77	125	50	48-0528 (I)
Ca ₂ Al ₂ SiO ₇	102	104	123	83	35-0755 (*)
Al	48	15	70	50	04-0787 (*)
Na(Si ₃ Al)O ₈	69	0	0	0	10-0393 (*)
CaAl ₂ Si ₂ O ₈	62	0	0	0	41-1486 (*)
Fe	34	34	82	100	06-0696 (*)
Al ₂ O ₃	62	0	0	0	50-1496 (I)
Al ₂ O ₃	0	28	63	0	47-1292 (I)
Ca ₃ Al ₂ O ₆	0	0	207	0	38-1429 (*)
Ca ₃ Al ₂ O ₆	0	0	72	0	32-0148 (I)
Ca ₃ Al ₂ O ₆	0	0	0	100	33-0251 (*)
NaAl ₁₁ O ₁₇ /0.5(Na ₂ O·11Al ₂ O ₃)	40	92	115	216	21-1096 (I)
K ₂ Al ₂₂ O ₃₄ /K ₂ O·11Al ₂ O ₃	20	138	62	0	31-0960 (I)
Ca(Al,Fe) ₁₂ O ₁₉	0	138	83	50	38-0469 (*)
(NO) ₂ Al ₂₂ O ₃₄ /(NO) ₂ O·11Al ₂ O ₃	0	125	83	83	23-0457 (I)
KFeO ₂	0	107	55	36	26-1319 (I)
(CaO) _x (Al ₂ O ₃) ₁₁	0	183	42	0	41-0358 (*)
Na ₂ Al ₂₂ O ₃₄ /Na ₂ O·11Al ₂ O ₃	0	77	83	66	31-1263 (I)
Na _{1.65} Al _{1.65} Si _{0.35} O ₄	48	0	0	0	49-0005 (*)
K _{1.25} Al _{1.25} Si _{0.75} O ₄	41	92	143	0	32-0731 (I)
Fe ₂ N	30	0	0	0	50-0957 (I)
K ₃ Ti ₈ O ₁₇	0	46	0	0	24-0901 (I)
Al ₈ O ₃ N ₆	0	46	39	0	48-1581 (I)
Ca ₃ Mg(SiO ₄) ₂	0	0	92	66	35-0591 (*)
CaAl ₁₂ O ₁₉	0	0	17	0	38-0470 (I)
AlFe	0	0	0	116	33-0020 (*)
AlFe ₃	0	0	0	50	50-0955 (*)
NaMg ₂ Al ₁₅ O ₂₅ /Na ₂ O·4MgO·15Al ₂ O ₃	0	0	0	133	27-0730 (I)
K ₂ MgSiO ₄	0	0	0	100	48-0900 (I)
KMg ₂ Al ₁₅ O ₂₅	0	0	0	83	42-0204 (I)

Only the reaction product utilizing a 19.44% aluminum stoichiometry retains measurable diffraction peaks for chemical species present in the unreacted JSC-1AF simulant. Two of the species are $\text{CaAl}_2\text{Si}_2\text{O}_8$ and $\text{Na}(\text{Si}_3\text{Al})\text{O}_8$, (41-1486) and (10-0393) respectively. The presence of the diffraction peaks in only the lowest aluminum stoichiometry indicates that insufficient aluminum is present to fully react with the chemical species present in the simulant. Largest intensities for unreacted aluminum are found in the lowest stoichiometry, which may indicate that insufficient heat is produced to fully oxidize all aluminum and reduce other reactants. Diffraction intensities for silicon are largest in the 28.85% aluminum stoichiometry, and smallest at the lowest aluminum stoichiometry, supporting the previous statement.

Iron silicide diffraction intensities are observed to be significantly larger in the two smallest aluminum stoichiometries than the intensities observed in the two largest aluminum stoichiometries. FeSi_2 (35-0822) diffraction intensity is significantly large in the 19.44% and 24.45% aluminum stoichiometry, while FeSi (38-1397) is significantly large in only the 19.44% stoichiometry. The largest diffraction intensities for MgAl_2O_4 are observed in the 19.44% and 33.33% aluminum stoichiometries, and the smallest are observed in the middle stoichiometries. Variation in the diffraction intensities for chemical species between reactant stoichiometries likely occurred due to differences in temperatures achieved during the reaction, and the quantity of aluminum available to react with the simulant.

CaAl_4O_7 (23-1037) diffraction peaks are at a maximum in the 28.85% aluminum stoichiometry. Intensities decrease as aluminum quantities increase or decrease from this point. CaAl_4O_7 (46-1475) diffraction peaks increase as the aluminum quantity increases in the reactant stoichiometries. Corundum (46-1212) and (10-0173) diffraction intensities are largest in the 19.44% aluminum stoichiometry, and decrease to negligible levels in the upper two stoichiometries. $\text{Ca}(\text{Al}, \text{Fe})_{12}\text{O}_{19}$ (38-0469) diffraction intensities are observed to be highest in the 24.45% aluminum stoichiometry, lower intensities are observed in higher aluminum stoichiometries, and negligible intensities observed in the lowest aluminum stoichiometry. Diffraction intensities of $\text{Mg}_{388}\text{Al}_{2408}\text{O}_4$ (48-0528) are highest in the 28.85% aluminum stoichiometry, while $\text{Ca}_2\text{Al}_2\text{SiO}_7$ (35-0755) intensities seem to be fairly similar throughout all stoichiometries. Various diffraction intensities and phases of $\text{Ca}_3\text{Al}_2\text{O}_6$ are found in the upper two aluminum stoichiometries.

***Chemical Species Present in Standard Atmosphere SHS Reaction Products Utilizing JSC-1A
Regolith Simulant***

19.44% Al by weight

The XRD pattern for the reaction product utilizing a 19.44% aluminum stoichiometry, with identified chemical species labeled, is shown in Figure L. The legend for the identified chemical species is shown in Table XV.

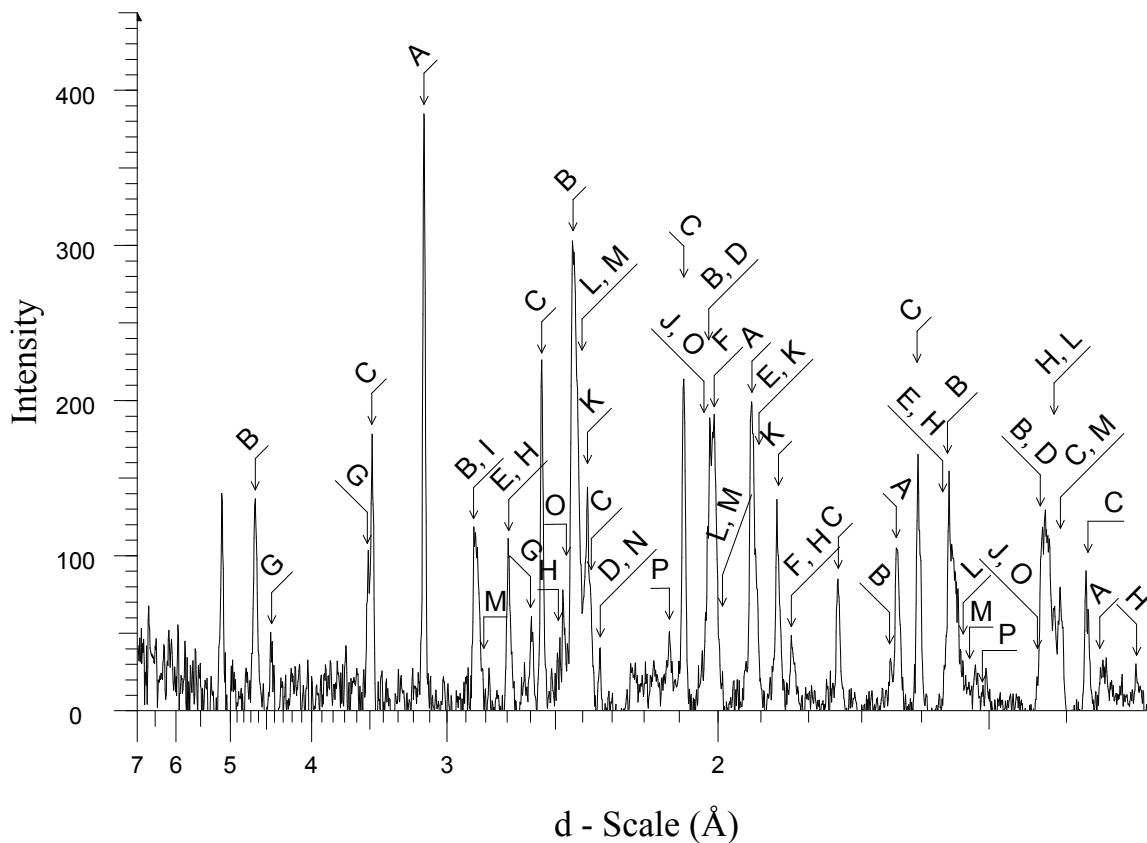


Figure L: XRD pattern for the reaction product of the 80.56% JSC-1A and 19.44% aluminum stoichiometry.

Table XV: Legend of Identified Chemical species in the Diffraction Pattern Shown in Figure L

	Compound Name	Formula	Y-Scale	PDF #
A	Silicon, syn	Si	97.04	27-1402 (*)
B	Spinel, syn	MgAl ₂ O ₄	65.46	21-1152 (*)
C	Corundum, syn	Al ₂ O ₃	50	46-1212 (*)
C	Corundum, syn	Al ₂ O ₃	45.83	10-0173 (I)
D	Aluminum Nitride (FCC)	AlN	35.42	46-1200 (*)
E	Calcium Aluminum Oxide tricalcium aluminate	Ca ₃ Al ₂ O ₆	29.17	38-1429 (*)
F	Fersilicite, syn [NR]	FeSi	25	38-1397 (*)
G	Grossite	CaAl ₄ O ₇	24.82	46-1475 (I)
I	Gehlenite, syn	Ca ₂ Al ₂ SiO ₇	22.81	35-0755 (*)
H	Aluminum Nitride (Hex)	AlN	18.75	25-1133 (*)
J	Iron, syn	Fe	16.67	06-0696 (*)
K	Ferdasilicite, syn [NR]	FeSi ₂	14.58	35-0822 (*)
L	Magnesium Aluminum Oxide	Mg _{0.388} Al _{2.408} O ₄	13.36	48-0528 (I)
G	Grossite, syn	CaAl ₄ O ₇ /CaO·2Al ₂ O ₃	10.94	23-1037 (*)
M	Aluminum Oxide Nitride	Al ₅ O ₆ N	10.85	48-0686 (*)
N	Aluminum, syn	Al	9.37	04-0787 (*)
O	Ringwoodite, ferroan	(Mg,Fe) ₂ SiO ₄	8.33	21-1258 (I)
P	Magnesium Iron Oxide	Mg _{1-x} Fe _x O	5.01	35-1393 (*)
	Diaoyudaoite, syn	NaAl ₁₁ O ₁₇ /0.5(Na ₂ O·11Al ₂ O ₃)	25	21-1096 (I)
	Magnesium Silicate	MgSiO ₃	10.42	39-0048 (I)
	Iron Nitride	FeN	8.96	50-1087 (I)

Figure LI shows two stacked XRD patterns from two different reaction products, synthesized using a 19.44% aluminum stoichiometry. The similarity of the diffraction patterns within Figure LI illustrates that the formation of specific crystalline chemical species in the reaction product is repeatable.

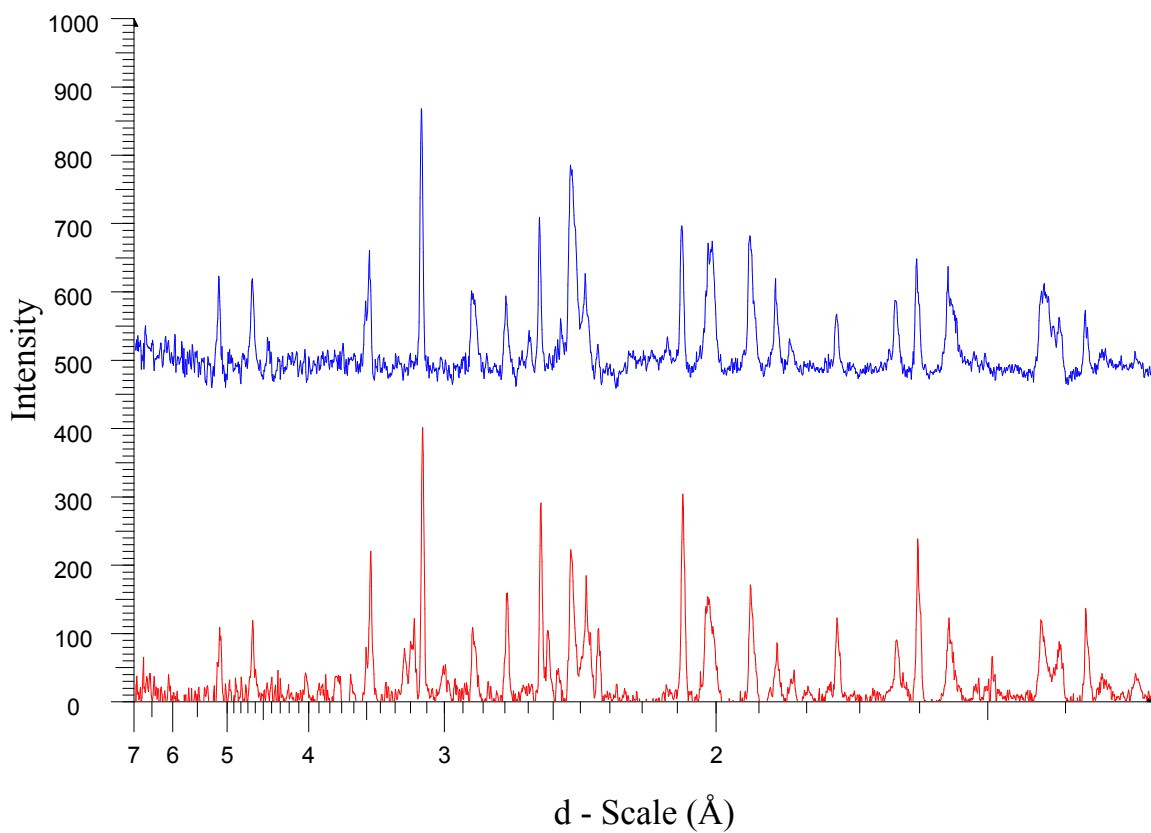


Figure LI: XRD patterns of two reacted samples of 80.56% JSC-1A and 19.44% Al by weight

Legend for Color Coding in Figure LI:

Blue: JSC-1A reaction product utilizing 19.44% aluminum

Red: JSC-1A reaction product utilizing 19.44% aluminum

24.45% Al by weight

The XRD pattern for the reaction product utilizing a 24.45% aluminum stoichiometry, with identified chemical species labeled, is shown in Figure LII. The legend for the identified chemical species is shown in Table XVI.

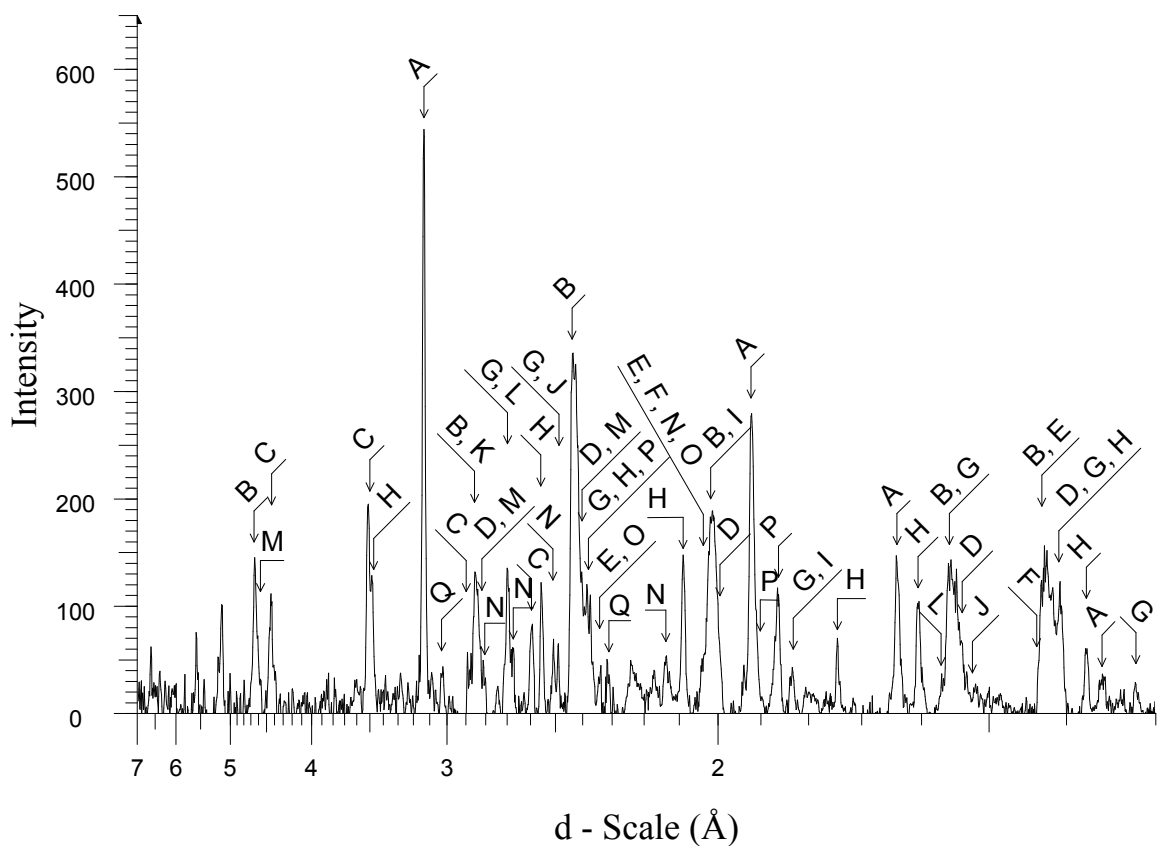


Figure LII: XRD pattern for the reaction product of the 75.55% JSC-1A and 24.45% aluminum stoichiometry.

Table XVI: Legend of Identified Chemical species in the Diffraction Pattern Shown in Figure LII

	Compound Name	Formula	Y-Scale	PDF #
A	Silicon, syn	Si	93.31	27-1402 (*)
B	Spinel, syn	MgAl ₂ O ₄	53.12	21-1152 (*)
C	Grossite	CaAl ₄ O ₇	28.99	46-1475 (I)
H	Corundum, syn	Al ₂ O ₃	23.43	10-0173 (I)
D	Magnesium Aluminum Oxide	Mg _{0.388} Al _{2.408} O ₄	21.87	48-0528 (I)
F	Iron, syn	Fe	20.83	06-0696 (*)
E	Aluminum Nitride (FCC)	AlN	20.83	46-1200 (*)
G	Aluminum Nitride (Hex)	AlN	19.96	25-1133 (*)
H	Corundum, syn	Al ₂ O ₃	19.53	46-1212 (*)
I	Fersilicite, syn [NR]	FeSi	14.58	38-1397 (*)
C	Grossite, syn	CaAl ₄ O ₇ /CaO·2Al ₂ O ₃	13.54	23-1037 (*)
L	Calcium Aluminum Oxide	Ca ₃ Al ₂ O ₆	10.42	32-0148 (I)
K	Gehlenite, syn	Ca ₂ Al ₂ SiO ₇	10.42	35-0755 (*)
J	Iron Nitride	FeN	10.42	50-1087 (I)
M	Aluminum Oxide	Al ₂ O ₃	10.42	47-1292 (I)
N	Hibonite-5H, ferroan	Ca(Al,Fe) ₁₂ O ₁₉	9.02	38-0469 (*)
O	Aluminum, syn	Al	8.68	04-0787 (*)
P	Ferdisilicite, syn [NR]	FeSi ₂	8.33	35-0822 (*)
Q	Nitratine	NaNO ₃	8.33	36-1474 (*)

Figure LIII shows two stacked XRD patterns from two different reaction products, synthesized using a 24.45% aluminum stoichiometry. The similarity of the diffraction patterns in Figure LIII illustrates that the formation of specific crystalline chemical species in the reaction product is repeatable.

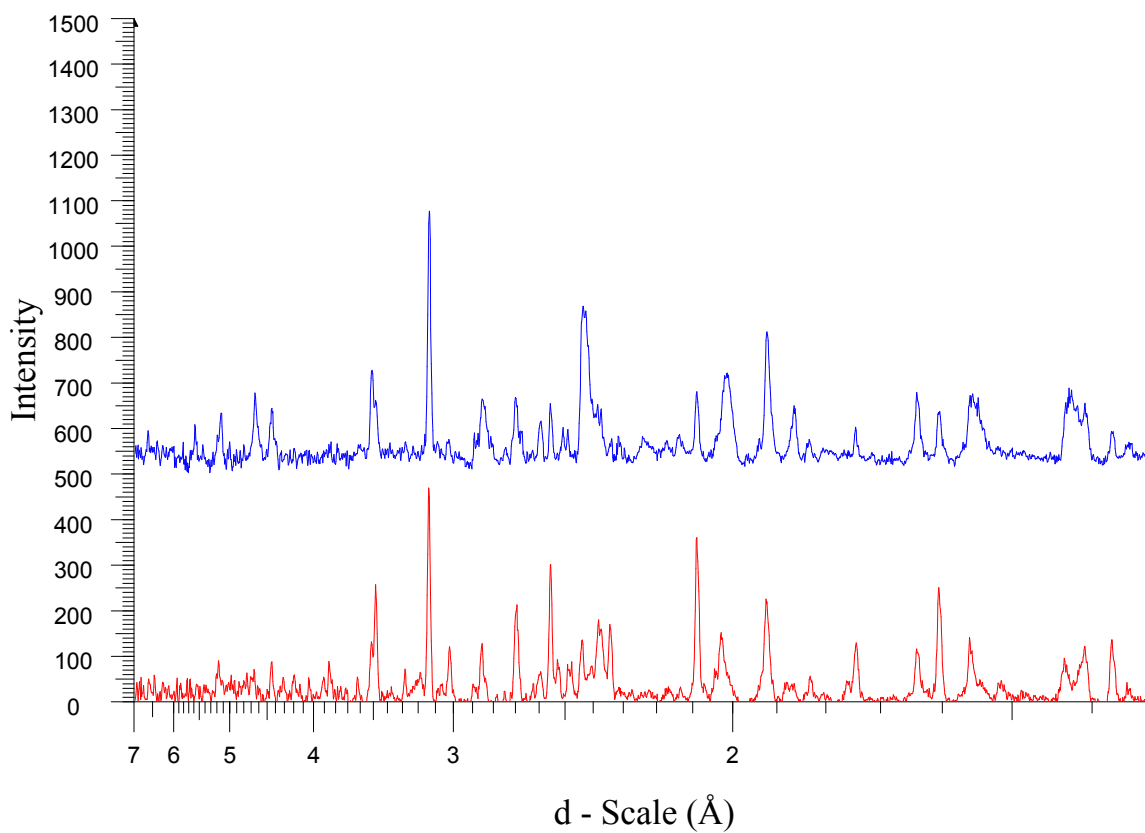


Figure LIII: XRD patterns of two reacted samples of 75.55% JSC-1A and 24.45% Al by weight

Legend for Color Coding in Figure LIII:

Blue: JSC-1A reaction product utilizing 24.45% aluminum

Red: JSC-1A reaction product utilizing 24.45% aluminum

28.85% Al by weight

The XRD pattern for the reaction product utilizing a 28.85% aluminum stoichiometry, with identified chemical species labeled, is shown in Figure LIV. The legend for the identified chemical species is shown in Table XVII.

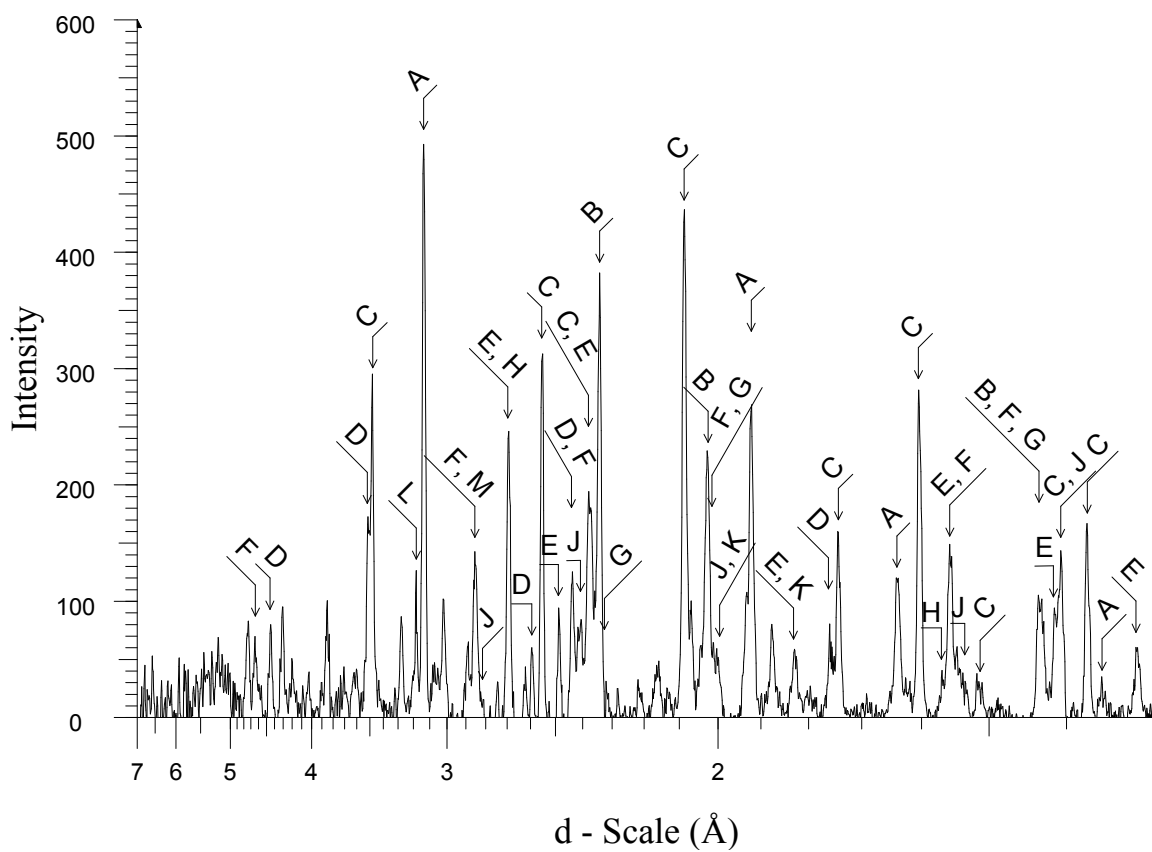


Figure LIV: XRD pattern for the reaction product of the 71.15% JSC-1A and 28.85% aluminum stoichiometry.

Table XVII: Legend of Identified Chemical species in the Diffraction Pattern Shown in Figure LIV

	Compound Name	Formula	Y-Scale	PDF #
A	Silicon, syn	Si	95.66	27-1402 (*)
B	Aluminum, syn	Al	77.08	04-0787 (*)
C	Corundum, syn	Al ₂ O ₃	66.67	10-0173 (I)
C	Corundum, syn	Al ₂ O ₃	62.5	46-1212 (*)
D	Grossite	CaAl ₄ O ₇	35.42	46-1475 (I)
E	Aluminum Nitride (Hex)	AlN	31.25	25-1133 (*)
F	Spinel, syn	MgAl ₂ O ₄	25	21-1152 (*)
G	Aluminum Nitride (FCC)	AlN	23.44	46-1200 (*)
D	Grossite, syn	CaAl ₄ O ₇ /CaO·2Al ₂ O ₃	20.83	23-1037 (*)
H	Calcium Aluminum Oxide	Ca ₃ Al ₂ O ₆	14.58	32-0150 (*)
I	Iron, syn	Fe	12.48	06-0696 (*)
J	Magnesium Aluminum Oxide	Mg _{0.388} Al _{2.408} O ₄	12.37	48-0528 (I)
K	Fersilicite, syn [NR]	FeSi	10.42	38-1397 (*)
L	Anorthite, sodian, disordered	(Ca,Na)(Si,Al) ₄ O ₈	9.37	41-1481 (I)
M	Gehlenite, syn	Ca ₂ Al ₂ SiO ₇	8.47	35-0755 (*)
	Aluminum Iron	Al ₁₃ Fe ₄	5.57	50-0797 (I)
	Sodium Calcium Aluminum Oxide	Na _{2x} Ca _{3-x} Al ₂ O ₆	14.58	26-0957 (I)
	Ringwoodite, ferroan	(Mg,Fe) ₂ SiO ₄	12.5	21-1258 (I)
	Akermanite, syn	Ca ₂ MgSi ₂ O ₇	10.42	35-0592 (*)

Figure LV shows two stacked XRD patterns from two different reaction products, synthesized using a 28.85% aluminum stoichiometry. The similarity of the diffraction patterns in Figure LV illustrates that the formation of specific crystalline chemical species in the reaction product is repeatable.

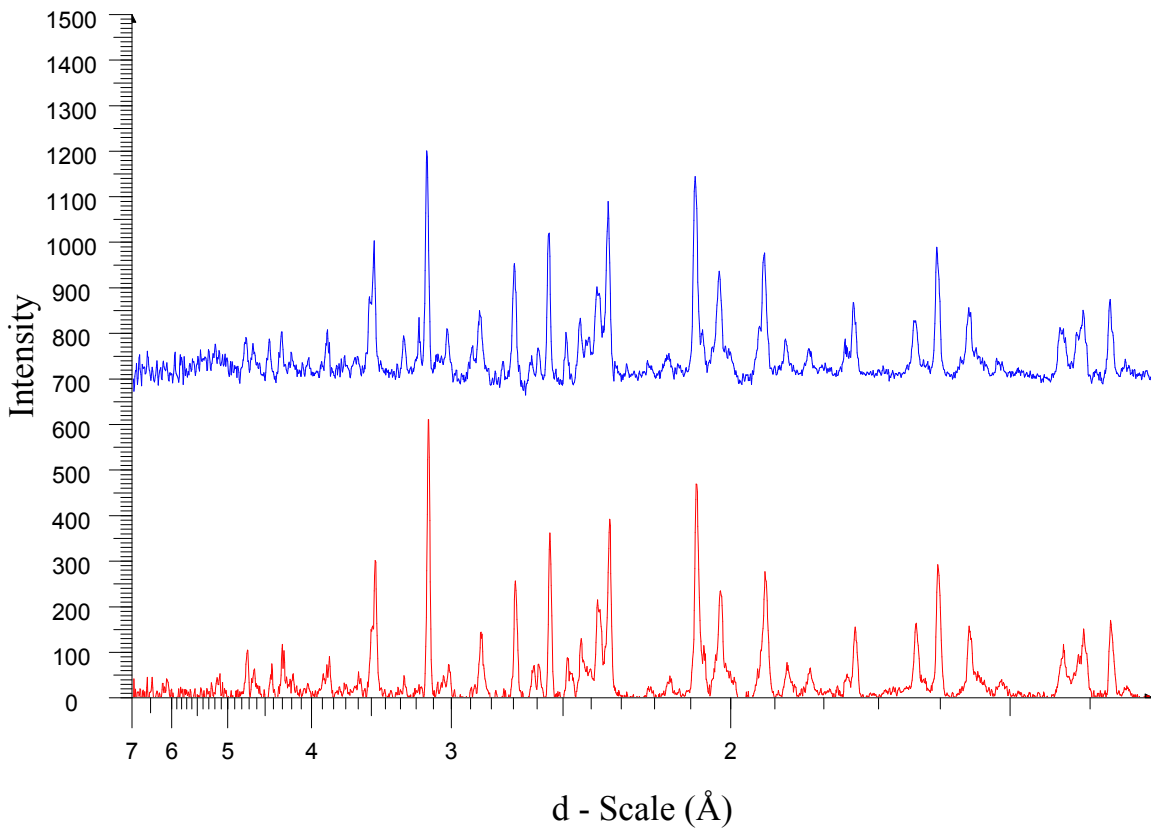


Figure LV: XRD patterns of two reacted samples of 71.15% JSC-1A and 28.85% Al by weight

Legend for Color Coding in Figure LV:

Blue: JSC-1A reaction product utilizing 28.85% aluminum

Red: JSC-1A reaction product utilizing 28.85% aluminum

Excess aluminum was indicated by the presence of significant diffraction peaks within the 28.85% stoichiometry utilizing the JSC-1A series of simulant shown in Figure LIV. The larger particle size of the JSC-1A series of simulant decreases the surface area/mass ratio of the reactant mixture. It is hypothesized that Al initiates oxidation-reduction reactions at the surface of the simulant particles. The overall particle surface area within the sample that is available to react with aluminum is substantially lower when utilizing the larger particle size of simulant. The lower particle surface area decreases the number of reactions that can occur. As the quantity of aluminum is increased to the 33.33% stoichiometry, there is not sufficient surface area on the simulant to accommodate all the aluminum. Subsequently, heat produced by the reaction is used

to melt the excess aluminum that has nothing to react with except atmospheric gases. It is hypothesized that reactions frequently failed to go to completion in the 33.33% Al stoichiometry using JSC-1A due to decreased particle surface area for reactions.

Comparison of Chemical species Formed in JSC-1A Reactant Stoichiometries

XRD patterns of the three JSC-1A reactant stoichiometries in Figure L, Figure LII, and Figure LIV are stacked and shown in Figure LVI, illustrating the differences in formation of chemical species using different stoichiometries of aluminum. Table XVIII compares relative diffraction intensities for chemical species present in the various reaction stoichiometries, which were identified in Table XV, Table XVI, and Table XVII.

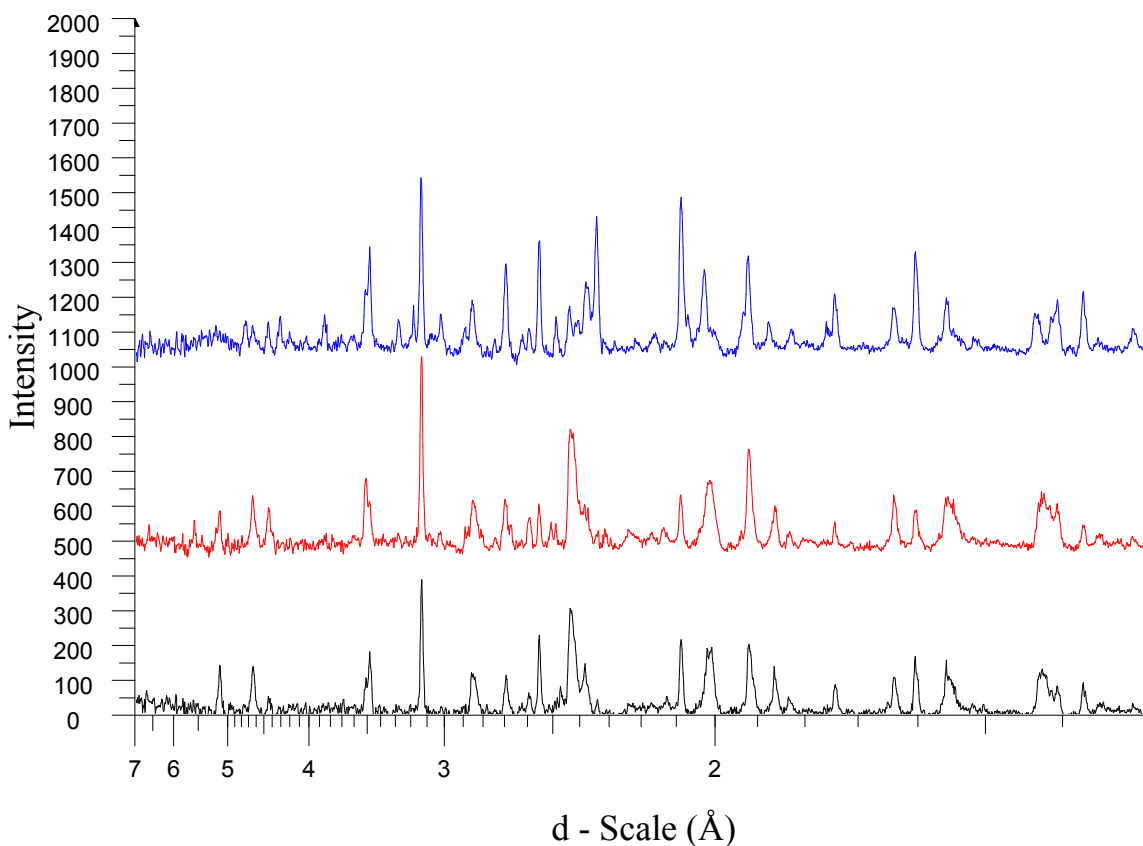


Figure LVI: Stacked XRD patterns of three reacted stoichiometries of Al and JSC-1A simulant

Legend of Color Coding in Figure LVI and Table XVIII:

Black: 80.56% JSC-1AF and 19.44% Al by weight

Red: 75.55% JSC-1AF and 24.45% Al by weight

Blue: 71.15% JSC-1AF and 28.85% Al by weight

Table XVIII: Identified Chemical species in the Diffraction Patterns in Figure LVI

Formula	Intensity			PDF #
	19.44A	24.45A	28.85A	
Si	375	510	474	27-1402 (*)
MgAl ₂ O ₄	253	291	124	21-1152 (*)
Al ₂ O ₃ (α)	193	107	310	46-1212 (*)
Al ₂ O ₃ (α)	177	128	331	10-0173 (I)
FeSi	97	80	52	38-1397 (*)
FeSi ₂	56	46	0	35-0822 (*)
AlN (FCC)	137	114	116	46-1200 (*)
AlN (Hex)	72	109	155	25-1133 (*)
CaAl ₄ O ₇	96	159	176	46-1475 (I)
CaAl ₄ O ₇ /CaO·2Al ₂ O ₃	42	74	103	23-1037 (*)
Mg _{0.388} Al _{2.408} O ₄	52	120	61	48-0528 (I)
Ca ₂ Al ₂ SiO ₇	88	57	42	35-0755 (*)
Al	36	47	382	04-0787 (*)
(Ca,Na)(Si,Al) ₄ O ₈	0	0	46	41-1481 (I)
Fe	64	114	62	06-0696 (*)
Al ₅ O ₆ N	42	0	0	48-0686 (*)
(Mg,Fe) ₂ SiO ₄	32	0	62	21-1258 (I)
Mg _{1-x} Fe _x O	19	0	0	35-1393 (*)
NaAl ₁₁ O ₁₇ /0.5(Na ₂ O·11Al ₂ O ₃)	97	0	0	21-1096 (I)
MgSiO ₃	40	0	0	39-0048 (I)
FeN	35	57	0	50-1087 (I)
Ca ₃ Al ₂ O ₆	113	0	0	38-1429 (*)
Ca ₃ Al ₂ O ₆	0	57	0	32-0148 (I)
Al ₂ O ₃	0	57	0	47-1292 (I)
Ca(Al,Fe) ₁₂ O ₁₉	0	49	0	38-0469 (*)
NaNO ₃	0	46	0	36-1474 (*)
Ca ₃ Al ₂ O ₆	0	0	72	32-0150 (*)
Al ₁₃ Fe ₄	0	0	28	50-0797 (I)
Na _{2x} Ca _{3-x} Al ₂ O ₆	0	0	72	26-0957 (I)
Ca ₂ MgSi ₂ O ₇	0	0	52	35-0592 (*)

Silicon (27-1402) has the largest diffraction intensity in the 24.45% stoichiometry for JSC-1A reaction products. Diffraction intensities are significantly larger for MgAl_2O_4 (21-1152) in the 19.44% and 24.45% aluminum stoichiometries. FeSi (38-1397), and FeSi_2 (35-0822) diffraction intensities increase with decreasing aluminum in the reactants. Diffraction peaks for AlN (46-1200) have similar intensities in all three stoichiometries, while diffraction peaks for AlN (25-1133) increase in intensity with increasing aluminum. Significant diffraction peaks for aluminum exist in the 28.85% aluminum stoichiometry, which indicates that all the aluminum did not react. Diffraction peaks for CaAl_4O_7 (46-1475) (23-1037) increase with increasing aluminum in the reactants. Diffraction peaks for Al_2O_3 (46-1212) (10-0173) are smallest in the 24.45% aluminum stoichiometry and largest in the 33.33% aluminum stoichiometry. Diffraction intensities for $\text{Ca}_2\text{Al}_2\text{SiO}_7$ (35-0755) increase with decreasing aluminum quantities. Diffraction peaks for $\text{Mg}_{0.388}\text{Al}_{2.408}\text{O}_4$ (45-0528) are larger in the 24.45% stoichiometry than the 19.44% and 28.85% stoichiometries. Variation in the diffraction intensities for chemical species between reactant stoichiometries likely occurred due to differences in temperatures achieved during the reaction, and the quantity of aluminum available to react with the simulant.

Table XIX shows a comparison of diffraction peak intensities for JSC-1AF and JSC-1A reaction products. Figure LVII shows the relative diffraction intensities for selected chemical species in reaction products synthesized in a standard atmosphere.

Table XIX: Identified Chemical species in the Reaction Products using JSC-1AF and JSC-1A simulants

Formula	Intensity							PDF #
	19.44 AF	24.45 AF	28.85 AF	33.33 AF	19.44 A	24.45 A	28.85 A	
Si	307	644	955	826	375	510	474	27-1402 (*)
MgAl ₂ O ₄	217	113	144	216	253	291	124	21-1152 (*)
Al ₂ O ₃ (α)	275	61	0	0	193	107	310	46-1212 (*)
Al ₂ O ₃ (α)	260	61	0	0	177	128	331	10-0173 (I)
FeSi	171	61	42	58	97	80	52	38-1397 (*)
FeSi ₂	178	245	63	0	56	46	0	35-0822 (*)
AlN (FCC)	93	46	122	100	137	114	116	46-1200 (*)
AlN (Hex)	0	31	76	131	72	109	155	25-1133 (*)
CaAl ₄ O ₇	27	138	444	486	96	159	176	46-1475 (I)
CaAl ₄ O ₇ /CaO·2Al ₂ O ₃	60	302	636	182	42	74	103	23-1037 (*)
Mg _{0.388} Al _{2.408} O ₄	27	77	125	50	52	120	61	48-0528 (I)
Ca ₂ Al ₂ SiO ₇	102	104	123	83	88	57	42	35-0755 (*)
Al	48	15	70	50	36	47	382	04-0787 (*)
Na(Si ₃ Al)O ₈	69	0	0	0	0	0	0	10-0393 (*)
CaAl ₂ Si ₂ O ₈	62	0	0	0	0	0	0	41-1486 (*)
(Ca,Na)(Si,Al) ₄ O ₈	0	0	0	0	0	0	46	41-1481 (I)
Fe	34	34	82	100	64	114	62	06-0696 (*)
Al ₂ O ₃	0	28	63	0	0	57	0	47-1292 (I)
Ca ₃ Al ₂ O ₆	0	0	207	0	113	0	0	38-1429 (*)
Ca ₃ Al ₂ O ₆	0	0	72	0	0	57	0	32-0148 (I)
Ca ₃ Al ₂ O ₆	0	0	0	100	0	0	0	33-0251 (*)
Ca ₃ Al ₂ O ₆	0	0	0	0	0	0	72	32-0150 (*)
NaAl ₁₁ O ₁₇ /0.5 (Na ₂ O·11Al ₂ O ₃)	40	92	115	216	97	0	0	21-1096 (I)
Ca(Al,Fe) ₁₂ O ₁₉	0	138	83	50	0	49	0	38-0469 (*)
Al ₂ O ₃	62	0	0	0	0	0	0	50-1496 (I)
(NO) ₂ Al ₂₂ O ₃₄ / (NO) ₂ O·11Al ₂ O ₃	0	125	83	83	0	0	0	23-0457 (I)
K ₂ Al ₂₂ O ₃₄ / K ₂ O·11Al ₂ O ₃	20	138	62	0	0	0	0	31-0960 (I)
Na _{1.65} Al _{1.65} Si _{0.35} O ₄	48	0	0	0	0	0	0	49-0005 (*)
K _{1.25} Al _{1.25} Si _{0.75} O ₄	41	0	0	0	0	0	0	32-0731 (I)
Fe ₂ N	30	0	0	0	0	0	0	50-0957 (I)
KFeO ₂	0	107	55	36	0	0	0	26-1319 (I)
(CaO) _x (Al ₂ O ₃) ₁₁	0	183	42	0	0	0	0	41-0358 (*)
K _{1.25} Al _{1.25} Si _{0.75} O ₄	0	92	143	0	0	0	0	32-0731 (I)
Na ₂ Al ₂₂ O ₃₄ / Na ₂ O·11Al ₂ O ₃	0	77	83	66	0	0	0	31-1263 (I)
K ₃ Ti ₈ O ₁₇	0	46	0	0	0	0	0	24-0901 (I)
Al ₈ O ₃ N ₆	0	46	39	0	0	0	0	48-1581 (I)
Ca ₃ Mg(SiO ₄) ₂	0	0	92	66	0	0	0	35-0591 (*)

Table XIX (continued)								
Formula	Intensity							PDF #
	19.44 AF	24.45 AF	28.85 AF	33.33 AF	19.44 A	24.45 A	28.85 A	
CaAl ₁₂ O ₁₉	0	0	17	0	0	0	0	38-0470 (I)
AlFe	0	0	0	116	0	0	0	33-0020 (*)
AlFe ₃	0	0	0	50	0	0	0	50-0955 (*)
NaMg ₂ Al ₁₅ O ₂₅ / Na ₂ O·4MgO·15Al ₂ O ₃	0	0	0	133	0	0	0	27-0730 (I)
K ₂ MgSiO ₄	0	0	0	100	0	0	0	48-0900 (I)
KMg ₂ Al ₁₅ O ₂₅	0	0	0	83	0	0	0	42-0204 (I)
Al ₅ O ₆ N	0	0	0	0	42	0	0	48-0686 (*)
(Mg,Fe) ₂ SiO ₄	0	0	0	0	32	0	62	21-1258 (I)
Mg _{1-x} Fe _x O	0	0	0	0	19	0	0	35-1393 (*)
MgSiO ₃	0	0	0	0	40	0	0	39-0048 (I)
FeN	0	0	0	0	35	57	0	50-1087 (I)
NaNO ₃	0	0	0	0	0	46	0	36-1474 (*)
Al ₁₃ Fe ₄	0	0	0	0	0	0	28	50-0797 (I)
Na _{2x} Ca _{3-x} Al ₂ O ₆	0	0	0	0	0	0	72	26-0957 (I)
Ca ₂ MgSi ₂ O ₇	0	0	0	0	0	0	52	35-0592 (*)

Standard Atmosphere Diffraction Intensities

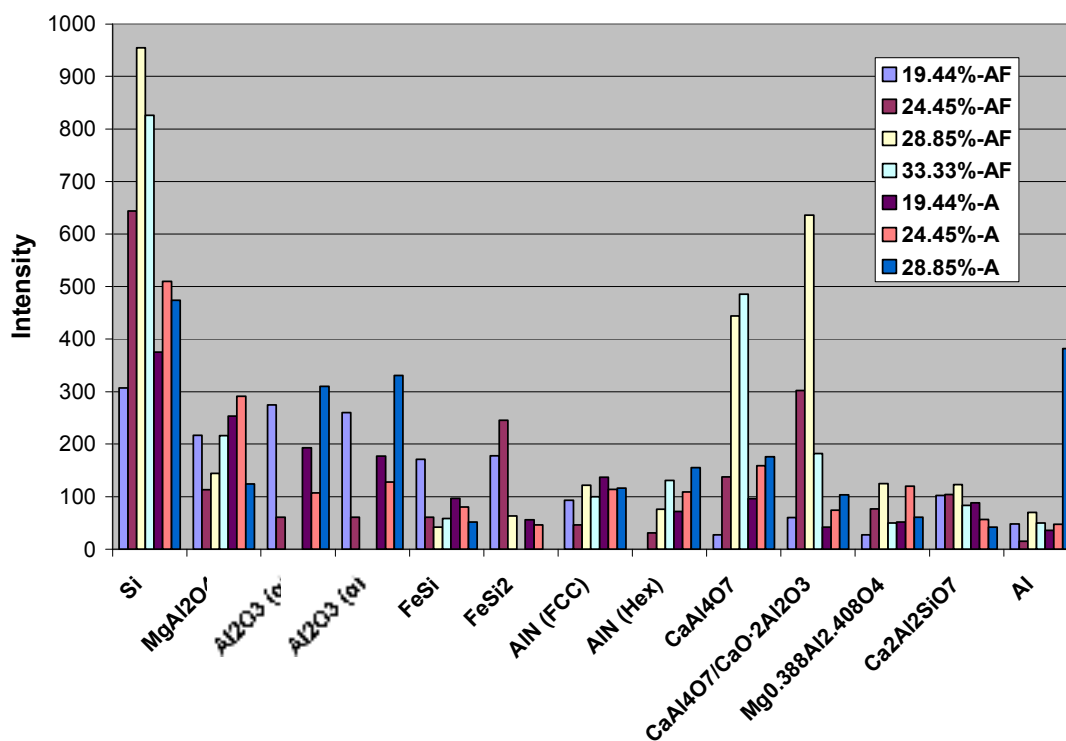


Figure LVII: Relative diffraction intensities for selected chemical species in the standard atmosphere reaction product.

When comparing diffraction intensities between JSC-1AF and JSC-1A reaction products in Figure LVII, it was observed that diffraction intensities for FeSi_2 (35-0822) and FeSi (38-1397) were larger in stoichiometries with lower aluminum quantities. MgAl_2O_4 (21-1152) diffraction peaks were largest in the low aluminum stoichiometries using JSC-1A simulant. The diffraction peaks for FeSi_2 (35-0822) are significantly more intense in the low aluminum stoichiometries using JSC-1AF simulant than the same stoichiometries using JSC-1A. Diffraction intensities for AlN (46-1200) and AlN (25-1133) are generally more intense in JSC-1A reaction products than in equivalent stoichiometries using JSC-1AF. Diffraction peaks are present for $\text{Mg}_{0.388}\text{Al}_{2.408}\text{O}_4$ in all reaction products. Intensities of the $\text{Mg}_{0.388}\text{Al}_{2.408}\text{O}_4$ diffraction peaks seem to reach a maximum in the middle stoichiometries for both simulants. The highest diffraction intensities for $\text{Mg}_{0.388}\text{Al}_{2.408}\text{O}_4$ are found in the 24.45% aluminum stoichiometry using JSC-1A, and the 28.85% stoichiometry using JSC-1AF, both of which correspond to the stoichiometries where the maximum silicon diffraction intensities are observed for the respective simulants. Diffraction intensities for CaAl_4O_7 (23-1037) are largest in the 28.85% aluminum stoichiometry of JSC-1AF simulant. Diffraction intensities for CaAl_4O_7 (46-1475) are largest in the 33.33% aluminum stoichiometry of JSC-1AF simulant. Diffraction peaks for $\text{Ca}_2\text{Al}_2\text{SiO}_7$ (35-0755) decrease in intensity as aluminum increases within the JSC-1A simulant, while diffraction intensities are fairly similar within the JSC-1AF stoichiometries. Diffraction peaks for several $\text{Ca}_3\text{Al}_2\text{O}_6$ phases are found in several reaction products, the specific phase present seems to be dictated by reactant stoichiometry and simulant. Variation in the diffraction intensities for chemical species between simulants using the same reactant stoichiometry likely occurred due to differences in temperatures achieved during the reaction. Temperatures achieved during the reaction would depend on the quantity of oxidation-reduction reactions able to occur, which is largely influenced by particle surface area.

Chemical Species Present in Vacuum SHS Reaction Products Utilizing JSC-1AF Regolith Simulant

19.44% Al by weight

The XRD pattern for the reaction product utilizing a 19.44% aluminum stoichiometry, with identified chemical species labeled, is shown in Figure LVIII. The legend for the identified chemical species is shown in Table XX.

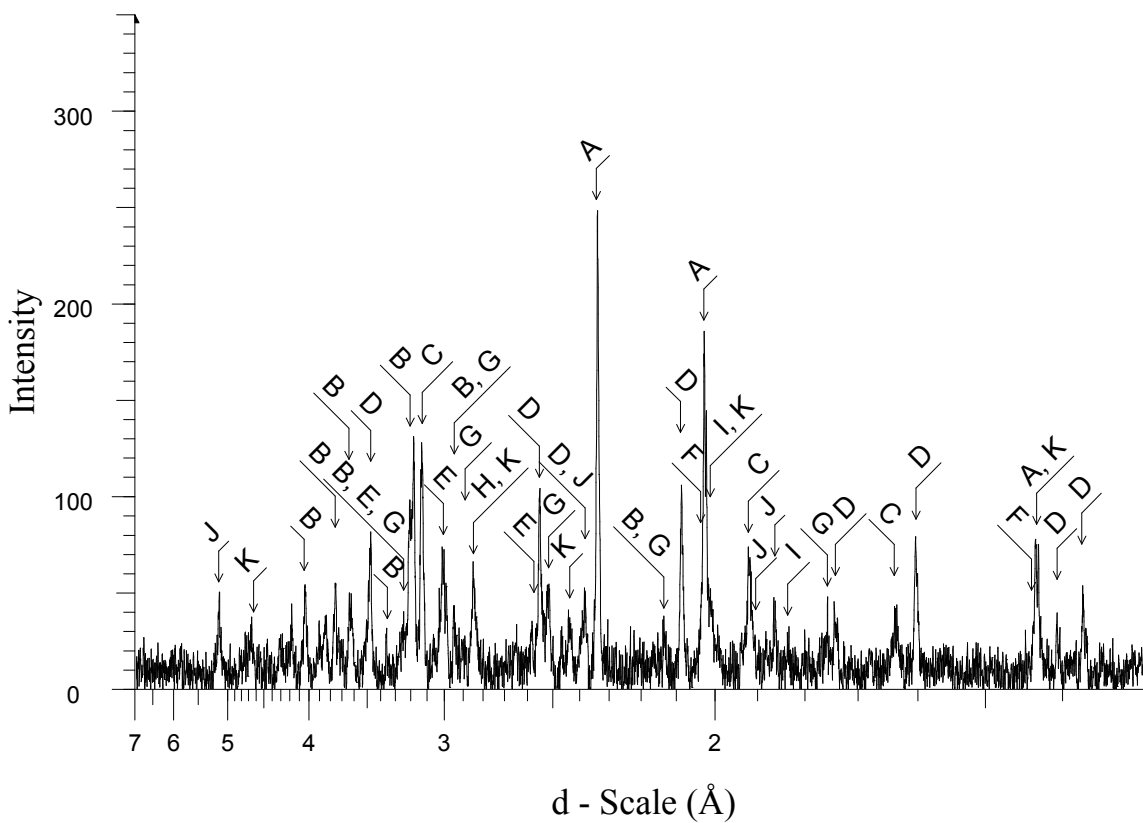


Figure LVIII: XRD pattern for the reaction product of the 80.56% JSC-1AF and 19.44% aluminum stoichiometry.

Table XX: Legend of Identified Chemical species in the Diffraction Pattern Shown in Figure LVIII

	Compound Name	Formula	Y-Scale	PDF #
A	Aluminum, syn	Al	101.12	04-0787 (*)
B	Albite, calcian, ordered	(Na,Ca)Al(Si,Al) ₃ O ₈	50.2	41-1480 (I)
B	Albite, disordered	Na(Si ₃ Al)O ₈	50.2	10-0393 (*)
B	Anorthite, sodian, disordered	(Ca,Na)(Si,Al) ₄ O ₈	50.2	41-1481 (I)
C	Silicon, syn	Si	48.11	27-1402 (*)
B	Anorthite, ordered	CaAl ₂ Si ₂ O ₈	43.93	41-1486 (*)
D	Corundum, syn	Al ₂ O ₃	40.09	10-0173 (I)
B	Anorthite, sodian, intermediate	(Ca,Na)(Si,Al) ₄ O ₈	31.38	18-1202 (I)
E	Hedenbergite	CaFe ⁺² Si ₂ O ₆	27.19	41-1372 (*)
F	Iron, syn	Fe	25.1	06-0696 (*)
G	Augite, aluminian	Ca(Mg,Fe,Al)(Si,Al) ₂ O ₆	20.91	41-1483 (I)
H	Gehlenite, syn	Ca ₂ Al ₂ SiO ₇	20.91	35-0755 (*)
I	Ferdisilicite, syn [NR]	FeSi ₂	18.83	35-0822 (*)
J	Fersilicite, syn [NR]	FeSi	18.83	38-1397 (*)
K	Spinel, syn	MgAl ₂ O ₄	16.74	21-1152 (*)
	Magnesium Aluminum Iron Oxide	MgFeAlO ₄	8.5	11-0009 (I)
	Aluminum Iron	AlFe	8.36	33-0020 (*)

24.45% Al by weight

The XRD pattern for the reaction product utilizing a 24.45% aluminum stoichiometry, with identified chemical species labeled, is shown in Figure LIX. The legend for the identified chemical species is shown in Table XXI.

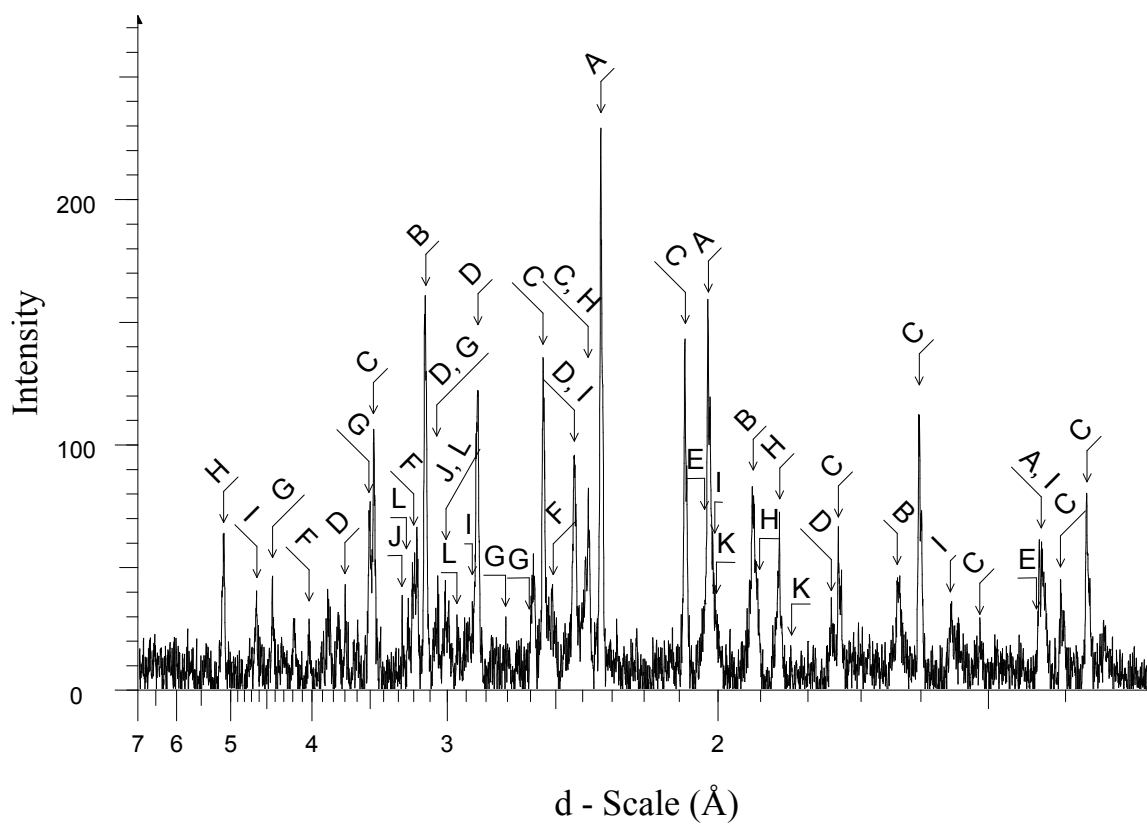


Figure LIX: XRD pattern for the reaction product of the 75.55% JSC-1AF and 24.45% aluminum stoichiometry.

Table XXI: Legend of Identified Chemical species in the Diffraction Pattern Shown in Figure LIX

	Compound Name	Formula	Y-Scale	PDF #
A	Aluminum, syn	Al	100.03	04-0787 (*)
B	Silicon, syn	Si	66.89	27-1402 (*)
C	Corundum, syn	Al ₂ O ₃	62.17	10-0173 (I)
D	Gehlenite, syn	Ca ₂ Al ₂ SiO ₇	51.09	35-0755 (*)
I	Spinel, syn	MgAl ₂ O ₄	39.05	21-1152 (*)
G	Grossite	CaAl ₄ O ₇	31.89	46-1475 (I)
E	Iron, syn	Fe	27.24	06-0696 (*)
F	Albite, disordered	Na(Si ₃ Al)O ₈	27.24	10-0393 (*)
F	Albite, calcian, ordered	(Na,Ca)Al(Si,Al) ₃ O ₈	25.16	41-1480 (I)
F	Anorthite, sodian, intermediate	(Ca,Na)(Si,Al) ₄ O ₈	24.82	18-1202 (I)
H	Ferdisilicite, syn [NR]	FeSi ₂	23.84	35-0822 (*)
F	Anorthite, ordered	CaAl ₂ Si ₂ O ₈	23.76	41-1486 (*)
G	Grossite, syn	CaAl ₄ O ₇ /CaO·2Al ₂ O ₃	23.76	23-1037 (*)
F	Anorthite, sodian, disordered	(Ca,Na)(Si,Al) ₄ O ₈	22.52	41-1481 (I)
J	Hedenbergite	CaFe ⁺² Si ₂ O ₆	14.3	41-1372 (*)
K	Fersilicite, syn [NR]	FeSi	12.24	38-1397 (*)
L	Augite	Ca(Mg,Fe)Si ₂ O ₆	8.08	24-0203 (I)
	Magnesium Aluminum Iron Oxide	MgFeAlO ₄	10.18	11-0009 (I)
	Aluminum Iron	AlFe	7.56	33-0020 (*)
	Aluminum Iron	Al _{0.5} Fe _{0.5}	3.12	45-0983 (I)

28.85% Al by weight

The XRD pattern for the reaction product utilizing a 28.85% aluminum stoichiometry, with identified chemical species labeled, is shown in Figure LX. The legend for the identified chemical species is shown in Table XXII.

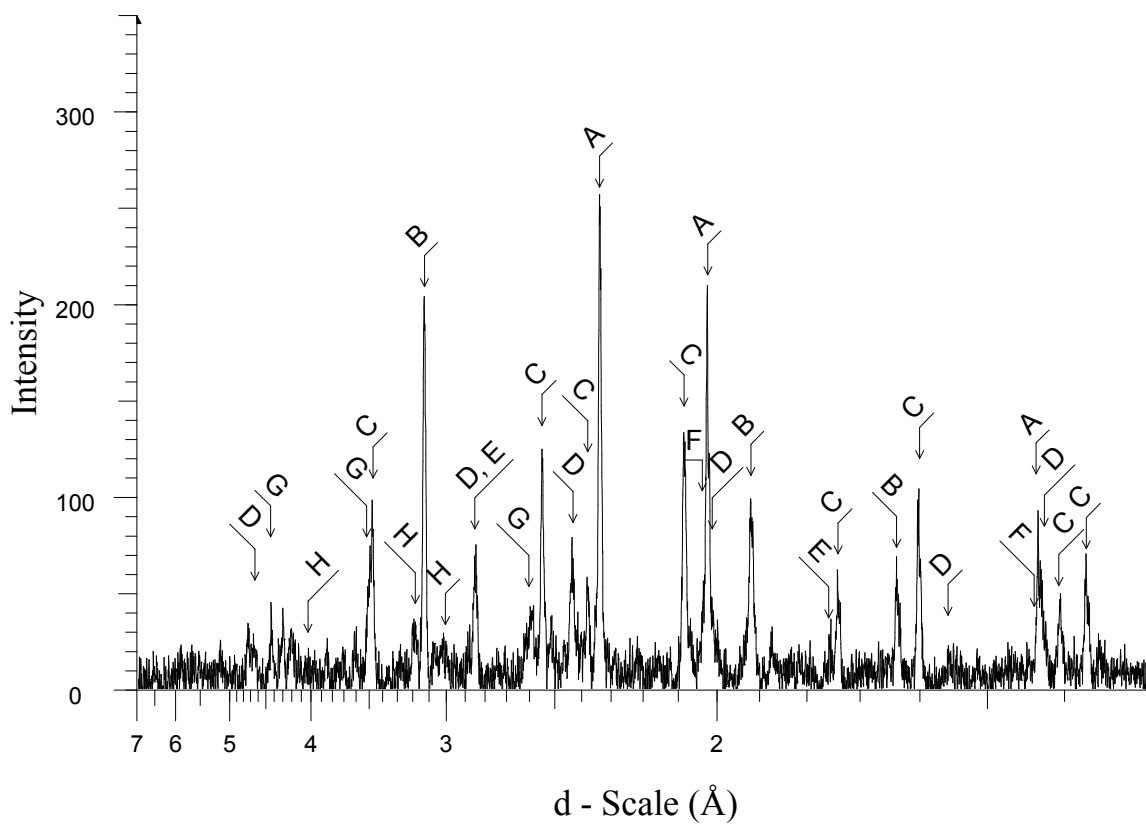


Figure LX: XRD pattern for the reaction product of the 71.15% JSC-1AF and 28.85% aluminum stoichiometry.

Table XXII: Legend of Identified Chemical species in the Diffraction Pattern Shown in Figure LX

	Compound Name	Formula	Y-Scale	SS-NNNN
A	Aluminum, syn	Al	98.4	04-0787 (*)
B	Silicon, syn	Si	73.03	27-1402 (*)
C	Corundum, syn	Al ₂ O ₃	53.88	10-0173 (I)
D	Spinel, syn	MgAl ₂ O ₄	30.24	21-1152 (*)
E	Gehlenite, syn	Ca ₂ Al ₂ SiO ₇	29.64	35-0755 (*)
F	Iron, syn	Fe	24.25	06-0696 (*)
G	Grossite	CaAl ₄ O ₇	21.28	46-1475 (I)
G	Grossite, syn	CaAl ₄ O ₇ /CaO·2Al ₂ O ₃	20.52	23-1037 (*)
H	Albite, disordered	Na(Si ₃ Al)O ₈	14.15	10-0393 (*)
	Fersilicite, syn [NR]	FeSi	13.68	38-1397 (*)
	Aluminum Oxide	Al ₂ O ₃	13.68	23-1009 (I)
H	Anorthite, ordered	CaAl ₂ Si ₂ O ₈	13.68	41-1486 (*)
H	Anorthite, sodian, disordered	(Ca,Na)(Si,Al) ₄ O ₈	12.12	41-1481 (I)
H	Albite, calcian, ordered	(Na,Ca)Al(Si,Al) ₃ O ₈	12.12	41-1480 (I)
	Aluminum Iron	AlFe	10.64	33-0020 (*)
	Magnesium Aluminum Oxide	Mg _{0.388} Al _{2.408} O ₄	9.88	48-0528 (I)
	Sodium Aluminum Silicate	(Na ₂ O)0.33NaAlSiO ₄	9.12	39-0101 (I)
	Sodium Magnesium Aluminum Silicate	Na ₃ MgAlSi ₂ O ₈	9.12	49-0008 (*)
	Magnesium Aluminum Iron Oxide	MgFeAlO ₄	8.8	11-0009 (I)
	Hedenbergite	CaFe ⁺² Si ₂ O ₆	8.76	41-1372 (*)
	Anorthite, sodian, intermediate	(Ca,Na)(Si,Al) ₄ O ₈	8.52	18-1202 (I)
	Augite, aluminian	Ca(Mg,Fe,Al)(Si,Al) ₂ O ₆	7.57	41-1483 (I)
	Sodium Iron Oxide Silicate	NaFeO _{2.35} Si _{0.175} /NaFeO ₂ ·0.175SiO ₂	7.13	40-0139 (*)

33.33% Al by weight

The XRD pattern for the reaction product utilizing a 33.33% aluminum stoichiometry, with identified chemical species labeled, is shown in Figure LXI. The legend for the identified chemical species is shown in Table XXIII.

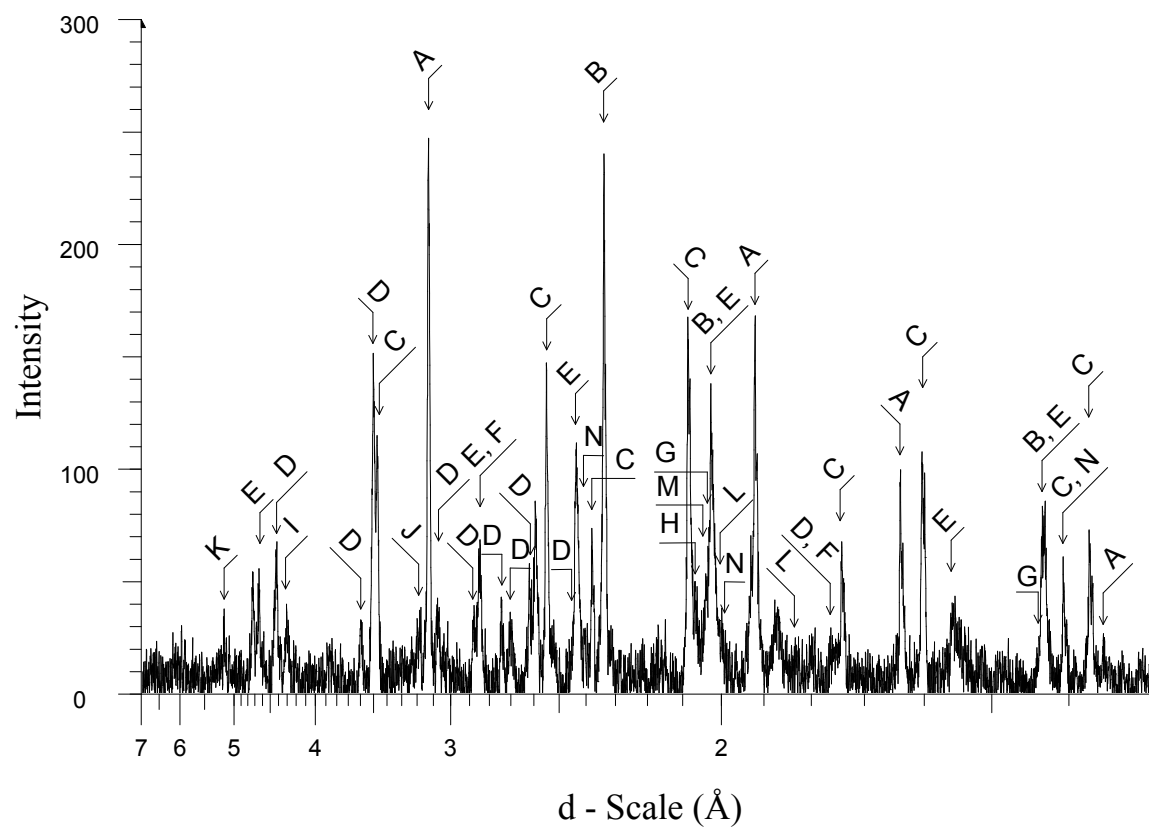


Figure LXI: XRD pattern for the reaction product of the 66.67% JSC-1AF and 33.33% aluminum stoichiometry.

Table XXIII: Legend of Identified Chemical species in the Diffraction Pattern Shown in Figure LXI

	Compound Name	Formula	Y-Scale	PDF #
A	Silicon, syn	Si	104.06	27-1402 (*)
B	Aluminum, syn	Al	101.51	04-0787 (*)
C	Corundum, syn	Al ₂ O ₃	65.46	10-0173 (I)
D	Grossite	CaAl ₄ O ₇	60.42	46-1475 (I)
D	Grossite, syn	CaAl ₄ O ₇ /CaO·2Al ₂ O ₃	50	23-1037 (*)
E	Spinel, syn	MgAl ₂ O ₄	45.83	21-1152 (*)
F	Gehlenite, syn	Ca ₂ Al ₂ SiO ₇	27.08	35-0755 (*)
G	Iron, syn	Fe	26.37	06-0696 (*)
H	Aluminum Iron	Al _{0.5} Fe _{0.5}	18.75	45-0983 (I)
I	Sodium Iron Oxide Silicate	NaFeO _{2,35} Si _{0,175} /NaFeO ₂ ·0.175SiO ₂	16.67	40-0139 (*)
J	Albite, disordered	Na(Si ₃ Al)O ₈	15.28	10-0393 (*)
J	Anorthite, ordered	CaAl ₂ Si ₂ O ₈	14.58	41-1486 (*)
J	Anorthite, sodian, intermediate	(Ca,Na)(Si,Al) ₄ O ₈	14.58	18-1202 (I)
J	Albite, calcian, ordered	(Na,Ca)Al(Si,Al) ₃ O ₈	14.58	41-1480 (I)
J	Anorthite, sodian, disordered	(Ca,Na)(Si,Al) ₄ O ₈	14.58	41-1481 (I)
K	Silicon Oxide Deca-dodecasil-3R	SiO ₂	13.46	38-0651 (I)
L	Fersilicite, syn [NR]	FeSi	12.5	38-1397 (*)
M	Aluminum Iron	AlFe	11.29	33-0020 (*)
N	Magnesium Aluminum Oxide	Mg _{0.388} Al _{2.408} O ₄	9.37	48-0528 (I)
	Sodium Aluminum Silicate	(Na ₂ O)0.33NaAlSiO ₄	9.37	39-0101 (I)
	Sodium Magnesium Aluminum Silicate	Na ₃ MgAlSi ₂ O ₈	8.18	49-0008 (*)
	Augite, aluminian	Ca(Mg,Fe,Al)(Si,Al) ₂ O ₆	6.25	41-1483 (I)
	Aluminum Oxide	Al ₂ O ₃	6.25	23-1009 (I)

Comparison of Chemical Species Formed in JSC-1AF Vacuum Products

XRD patterns of the four JSC-1AF reactant stoichiometries in Figure LVIII, Figure LIX, Figure LX, and Figure LXI are stacked and shown in Figure LXII, illustrating the differences in formation of chemical species using different stoichiometries of aluminum. Table XXIV compares relative diffraction intensities for chemical species present in the various reaction stoichiometries, which were identified in Table XX, Table XXI, Table XXII, and Table XXIII.

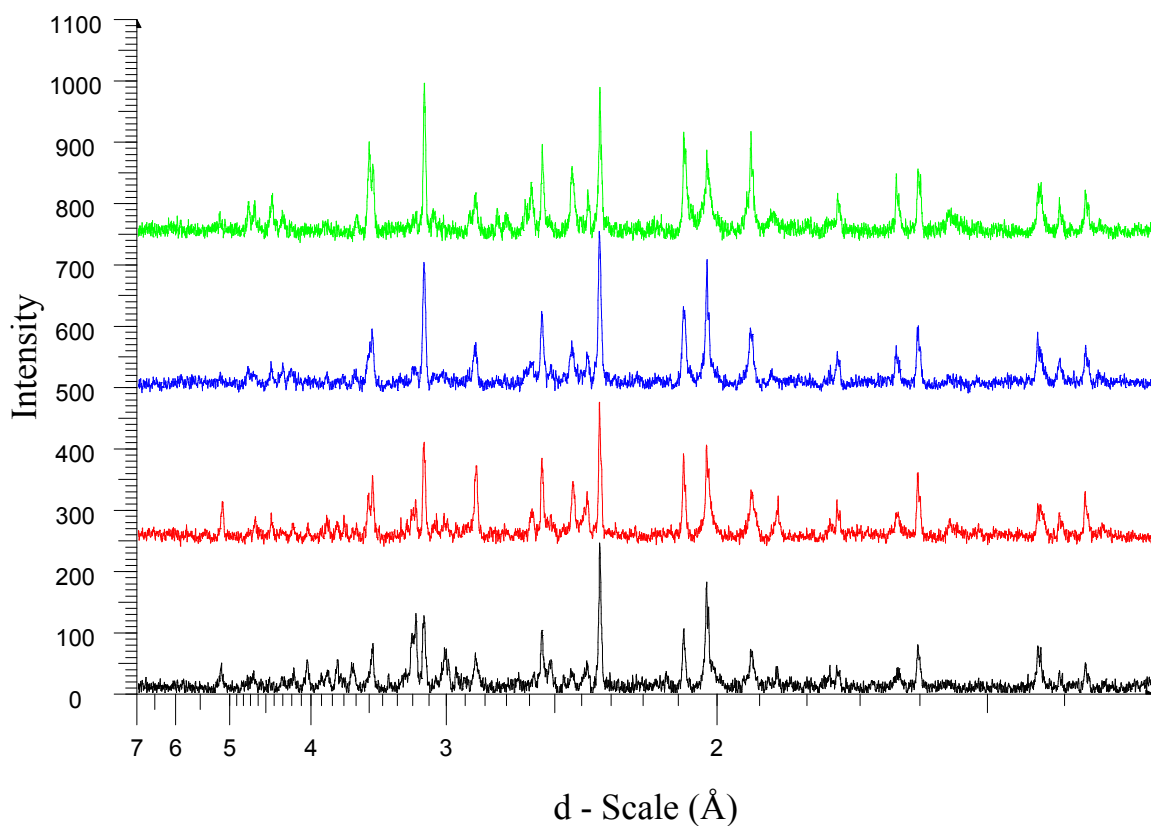


Figure LXII: Stacked XRD patterns of four reacted stoichiometries of Al and JSC-1AF simulant

Legend of Color Coding in Figure LXII and Table XXIV:

Black: 80.56% JSC-1AF and 19.44% Al by weight

Red: 75.55% JSC-1AF and 24.45% Al by weight

Blue: 71.15% JSC-1AF and 28.85% Al by weight

Green: 66.67% JSC-1AF and 33.33% Al by weight

Bold-typeface Chemical Species: Products of reaction

Normal-typeface Chemical Species: Reactants

Table XXIV: Identified Chemical species in the Diffraction Patterns in Figure LXII

Formula	Intensity				PDF #
	19.44AF	24.45AF	28.85AF	33.33AF	
Al	251	229	255	253	04-0787 (*)
(Na,Ca)Al(Si,Al) ₃ O ₈	124	58	31	36	41-1480 (I)
Na(Si ₃ Al)O ₈	124	62	37	38	10-0393 (*)
(Ca,Na)(Si,Al) ₄ O ₈	124	52	31	36	41-1481 (I)
CaAl ₂ Si ₂ O ₈	109	54	35	36	41-1486 (*)
(Ca,Na)(Si,Al) ₄ O ₈	78	57	22	36	18-1202 (I)
Ca(Mg,Fe,Al)(Si,Al) ₂ O ₆	52	0	20	16	41-1483 (I)
CaFe ⁺² Si ₂ O ₆	67	33	23	0	41-1372 (*)
Ca(Mg,Fe)Si ₂ O ₆	0	19	0	0	24-0203 (I)
Si	119	153	189	259	27-1402 (*)
MgAl ₂ O ₄	42	89	78	114	21-1152 (*)
Al ₂ O ₃ (α)	99	142	140	163	10-0173 (I)
FeSi	47	28	35	31	38-1397 (*)
FeSi ₂	47	55	0	0	35-0822 (*)
CaAl ₄ O ₇	0	73	55	150	46-1475 (I)
CaAl ₄ O ₇ /CaO·2Al ₂ O ₃	0	54	53	125	23-1037 (*)
Mg _{0.388} Al _{2.408} O ₄	0	0	26	23	48-0528 (I)
Ca ₂ Al ₂ SiO ₇	52	117	77	67	35-0755 (*)
MgFeAlO ₄	21	23	23	0	11-0009 (I)
AlFe	21	17	28	28	33-0020 (*)
Fe	62	62	63	66	06-0696 (*)
Al _{0.5} Fe _{0.5}	0	7	0	47	45-0983 (I)
Al ₂ O ₃	0	0	35	16	23-1009 (I)
(Na ₂ O)0.33NaAlSiO ₄	0	0	24	23	39-0101 (I)
Na ₃ MgAlSi ₂ O ₈	0	0	24	20	49-0008 (*)
NaFeO _{2.35} Si _{0.175} /NaFeO ₂ ·0.175SiO ₂	0	0	18	42	40-0139 (*)
SiO ₂	0	0	0	34	38-0651 (I)

The 19.44% aluminum stoichiometry had diffraction peaks of considerable intensity for several minerals within the reactants, including anorthite, albite, hedenbergite, and augite. The presence of the reactant materials in the product would indicate that the product was not fully reacted. The diffraction intensities for JSC-1AF simulant constituents within vacuum synthesized reaction products decrease substantially with an increase in aluminum in the reactants. Diffraction peaks for silicon increase substantially in intensity with increasing aluminum used in the reactant mixture. The highest intensity diffraction peaks for corundum (10-0173), spinel (21-1152), and CaAl₄O₇ (46-1475) (23-1037) are found in the 33.33%

aluminum stoichiometry. The intensity of iron (06-0696) diffraction peaks is questionable in all instances within this study due to their proximity to aluminum diffraction peaks. Diffraction peaks for FeSi₂ (35-0822) are only present in the low aluminum stoichiometries. The chemical species of FeSi (38-1397), AlFe (33-0020), and Ca₂Al₂SiO₇ (35-0755) have identified diffraction peaks in all stoichiometries. The 24.45% stoichiometry has significantly larger diffraction peaks for Ca₂Al₂SiO₇ (35-0755) than other stoichiometries. Variation in the diffraction intensities for chemical species between reactant stoichiometries likely occurred due to differences in temperatures achieved during the reaction and the availability of aluminum to react with the simulant.

Chemical Species Present in Vacuum SHS Reaction Products Utilizing JSC-1A Regolith Simulant

19.44% Al by weight

The XRD pattern for the reaction product utilizing a 19.44% aluminum stoichiometry, with identified chemical species labeled, is shown in Figure LXIII. The legend for the identified chemical species is shown in Table XXV.

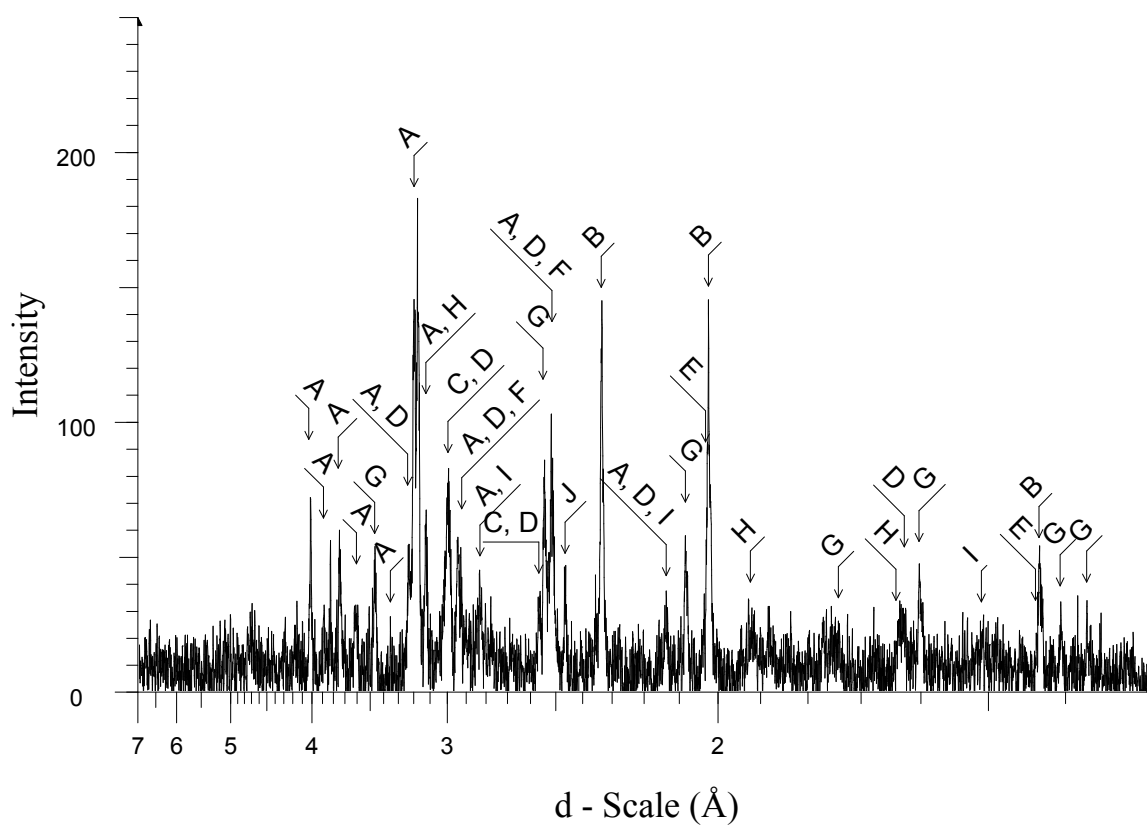


Figure LXIII: XRD pattern for the reaction product of the 80.56% JSC-1A and 19.44% aluminum stoichiometry.

Table XXV: Legend of Identified Chemical species in the Diffraction Pattern Shown in Figure LXIII

	Compound Name	Formula	Y-Scale	PDF #
A	Albite, disordered	Na(Si ₃ Al)O ₈	99.75	10-0393 (*)
A	Anorthite, sodian, disordered	(Ca,Na)(Si,Al) ₄ O ₈	90.85	41-1481 (I)
A	Anorthite, ordered	CaAl ₂ Si ₂ O ₈	88.81	41-1486 (*)
A	Albite, calcian, ordered	(Na,Ca)Al(Si,Al) ₃ O ₈	83.26	41-1480 (I)
B	Aluminum, syn	Al	79.8	04-0787 (*)
A	Anorthite, sodian, intermediate	(Ca,Na)(Si,Al) ₄ O ₈	42.59	18-1202 (I)
C	Hedenbergite	CaFe ⁺² Si ₂ O ₆	36.91	41-1372 (*)
D	Augite	Ca(Mg,Fe)Si ₂ O ₆	35.8	24-0203 (I)
E	Iron, syn	Fe	35.7	06-0696 (*)
F	Magnesioferrite, ordered, syn	MgFe ₂ ⁺³ O ₄	27.99	17-0464 (I)
G	Corundum, syn	Al ₂ O ₃	33.07	10-0173 (I)
	Diaoyudaoite, syn	NaAl ₁₁ O ₁₇ /0.5(Na ₂ O·11Al ₂ O ₃)	21	21-1096 (I)
H	Silicon, syn	Si	29.4	27-1402 (*)
I	Magnesium Iron Oxide	Mg _{1-x} Fe _x O	16.8	35-1393 (*)
	Gehlenite, syn	Ca ₂ Al ₂ SiO ₇	16.8	35-0755 (*)
J	Hercynite, syn	Fe ⁺² Al ₂ O ₄	16.7	34-0192 (*)
	Magnesium Aluminum Iron Oxide	MgFeAlO ₄	12.25	11-0009 (I)

24.45% Al by weight

The XRD pattern for the reaction product utilizing a 24.45% aluminum stoichiometry, with identified chemical species labeled, is shown in Figure LXIV. The legend for the identified chemical species is shown in Table XXVI.

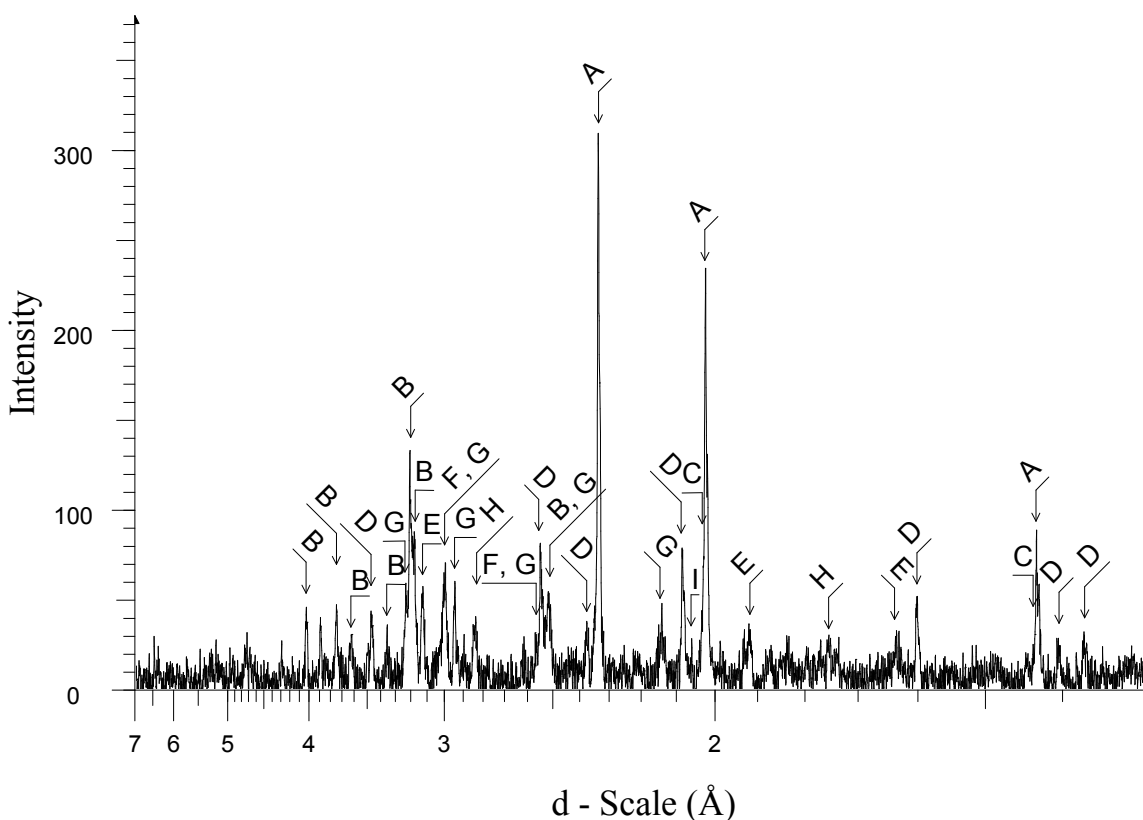


Figure LXIV: XRD pattern for the reaction product of the 75.55% JSC-1A and 24.45% aluminum stoichiometry.

Table XXVI: Legend of Identified Chemical species in the Diffraction Pattern Shown in Figure LXIV

	Compound Name	Formula	Y-Scale	PDF #
A	Aluminum, syn	Al	105.31	04-0787 (*)
B	Albite, disordered	Na(Si ₃ Al)O ₈	26.28	10-0393 (*)
B	Anorthite, ordered	CaAl ₂ Si ₂ O ₈	25.2	41-1486 (*)
B	Anorthite, sodian, disordered	(Ca,Na)(Si,Al) ₄ O ₈	24.99	41-1481 (I)
B	Albite, calcian, ordered	(Na,Ca)Al(Si,Al) ₃ O ₈	24.97	41-1480 (I)
C	Iron, syn	Fe	22.67	06-0696 (*)
D	Corundum, syn	Al ₂ O ₃	21.28	10-0173 (I)
B	Anorthite, sodian, intermediate	(Ca,Na)(Si,Al) ₄ O ₈	18.88	18-1202 (I)
E	Silicon, syn	Si	17.89	27-1402 (*)
F	Hedenbergite	CaFe ⁺² Si ₂ O ₆	15.6	41-1372 (*)
G	Augite	Ca(Mg,Fe)Si ₂ O ₆	14.61	24-0203 (I)
H	Gehlenite, syn	Ca ₂ Al ₂ SiO ₇	12.35	35-0755 (*)
I	Aluminum Iron	Al _{0.5} Fe _{0.5}	8.53	45-0983 (I)
	Spinel, syn	MgAl ₂ O ₄	7.27	21-1152 (*)
	Fersilicite, syn [NR]	FeSi	5.7	38-1397 (*)

28.85% Al by weight

The XRD pattern for the reaction product utilizing a 28.85% aluminum stoichiometry, with identified chemical species labeled, is shown in Figure LXV. The legend for the identified chemical species is shown in Table XXVII.

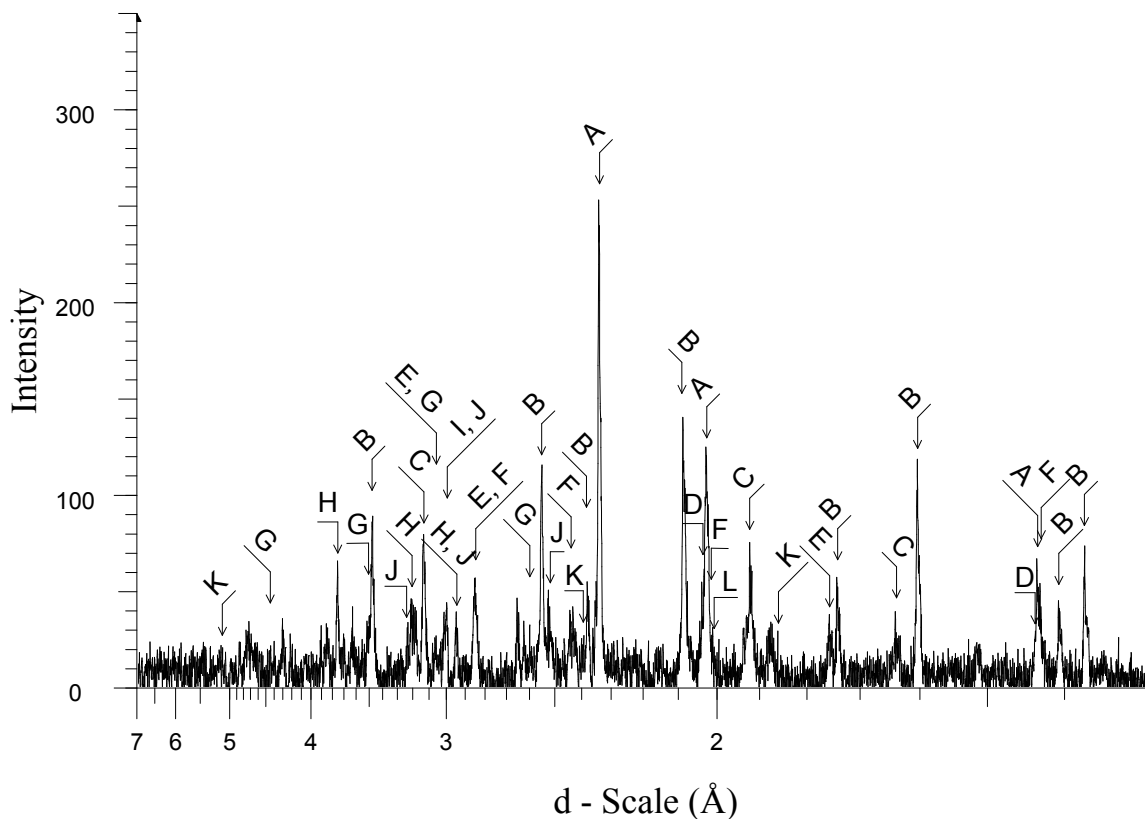


Figure LXV: XRD pattern for the reaction product of the 71.15% JSC-1A and 28.85% aluminum stoichiometry.

Table XXVII: Legend of Identified Chemical species in the Diffraction Pattern Shown in Figure LXV

	Compound Name	Formula	Y-Scale	PDF #
A	Aluminum, syn	Al	101.06	04-0787 (*)
B	Corundum, syn	Al ₂ O ₃	49.98	10-0173 (I)
C	Silicon, syn	Si	30.9	27-1402 (*)
D	Iron, syn	Fe	24.64	06-0696 (*)
E	Gehlenite, syn	Ca ₂ Al ₂ SiO ₇	21.33	35-0755 (*)
F	Spinel, syn	MgAl ₂ O ₄	16.41	21-1152 (*)
G	Grossite, syn	CaAl ₄ O ₇ /CaO·2Al ₂ O ₃	15.63	23-1037 (*)
H	Anorthite, sodian, intermediate	(Ca,Na)(Si,Al) ₄ O ₈	15.4	18-1202 (I)
I	Hedenbergite	CaFe ⁺² Si ₂ O ₆	14.78	41-1372 (*)
J	Augite	Ca(Mg,Fe)Si ₂ O ₆	14.72	24-0203 (I)
H	Albite, calcian, ordered	(Na,Ca)Al(Si,Al) ₃ O ₈	14.37	41-1480 (I)
H	Anorthite, ordered	CaAl ₂ Si ₂ O ₈	12.58	41-1486 (*)
G	Grossite	CaAl ₄ O ₇	11.49	46-1475 (I)
K	Ferdisilicite, syn [NR]	FeSi ₂	10.78	35-0822 (*)
	Magnesium Aluminum Iron Oxide	MgFeAlO ₄	10.52	11-0009 (I)
H	Anorthite, sodian, disordered	(Ca,Na)(Si,Al) ₄ O ₈	10.26	41-1481 (I)
L	Fersilicite, syn [NR]	FeSi	9.84	38-1397 (*)
H	Albite, disordered	Na(Si ₃ Al)O ₈	8.21	10-0393 (*)
	Aluminum Iron	AlFe	6.84	33-0020 (*)
	Aluminum Iron	Al _{0.5} Fe _{0.5}	6.76	45-0983 (I)

Comparison of Chemical Species Formed in JSC-1A Vacuum Products

XRD patterns of the three reactant stoichiometries using JSC-1A simulant in Figure LXIII, Figure LXIV, and Figure LXV are stacked and shown in Figure LXVI. Table XXVIII compares relative diffraction intensities for chemical species present in the various reaction stoichiometries, which were identified in Table XXV, Table XXVI, and Table XXVII.

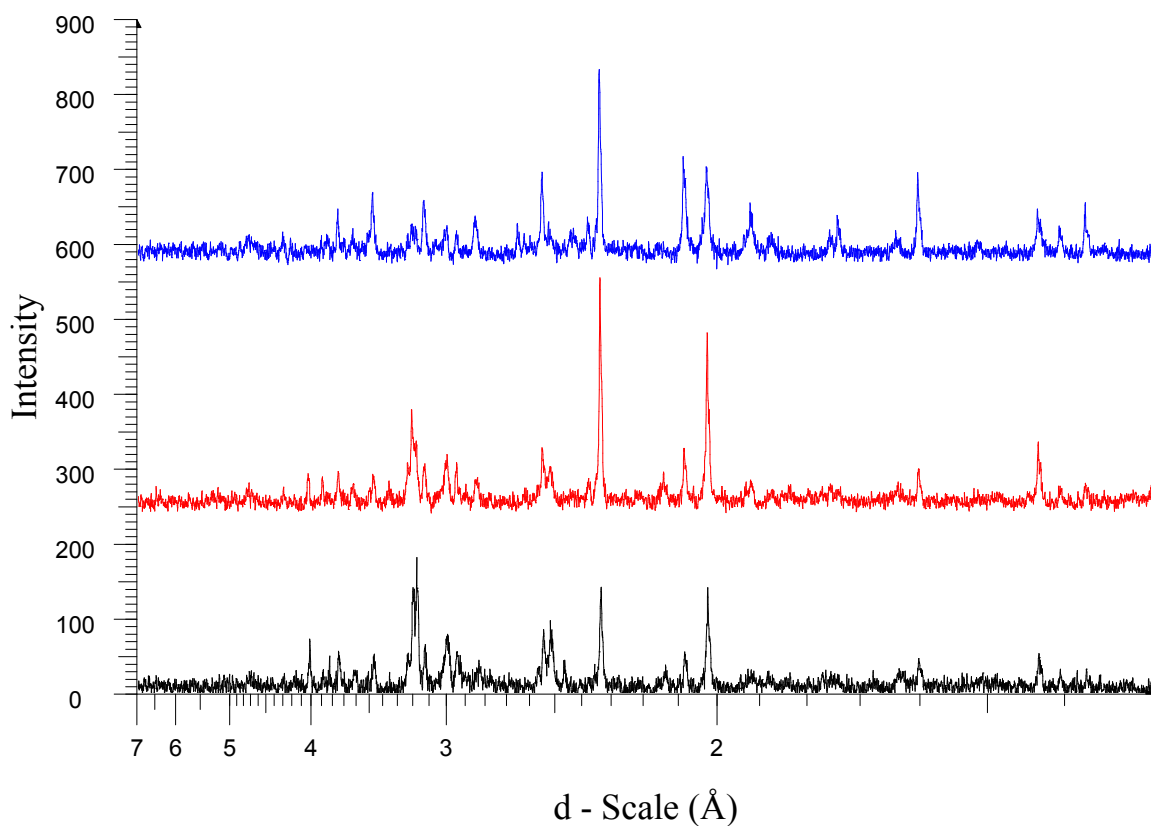


Figure LXVI: Stacked XRD patterns of three reacted stoichiometries of Al and JSC-1A simulant

Legend of Color Coding in Figure LXVI and Table XXVIII:

Black: 80.56% JSC-1A and 19.44% Al by weight

Red: 75.55% JSC-1A and 24.45% Al by weight

Blue: 71.15% JSC-1A and 28.85% Al by weight

Bold-typeface Chemical Species: Products of reaction

Normal-typeface Chemical Species: Reactants

Table XXVIII: Identified Chemical species in the Reaction Products using JSC-1A simulant

Formula	Intensity			PDF #
	19.44A	24.45A	28.85A	
Al	146	329	257	04-0787 (*)
Na(Si ₃ Al)O ₈	183	82	21	10-0393 (*)
(Ca,Na)(Si,Al) ₄ O ₈	166	78	26	41-1481 (I)
CaAl ₂ Si ₂ O ₈	163	79	32	41-1486 (*)
(Na,Ca)Al(Si,Al) ₃ O ₈	152	78	36	41-1480 (I)
(Ca,Na)(Si,Al) ₄ O ₈	78	59	39	18-1202 (I)
CaFe ⁺² Si ₂ O ₆	68	49	38	41-1372 (*)
Ca(Mg,Fe)Si ₂ O ₆	66	46	0	24-0203 (I)
MgFe ₂ ⁺³ O ₄	51	0	0	17-0464 (I)
Si	54	56	78	27-1402 (*)
MgAl ₂ O ₄	0	23	42	21-1152 (*)
Al ₂ O ₃ (α)	61	66	127	10-0173 (I)
FeSi	0	18	25	38-1397 (*)
FeSi ₂	0	0	27	35-0822 (*)
CaAl ₄ O ₇	0	0	29	46-1475 (I)
CaAl ₄ O ₇ /CaO·2Al ₂ O ₃	0	0	40	23-1037 (*)
Ca ₂ Al ₂ SiO ₇	31	39	54	35-0755 (*)
MgFeAlO ₄	22	0	27	11-0009 (I)
Fe ⁺² Al ₂ O ₄	31	0	0	34-0192 (*)
Fe	65	71	63	06-0696 (*)
Ca(Mg,Fe)Si ₂ O ₆	0	0	37	24-0203 (I)
Mg _{1-x} Fe _x O	31	0	0	35-1393 (*)
NaAl ₁₁ O ₁₇ /0.5(Na ₂ O·11Al ₂ O ₃)	38	0	0	21-1096 (I)
Al _{0.5} Fe _{0.5}	0	27	17	45-0983 (I)
AlFe	0	0	17	33-0020 (*)

As aluminum quantity increased within the reactant stoichiometry using JSC-1A simulant, the intensity of diffraction peaks for minerals contained within the simulant significantly decreased. The decrease in diffraction intensity would likely indicate that the reaction proceeded further towards completion. Diffraction peaks for Al (04-0787), Si (27-1402), Al₂O₃ (10-0173), and CaAl₂SiO₇ (35-0755) are found within all JSC-1A stoichiometries. Diffraction peaks for MgAl₂O₄ (21-1152) and FeSi (38-1397) are first observed in the 24.45% stoichiometry, and their intensities increase in the 28.85% stoichiometry. Diffraction peaks for CaAl₄O₇ (23-1037) (46-1475), FeSi₂ (35-0822), and AlFe (33-0020) are only observed in the 28.85% stoichiometry. The chemical species of MgFeAlO₄ (11-0009) and FeAl₂O₄ (34-0192) were present in some stoichiometries. Table XXIX shows a comparison of diffraction peak

intensities for JSC-1AF and JSC-1A reaction products. Figure LXVII shows the relative diffraction intensities of selected chemical species with the reaction product conducted in a vacuum environment. Variation in the diffraction intensities for chemical species between reactant stoichiometries likely occurred due to differences in temperatures achieved during the reaction and the availability of aluminum to react with the simulant.

Legend for Table XXIX:

Bold-typeface Chemical Species: Products of reaction

Normal-typeface Chemical Species: Reactants

Table XXIX: Identified Chemical species in the Reaction Products using JSC-1AF and JSC-1A simulants

Formula	Intensity							SS-NNNN
	19.44 AF	24.45 AF	28.85 AF	33.33 AF	19.44 A	24.45 A	28.85 A	
Al	251	229	255	253	146	329	257	04-0787 (*)
Na(Si ₃ Al)O ₈	124	62	37	38	183	82	21	10-0393 (*)
(Ca,Na)(Si,Al) ₄ O ₈	124	52	31	36	166	78	26	41-1481 (I)
CaAl ₂ Si ₂ O ₈	109	54	35	36	163	79	32	41-1486 (*)
(Na,Ca)Al(Si,Al) ₃ O ₈	124	58	31	36	152	78	36	41-1480 (I)
(Ca,Na)(Si,Al) ₄ O ₈	78	57	22	36	78	59	39	18-1202 (I)
CaFe ⁺² Si ₂ O ₆	67	33	23	0	68	49	38	41-1372 (*)
Ca(Mg,Fe)Si ₂ O ₆	0	19	0	0	66	46	0	24-0203 (I)
MgFe ₂ ⁺³ O ₄	0	0	0	0	51	0	0	17-0464 (I)
Ca(Mg,Fe,Al)(Si,Al) ₂ O ₆	52	0	20	16	0	0	0	41-1483 (I)
Si	119	153	189	259	54	56	78	27-1402 (*)
MgAl ₂ O ₄	42	89	78	114	0	23	42	21-1152 (*)
Al ₂ O ₃ (α)	99	142	140	163	61	66	127	10-0173 (I)
FeSi	47	28	35	31	0	18	25	38-1397 (*)
FeSi ₂	47	55	0	0	0	0	27	35-0822 (*)
CaAl ₄ O ₇	0	73	55	150	0	0	29	46-1475 (I)
CaAl ₄ O ₇ /CaO·2Al ₂ O ₃	0	54	53	125	0	0	40	23-1037 (*)
Mg _{0.388} Al _{2.408} O ₄	0	0	26	23	0	0	0	48-0528 (I)
Ca ₂ Al ₂ SiO ₇	52	117	77	67	31	39	54	35-0755 (*)
MgFeAlO ₄	21	23	23	0	22	0	27	11-0009 (I)
Fe ⁺² Al ₂ O ₄	0	0	0	0	31	0	0	34-0192 (*)
Fe	62	62	63	66	65	71	63	06-0696 (*)
Ca(Mg,Fe)Si ₂ O ₆	0	0	0	0	0	0	37	24-0203 (I)
Al _{0.5} Fe _{0.5}	0	7	0	47	0	27	17	45-0983 (I)
AlFe	21	17	28	28	0	0	17	33-0020 (*)
Mg _{1-x} Fe _x O	0	0	0	0	31	0	0	35-1393 (*)
NaAl ₁₁ O ₁₇ /0.5(Na ₂ O·11Al ₂ O ₃)	0	0	0	0	38	0	0	21-1096 (I)
Al ₂ O ₃	0	0	35	16	0	0	0	23-1009 (I)
(Na ₂ O)0.33NaAlSiO ₄	0	0	24	23	0	0	0	39-0101 (I)
Na ₃ MgAlSi ₂ O ₈	0	0	24	20	0	0	0	49-0008 (*)
NaFeO _{2.35} Si _{0.175} /NaFeO ₂ ·0.175SiO ₂	0	0	18	42	0	0	0	40-0139 (*)
SiO ₂	0	0	0	34	0	0	0	38-0651 (I)

Vacuum Synthesis Diffraction Intensities

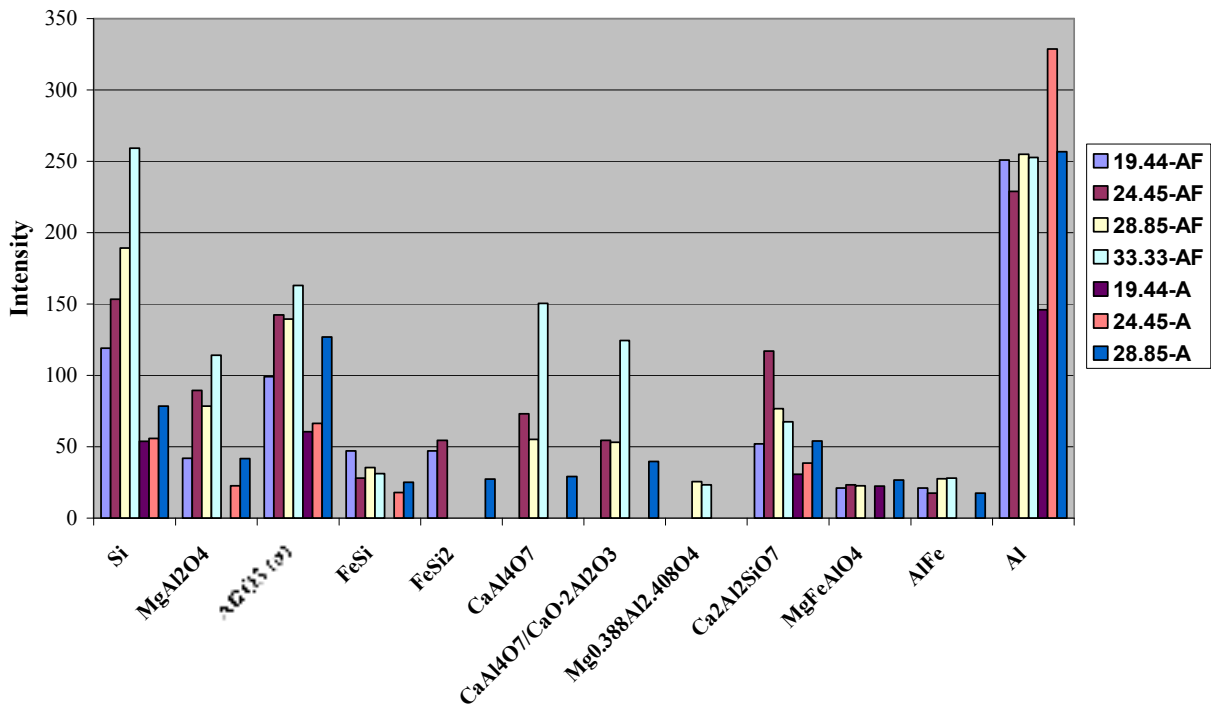


Figure LXVII: Relative diffraction intensities for selected chemical species in the vacuum reaction product.

The data assembled in Table XXIX indicate that diffraction intensities for constituents within the regolith simulant including anorthite, albite, hedenbergite, and albite seem to be more intense in the JSC-1A simulant using 19.44% and 24.45% stoichiometries. The diffraction intensities in the 28.85% stoichiometries of both simulants are relatively similar. The presence of unreacted regolith simulant minerals in the reaction product would indicate an incomplete reaction. The data in Figure LXVII indicate that diffraction peaks for silicon (27-1402) are significantly more intense in the JSC-1AF reaction products. Corundum (10-0173) diffraction peaks are significantly larger in the JSC-1AF simulant, except for the 28.85% stoichiometry where the corundum peaks are only slightly higher. $\text{CaAl}_2\text{Si}_2\text{O}_7$ (35-0755) diffraction peaks have higher intensities in the JSC-1AF simulant. CaAl_4O_7 (23-1037) (46-1475) diffraction peaks are absent from the 19.44% stoichiometries of both simulants. The 24.45% stoichiometry utilizing JSC-1AF simulant exhibits significant diffraction peaks for CaAl_4O_7 (23-1037) (46-1475), while the JSC-1A stoichiometry exhibits none. Diffraction peaks for CaAl_4O_7 (23-1037) (46-1475) are larger in the 28.85% stoichiometry using JSC-1AF than the same stoichiometry

using JSC-1A. Diffraction peaks for MgFeAlO_4 (11-0009) are found in several stoichiometries for both simulants. Variation in the diffraction intensities for chemical species between simulants using the same reactant stoichiometry likely occurred due to differences in temperatures achieved during the reaction. Temperatures achieved during the reaction would depend on the quantity of oxidation-reduction reactions able to occur, which is largely influenced by particle surface area.

C. Characterization of Microstructures and Elemental Analysis

This section discusses SEM and EDS analysis of unreacted JSC-1AF and JSC-1A simulants and reaction products synthesized in ambient and vacuum conditions using JSC-1AF and JSC-1A simulant. Micrographs of reaction products are grouped together by magnification, reaction environment, and simulant type. Comparison of microstructures between different reactant stoichiometries and simulants at 500x, 2kx, and 10kx magnifications are facilitated by the grouping arrangement. EDS analyses are grouped together by reactant stoichiometries and simulant type.

Micrographs of Unreacted JSC-1AF Simulant

Micrographs of a sample of unreacted JSC-1AF simulant are shown in Figure LXVIII, Figure LXIX, and Figure LXX, at magnifications of 500x, 1kx, and 2.5kx respectively. Many sub-angular and angular particles are observed in Figure LXVIII and Figure LXIX, having sizes ranging from $\sim 10 \mu\text{m}$ to $50 \mu\text{m}$. Particles ranging in size from $\sim 30 \mu\text{m}$ to less than $1 \mu\text{m}$ are present in Figure LXX.

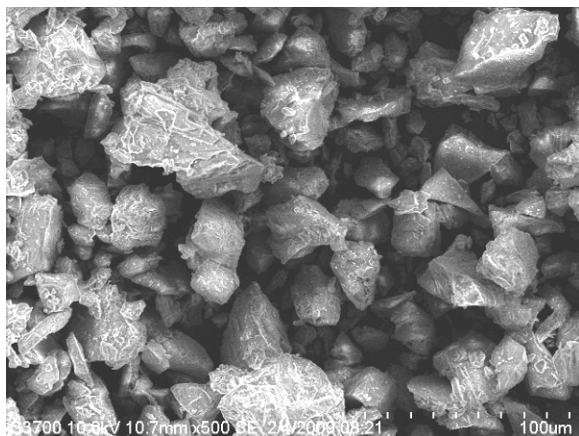


Figure LXVIII: SEM micrograph of unreacted JSC-1AF simulant at 500x.

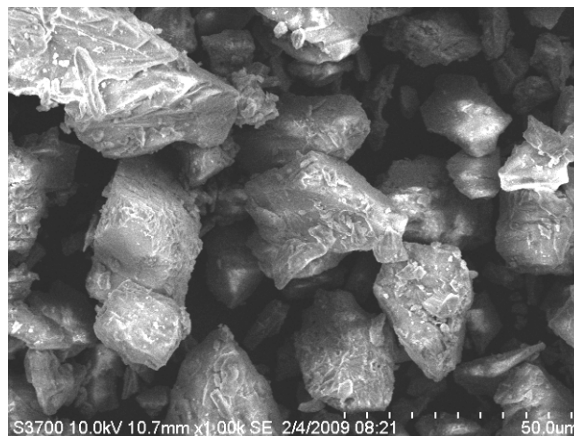


Figure LXIX: SEM micrograph of unreacted JSC-1AF simulant at 1kx.

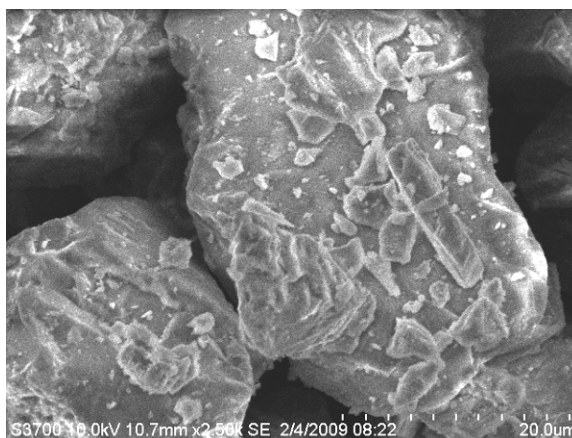


Figure LXX: SEM micrograph of unreacted JSC-1AF simulant at 2.5kx.

Elemental Analysis of Unreacted JSC-1AF Simulant

EDS analysis was performed on the JSC-1AF simulant in order to establish that the simulant had reasonable uniformity of elemental composition, as well as to compare the results with the JSC-1A simulant. It is important to establish that the simulants have approximately the same elemental abundances throughout, in order to compare reactions within the same simulant and between the two simulants. Although JSC-1AF is just a fine particle size distribution of JSC-1A, it is possible that the particle size refining process could have preferentially eliminated components, such as chemical species with a greater hardness. Table XXX lists the results of

elemental analysis for four regions of JSC-1AF simulant, along with the calculated mean and deviation ($\pm 1 \sigma$). The data in Table XXX indicate a fairly uniform elemental composition within JSC-1AF simulant.

Table XXX: EDS Analysis of JSC-1AF Regions (Values in Atomic %)

	Region 1	Region 2	Region 3	Region 4	Mean
O	65.21	64.88	64.54	64.65	64.82 \pm 0.30
Na	2.02	2.17	2.18	2.12	2.12 \pm 0.07
Mg	2.18	2.14	2.21	2.10	2.16 \pm 0.05
Al	6.82	6.64	6.87	6.86	6.80 \pm 0.11
Si	14.04	13.95	14.12	14.13	14.06 \pm 0.08
P	0.17	0.15	0.21	0.18	0.18 \pm 0.03
K	0.39	0.35	0.37	0.38	0.37 \pm 0.02
Ca	4.44	4.50	4.57	4.64	4.54 \pm 0.09
Ti	0.52	0.58	0.59	0.54	0.56 \pm 0.03
Mn	0.07	0	0.08	0	0.04 \pm 0.04
Fe	4.08	4.64	4.26	4.40	4.35 \pm 0.24
Mo	0.07	0	0	0	0.02 \pm 0.04

Micrographs of Unreacted JSC-1A Simulant

Micrographs of a sample of JSC-1A simulant are shown in Figure LXXI, Figure LXXII, and Figure LXXIII, at magnifications of 100x, 250x, and 500x, respectively. Two sub-rounded oblong particles with lengths \sim 500 μ m are present in Figure LXXI. Many sub-angular and angular particles are observed in Figure LXXII, having sizes ranging from \sim 40 μ m to 200 μ m. Particles ranging in size from \sim 30 μ m to 100 μ m are present in Figure LXXIII.

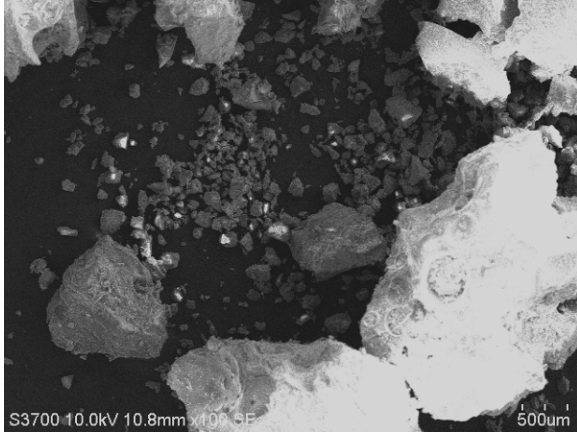


Figure LXXI: SEM micrograph of unreacted JSC-1A simulant at 100x.

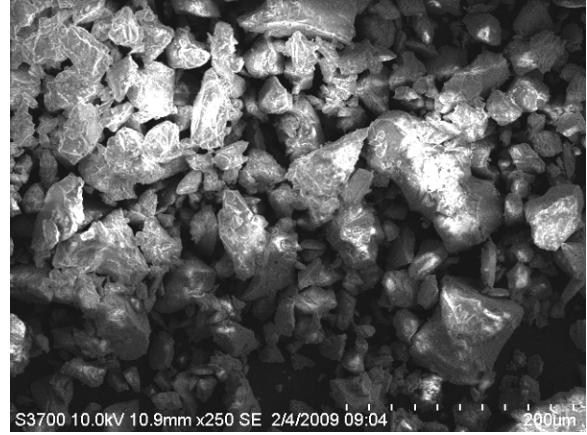


Figure LXXII: SEM micrograph of unreacted JSC-1A simulant at 250x.

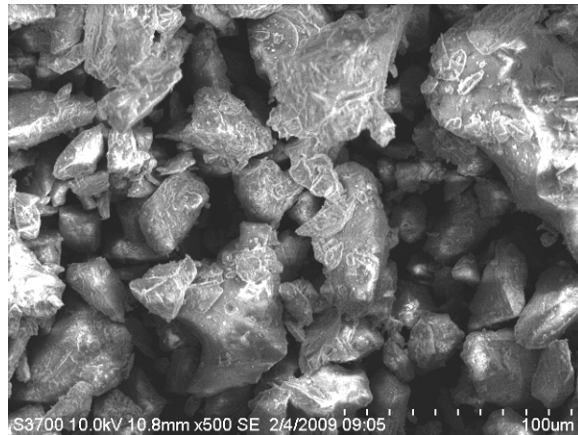


Figure LXXIII: SEM micrograph of unreacted JSC-1A simulant at 500x.

Elemental Analysis of Unreacted JSC-1A Simulant

Table XXXI lists the results of elemental analysis for five regions of JSC-1A simulant, along with the calculated mean and deviation ($\pm 1 \sigma$). The data in Table XXXI indicate a fairly uniform elemental composition within the JSC-1A simulant.

Table XXXI: EDS Analysis of JSC-1A Regions (Values in Atomic %)

	Region 1	Region 2	Region 3	Region 4	Region 5	Mean
O	67.89	67.63	67.77	68.02	67.35	67.73 ± 0.26
Na	2.14	2.34	2.17	2.17	2.35	2.23 ± 0.10
Mg	2.26	2.28	2.56	2.39	2.25	2.35 ± 0.13
Al	6.38	6.14	6.05	6.23	6.16	6.19 ± 0.12
Si	13.59	13.64	13.43	13.55	13.99	13.64 ± 0.21
P	0.15	0.22	0.19	0.19	0.19	0.19 ± 0.02
K	0.30	0.36	0.36	0.33	0.36	0.34 ± 0.03
Ca	3.68	3.48	3.51	3.49	3.48	3.53 ± 0.09
Ti	0.45	0.47	0.46	0.43	0.48	0.46 ± 0.02
Mn	0	0.07	0	0	0	0.01 ± 0.03
Fe	3.17	3.36	3.48	3.21	3.40	3.32 ± 0.13

Comparison of Elemental Analyses for Unreacted JSC-1AF and JSC-1A Simulant

Table XXXII lists compares the mean atomic percentage and deviation ($\pm 1 \sigma$) for each element in the JSC-1AF and JSC-1A simulants. The data in Table XXXII does not indicate a substantial difference in elemental composition between simulants.

Table XXXII: Mean EDS Analysis of JSC-1AF and JSC-1A Regions (Values in Atomic %)

	Mean	
	JSC-1AF	JSC-1A
O	64.82 ± 0.30	67.73 ± 0.26
Na	2.12 ± 0.07	2.23 ± 0.10
Mg	2.16 ± 0.05	2.35 ± 0.13
Al	6.80 ± 0.11	6.19 ± 0.12
Si	14.06 ± 0.08	13.64 ± 0.21
P	0.18 ± 0.03	0.19 ± 0.02
K	0.37 ± 0.02	0.34 ± 0.03
Ca	4.54 ± 0.09	3.53 ± 0.09
Ti	0.56 ± 0.03	0.46 ± 0.02
Mn	0.04 ± 0.04	0.01 ± 0.03
Fe	4.35 ± 0.24	3.32 ± 0.13
Mo	0.02 ± 0.04	0

Microstructures within the Reaction Products of a Standard Atmosphere SHS Reaction

500x Magnification

Microstructures for reaction products synthesized using JSC-1AF simulant are shown in Figure LXXIV-Figure LXXVII at 500x magnification.

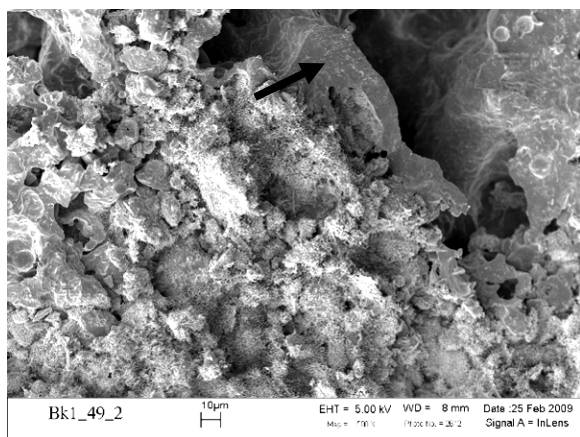


Figure LXXIV: Standard atmosphere synthesized 19.44% aluminum stoichiometry utilizing JSC-1AF.

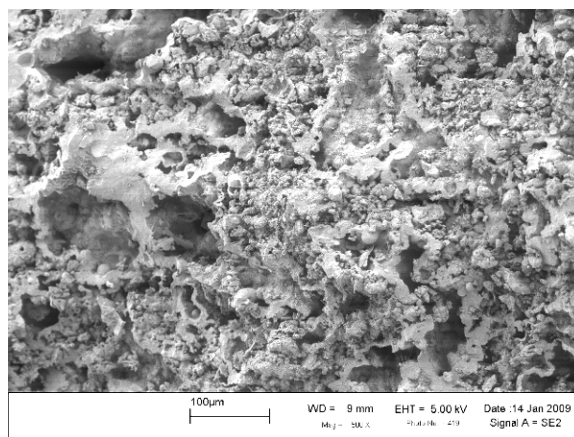


Figure LXXV: Standard atmosphere synthesized 24.45% aluminum stoichiometry utilizing JSC-1AF.

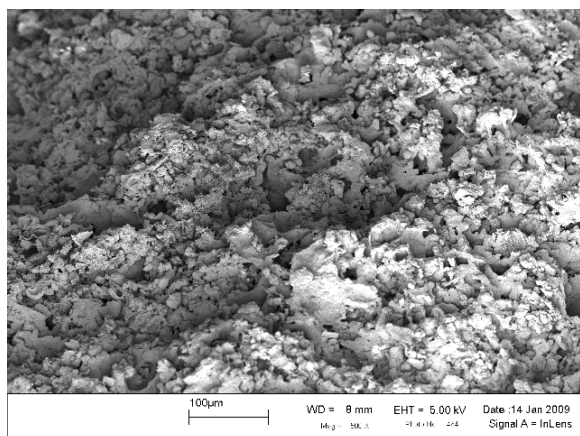


Figure LXXVI: Standard atmosphere synthesized 28.85% aluminum stoichiometry utilizing JSC-1AF.

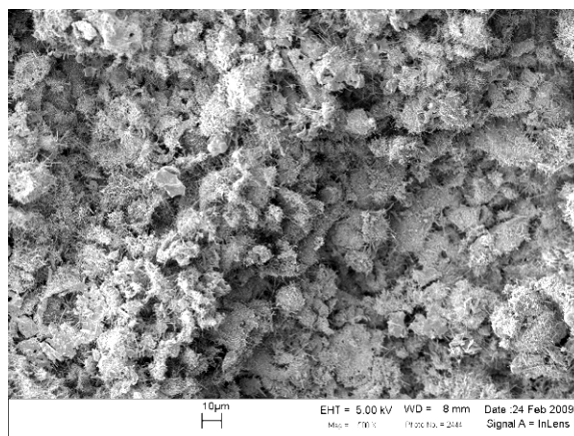


Figure LXXVII: Standard atmosphere synthesized 33.33% aluminum stoichiometry utilizing JSC-1AF.

Melted areas appear to be present in Figure LXXIV and Figure LXXV, which could indicate that liquid phase sintering is occurring. The abundance of whiskers in Figure LXXVI and Figure LXXVII prevents locating regions where melting may be evident. The formation of whiskers appears to increase with increasing aluminum used in the reaction. Microstructures for

reaction products synthesized using JSC-1A simulant are shown in Figure LXXVIII-Figure LXXXI at 500x magnification.

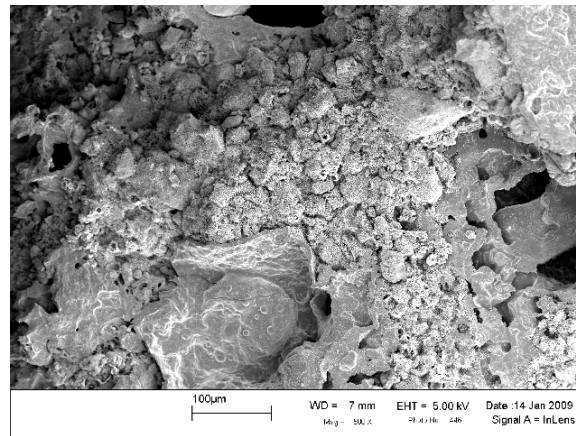


Figure LXXVIII: Standard atmosphere synthesized 19.44% aluminum stoichiometry utilizing JSC-1A.

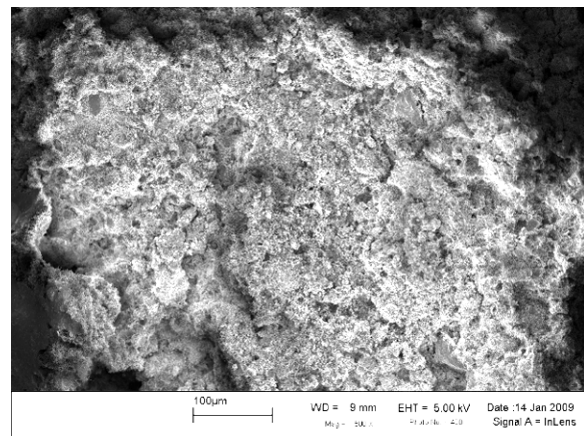
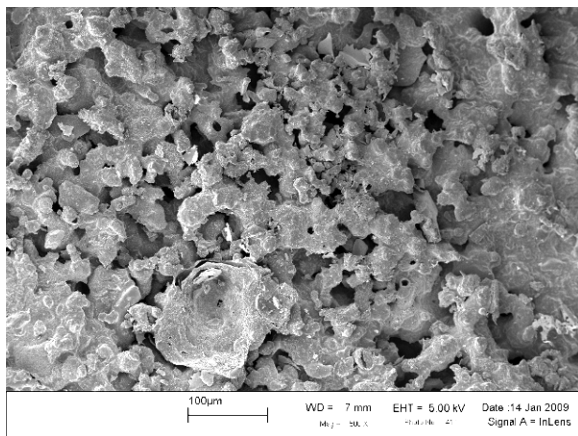


Figure LXXIX: Standard atmosphere synthesized 24.45% aluminum stoichiometry utilizing JSC-1A.

Figure LXXX: Standard atmosphere synthesized 24.45% aluminum stoichiometry utilizing JSC-1A.

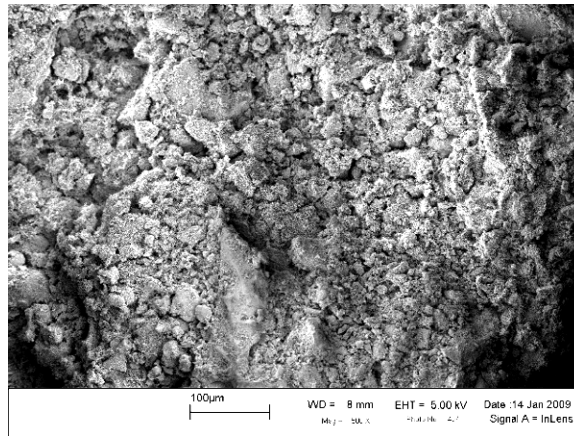


Figure LXXXI: Standard atmosphere synthesized 28.85% aluminum stoichiometry utilizing JSC-1A.

Liquid phase sintering appears to have occurred in several areas in the two lowest aluminum stoichiometries in the coarse simulant, shown in Figure LXXVIII and Figure LXXIX. There are some regions that appear to be completely melted. The 28.85% Al stoichiometry, shown in Figure LXXXI, has large concentrations of whiskers that obscure particles. Whisker formation appears to increase with increasing aluminum in the reactants.

2kx Magnification

Microstructures for reaction products synthesized using JSC-1AF simulant are shown in Figure LXXXII-Figure LXXXV at 2kx magnification.

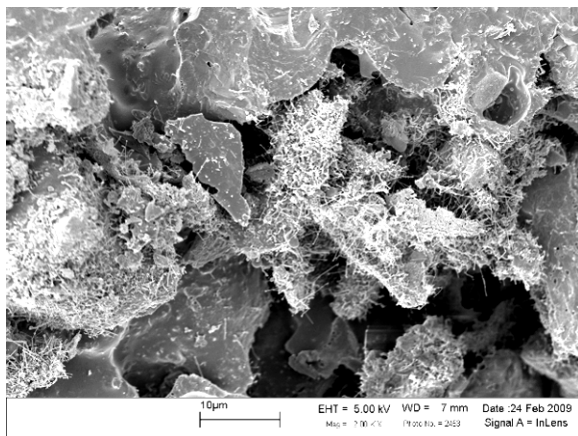


Figure LXXXII: Standard atmosphere synthesized 19.44% aluminum stoichiometry utilizing JSC-1AF.

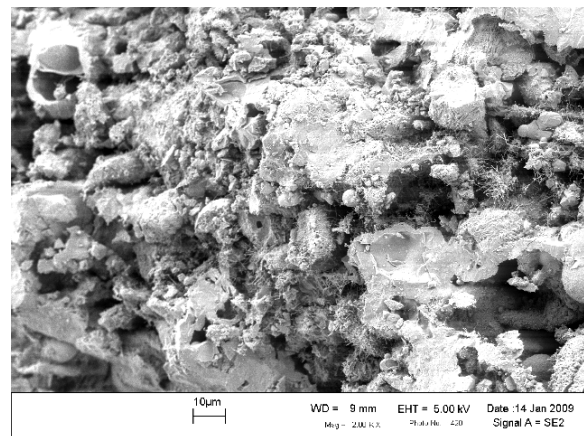


Figure LXXXIII: Standard atmosphere synthesized 24.45% aluminum stoichiometry utilizing JSC-1AF.

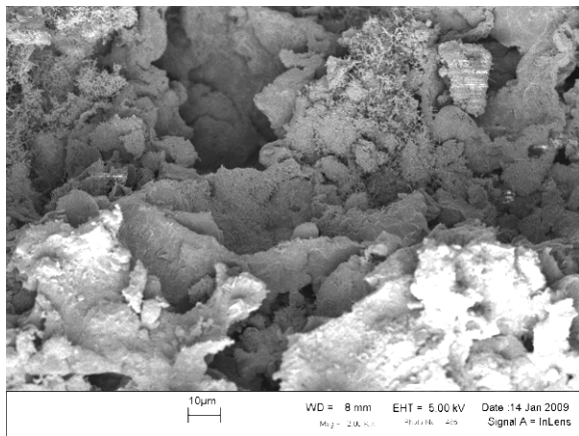


Figure LXXXIV: Standard atmosphere synthesized 28.85% aluminum stoichiometry utilizing JSC-1AF.

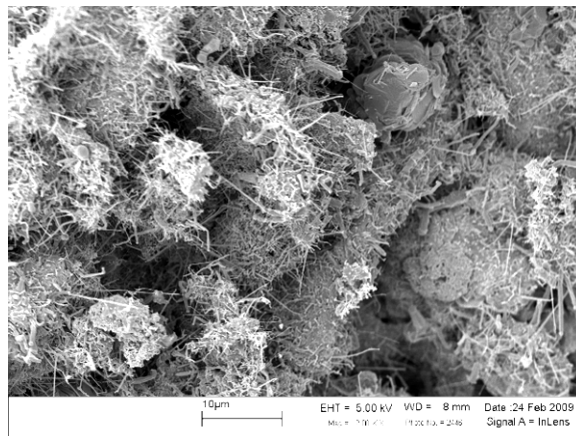


Figure LXXXV: Standard atmosphere synthesized 33.33% aluminum stoichiometry utilizing JSC-1AF.

The 19.44% stoichiometry, shown in Figure LXXXII, appears to contain areas of melting. Whisker formation in all the micrographs seems roughly equivalent, except for the 33.33% Al stoichiometry shown in Figure LXXXV. Figure LXXXV exhibits substantially larger quantities of whiskers. Microstructures for reaction products synthesized using JSC-1A simulant are shown in Figure LXXXVI-Figure LXXXVIII at 2kx magnification.

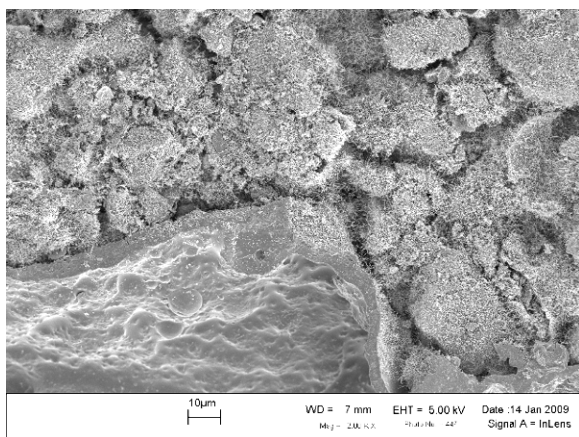


Figure LXXXVI: Standard atmosphere synthesized 19.44% aluminum stoichiometry utilizing JSC-1A.

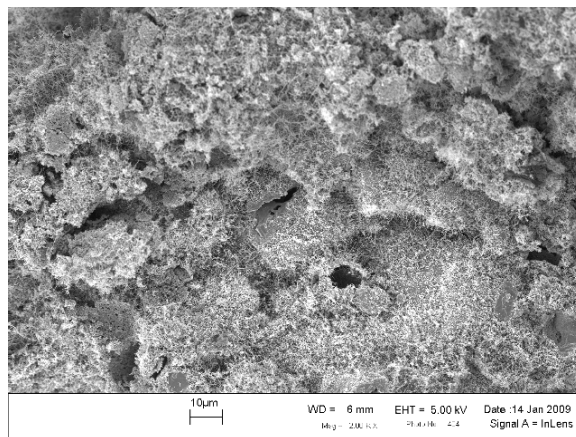


Figure LXXXVII: Standard atmosphere synthesized 24.45% aluminum stoichiometry utilizing JSC-1A.

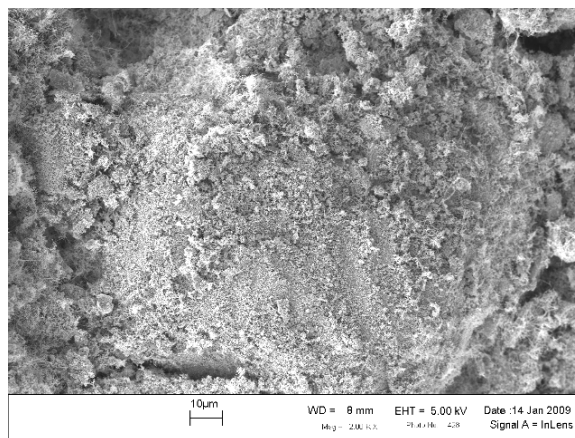


Figure LXXXVIII: Standard atmosphere synthesized 28.85% aluminum stoichiometry utilizing JSC-1A.

Very small clusters of whiskers can be seen radiating from particles in the JSC-1A products, shown in Figure LXXXVI-Figure LXXXVIII. The outlines of many particles can be observed through the whiskers. The whiskers form an internetwork between particles. The formation of the whisker networks is likely due to ambient gases interacting with the chemical species in the reaction. It is hypothesized that Al_2O gas is produced during the reaction, and reacts with nitrogen and oxygen in the air forming the whisker networks. A region that appears to have melted is observed in the 19.44% Al stoichiometry, shown in Figure LXXXVI.

10kx Magnification

Microstructures for reaction products synthesized using JSC-1AF simulant are shown in Figure LXXXIX-Figure XCII at 10kx magnification.

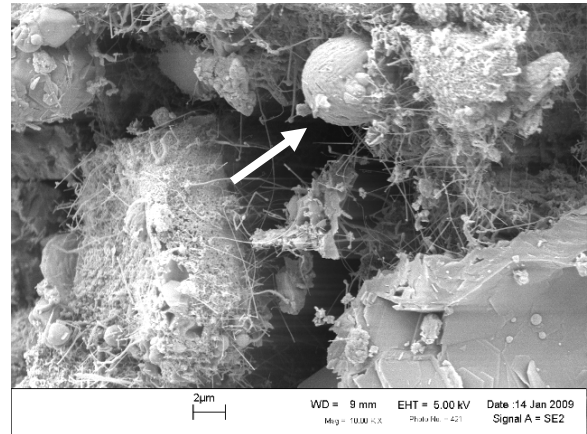
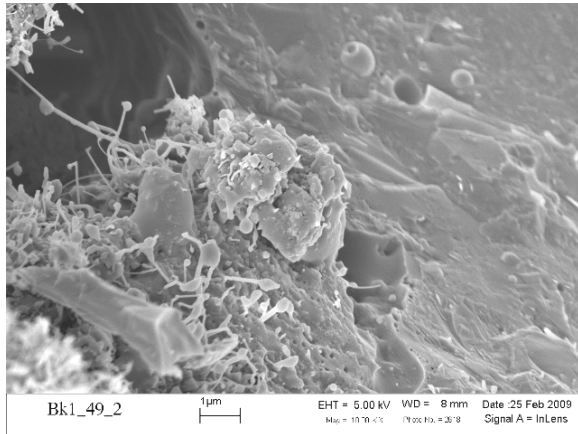


Figure LXXXIX: Standard atmosphere synthesized 19.44% aluminum stoichiometry utilizing JSC-1AF.

Figure XC: Standard atmosphere synthesized 24.45% aluminum stoichiometry utilizing JSC-1AF.

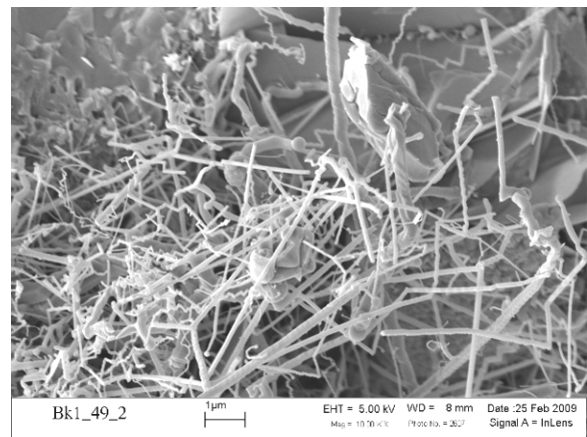
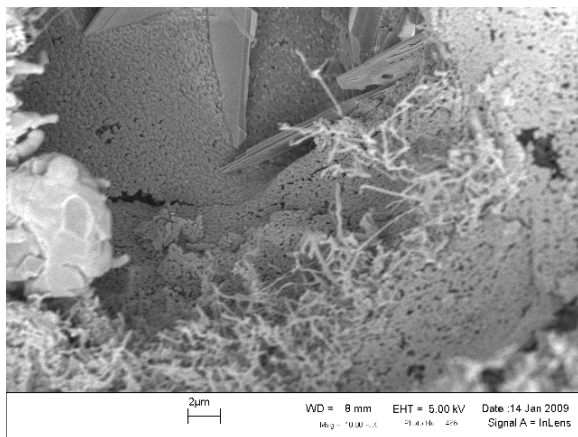


Figure XCI: Standard atmosphere synthesized 28.85% aluminum stoichiometry utilizing JSC-1AF.

Figure XCII: Standard atmosphere synthesized 33.33% aluminum stoichiometry utilizing JSC-1AF.

Whisker networks are observed in all four reactant stoichiometries shown in Figure LXXXIX-Figure XCII. Many of whiskers observed in Figure LXXXIX-Figure XCII terminate in a spherical shape, possibly indicating a vaporization process occurred. The termination of whiskers in a spherical shape would indicate that growth occurred by the VLS mechanism. Growth by the VLS mechanism would indicate that a liquid phase was present at the whisker tip, creating a preferential deposition surface for gas molecules. Precipitation from the super-saturated liquid phase would have caused whisker growth at the tip. A spherical particle is observed in Figure XC, which is likely to be composed of aluminum. Microstructures for

reaction products synthesized using JSC-1A simulant are shown in Figure XCIII-Figure XCV at 10kx magnification.

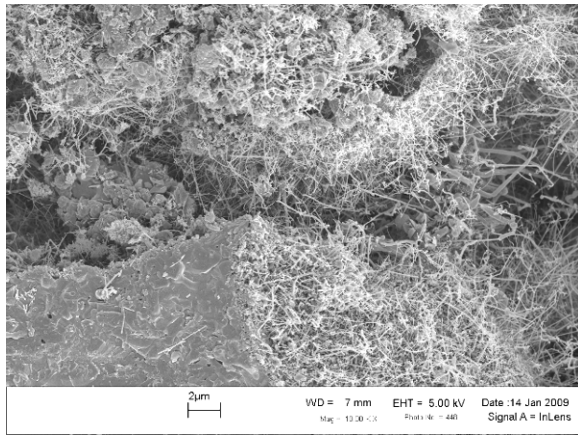


Figure XCIII: Standard atmosphere synthesized 19.44% aluminum stoichiometry utilizing JSC-1A.

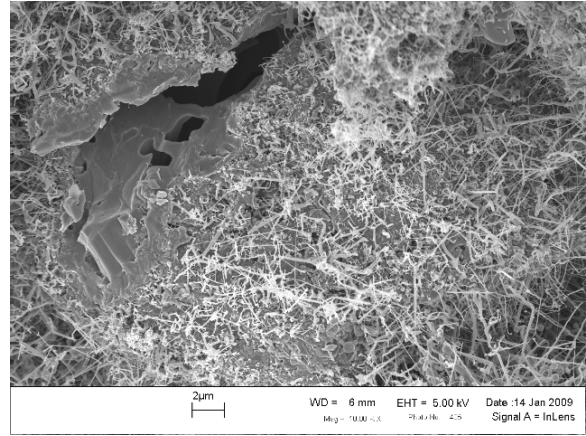


Figure XCIV: Standard atmosphere synthesized 24.45% aluminum stoichiometry utilizing JSC-1A.

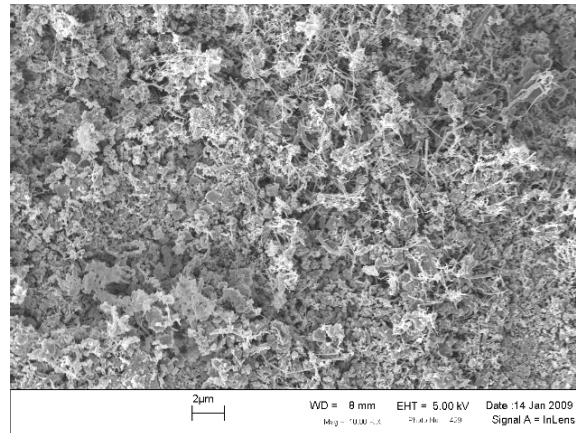


Figure XCV: Standard atmosphere synthesized 28.85% aluminum stoichiometry utilizing JSC-1A.

Growth of whiskers on particles can be observed in the 19.44% and the 24.45% Al stoichiometries, shown in Figure XCIII and Figure XCIV. An area of melting appears to be visible in Figure XCIV. The abundance of whiskers prevents observation of any particles in the 33.33% Al stoichiometry, shown in Figure XCV. The whisker networks appear to be denser in the JSC-1A reaction products. Denser whisker networks may occur due to the presence of smaller surface areas on regolith particles available for aluminum to react with when utilizing the coarse particle simulant. The smaller surface areas may reduce the primary oxidation-reduction

reactions producing silicon, and increase reactions leading to the growth of whiskers between particles.

Nanostructures and Elemental Analysis within the Reaction Products of a Standard Atmosphere SHS Reaction Utilizing JSC-1AF Regolith Simulant

19.44% Al by weight

Figure XCVI and Figure XCVII show 50kx and 100kx magnifications, respectively, of microstructures within the 19.44% Al stoichiometry. Figure XCVI and Figure XCVII show the presence of nano-scale whiskers, with the diameters of selected whiskers labeled. Measured whiskers range in diameter from 18 – 40 nm. Many of the whiskers are observed to terminate in spherical shapes.

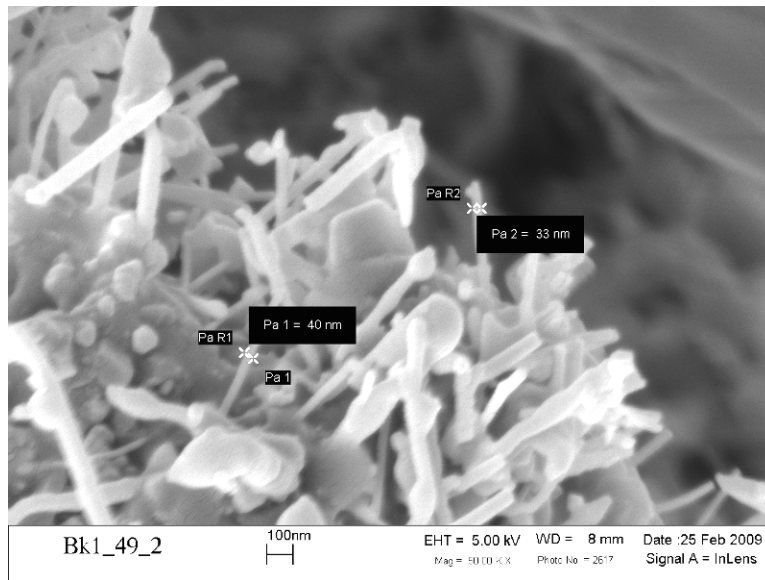


Figure XCVI: Standard atmosphere synthesized 19.44% aluminum stoichiometry utilizing JSC-1AF.

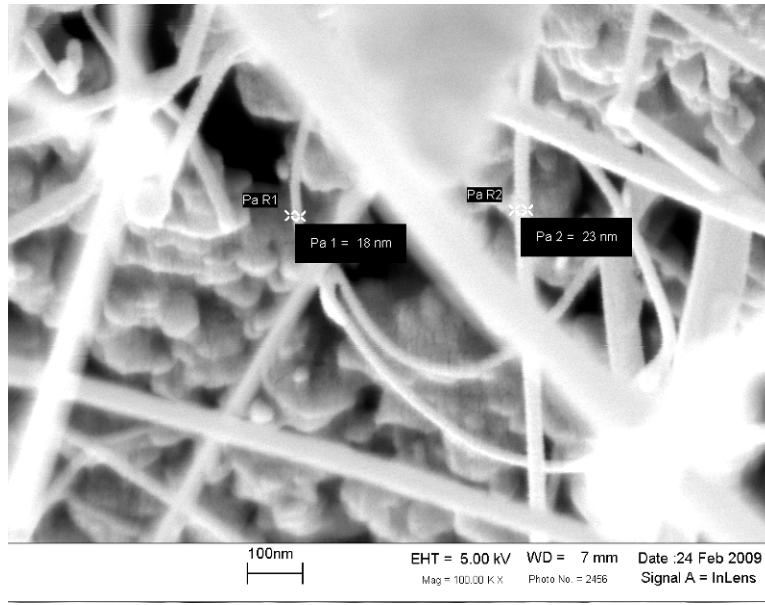


Figure XCVII: Standard atmosphere synthesized 19.44% aluminum stoichiometry utilizing JSC-1AF.

EDS

The microstructure of the reaction product for Region A of a JSC-1AF reaction product utilizing a 19.44% Al stoichiometry is shown in Figure XCVIII. Table XXXIII shows the chemical data obtained from analysis of Spectrum 2. Spectrum 2 is located on a cluster of whiskers that likely formed through a chemical reaction involving a vapor phase due to the small whisker diameters and the spherical shapes terminating many of the whiskers. Chemical analysis indicated high concentrations of aluminum, silicon, and oxygen within Spectrum 2. No nitrogen was detected by EDS. The chemical analysis data from Spectrum 2 likely indicates that the whiskers are composed of a chemical species incorporating aluminum oxide and reduced silicon.

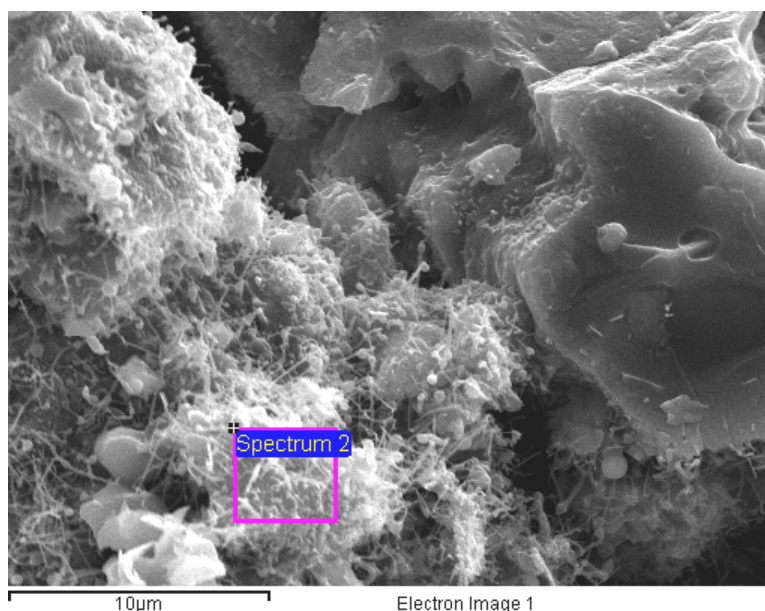


Figure XCVIII: SEM micrograph for Region A of the standard atmosphere synthesized 19.44% aluminum stoichiometry utilizing JSC-1AF simulant with the region of EDS highlighted.

Table XXXIII: EDS Analysis of Spectrum 2 shown in Figure XCVIII

Element	Weight%	Atomic%
O	40.15	54.20
Na	1.01	0.95
Mg	1.07	0.95
Al	34.50	27.62
Si	18.42	14.17
Ca	1.38	0.74
Ti	0.62	0.28
Fe	2.85	1.10

The microstructures of the reaction product for Region B of a JSC-1AF reaction product utilizing a 19.44% Al stoichiometry are shown in Figure XCIX and Figure C, respectively. Table XXXIV and Table XXXV show the chemical data obtained from analysis of Spectrum 1 and 2, respectively. Spectra 1 and 2 are both located on clusters of whiskers that likely formed through a chemical reaction involving a vapor phase due to the small whisker diameters and the spherical shapes terminating many of the whiskers. Chemical analysis indicated high concentrations of aluminum and oxygen within Spectra 1 and 2. Silicon and magnesium were also present in smaller quantities. No nitrogen was detected by EDS. The data from Spectrum 1 and 2 likely indicate that the whiskers are composed of a phase incorporating aluminum, oxygen,

silicon, and magnesium. Many of the whiskers terminate in a spherical shape. EDS data indicate that most of the whiskers are likely to be composed of aluminum oxide. Some of the whiskers could be composed of $Mg_{0.338}Al_{2.408}O_4$, a chemical species detected by XRD.

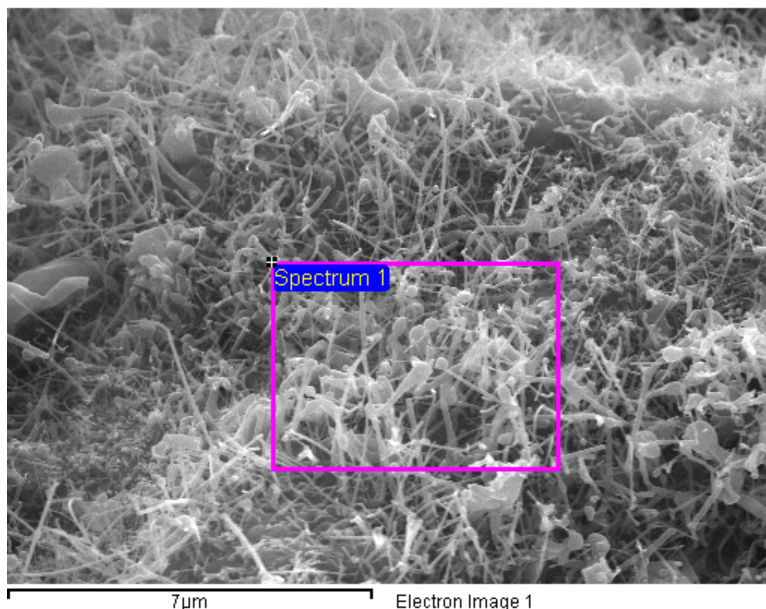


Figure XCIX: SEM micrograph for Region B of the standard atmosphere synthesized 19.44% aluminum stoichiometry utilizing JSC-1AF simulant with the region of EDS highlighted.

Table XXXIV: EDS Analysis of Spectrum 1 shown in Figure XCIX

Element	Weight%	Atomic%
O	49.80	63.05
Na	0.99	0.87
Mg	4.51	3.75
Al	35.98	27.01
Si	5.19	3.74
Ca	2.03	1.03
Fe	1.51	0.55

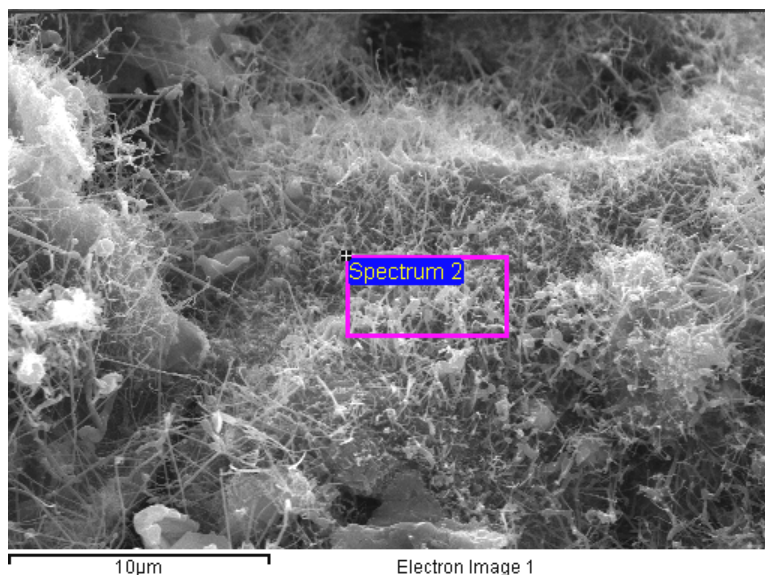


Figure C: SEM micrograph for Region B of the standard atmosphere synthesized 19.44% aluminum stoichiometry utilizing JSC-1AF simulant with the region of EDS highlighted.

Table XXXV: EDS Analysis of Spectrum 2 shown in Figure C

Element	Weight%	Atomic%
O	47.29	60.73
Na	0.98	0.88
Mg	4.60	3.89
Al	37.29	28.40
Si	5.88	4.30
Ca	2.34	1.20
Fe	1.62	0.59

The microstructures of the reaction product for Region C and Region D of a JSC-1AF reaction product utilizing a 19.44% Al stoichiometry are shown in Figure CI and Figure CII. Table XXXVI and Table XXXVII show the chemical data obtained from analysis of Spectrum 3 and Spectrum 1, respectively. Both Spectra are located on regions which appear to have been melted. Chemical analysis indicated high concentrations of aluminum, silicon, and oxygen. Sodium and potassium were present in both analyses, the presence of which could have lowered the temperature necessary for melting if the region was composed of glass.

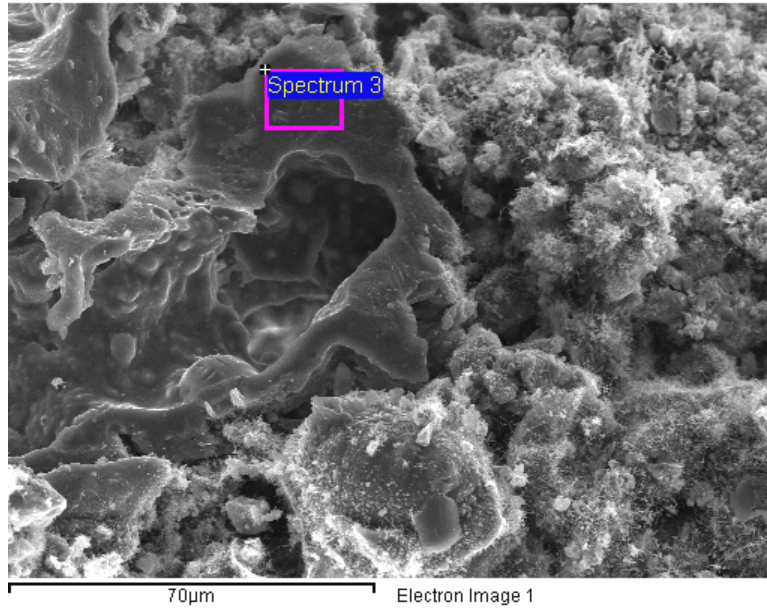


Figure CI: SEM micrograph for Region C of the standard atmosphere synthesized 19.44% aluminum stoichiometry utilizing JSC-1AF simulant with the region of EDS highlighted.

Table XXXVI: EDS Analysis of Spectrum 3 shown in Figure CI

Element	Weight%	Atomic%
O	41.77	56.56
Na	3.25	3.06
Mg	2.78	2.48
Al	24.08	19.33
Si	17.47	13.48
K	0.76	0.42
Ca	5.22	2.82
Ti	0.61	0.28
Fe	4.04	1.57

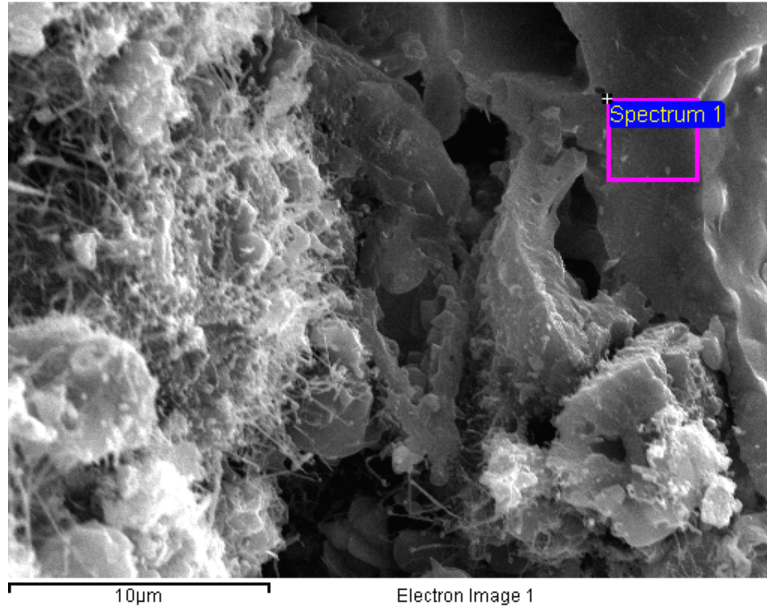


Figure CII: SEM micrograph for Region D of the standard atmosphere synthesized 19.44% aluminum stoichiometry utilizing JSC-1AF simulant with the region of EDS highlighted.

Table XXXVII: EDS Analysis of Spectrum 1 shown in Figure CII

Element	Weight%	Atomic%
O	31.15	45.32
Na	1.80	1.82
Mg	3.89	3.73
Al	32.15	27.73
Si	15.08	12.49
K	0.89	0.53
Ca	12.88	7.48
Fe	2.16	0.90

The microstructures of the reaction product for Region E, F, and G of a JSC-1AF reaction product utilizing a 19.44% Al stoichiometry are shown in Figure CIII, Figure CIV, and Figure CV, respectively. Table XXXVIII, Table XXXIX, and Table XL show the chemical data obtained from analysis of Spectra 2, 1, and 2, respectively. All spectra are located on clusters of whiskers that likely formed through a chemical reaction involving a vapor phase due to the small whisker diameters and the spherical shapes terminating many of the whiskers. Chemical analysis indicated high concentrations of aluminum, oxygen, and nitrogen within all the spectra. Silicon is also present in varying quantities. The chemical analysis data likely indicate that the whiskers are composed of phases of aluminum nitride, aluminum oxynitride, and/or aluminum oxide. The

data also indicate that there is some silicon in the whiskers, as seen in areas of whiskers in earlier micrographs.

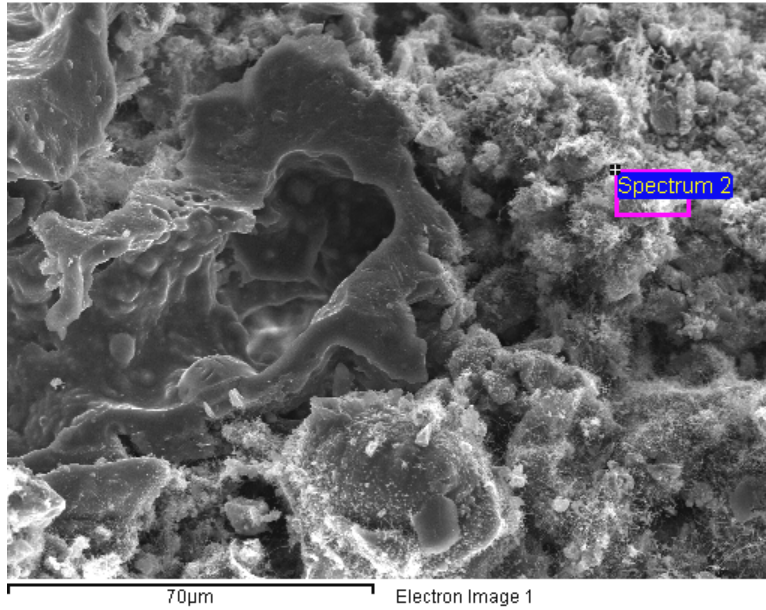


Figure CIII: SEM micrograph for Region E of the standard atmosphere synthesized 19.44% aluminum stoichiometry utilizing JSC-1AF simulant with the region of EDS highlighted.

Table XXXVIII: EDS Analysis of Spectrum 2 shown in Figure CIII

Element	Weight%	Atomic%
N	20.16	27.57
O	33.52	40.12
Na	0.77	0.64
Mg	0.43	0.34
Al	34.44	24.45
Si	9.29	6.33
Ca	0.49	0.24
Fe	0.92	0.32

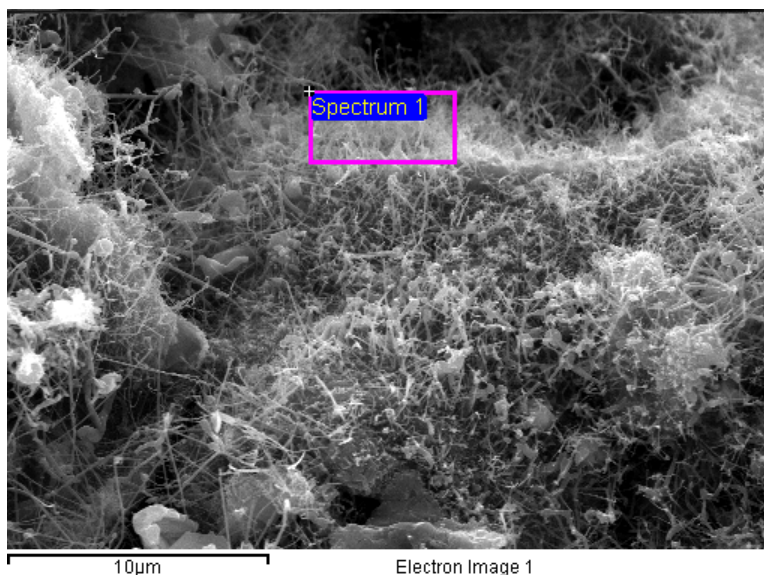


Figure CIV: SEM micrograph for Region F of the standard atmosphere synthesized 19.44% aluminum stoichiometry utilizing JSC-1AF simulant with the region of EDS highlighted.

Table XXXIX: EDS Analysis of Spectrum 1 shown in Figure CIV

Element	Weight%	Atomic%
N	8.91	12.33
O	46.82	56.74
Na	0.99	0.84
Mg	1.97	1.57
Al	32.43	23.30
Si	5.66	3.91
Ca	1.37	0.67
Fe	1.85	0.64

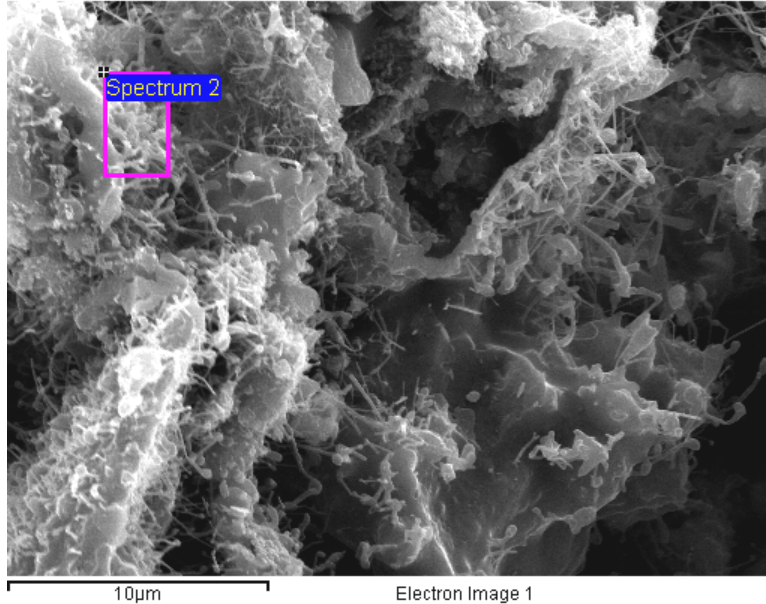


Figure CV: SEM micrograph for Region G of the standard atmosphere synthesized 19.44% aluminum stoichiometry utilizing JSC-1AF simulant with the region of EDS highlighted.

Table XL: EDS Analysis of Spectrum 2 shown in Figure CV

Element	Weight%	Atomic%
N	15.02	21.54
O	32.62	40.94
Na	1.39	1.21
Mg	0.71	0.58
Al	29.89	22.25
Si	16.31	11.67
Ca	2.37	1.18
Fe	1.71	0.61

24.45% Al by weight

Figure CVI shows the reaction product utilizing a 24.45% Al stoichiometry at 50kx magnification. Figure CVI shows the presence of nano-scale whiskers, with the diameters of selected whiskers labeled. Measured whiskers range in diameter from 39 – 60 nm. Many of the whiskers terminate in a spherical shape.

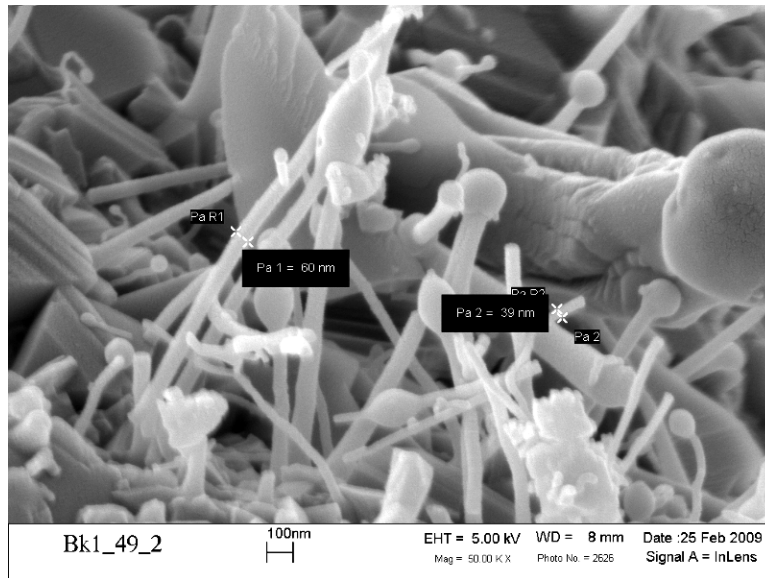


Figure CVI: SEM micrograph of the standard atmosphere synthesized 24.45% aluminum stoichiometry utilizing JSC-1AF simulant at 50kx.

EDS

Region A

The microstructure of the reaction product for Region A of a JSC-1AF reaction product utilizing a 24.45% Al stoichiometry is shown in Figure CVII, as are EDS Spectra 1, 2, and 3. Table XLI shows the chemical data obtained from analysis of Spectrum 1, 2, and 3. Numerous whiskers are observed emanating from particle surfaces and terminating with a spherical shape. Chemical analysis of regions abundant with whiskers (Spectra 1 and 3) indicated high aluminum and oxygen content, along with significant magnesium, and some silicon. Spectrum 2 is located on a particle surface and has slightly less aluminum and magnesium, more calcium, and both sodium and potassium are present. Chemical analysis indicates that the primary components of the whiskers observed in this region are magnesium, aluminum, oxygen, and possibly silicon. It is possible that the whiskers are composed of $Mg_{0.338}Al_{2.408}O_4$ and aluminum oxide. Spectrum 2 may be composed of grossite, spinel, corundum, and reduced silicon.

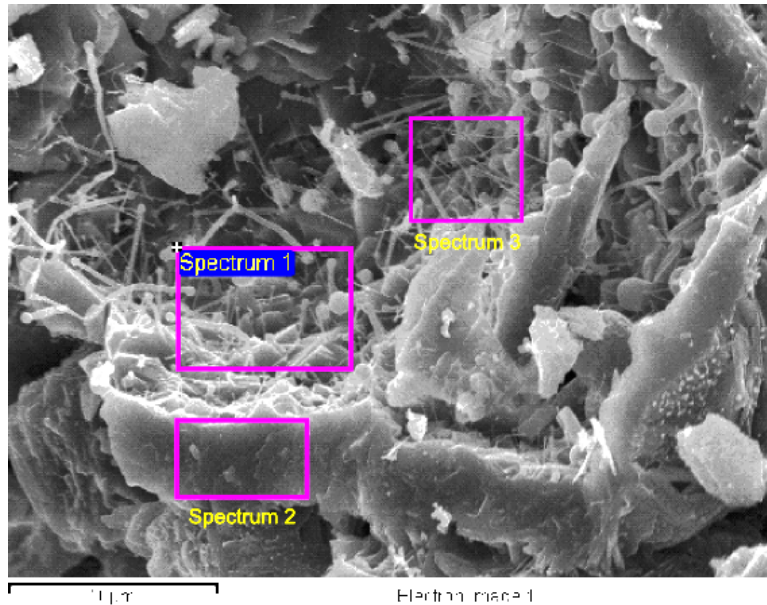


Figure CVII: SEM micrograph of the microstructure in Region A for the 24.45% aluminum stoichiometry with the regions of EDS highlighted.

Table XLI: EDS Analysis of Spectra 1, 2, and 3 shown in Figure CVII

Element	Spectrum 1		Spectrum 2		Spectrum 3	
	Weight%	Atomic%	Weight%	Atomic%	Weight%	Atomic%
O	48.35	61.43	44.93	58.41	35.81	49.07
Na	-	-	1.39	1.26	-	-
Mg	10.27	8.59	6.89	5.90	10.09	9.10
Al	33.36	25.14	35.14	27.09	42.65	34.65
Si	4.71	3.41	5.83	4.32	5.84	4.55
K	-	-	0.54	0.29	-	-
Ca	1.38	0.70	5.29	2.75	2.72	1.49
Ti	0.41	0.17	-	-	-	-
Fe	1.54	0.56	-	-	2.89	1.13

Region B

The microstructure of the reaction product for Region B of a JSC-1AF reaction product utilizing a 24.45% Al stoichiometry is shown in Figure CVIII, as are EDS Spectra 1 and 2. Table XLII shows the chemical data obtained from analysis of Spectrum 1 and 2. As in Region A, numerous whiskers are observed emanating from particle surfaces and many of them terminate with a spherical shape. Chemical analysis of Spectrum 1, which contains no whiskers, indicated high silicon and oxygen content, along with some aluminum. Spectrum 2 encompasses a region with large quantities of whiskers and has large amounts of aluminum and oxygen along

with significant nitrogen. Within Region B it appears that the primary components of the whiskers are aluminum, nitrogen, and oxygen. It is likely that the whiskers in this region are composed of aluminum nitride, aluminum oxynitride, and/or aluminum oxide. Formation of aluminum nitrides, aluminum oxynitrides, and/or aluminum oxides could occur by evolution of Al_2O gas during the reaction and subsequent reaction with ambient nitrogen and oxygen. When compared with other aluminum stoichiometries, the XRD pattern for the 24.45% aluminum stoichiometry had distinctly lower peak intensities for aluminum nitrides. The XRD data appears to correlate with EDS data which shows relative low quantities of aluminum nitride whiskers when compared with other stoichiometries. It is also possible that formation of $\text{Mg}_{0.338}\text{Al}_{2.408}\text{O}_4$ whiskers is preferred in the 24.45% Al stoichiometry.

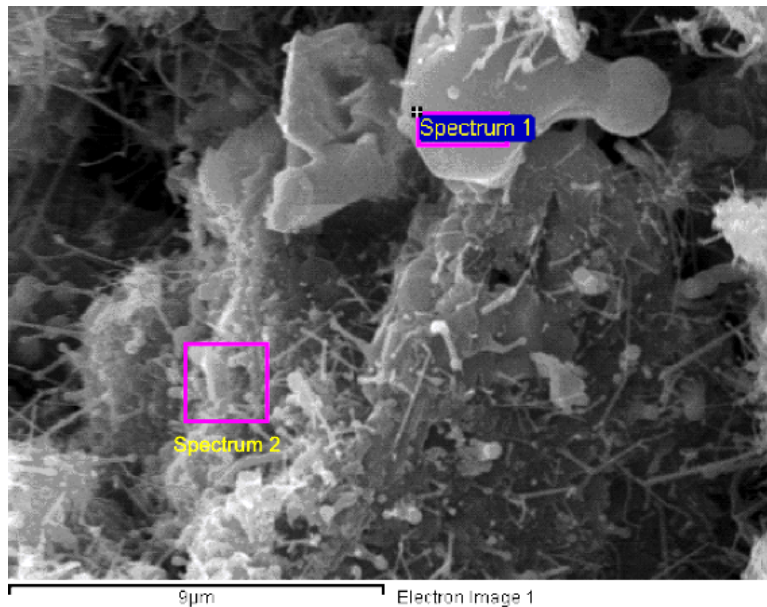


Figure CVIII: SEM micrograph of the microstructure in Region B for the 24.45% aluminum stoichiometry with the regions of EDS highlighted.

Table XLII: EDS Analysis of Spectra 1 and 2 shown in Figure CVIII

Element	Spectrum 1		Spectrum 2	
	Weight%	Atomic%	Weight%	Atomic%
N	-	-	11.11	15.88
O	18.73	29.10	39.08	48.93
Na	0.52	0.57	1.45	1.26
Mg	-	-	1.26	1.04
Al	11.72	10.80	34.42	25.55
Si	64.71	57.27	5.64	4.02
K	-	-	0.30	0.16
Ca	1.70	1.06	5.19	2.60
Ti	0.56	0.29	-	-
Fe	2.05	0.91	1.54	0.55

28.85% Al by weight

Figure CIX and Figure CX show the reaction product utilizing a 28.85% Al stoichiometry at 50kx and 200kx magnifications, respectively. Figure CIX and Figure CX show the presence of nano-scale whiskers, with the diameters of selected whiskers labeled. Measured whiskers range in diameter from 35 – 131 nm. Many of the whiskers are observed to terminate in spherical shapes, possibly indicating a vaporization process occurred.

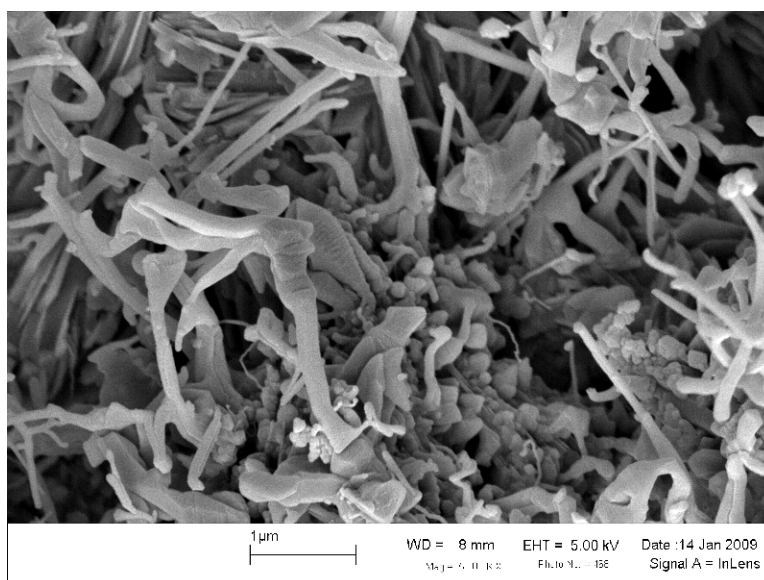


Figure CIX: SEM micrograph of the standard atmosphere synthesized 28.85% aluminum stoichiometry utilizing JSC-1AF simulant at 50kx.

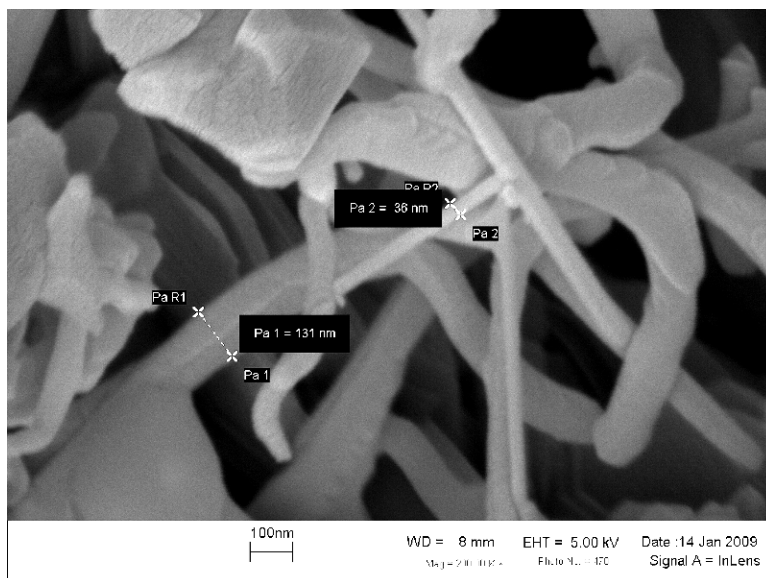


Figure CX: SEM micrograph of the standard atmosphere synthesized 28.85% aluminum stoichiometry utilizing JSC-1AF simulant at 200kx.

EDS

Region A

The microstructure of the reaction product for Region A of a JSC-1AF reaction product utilizing a 28.85% Al stoichiometry is shown in Figure CXI, as are EDS Spectra 2 and 3. Table XLIII shows the chemical data obtained from analysis of Spectrum 2 and 3. Chemical analyses were performed on areas with large quantities of whiskers, denoted by Spectrum 2 and Spectrum 3. Both of these areas had over 20 at.% nitrogen, and had high concentrations of aluminum and oxygen. The increase in bound nitrogen for the 28.85% aluminum stoichiometry when compared with the 24.45% stoichiometry correlates with an increase in nitride peak intensity observed in the XRD pattern. The chemical analyses likely indicate that the whiskers in Spectrum 2 and 3 are composed of aluminum nitrides and aluminum oxynitrides.

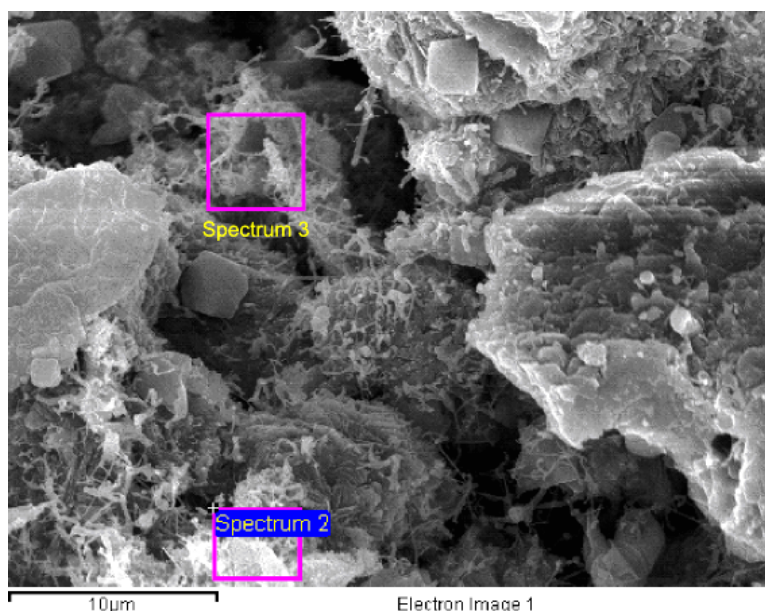


Figure CXI: SEM micrograph of the microstructure in Region A for the 28.85% aluminum stoichiometry with the regions of EDS highlighted.

Table XLIII: EDS Analysis of Spectra 2 and 3 shown in Figure CXI

Element	Spectrum 2		Spectrum 3	
	Weight%	Atomic%	Weight%	Atomic%
N	20.05	27.13	19.36	25.37
O	36.95	43.77	43.67	50.07
Na	-	-	0.43	0.35
Mg	1.60	1.25	2.09	1.58
Al	27.26	19.15	28.06	19.08
Si	11.31	7.63	3.88	2.53
Ca	0.88	0.41	1.61	0.74
Fe	1.95	0.66	0.89	0.29

Region B

The microstructure of the reaction product for Region B of a JSC-1AF reaction product utilizing a 28.85% Al stoichiometry is shown in Figure CXII, as is EDS Spectrum 2. Table XLIV shows the chemical data obtained from analysis of Spectrum 2. The region analyzed in Spectrum 2 appears to be a well-formed crystal having octahedral geometry. The region is rich in aluminum, silicon, and oxygen. Spectrum 2 also has trace amounts of magnesium, calcium, and iron. If the region was not reacted, it could be partially composed of the mineral augite. If

the region did react, spinel, grossite, corundum, iron silicides, and reduced silicon could be present.

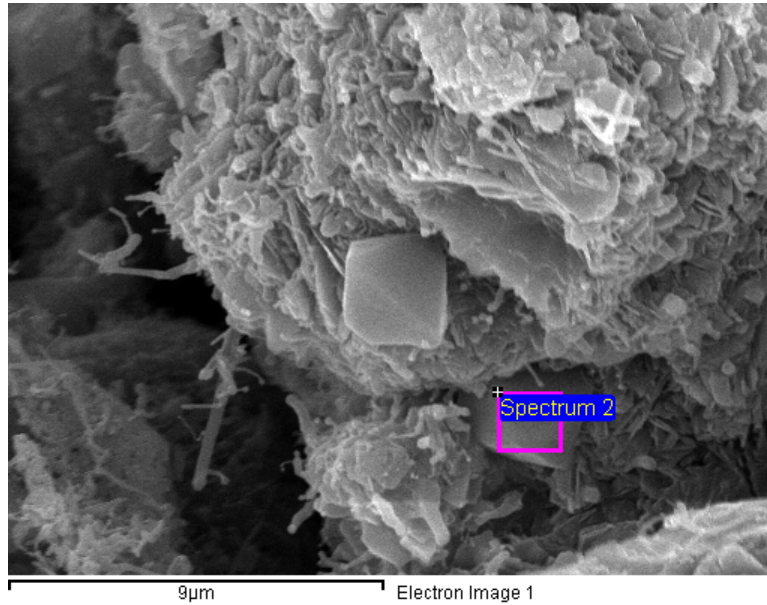


Figure CXII: SEM micrograph of the microstructure in Region B for the 28.85% aluminum stoichiometry with the region of EDS highlighted.

Table XLIV: EDS Analysis of Spectrum 2 shown in Figure CXII

Element	Weight%	Atomic%
O	38.48	53.62
Mg	3.10	2.85
Al	30.07	24.84
Si	16.10	12.78
Ca	6.55	3.64
Fe	5.70	2.27

33.33% Al by weight

Figure CXIII and Figure CXIV show the reaction product utilizing a 33.33% Al stoichiometry at 50kx and 200kx magnifications, respectively. Figure CXIII and Figure CXIV show the presence of nano-scale whiskers, with the diameters of selected whiskers labeled. Measured whiskers range in diameter from 34 – 115 nm. The small diameters of the whiskers

would likely indicate growth from vapor since the reactants had particle sizes on the order of microns.

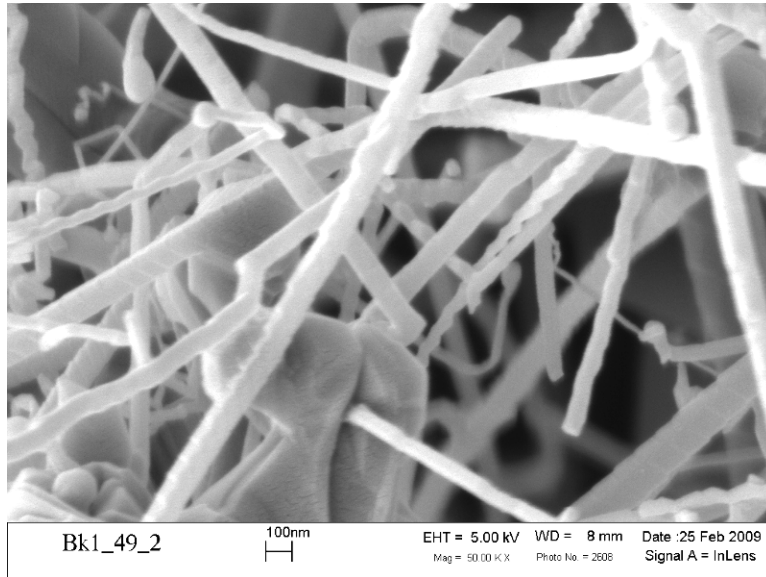


Figure CXIII: SEM micrograph of the standard atmosphere synthesized 33.33% aluminum stoichiometry utilizing JSC-1AF simulant at 50kx.

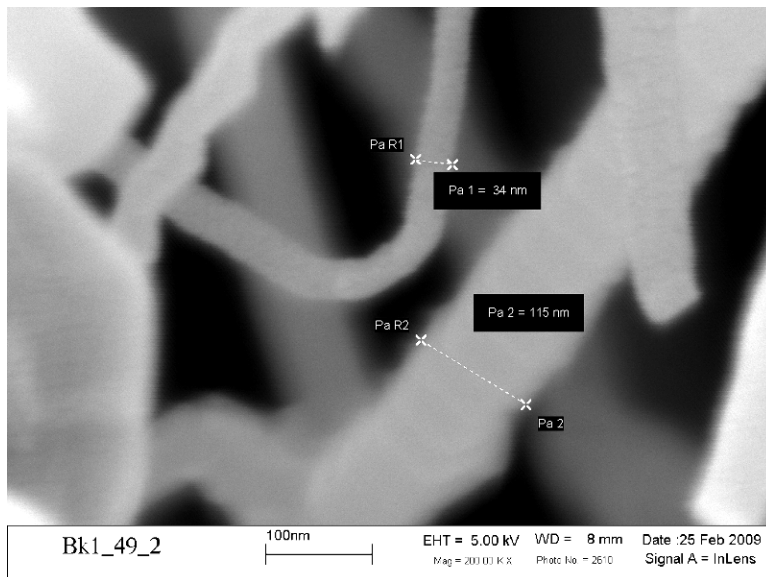


Figure CXIV: SEM micrograph of the standard atmosphere synthesized 33.33% aluminum stoichiometry utilizing JSC-1AF simulant at 200kx.

EDS

Region A

The microstructure of the reaction product for Region A of the JSC-1AF reaction product utilizing a 33.33% Al stoichiometry is shown in Figure CXV, as is EDS Spectrum 1. Table XLV shows the chemical data obtained from analysis of Spectrum 1. Spectrum 1 is located in a region with a high concentration of whiskers that likely formed through a chemical reaction involving a vapor phase due to the small whisker diameters and the spherical shapes terminating many of the whiskers. Chemical analysis of Spectrum 1 indicates the nitrogen content is around 20 at.%. Spectrum 1 also has high concentrations of aluminum and oxygen. It is likely that the region is composed of aluminum nitrides, aluminum oxynitrides, and/or aluminum oxides.

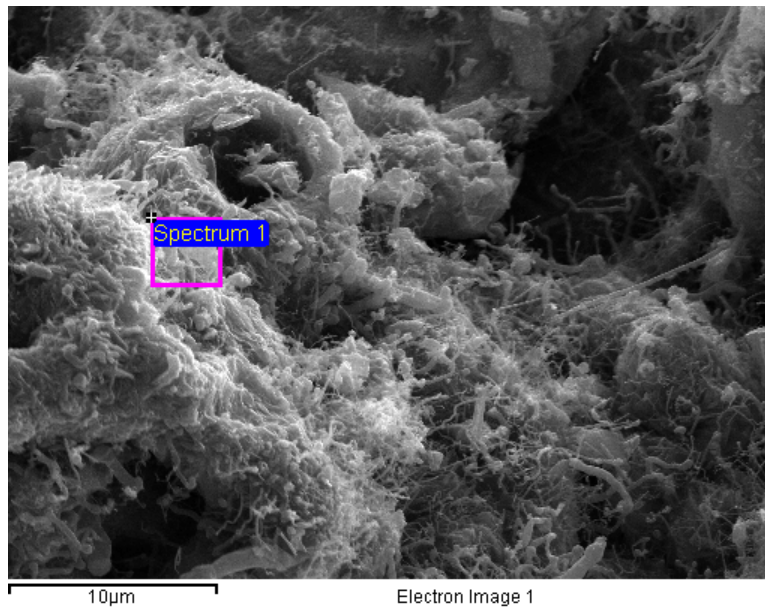


Figure CXV: SEM micrograph of the microstructure in Region A for the 33.33% aluminum stoichiometry with the region of EDS highlighted.

Table XLV: EDS Analysis of Spectrum 1 shown in Figure CXV

Element	Weight%	Atomic%
N	13.64	19.29
O	37.25	46.11
Na	0.67	0.58
Mg	1.63	1.33
Al	35.35	25.95
Si	6.18	4.36
K	0.33	0.16
Ca	3.35	1.65
Fe	1.62	0.58

The microstructure of the reaction product for Region B and Region C of the JSC-1AF reaction product utilizing a 33.33% Al stoichiometry is shown in Figure CXVI and Figure CXVII, respectively. Table XLVI and Table XLVII show the chemical data obtained from EDS analysis of the regions denoted in Figure CXVI and Figure CXVII, respectively. Both regions of EDS analysis are located around a large concentration of whiskers. Elemental analysis found the regions to have around 25 at.% nitrogen, along with high concentrations of aluminum and oxygen. The data from the chemical analysis of Regions A, B, and C indicate that the whiskers are likely to be composed of a phase of aluminum nitride and/or aluminum oxynitride.

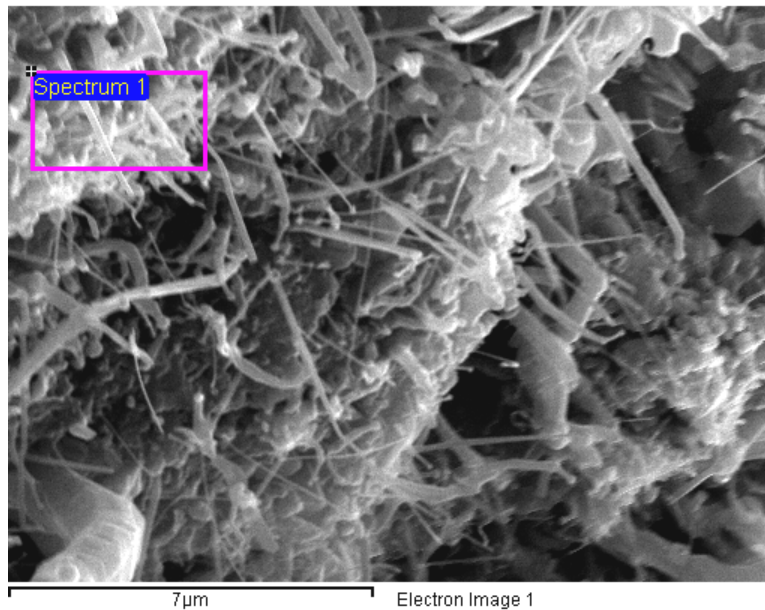


Figure CXVI: SEM micrograph of Region B for the standard atmosphere synthesized 33.33% aluminum stoichiometry utilizing JSC-1AF simulant with the region of EDS highlighted.

Table XLVI: EDS Analysis of Spectrum 1 shown in Figure CXVI

Element	Weight%	Atomic%
N	15.78	24.99
O	13.95	19.34
Mg	3.06	2.80
Al	55.64	45.74
Si	4.86	3.84
Ca	4.07	2.25
Fe	2.63	1.05

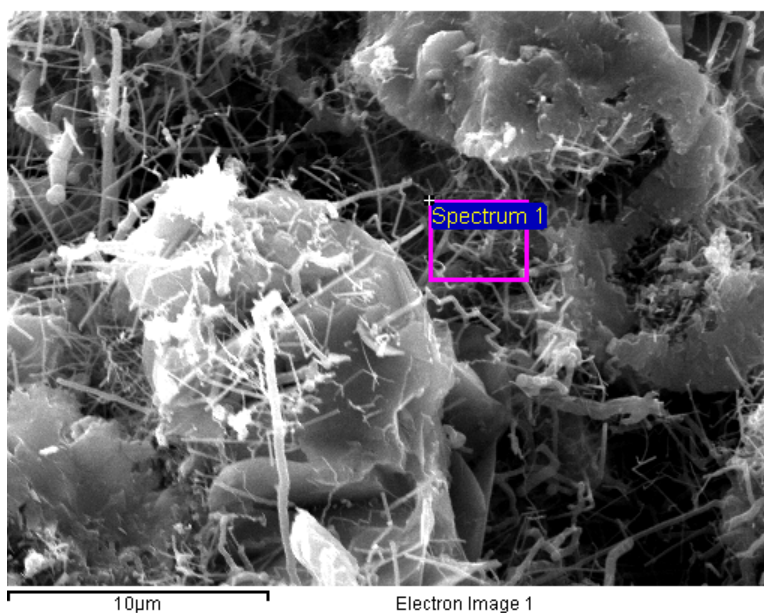


Figure CXVII: SEM micrograph of Region C for the standard atmosphere synthesized 33.33% aluminum stoichiometry utilizing JSC-1AF simulant with the region of EDS highlighted.

Table XLVII: EDS Analysis of Spectrum 1 shown in Figure CXVII

Element	Weight%	Atomic%
N	18.70	27.63
O	22.65	29.30
Mg	2.63	2.24
Al	46.68	35.80
Si	2.68	1.98
Ca	4.03	2.08
Fe	2.63	0.97

The microstructure of the reaction product for Region D of the JSC-1AF reaction product utilizing a 33.33% Al stoichiometry is shown in Figure CXVIII. Table XLVIII shows the

chemical data obtained from analysis of Spectrum 2 and Spectrum 3, denoted in Figure CXVIII. Spectrum 2 is located on a fairly flat particle and has high concentrations of aluminum, silicon, and oxygen. The data from Spectrum 2 indicate that the region is composed of corundum, grossite, reduced silicon, and iron silicides. Spectrum 3 is located on a large whisker that likely formed through a chemical reaction involving a vapor phase due to the small whisker diameter. Elemental analysis found Spectrum 3 to have around 35 at.% nitrogen, along with concentrations of aluminum and oxygen around 30 at.%. The data from Spectrum 3 likely indicate that the whisker is primarily composed of aluminum nitride, aluminum oxynitride, and/or aluminum oxide.

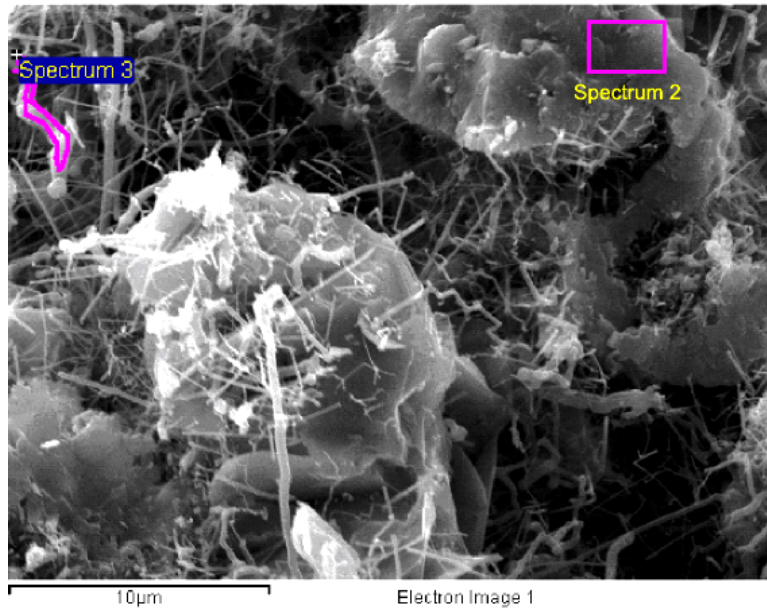


Figure CXVIII: SEM micrograph of Region D for the standard atmosphere synthesized 33.33% aluminum stoichiometry utilizing JSC-1AF simulant with the regions of EDS highlighted.

Table XLVIII: EDS Analysis of Spectra 2 and 3 shown in Figure CXVIII

Element	Spectrum 2		Spectrum 3	
	Weight%	Atomic%	Weight%	Atomic%
N	-	-	25.70	35.31
O	31.79	47.53	25.09	30.19
Mg	0.93	0.91	1.91	1.51
Al	34.25	30.36	42.60	30.39
Si	14.19	12.09	2.37	1.63
Ca	5.38	3.21	1.25	0.60
Ti	1.68	0.83	-	-
Fe	11.79	5.05	1.08	0.37

The microstructure of the reaction product for Region E of the JSC-1AF reaction product utilizing a 33.33% Al stoichiometry is shown in Figure CXIX. Table XLIX shows the chemical data obtained from analysis of Spectrum 1 and Spectrum 2, denoted in Figure CXIX. Spectrum 1 is located on a large whisker. Elemental analysis found the region to have around 35 at.% nitrogen, along with concentrations of aluminum and oxygen around 30 at.%. The data from Spectrum 1 likely indicate that the whisker is composed of aluminum nitrides, aluminum oxynitrides, and/or aluminum oxides. Spectrum 2 is located on a fairly flat particle and has high concentrations of aluminum and oxygen. Spectrum 2 also has some silicon, magnesium, and calcium present. It is likely that Spectrum 2 is composed of corundum, spinel, and grossite.



Figure CXIX: SEM micrograph of Region E for the standard atmosphere synthesized 33.33% aluminum stoichiometry utilizing JSC-1AF simulant with the regions of EDS highlighted.

Table XLIX: EDS Analysis of Spectra 1 and 2 shown in Figure CXIX

Element	Spectrum 1		Spectrum 2	
	Weight%	Atomic%	Weight%	Atomic%
N	24.94	34.90	-	-
O	23.10	28.31	39.77	53.85
Mg	2.02	1.63	2.67	2.38
Al	43.77	31.80	44.21	35.50
Si	2.62	1.83	5.16	3.98
Ca	2.00	0.98	7.33	3.96
Fe	1.53	0.54	0.85	0.33

Nanostructures and Elemental Analysis within the Reaction Product of a Standard Atmosphere SHS Reaction Utilizing JSC-1A Regolith Simulant

19.44% Al by weight

Figure CXX and Figure CXXI show the reaction product utilizing a 19.44% Al stoichiometry at 50kx and 200kx magnifications, respectively. Figure CXX and Figure CXXI show the presence of nano-scale whiskers ranging from ~20 nm to 100 nm in diameter. Figure CXX shows the whiskers growing off the surface of a particle. The abundance of spherical particles near the large particle surface may indicate whisker growth by the VLS mechanism and possibly Al₂O gas evolution. Many of the whiskers are observed to terminate in spherical shapes.

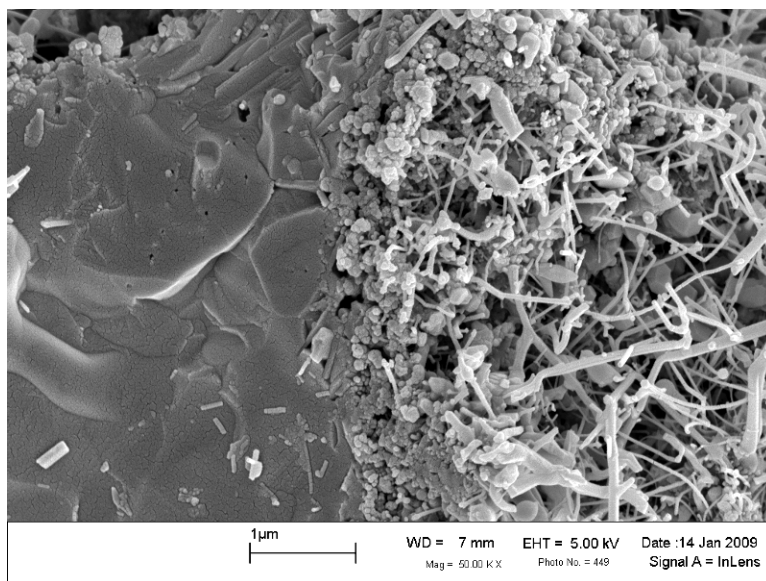


Figure CXX: SEM micrograph of the standard atmosphere synthesized 19.44% aluminum stoichiometry utilizing JSC-1A simulant at 50kx.

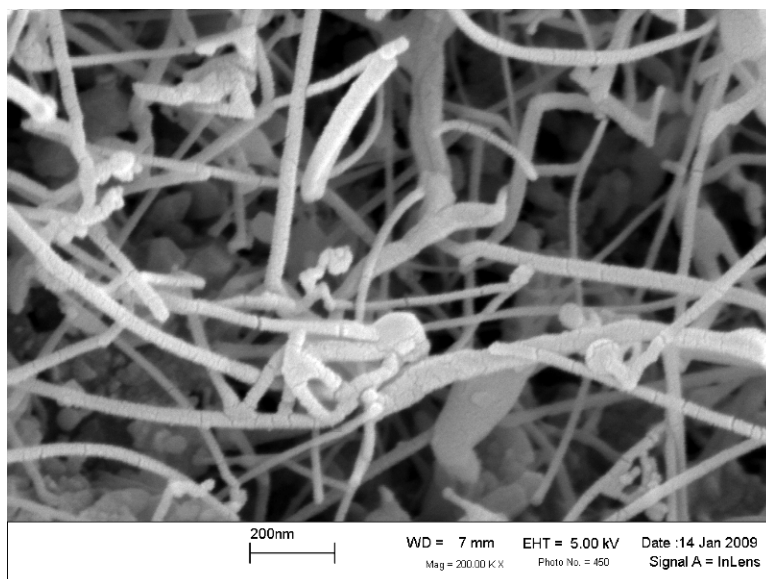


Figure CXXI: SEM micrograph of the standard atmosphere synthesized 19.44% aluminum stoichiometry utilizing JSC-1A simulant at 200kx.

EDS

Region A

The microstructure of the reaction product for Region A of a JSC-1A reaction product utilizing a 19.44% Al stoichiometry is shown in Figure CXXII, as are EDS Spectra 1, 2, and 3. Table L shows the chemical data obtained from analysis of Spectrum 1, 2, and 3. Spectrum 1 is located in a region with a high concentration of whiskers. Chemical analysis of Spectrum 1 indicates that no nitrogen is present. The area has high concentrations of silicon, aluminum, and oxygen. There is also some magnesium present in Spectrum 1. It is possible that the whiskers are composed of aluminum oxide and $\text{Mg}_{0.388}\text{Al}_{2.408}\text{O}_4$. Spectrum 2 is located on a smooth region that does not appear to have whiskers emanating from it. Elemental abundance analysis indicates the region is composed primarily of aluminum and oxygen, the region also contains roughly equivalent amounts of silicon, calcium, magnesium, and iron. Data from Spectrum 2 indicate that it is likely composed of grossite, spinel, corundum, and iron silicides. Spectrum 3 is located near the interface of the smooth region and the regions with the whisker networks. Spectrum 3 contains whiskers and the smoother surface. Elemental abundance indicates that no nitrogen is present. Spectrum 3 is composed primarily of aluminum and oxygen, and contains roughly equivalent amounts of magnesium and silicon. Spectrum 3 is probably composed of the same chemical species as Spectrum 1, aluminum oxide and $\text{Mg}_{0.388}\text{Al}_{2.408}\text{O}_4$.

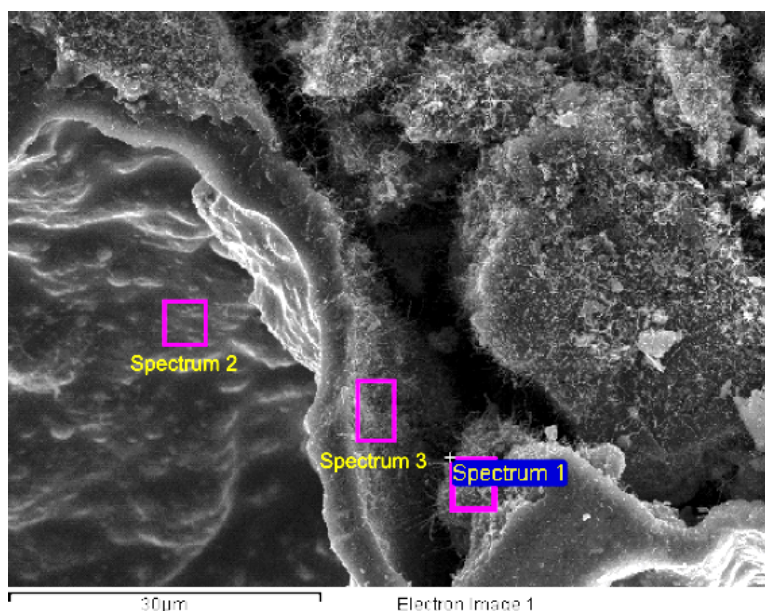


Figure CXXII: SEM micrograph of the microstructure in Region A for the 19.44% aluminum stoichiometry, with the regions of EDS highlighted.

Table L: EDS Analysis of Spectra 1, 2, and 3 shown in Figure CXXII

Element	Spectrum 1		Spectrum 2		Spectrum 3	
	Weight%	Atomic%	Weight%	Atomic%	Weight%	Atomic%
O	35.65	49.34	41.32	58.36	35.95	49.33
Na	0.71	0.69	-	-	-	-
Mg	5.02	4.57	5.52	5.13	5.56	5.02
Al	38.28	31.42	22.41	18.77	45.39	36.93
Si	14.20	11.19	9.53	7.66	8.30	6.48
Ca	2.05	1.14	9.37	5.28	2.22	1.22
Ti	0.51	0.24	-	-	-	-
Fe	3.58	1.42	11.85	4.79	2.58	1.01

Region B

The microstructure of the reaction product for Region B of a JSC-1A reaction product utilizing a 19.44% Al stoichiometry is shown in Figure CXXIII, as are EDS Spectra 1 and 2. Many spherical particles are observed around the interface between the particle and the whisker networks. The spherical particles may be evidence of gas evolution, possibly Al_2O_3 . Table LI shows the chemical data obtained from analysis of Spectrum 1 and 2. Spectrum 1 contains a smooth microstructure, likely indicative of melting, without any whiskers. The chemical composition is primarily aluminum and oxygen, the region also has significant calcium and

silicon. Spectrum 1 also has some magnesium. EDS data likely indicate that Spectrum 1 is composed of spinel, grossite, corundum, and reduced silicon. Spectrum 2 is located in a network of whiskers, most of which terminate in spherical shapes. Elemental analysis indicates that Spectrum 2 has over 25 at.% nitrogen, and contains large amounts of aluminum and oxygen. Spectrum 2 also contains significant silicon content. It is likely that the region is composed of aluminum nitrides, aluminum oxynitrides, and/or aluminum oxides.

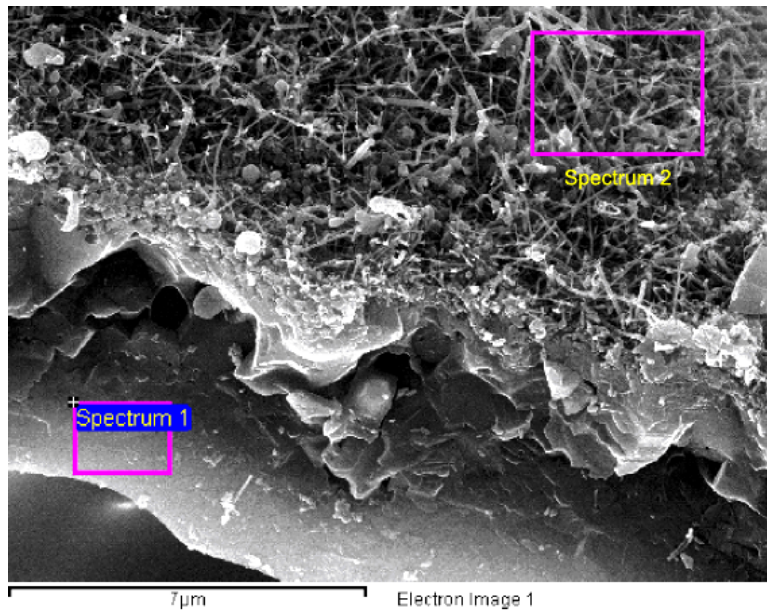


Figure CXXIII: SEM micrograph of the microstructure in Region B for the 19.44% aluminum stoichiometry with the regions of EDS highlighted.

Table LI: EDS Analysis of Spectra 1 and 2 shown in Figure CXXIII

Element	Spectrum 1		Spectrum 2	
	Weight%	Atomic%	Weight%	Atomic%
N	-	-	18.30	26.56
O	33.96	48.98	26.37	33.49
Na	1.46	1.46	0.58	0.52
Mg	4.87	4.62	0.87	0.72
Al	29.85	25.53	38.40	28.92
Si	10.79	8.87	11.16	8.08
Ca	16.39	9.43	0.75	0.38
Ti	-	-	0.48	0.20
Fe	2.69	1.11	3.09	1.13

24.45% Al by weight

Figure CXXIV and Figure CXXV show the reaction product utilizing a 24.45% Al stoichiometry at 50kx and 200kx magnifications, respectively. Figure CXXIV and Figure CXXV show the presence of nano-scale whiskers, with the diameters of selected whiskers labeled. Measured whiskers range in diameter from 21-106 nm. Some of the whiskers are observed to terminate in spherical shapes. Figure CXXV appears to have multiple single crystal “steps” incorporated into some of the whiskers.

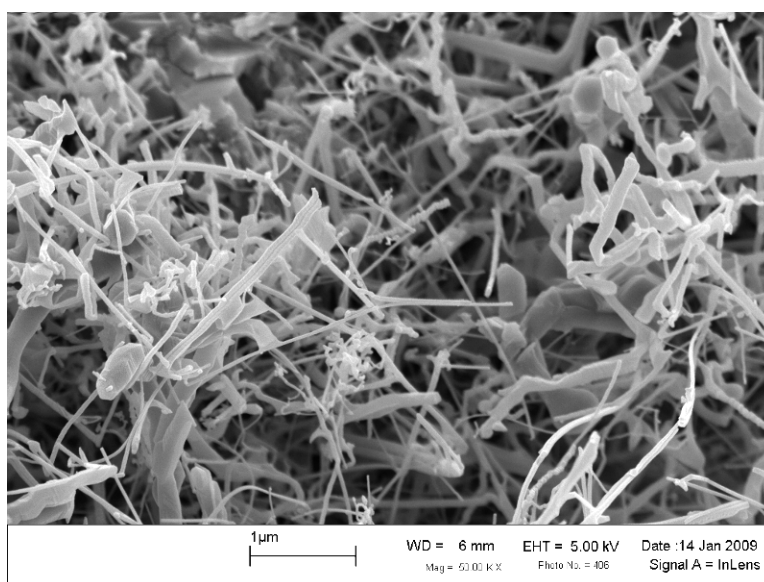


Figure CXXIV: SEM micrograph of the standard atmosphere synthesized 24.45% aluminum stoichiometry utilizing JSC-1A simulant at 50kx.

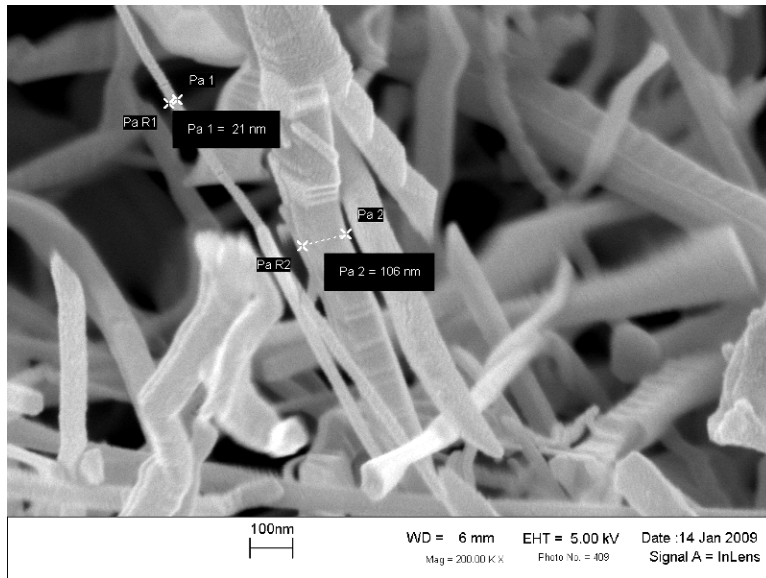


Figure CXXV: SEM micrograph of the standard atmosphere synthesized 24.45% aluminum stoichiometry utilizing JSC-1A simulant at 200kx.

EDS

Region A

The microstructure of the reaction product for Region A of a JSC-1A reaction product utilizing a 24.45% Al stoichiometry is shown in Figure CXXVI, as are EDS Spectra 1 and 3. Table LII shows the chemical data obtained from analysis of Spectrum 1 and 3. Spectrum 1 is located on a smooth surface of a particle, with no whiskers in the vicinity. The elemental composition is primarily aluminum and oxygen, with some silicon. EDS data likely indicate that Spectrum 1 is composed of corundum and grossite. Spectrum 3 is located on a region of whiskers. The elemental composition is primarily aluminum and oxygen, with over 20 at.% nitrogen. The elemental composition indicates that the whiskers are likely to be composed of chemical species of aluminum nitride, aluminum oxynitride, and/or aluminum oxide.

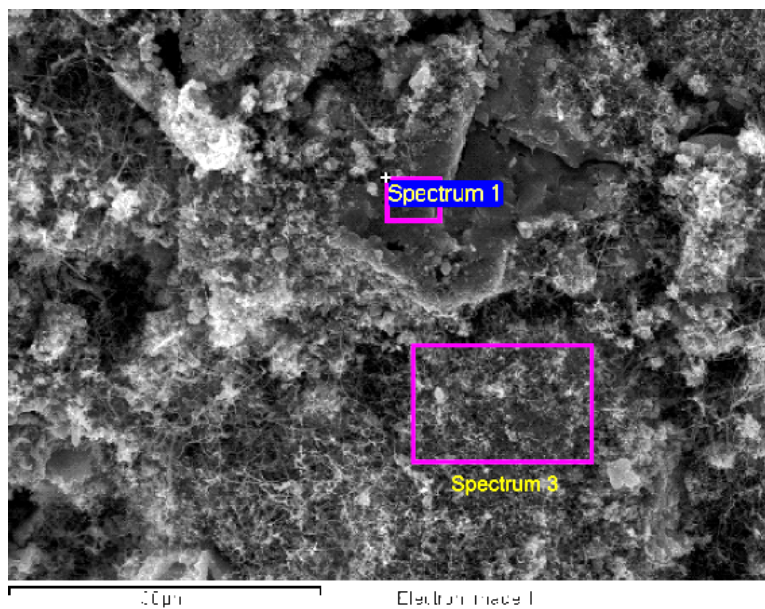


Figure CXXVI: SEM micrograph of the microstructure in Region A for the 24.45% aluminum stoichiometry, with the regions of EDS highlighted.

Table LII: EDS Analysis of Spectra 1 and 3 shown in Figure CXXVI

Element	Spectrum 1		Spectrum 3	
	Weight%	Atomic%	Weight%	Atomic%
N	-	-	14.09	20.96
O	45.09	59.36	25.95	33.80
Mg	0.54	0.46	1.12	0.96
Al	37.33	29.14	52.94	40.88
Si	10.05	7.54	2.29	1.70
Ca	5.81	3.05	2.41	1.25
Fe	1.19	0.45	1.19	0.44

Region B

The microstructure of the reaction product for Region B of a JSC-1A reaction product utilizing a 24.45% Al stoichiometry is shown in Figure CXXVII, as are EDS Spectra 1 and 2. Table LIII shows the chemical data obtained from analysis of Spectrum 1 and 2. Spectrum 1 and 2 are both located on networks of whiskers. The elemental analysis of both regions are roughly equivalent, being composed primarily of aluminum and oxygen, and having over 30 at.% nitrogen. The compositions of the regions indicate that they are likely to be composed primarily of aluminum nitride. Figure CXXVII is a good example of the formation of whisker networks between particles.

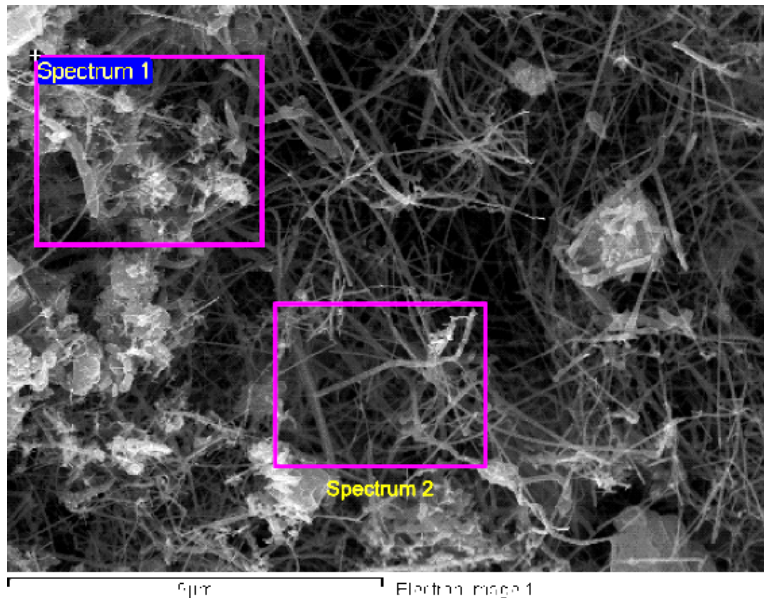


Figure CXXVII: SEM micrograph of the microstructure in Region B for the 24.45% aluminum stoichiometry with the regions of EDS highlighted.

Table LIII: EDS Analysis of Spectra 1 and 2 shown in Figure CXXVII

Element	Spectrum 1		Spectrum 2	
	Weight%	Atomic%	Weight%	Atomic%
N	19.34	30.31	22.12	33.47
O	9.55	13.10	11.57	15.32
Mg	-	-	1.28	1.12
Al	64.35	52.34	55.11	43.29
Si	3.77	2.94	8.09	6.11
Ca	0.81	0.44	-	-
Fe	2.18	0.86	1.82	0.69

28.85% Al by weight

Figure CXXVIII and Figure CXXIX show the reaction product utilizing a 28.85% Al stoichiometry at 50kx and 200kx magnifications, respectively. Figure CXXVIII and Figure CXXIX show the presence of nano-scale whiskers of many different diameters, with the diameters of selected whiskers labeled. Measured whiskers range in diameter from 31-56 nm. The whiskers in the 28.85% stoichiometry appear more dendritic and branched in morphology than other stoichiometries. Some of the whiskers are observed to terminate in spherical shapes.

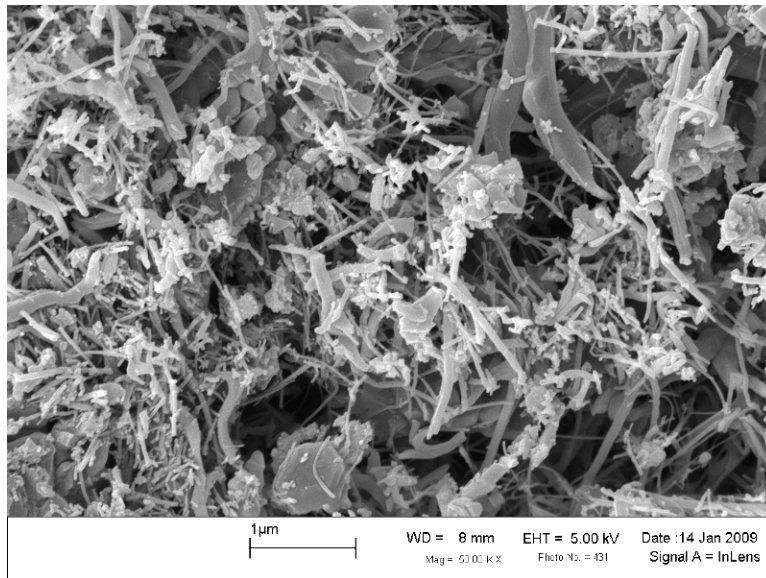


Figure CXXVIII: SEM micrograph of the standard atmosphere synthesized 28.85% aluminum stoichiometry utilizing JSC-1A simulant at 50kx.

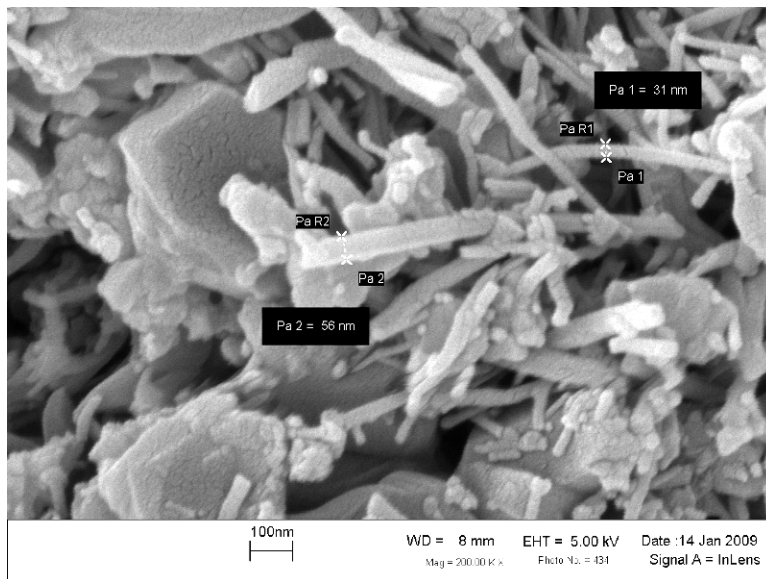


Figure CXXIX: SEM micrograph of the standard atmosphere synthesized 28.85% aluminum stoichiometry utilizing JSC-1A simulant at 200kx.

EDS

Region A

The microstructure of the reaction product for Region A of a JSC-1A reaction product utilizing a 28.85% Al stoichiometry is shown in Figure CXXX, as are EDS Spectra 1, 2, and 3. Table LIV shows the chemical data obtained from analysis of Spectrum 1, 2, and 3. Spectrum 1 is located on a particle that appears to have a fairly flat surface. Elemental analysis indicates that the particle has over 40 at.% nitrogen, and large amounts of aluminum and oxygen. It is likely that the particle consists of aluminum nitrides, aluminum oxynitrides, and/or aluminum oxides. Spectrum 2 is located on a region with a high concentration of small diameter whiskers. Elemental analysis indicates that the area has over 25 at.% nitrogen, along with substantial aluminum and oxygen. The area of Spectrum 3 has larger diameter whiskers than Spectrum 2. Analysis indicates that Spectrum 3 has over 25 at.% nitrogen, with high concentrations of aluminum and oxygen. Spectra 2 and 3 are likely to be composed of chemical species of aluminum nitride, aluminum oxynitride, and/or aluminum oxides.

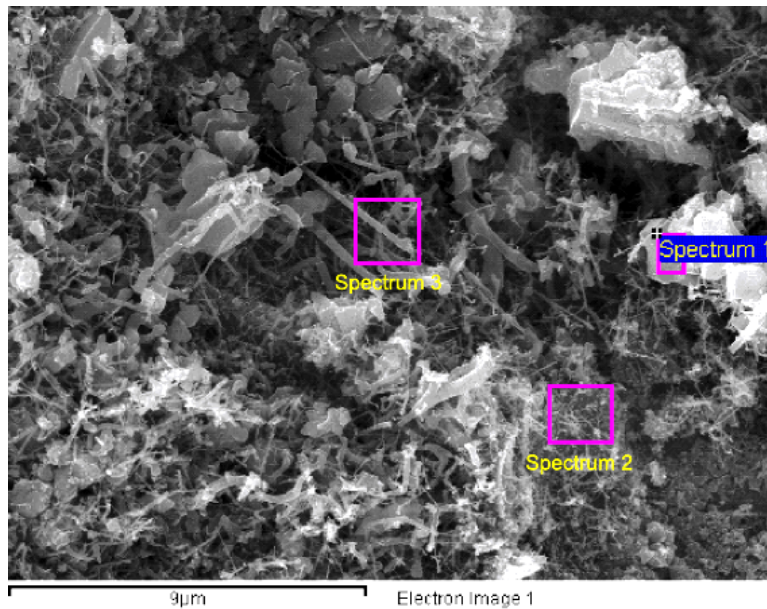


Figure CXXX: SEM micrograph of the microstructure in Region A for the 28.85% aluminum stoichiometry with the regions of EDS highlighted.

Table LIV: EDS Analysis of Spectra 1, 2, and 3 shown in Figure CXXX

Element	Spectrum 1		Spectrum 2		Spectrum 3	
	Weight%	Atomic%	Weight%	Atomic%	Weight%	Atomic%
N	31.89	42.09	21.56	28.81	18.89	25.76
O	24.57	28.40	36.50	42.72	35.79	42.72
Mg	0.42	0.32	0.53	0.41	-	-
Al	39.14	26.82	36.21	25.13	41.65	29.48
Si	3.23	2.12	3.48	2.32	2.31	1.57
Ca	-	-	0.27	0.13	-	-
Fe	0.75	0.25	1.45	0.49	1.37	0.47

Whiskers were observed in all reaction products synthesized in ambient conditions. Two types of whiskers were observed during EDS analyses. Type I whiskers had significant quantities of aluminum and nitrogen, along with some oxygen. Type I whiskers were likely to be composed primarily of aluminum nitride and aluminum oxynitride. Type II whiskers had significant aluminum and oxygen, and no nitrogen. Magnesium was sometimes present within Type II whiskers. Type II whiskers were likely to be composed of aluminum oxide and possibly $Mg_{0.388}Al_{2.408}O_4$. Silicon appeared to be present in small quantities in most Type I and Type II whiskers.

Most of the whiskers were observed to terminate in spherical shapes. The termination of whiskers in a spherical shape would indicate that growth occurred by the VLS mechanism. Growth by the VLS mechanism would indicate that a liquid phase was present at the whisker tip, creating a preferential deposition surface for gas molecules. Precipitation from the super-saturated liquid phase would have caused whisker growth at the solid-liquid interface. Impurities such as silicon, magnesium, and oxygen could have been incorporated within the AlN whiskers and assisted in the growth process. It is possible that silicon acted as the liquid catalyst during the VLS process. It is possible that a VTR process is also involved in the whisker growth. The VTR process could have involved the evolution of Al_2O gas, reaction of the Al_2O gas with ambient nitrogen and oxygen, followed by nucleation and whisker growth. The nanoscale diameters of the whiskers would also indicate growth from vapor since the reactants had particle sizes on the order of microns.

Microstructures within the Reaction Products of a Vacuum SHS Reaction

500x Magnification

Microstructures for reaction products synthesized in a vacuum environment utilizing JSC-1AF simulant are shown in Figure CXXXI - Figure CXXXIV at 500x magnification.

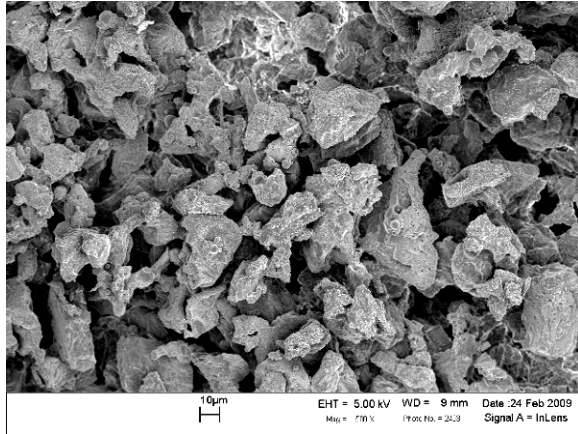


Figure CXXXI: Vacuum synthesized 19.44% aluminum stoichiometry utilizing JSC-1AF.

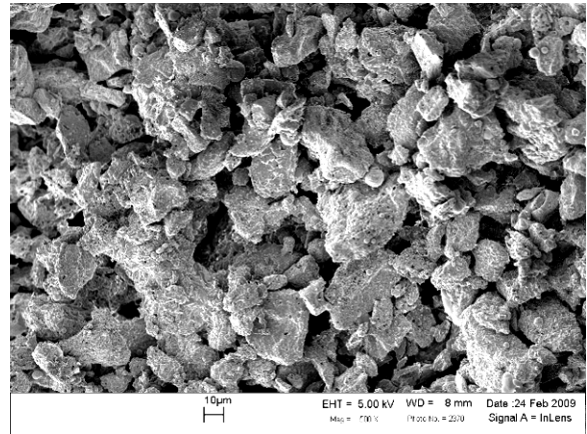


Figure CXXXII: Vacuum synthesized 24.45% aluminum stoichiometry utilizing JSC-1AF.

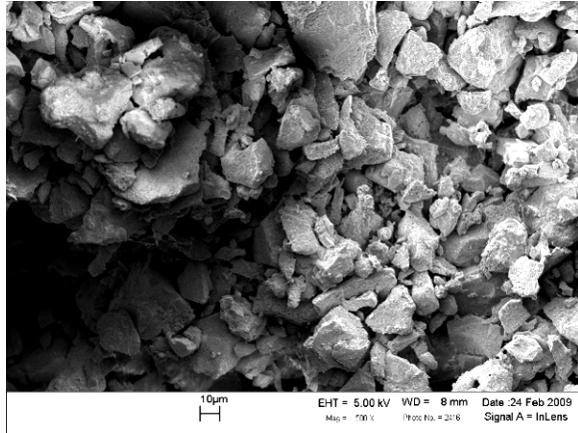


Figure CXXXIII: Vacuum synthesized 28.85% aluminum stoichiometry utilizing JSC-1AF.

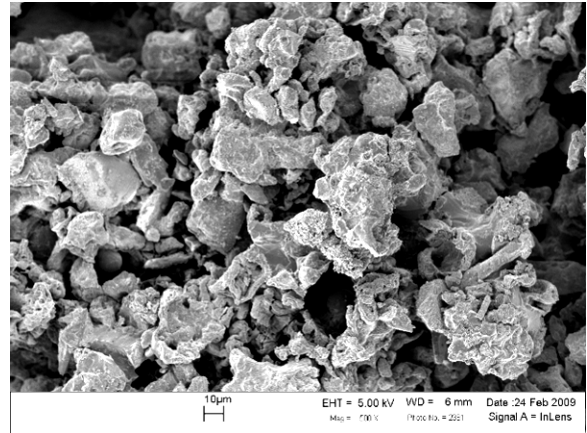


Figure CXXXIV: Vacuum synthesized 33.33% aluminum stoichiometry utilizing JSC-1AF.

The microstructures of the aluminum stoichiometries in Figure CXXXI-Figure CXXXIV exhibit many discrete particles, unlike the microstructures of standard atmosphere reaction products. The particles have a variety of shapes, including sub-rounded, sub-angular, and angular. The discrete nature of the particles suggests significantly less sintering and intergranular bonding than found in standard atmosphere reaction products. The absence of

substantial quantities of air molecules in a vacuum environment restricts the majority of heat transfer to conduction by particle-particle contact, and likely inhibits whisker formation. The lower pressures that exist in a vacuum environment likely allow more vaporization that can increase porosity and decrease sintering. At 500x magnification the microstructures of the different aluminum stoichiometries are very similar. A higher porosity is also present in the vacuum product, at least in part due to the absence of whisker formation.

Microstructures for reaction products synthesized in a vacuum environment utilizing JSC-1A simulant are shown in Figure CXXXV - Figure CXXXVII at 500x magnification.

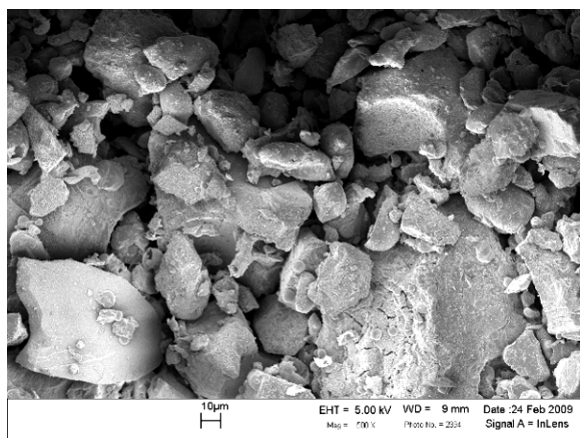


Figure CXXXV: Vacuum synthesized 19.44% aluminum stoichiometry utilizing JSC-1A.

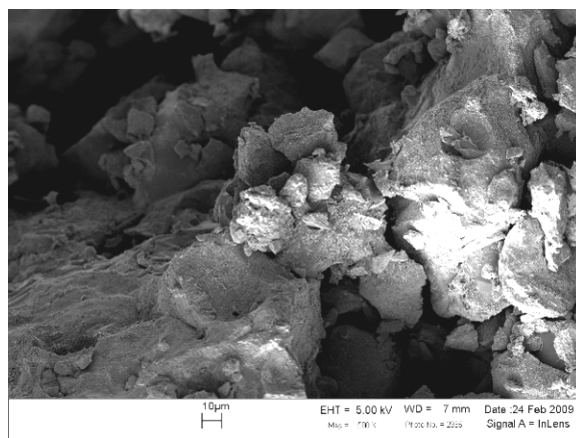


Figure CXXXVI: Vacuum synthesized 24.45% aluminum stoichiometry utilizing JSC-1A.

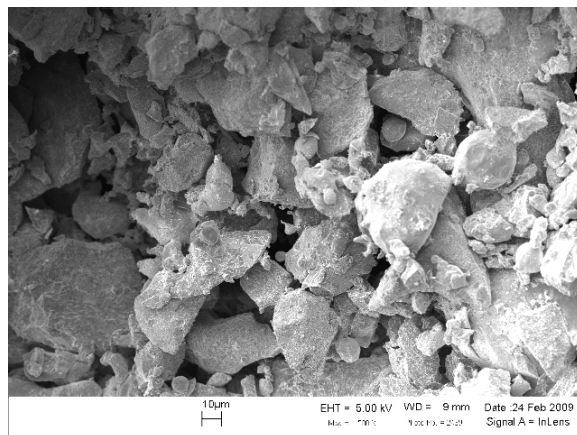


Figure CXXXVII: Vacuum synthesized 28.85% aluminum stoichiometry utilizing JSC-1A.

As observed with the JSC-1AF simulant, the reaction products utilizing the JSC-1A simulant in Figure CXXXV-Figure CXXXVII exhibit many discrete particles. The absence of

substantial quantities of air molecules in a vacuum environment restricts the majority of heat transfer to conduction by particle-particle contact, and likely inhibits whisker formation. The lower pressures that exist in a vacuum environment likely allow more vaporization that can increase porosity and decrease sintering. Particle shapes range from sub-rounded, to sub-angular, and angular. No whiskers are observed within the microstructures of the JSC-1A simulant.

2kx Magnification

Microstructures for reaction products synthesized in a vacuum environment utilizing JSC-1AF simulant are shown in Figure CXXXVIII - Figure CXLI at 2kx magnification.

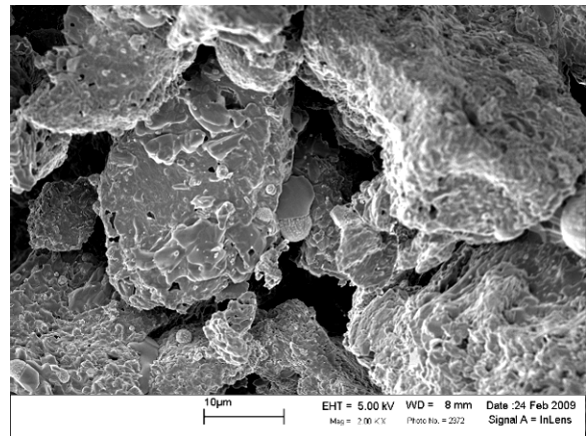
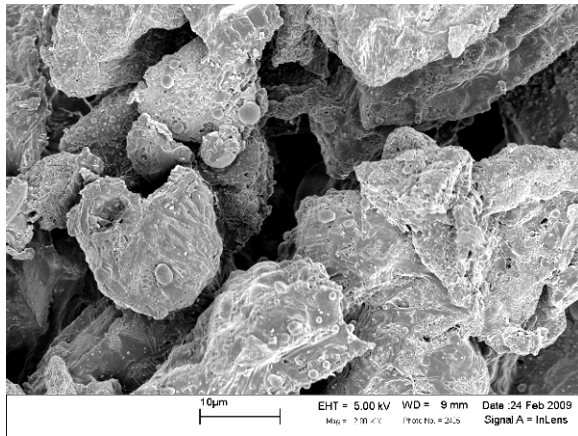


Figure CXXXVIII: Vacuum synthesized 19.44% aluminum stoichiometry utilizing JSC-1AF.

Figure CXXXIX: Vacuum synthesized 24.45% aluminum stoichiometry utilizing JSC-1AF.

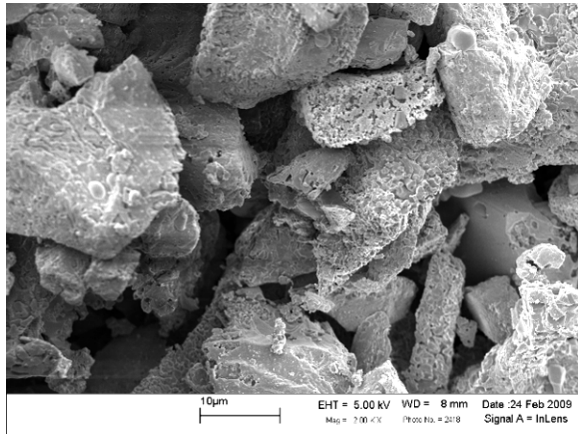


Figure CXL: Vacuum synthesized 28.85% aluminum stoichiometry utilizing JSC-1AF.

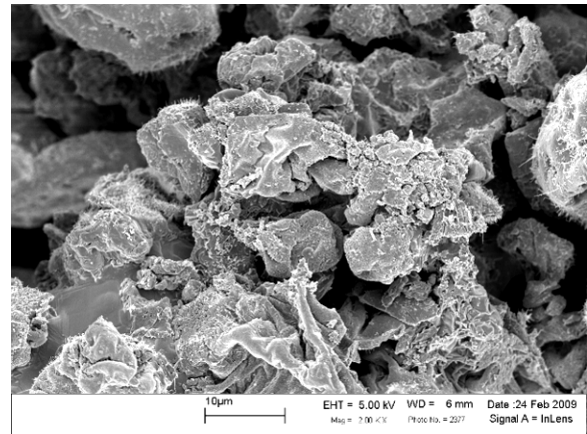


Figure CXLI: Vacuum synthesized 33.33% aluminum stoichiometry utilizing JSC-1AF.

The JSC-1AF microstructures in Figure CXXXVIII-Figure CXL exhibit discrete particles, as observed in lower magnifications. Small spherical and sub-spherical particles are observed in all the reactant stoichiometries. The spherical particles are likely to be composed of aluminum or intermetallic compounds such as iron silicides. In addition, pitting is observed on particles in all reactant stoichiometries and is likely induced by the low pressure found in the vacuum environment. Low pressure allows the volatilization of more constituents than can occur at equivalent temperatures in a standard atmosphere. Some elements that could be easily volatilized include sodium, potassium, and magnesium.

Microstructures for reaction products synthesized in a vacuum environment utilizing JSC-1A simulant are shown in Figure CXLII - Figure CXLIV at 2kx magnification.

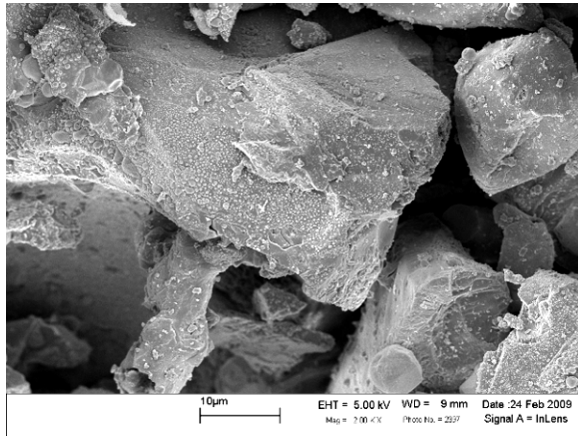


Figure CXLII: Vacuum synthesized 19.44% aluminum stoichiometry utilizing JSC-1A.

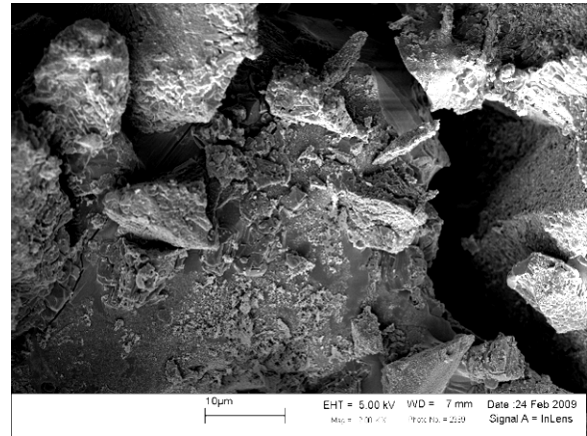


Figure CXLIII: Vacuum synthesized 24.45% aluminum stoichiometry utilizing JSC-1A.

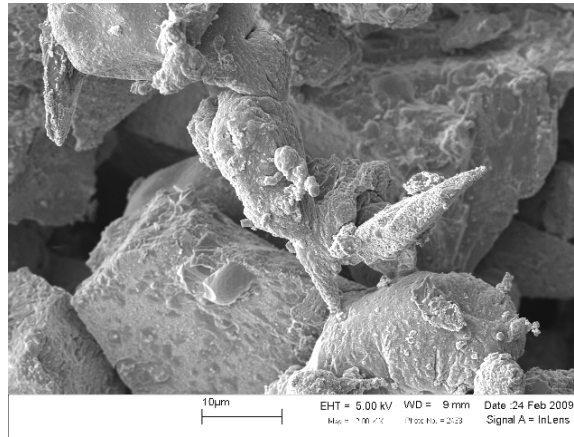


Figure CXLIV: Vacuum synthesized 28.85% aluminum stoichiometry utilizing JSC-1A.

The JSC-1A microstructures in Figure CXLII-Figure CXLIV exhibit discrete particles, as observed with the reaction products utilizing the JSC-1AF simulant. Spherical and sub-spherical particles are observed in all the reactant stoichiometries. Particle pitting is not as predominant with JSC-1A reaction products as it is with JSC-1AF reaction products. The decrease in observed particle pitting may be a result of a larger transfer of heat into the interior of the larger sized particles, resulting in decreased particle surface temperatures and decreased volatilization. Many of the particle surfaces are covered with small spherical particles, likely to be composed of aluminum or intermetallic compounds such as iron silicides.

10kx Magnification

Microstructures for reaction products synthesized in a vacuum environment utilizing JSC-1AF simulant are shown in Figure CXLV - Figure CLI at 10kx magnification. Two microstructures of each aluminum stoichiometry are shown below.

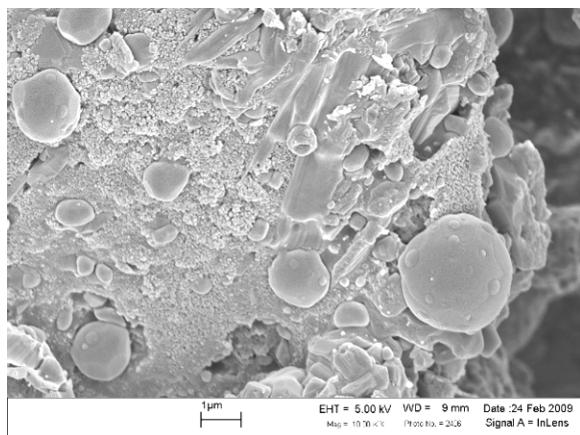


Figure CXLV: Vacuum synthesized 19.44% aluminum stoichiometry utilizing JSC-1AF.

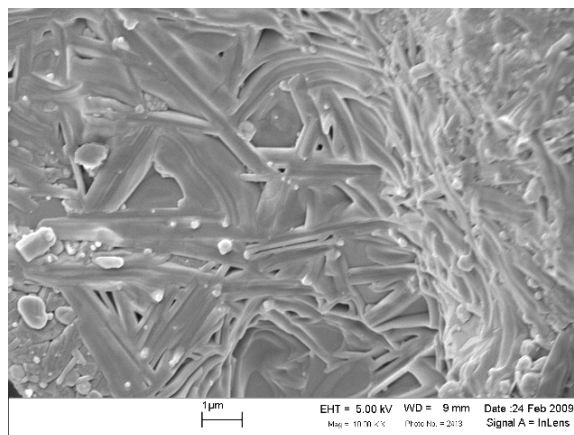


Figure CXLVI: Vacuum synthesized 19.44% aluminum stoichiometry utilizing JSC-1AF.

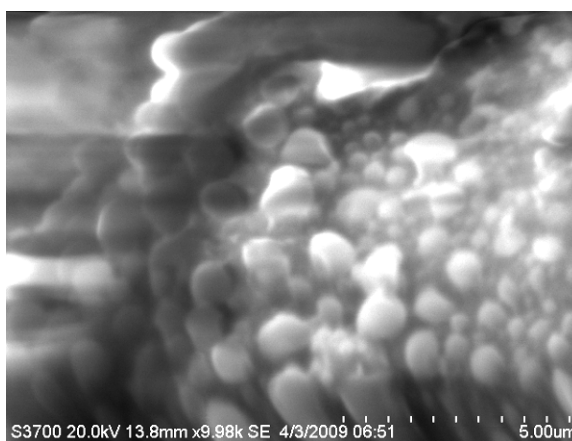


Figure CXLVII: Vacuum synthesized 24.45% aluminum stoichiometry utilizing JSC-1AF.

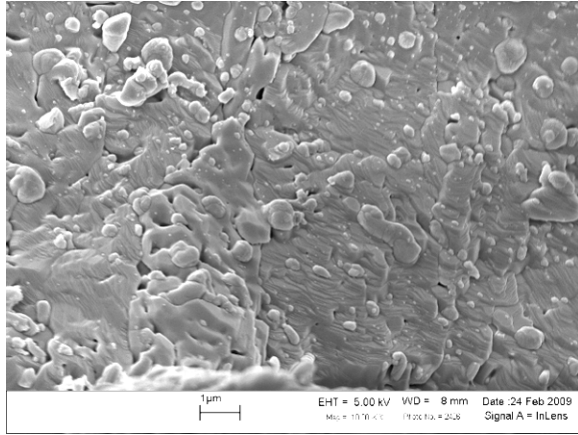


Figure CXLVIII: Vacuum synthesized 28.85% aluminum stoichiometry utilizing JSC-1AF.

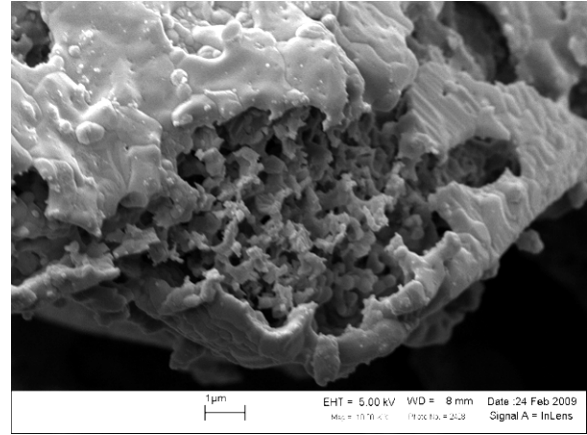


Figure CXLIX: Vacuum synthesized 28.85% aluminum stoichiometry utilizing JSC-1AF.

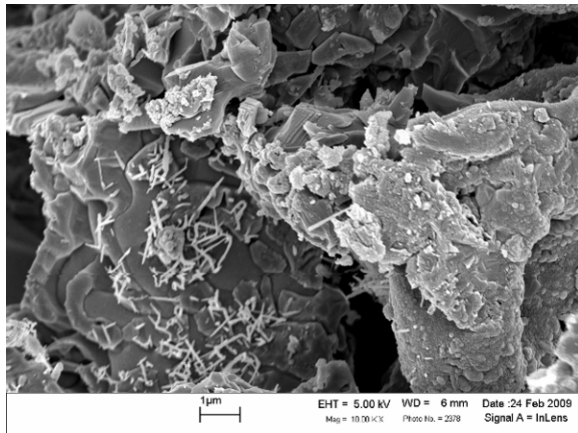


Figure CL: Vacuum synthesized 33.33% aluminum stoichiometry utilizing JSC-1AF.

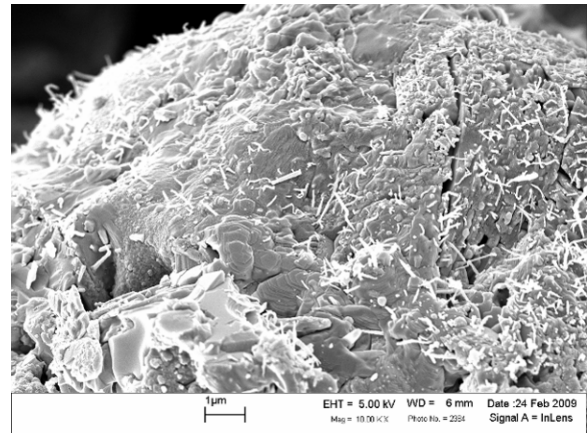


Figure CLI: Vacuum synthesized 33.33% aluminum stoichiometry utilizing JSC-1AF.

Figure CXLV exhibits an abundance of spherical and sub-spherical particles, while Figure CXLVI shows a rod-like growth within a particle and may indicate the beginning of a eutectic microstructure. Both Figure CXLV and Figure CXLVI show evidence of sintering and melting. In Figure CXLV tiny spheres are observed nucleating on larger spherical particles. The tiny spheres could be evidence of phase separation and nucleation of intermetallic iron silicides. It is also possible that vaporization is producing the tiny spheres on the larger spherical particles. Figure CXLVII and Figure CXLVIII have many spherical and sub-spherical particles; Figure CXLVIII shows evidence of sintering and melting. Figure CXLIX shows the pitting of a particle, likely caused by volatilization of some of its constituents due to the low pressures within

the vacuum environment. Both Figure CL and Figure CLI show evidence of sintering and melting, as well as the growth of whiskers.

Microstructures for reaction products synthesized in a vacuum environment utilizing JSC-1A simulant are shown in Figure CLII - Figure CLV at 10kx magnification.

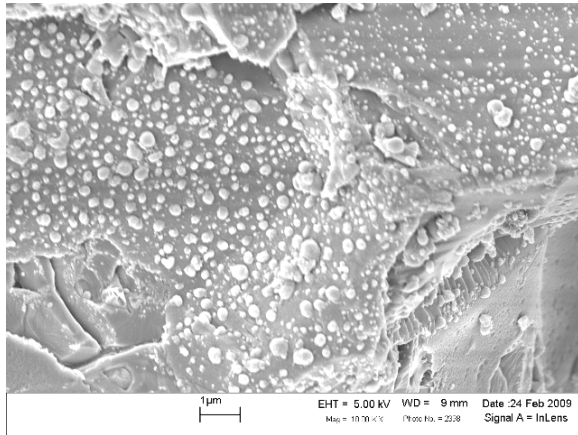


Figure CLII: Vacuum synthesized 19.44% aluminum stoichiometry utilizing JSC-1A.

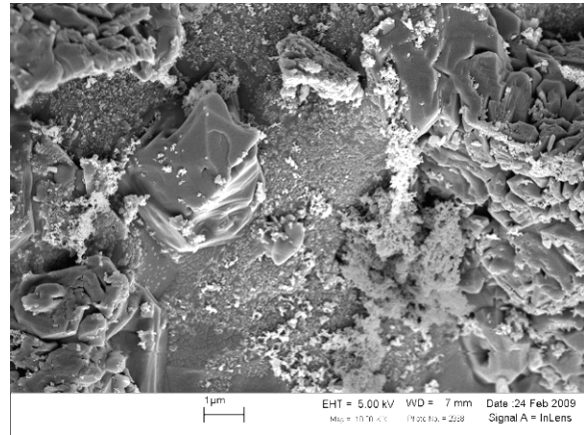


Figure CLIII: Vacuum synthesized 24.45% aluminum stoichiometry utilizing JSC-1A.

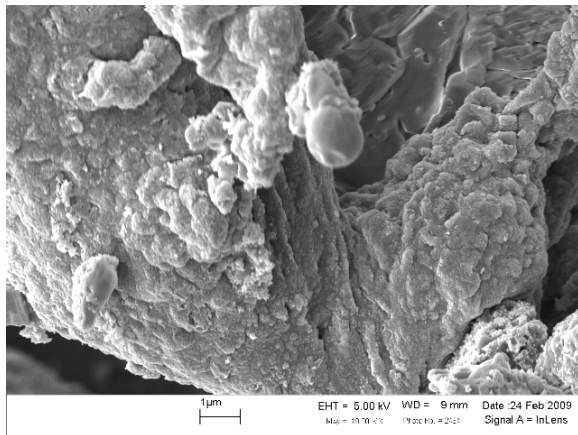


Figure CLIV: Vacuum synthesized 28.85% aluminum stoichiometry utilizing JSC-1A.

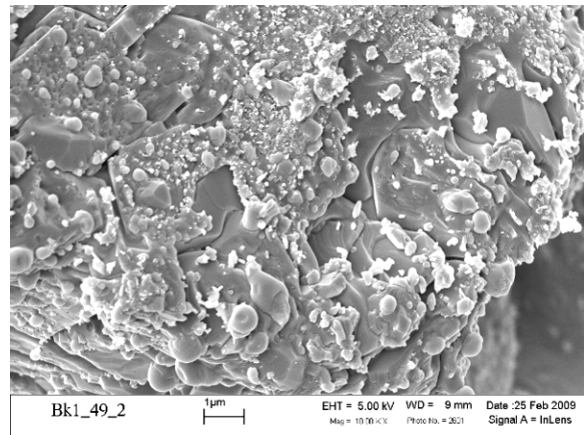


Figure CLV: Vacuum synthesized 28.85% aluminum stoichiometry utilizing JSC-1A.

Many spherical and sub-spherical particles are observed on the particle surface in Figure CLII and Figure CLV. Small clusters of whiskers are observed on the particle surface in Figure CLIII.

Elemental Analysis for Vacuum Synthesized Reaction Products Utilizing JSC-1AF Regolith Simulant

19.44% Al by weight

Region A

The microstructure of the reaction product for Region A of a JSC-1AF reaction product utilizing a 19.44% Al stoichiometry is shown in Figure CLVI, as are EDS Spectra 1, 2, and 3. Table LV shows the chemical data obtained from analysis of Spectrum 1, 2, and 3. Spectrum 1 is located on a spherical particle. Elemental analysis indicated that the particle had significant silicon and iron. The presence of significant iron and silicon could indicate that this particle is an intermetallic iron-silicide. Spectrum 2 is located of a flat surface of a particle. Chemical analysis of the region indicates large concentrations of aluminum, silicon, and oxygen. EDS data could indicate that Spectrum 2 is composed of grossite, spinel, and reduced silicon. It is also possible that the area is an unreacted mineral, such as anorthite. Spectrum 3 is located on a sub-spherical particle. EDS indicates large concentrations of silicon, iron, aluminum, and oxygen. The chemical analysis could indicate that the particle in Spectrum 3 is composed of iron-silicides and aluminum oxides. The spherical particles of iron-silicides may have been formed by phase separation from the larger particle; the spherical shape suggests a low degree of surface wetting with regards to the larger particle surface.

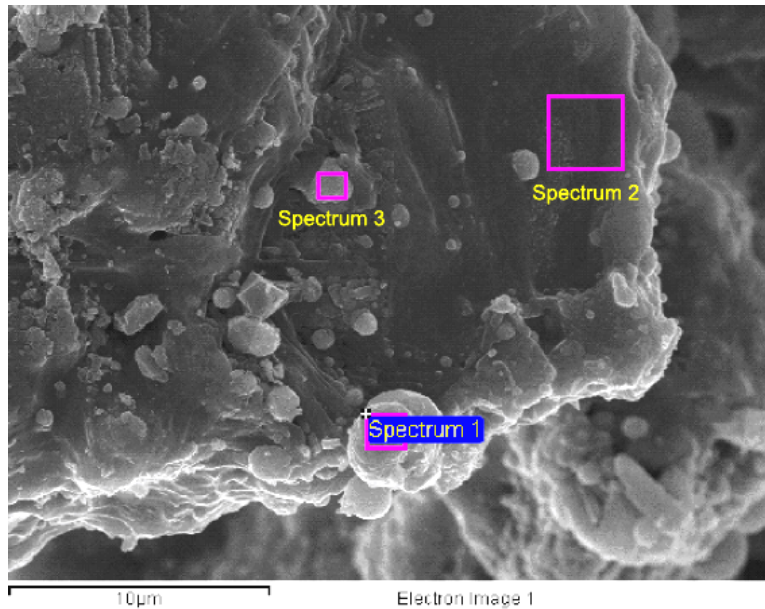


Figure CLVI: SEM micrograph of the microstructure in Region A for the 19.44% aluminum stoichiometry with the regions of EDS highlighted.

Table LV: EDS Analysis of Spectra 1, 2, and 3 shown in Figure CLVI

Element	Spectrum 1		Spectrum 2		Spectrum 3	
	Weight%	Atomic%	Weight%	Atomic%	Weight%	Atomic%
O	10.38	20.16	44.68	59.44	21.60	36.86
Mg	-	-	2.82	2.46	2.01	2.25
Al	3.57	4.10	23.84	18.80	10.44	10.58
Si	49.91	55.20	17.96	13.61	36.33	35.32
Ca	0.40	0.30	10.72	5.69	0.99	0.68
Ti	3.64	2.36	-	-	3.68	2.10
Mn	-	-	-	-	0.70	0.34
Fe	32.11	17.86	-	-	24.27	11.86

Region B

The microstructure of the reaction product for Region B of a JSC-1AF reaction product utilizing a 19.44% Al stoichiometry is shown in Figure CLVII, as are EDS Spectra 1, 2, 3, and 4. Table LVI shows the chemical data obtained from analysis of Spectrum 1, 2, 3, and 4. Spectrum 1 is located on a spherical particle. Elemental analysis indicated that the particle has significant silicon and iron. The presence of significant iron and silicon could indicate that this particle is an intermetallic iron-silicide. Spectrum 2 is located of a flat surface of a particle. Chemical

analysis of the region indicates large concentrations of aluminum, magnesium, and oxygen. EDS data from Spectrum 2 could indicate the region is composed of spinel. Spectrum 3 is located on a spherical particle. EDS indicates large concentrations of silicon, iron, aluminum, and oxygen. The chemical analysis could indicate that the particle in Spectrum 3 is composed of iron-silicides and aluminum oxides. Spectrum 4 is also located on a spherical particle. EDS data indicate high concentrations of iron and silicon which could indicate that the particle is composed primarily of iron silicides. The spherical particles of iron-silicides may have been formed by phase separation from the larger particle; the spherical shape suggests a low degree of surface wetting with regards to the larger particle surface.

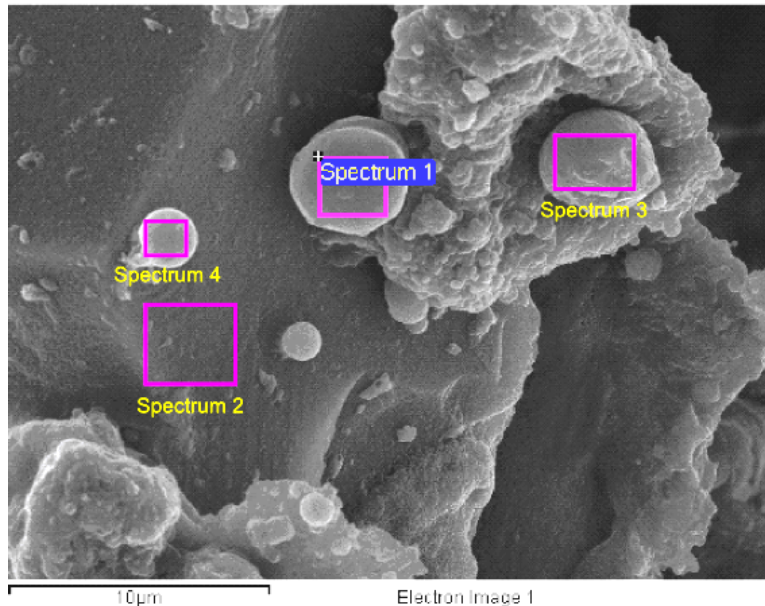


Figure CLVII: SEM micrograph of the microstructure in Region B for the 19.44% aluminum stoichiometry with the regions of EDS highlighted.

Table LVI: EDS Analysis of Spectra 1, 2, 3, and 4 shown in Figure CLVII

Element	Spectrum 1		Spectrum 2		Spectrum 3		Spectrum 4	
	Weight%	Atomic%	Weight%	Atomic%	Weight%	Atomic%	Weight%	Atomic%
O	8.45	16.99	31.87	43.97	12.95	25.98	14.02	26.28
Mg	-	-	15.42	14.00	1.28	1.69	1.35	1.68
Al	2.89	3.43	45.03	36.84	8.44	10.05	6.31	7.01
Si	49.80	57.09	4.11	3.23	29.89	34.18	43.23	46.14
Ca	0.40	0.32	3.56	1.96	1.03	0.82	0.36	0.26
Ti	-	-	-	-	6.21	4.16	-	-
Mn	-	-	-	-	-	-	0.74	0.40
Fe	38.46	22.17	-	-	40.22	23.13	33.99	18.25

24.45% Al by weight

Region A

The microstructure of the reaction product for Region A of a JSC-1AF reaction product utilizing a 24.45% Al stoichiometry is shown in Figure CLVIII, as are EDS Spectra 1 and 2. Table LVII shows the chemical data obtained from analysis of Spectrum 1 and 2. Spectrum 1 is located on a surface feature of a particle. Chemical analysis indicates large quantities of aluminum and oxygen, along with some silicon, and many trace elements. Spectrum 1 is likely to be composed primarily of aluminum oxide and reduced silicon. The formation of aluminum oxide and silicon could occur by an oxidation-reduction reaction involving a mineral such as anorthite, and aluminum. Spectrum 2 is located on a flat and smooth particle surface. Elemental analysis indicates that there is significant aluminum, magnesium, silicon, and oxygen present. Spectrum 2 is likely composed of spinel and iron silicides. The formation of spinel and iron silicides could occur during a subsequent reaction incorporating the products of oxidation-reduction reactions involving minerals such as hedenbergite and diopside with aluminum. It is also possible that the regions could contain unreacted minerals, such as diopside.

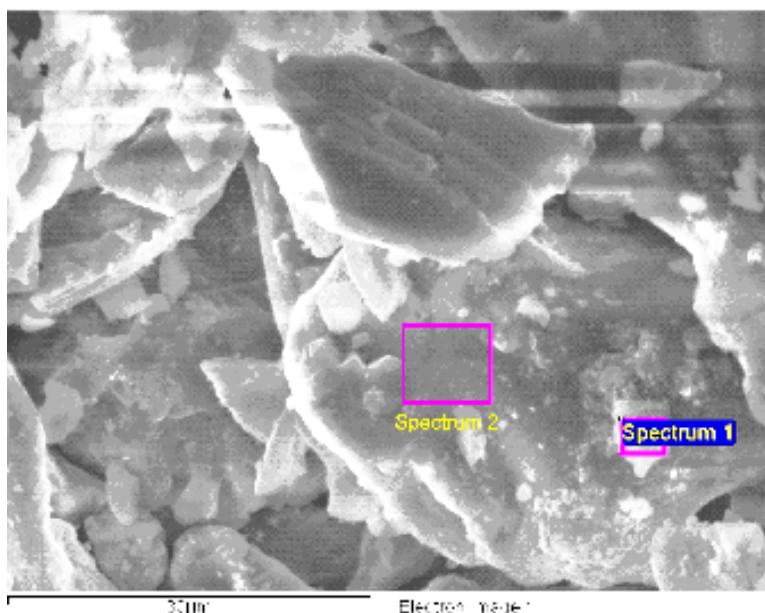


Figure CLVIII: SEM micrograph of the microstructure in Region A for the 24.45% aluminum stoichiometry with the regions of EDS highlighted.

Table LVII: EDS Analysis of Spectra 1 and 2 shown in Figure CLVIII

Element	Spectrum 1		Spectrum 2	
	Weight%	Atomic%	Weight%	Atomic%
O	44.56	59.35	35.90	51.54
Na	2.08	1.93	0.76	0.76
Mg	3.98	3.49	14.09	13.31
Al	26.47	20.91	18.77	15.98
Si	13.34	10.12	13.88	11.35
K	0.86	0.47	0.31	0.18
Ca	2.43	1.29	0.99	0.57
Ti	0.75	0.33	0.22	0.10
Fe	5.52	2.11	15.09	6.20

Region B

The microstructure of the reaction product for Region B of a JSC-1AF reaction product utilizing a 24.45% Al stoichiometry is shown in Figure CLIX, as are EDS Spectra 1, 2, and 3. Table LVIII shows the chemical data obtained from analysis of Spectrum 1, 2, and 3. Spectrum 1 is located on a smooth and flat particle surface. Chemical analysis indicates large quantities of aluminum, iron, and oxygen, along with some silicon. Spectrum 1 is likely to be composed primarily of aluminum oxide and an iron-aluminum alloy. The formation of aluminum oxide could occur during an oxidation-reduction reaction involving a mineral, such as anorthite with

aluminum. An iron-aluminum alloy could form from reduced iron produced by the reduction of a mineral such as hedenbergite, which subsequently bonds with aluminum. Spectrum 2 is located on a rough particle surface. Elemental analysis indicates that there is significant aluminum and oxygen, along with some iron and silicon present. Spectrum 2 is likely composed of aluminum oxide and iron silicides. The formation of iron silicides could occur during a subsequent reaction incorporating the products of oxidation-reduction reactions involving minerals such as hedenbergite with aluminum. Elemental analysis of Spectrum 3 indicates large quantities of aluminum and oxygen, along with some calcium and silicon. It is likely that Spectrum 3 is composed of grossite, corundum, and reduced silicon. It is possible that the formation of grossite, corundum, and silicon occurred during an oxidation-reduction reaction between anorthite and aluminum.

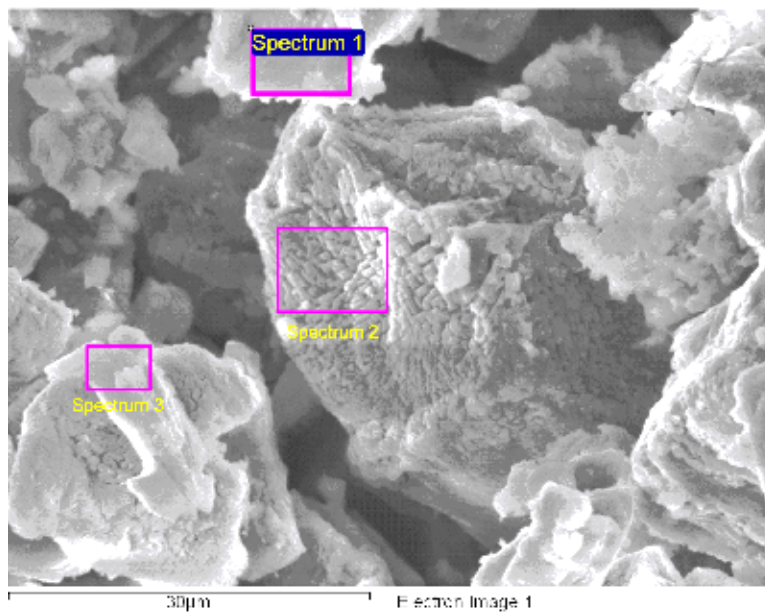


Figure CLIX: SEM micrograph of the microstructure in Region B for the 24.45% aluminum stoichiometry with the regions of EDS highlighted.

Table LVIII: EDS Analysis of Spectra 1, 2, and 3 shown in Figure CLIX

Element	Spectrum 1		Spectrum 2		Spectrum 3	
	Weight%	Atomic%	Weight%	Atomic%	Weight%	Atomic%
O	19.80	39.42	29.66	45.17	38.15	53.57
Na	-	-	-	-	0.74	0.72
Mg	-	-	-	-	1.06	0.98
Al	18.39	21.71	45.17	40.80	32.77	27.28
Si	4.52	5.12	6.42	5.57	12.15	9.72
Ca	4.75	3.78	1.35	0.82	10.32	5.79
Ti	-	-	0.74	0.38	-	-
Fe	52.54	29.97	16.66	7.27	4.80	1.93

28.85% Al by weight

Region A

The microstructure of the reaction product for Region A of a JSC-1AF reaction product utilizing a 28.85% Al stoichiometry is shown in Figure CLX, as are EDS Spectra 1, 2, and 3. Table LIX shows the chemical data obtained from analysis of Spectra 1, 2, and 3. Region A is located on a pitted particle. Spectrum 1 is located on an outer smooth surface of the particle, Spectrum 2 is located on a fairly smooth outer surface of the particle, and Spectrum 3 is located on an interior rough surface of the particle. Elemental analysis indicated that there is little difference in elemental composition of the different regions of the particle. All had significant aluminum and oxygen, along with some calcium. The presence of aluminum, oxygen, and calcium could indicate that the region is composed of grossite and aluminum oxide. It is possible that the pitting of the particle could have occurred due to volatilization of sodium, potassium, or magnesium from the region.

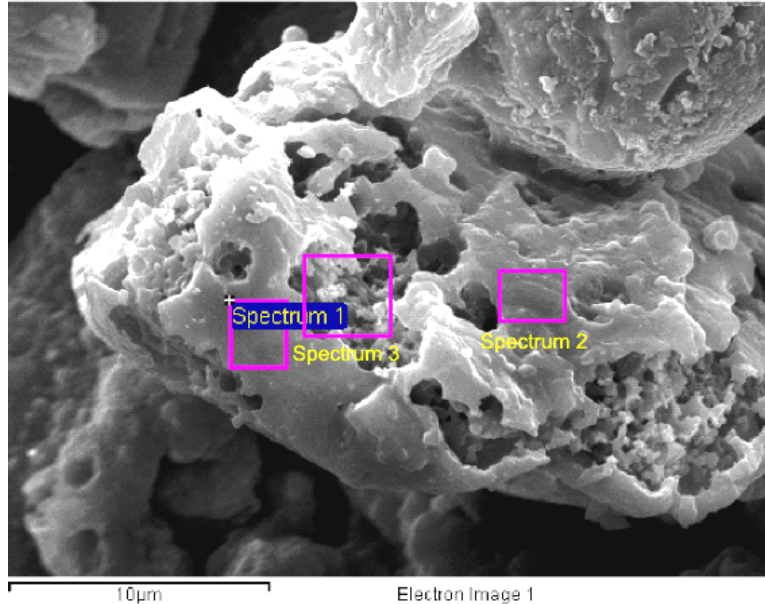


Figure CLX: SEM micrograph of the microstructure in Region A for the 28.85% aluminum stoichiometry with the regions of EDS highlighted.

Table LIX: EDS Analysis of Spectra 1, 2, and 3 shown in Figure CLX

Element	Spectrum 1		Spectrum 2		Spectrum 3	
	Weight%	Atomic%	Weight%	Atomic%	Weight%	Atomic%
O	43.19	57.88	50.52	64.86	45.84	60.53
Mg	1.84	1.62	1.47	1.24	2.26	1.97
Al	39.60	31.46	33.54	25.53	35.32	27.66
Si	4.81	3.66	5.51	4.02	6.90	5.19
Ca	8.65	4.63	7.22	3.71	6.53	3.44
Ti	-	-	-	-	0.38	0.17
Fe	1.91	0.73	1.75	0.65	2.76	1.04

Region B

The microstructure of the reaction product for Region B of a JSC-1AF reaction product utilizing a 28.85% Al stoichiometry is shown in Figure CLXI, as are EDS Spectra 1, 2, and 3. Table LX shows the chemical data obtained from analysis of Spectrum 1, 2, and 3. Spectrum 1 is located on a protrusion from a particle surface. The chemical composition indicates significant quantities of silicon, iron, aluminum, and oxygen. From the EDS data, it is possible that the spherical particle could contain iron silicides and aluminum oxides. Spectrum 2 is located on a spherical particle. EDS analysis shows significant quantities of silicon, iron, aluminum and oxygen, potentially indicating iron silicides and aluminum oxides. Spectrum 3 is

located on a large particle. Elemental analysis indicated large quantities of aluminum and oxygen, along with some calcium and magnesium within Spectrum 3. It is possible that Spectrum 3 is composed of corundum, spinel, and grossite. The spherical particles of iron-silicides may have been formed by phase separation from the larger particle; the spherical shape suggests a low degree of surface wetting with regards to the larger particle surface.

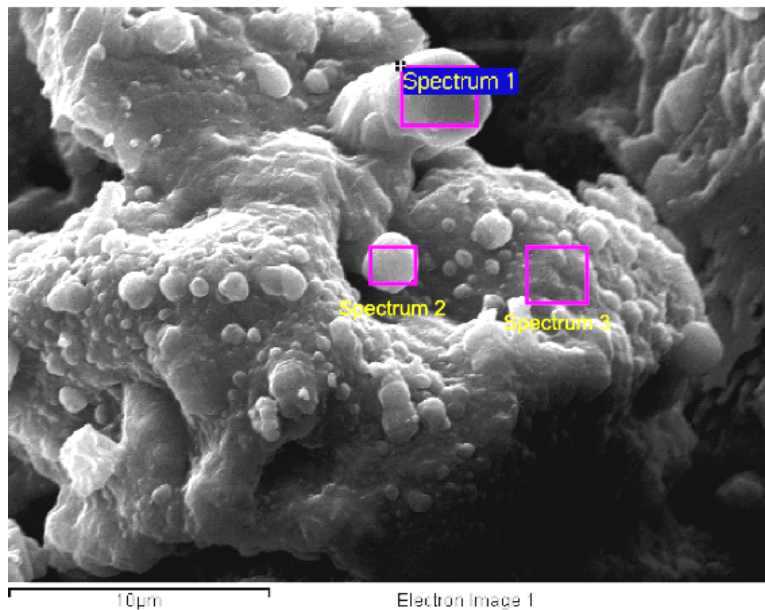


Figure CLXI: SEM micrograph of the microstructure in Region B for the 28.85% aluminum stoichiometry, with the regions of EDS highlighted.

Table LX: EDS Analysis of Spectra 1, 2, and 3 shown in Figure CLXI

Element	Spectrum 1		Spectrum 2		Spectrum 3	
	Weight%	Atomic%	Weight%	Atomic%	Weight%	Atomic%
O	10.98	20.94	22.37	37.19	49.51	63.83
Mg	-	-	-	-	2.56	2.18
Al	12.58	14.22	20.85	20.57	35.12	26.85
Si	42.39	46.05	31.15	29.52	3.51	2.57
Ca	0.73	0.56	2.80	1.85	7.81	4.02
Ti	0.48	0.31	-	-	-	-
Fe	32.82	17.92	22.83	10.87	1.49	0.55

33.33% Al by weight

Region A

The microstructure of the reaction product for Region A of a JSC-1AF reaction product utilizing a 33.33% Al stoichiometry is shown in Figure CLXII, as are EDS Spectra 1, 2, and 3. Table LXI shows the chemical data obtained from analysis of Spectrum 1, 2, and 3. Spectrum 1 is located on a region of small whiskers on a particle surface. The chemical composition indicates significant quantities of aluminum and oxygen, along with some silicon and iron. Spectrum 2 is located on a smooth particle surface. EDS analysis shows significant quantities of aluminum and oxygen, along with some silicon, iron, and magnesium. It is likely that the particle is composed primarily of corundum and spinel. Corundum and spinel could form during oxidation-reduction reactions involving minerals such as anorthite and diopside with aluminum. Spectrum 3 is located on a particle with some small whiskers emanating from it. Elemental analysis indicated large quantities of aluminum and oxygen within Spectrum 3. It is likely that Spectrum 3 is also composed of corundum.

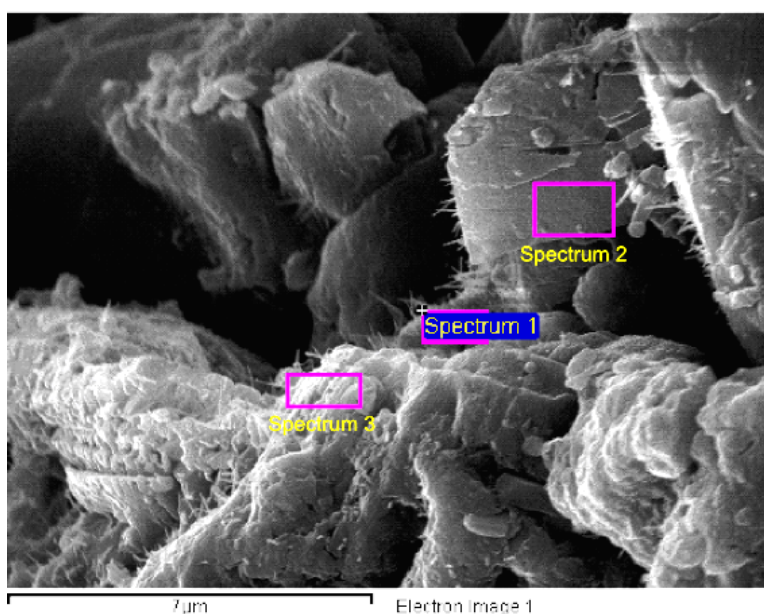


Figure CLXII: SEM micrograph of the microstructure in Region A for the 33.33% aluminum stoichiometry with EDS regions highlighted.

Table LXI: EDS Analysis of Spectrum 1 shown in Figure CLXII

Element	Spectrum 1		Spectrum 2		Spectrum 3	
	Weight%	Atomic%	Weight%	Atomic%	Weight%	Atomic%
O	43.48	58.70	30.45	43.95	54.80	67.69
Mg	1.09	0.97	2.96	2.81	-	-
Al	39.20	31.38	51.30	43.91	40.27	29.50
Si	5.93	4.56	6.62	5.45	3.03	2.14
Ca	1.25	0.67	1.88	1.08	-	-
Ti	3.37	1.52	-	-	-	-
Fe	5.67	2.19	6.79	2.81	1.90	0.67

Region B

The microstructure of the reaction product for Region B of a JSC-1AF reaction product utilizing a 33.33% Al stoichiometry is shown in Figure CLXIII, as are EDS Spectra 1, 2, and 3. Table LXII shows the chemical data obtained from analysis of Spectrum 1, 2, and 3. Spectrum 1 is located on a somewhat rough particle surface. The chemical composition indicates significant quantities of aluminum and oxygen, along with some silicon. EDS data from Spectrum 1 likely indicates the region is composed primarily of corundum. Corundum could have been formed during an oxidation-reduction reaction involving anorthite and aluminum. Spectrum 2 is located on a protrusion from the particle surface. EDS analysis again shows significant quantities of aluminum and oxygen, along with trace silicon. The element analysis would likely indicate that Spectrum 2 is primarily composed of corundum. Spectrum 3 is located on a fairly smooth particle surface. Elemental analysis indicates roughly the same composition as Spectrum 1 and Spectrum 2; therefore the region is likely to be composed primarily of corundum.

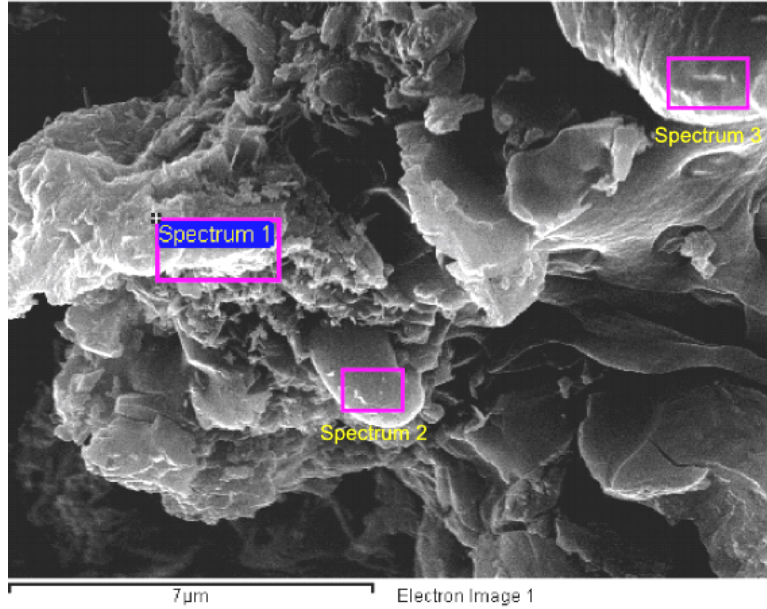


Figure CLXIII: SEM micrograph of the microstructure in Region B for the 33.33% aluminum stoichiometry with EDS regions highlighted.

Table LXII: EDS Analysis of Spectra 1, 2, and 3 shown in Figure CLXIII

	Spectrum 1		Spectrum 2		Spectrum 3	
Element	Weight%	Atomic%	Weight%	Atomic%	Weight%	Atomic%
O	42.41	55.91	20.54	30.40	31.00	43.19
Al	51.05	39.91	76.10	66.77	63.10	52.13
Si	3.95	2.97	3.36	2.83	5.90	4.68
Ca	1.60	0.84	-	-	-	-
Fe	0.99	0.37	-	-	-	-

Region C

The microstructure of the reaction product for Region C of a JSC-1AF reaction product utilizing a 33.33% Al stoichiometry is shown in Figure CLXIV, as are EDS Spectra 1, 2, and 3. Table LXIII shows the chemical data obtained from analysis of Spectrum 1, 2, and 3. Spectrum 1 is located on an angular particle with a smooth surface. The chemical composition indicates significant quantities of aluminum and oxygen, along with some iron and silicon. EDS data from Spectrum 1 likely indicate the region is composed primarily of aluminum and aluminum oxide, along with some iron silicides. Aluminum oxide could have been formed during an oxidation-reduction reaction involving a mineral such as anorthite reacting with aluminum. The formation of iron silicides could occur during a subsequent reaction incorporating the products of

oxidation-reduction reactions involving minerals such as hedenbergite with aluminum. Spectrum 2 is located on the surface of a large spherical particle. EDS analysis again shows significant quantities of aluminum and oxygen, along with some silicon, calcium, and magnesium. The element analysis would likely indicate that Spectrum 2 is primarily composed of aluminum and aluminum oxide, and also contains some grossite and spinel. Grossite and spinel could be formed by oxidation-reduction reactions involving minerals such as anorthite and diopside reacting with aluminum. Spectrum 3 is located on a material on the surface of the spherical particle examined in Spectrum 2. Elemental analysis indicates large quantities of aluminum, along with some oxygen. The region is likely composed primarily of aluminum and aluminum oxide.

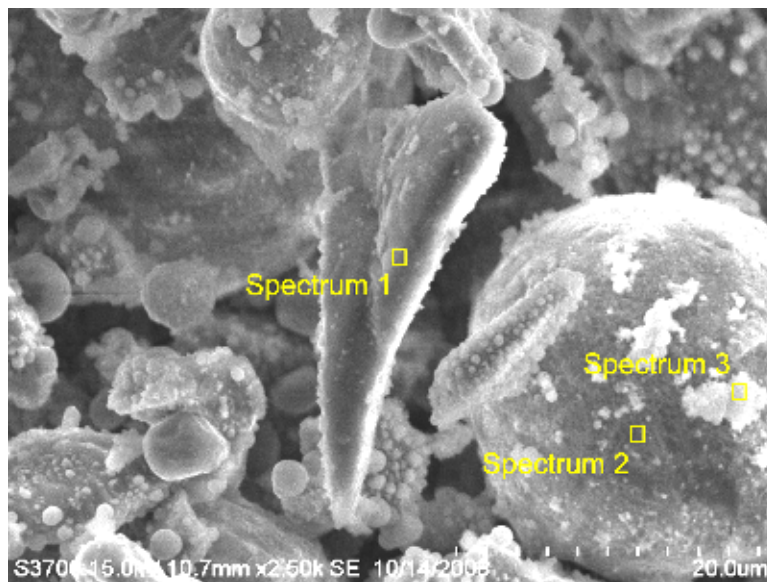


Figure CLXIV: SEM micrograph of the microstructure in Region C for the 33.33% aluminum stoichiometry with EDS regions highlighted.

Table LXIII: EDS Analysis of Spectra 1, 2, and 3 shown in Figure CLXIV

Element	Spectrum 1		Spectrum 2		Spectrum 3	
	Weight%	Atomic%	Weight%	Atomic%	Weight%	Atomic%
C	-	-	1.82	3.63	-	-
O	12.29	21.54	20.72	31.04	17.18	25.98
Na	0.40	0.49	0.19	0.19	0.11	0.12
Mg	0.98	1.13	2.82	2.78	0.11	0.10
Al	55.66	57.84	56.26	49.97	81.03	72.64
Si	5.33	5.32	8.73	7.45	1.12	0.97
K	0.41	0.29	-	-	-	-
Ca	3.95	2.76	5.04	3.01	-	-
Ti	1.14	0.67	0.40	0.20	-	-
Fe	19.85	9.97	4.02	1.72	0.46	0.20

Elemental Analysis for Vacuum Synthesized Reaction Products Utilizing JSC-1A Regolith Simulant

19.44% Al by weight

The microstructure of the reaction product for Region A of a JSC-1A reaction product utilizing a 19.44% Al stoichiometry is shown in Figure CLXV, as are EDS Spectra 1, 2, and 3. Table LXIV shows the chemical data obtained from analysis of Spectrum 1, 2, and 3. Spectrum 1 is located on a spherical particle. The chemical composition indicates significant quantities of aluminum, silicon, and oxygen, along with some iron and calcium. EDS data from Spectrum 1 likely indicates the region is composed primarily of aluminum oxide, potentially containing some grossite, reduced silicon and iron silicides. The formation of aluminum oxide could occur during an oxidation-reduction reaction between anorthite and aluminum. Spectrum 2 is located on a smooth and flat particle surface. EDS analysis again shows significant quantities of silicon, aluminum and oxygen, along with some calcium and sodium. EDS data likely indicate that Spectrum 2 is composed of grossite and reduced silicon. Spectrum 3 is located on a small spherical particle. Elemental analysis indicates large concentrations of aluminum, silicon, and oxygen, along with some iron and magnesium. The chemical analysis of Spectrum 3 likely indicates the presence of aluminum oxide, reduced silicon, and iron silicides. The spherical particles of iron-silicides may have been formed by phase separation from the larger particle; the spherical shape suggests a low degree of surface wetting with regards to the larger particle surface.

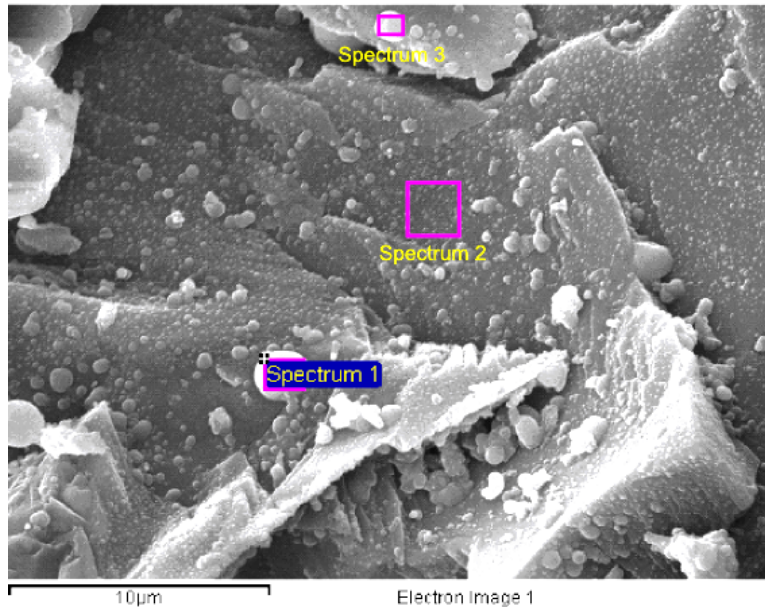


Figure CLXV: SEM micrograph of the microstructure in Region A for the 19.44% aluminum stoichiometry with EDS regions highlighted.

Table LXIV: EDS Analysis of Spectra 1, 2, and 3 shown in Figure CLXV

Element	Spectrum 1		Spectrum 2		Spectrum 3	
	Weight%	Atomic%	Weight%	Atomic%	Weight%	Atomic%
O	30.38	44.62	49.11	63.63	33.45	47.94
Na	-	-	1.47	1.32	-	-
Mg	1.74	1.68	0.52	0.44	2.83	2.67
Al	39.49	34.39	18.33	14.08	37.41	31.80
Si	16.04	13.41	21.95	16.20	15.13	12.36
Ca	4.15	2.43	7.81	4.04	3.95	2.26
Fe	8.22	3.46	0.81	0.30	7.22	2.97

Region B

The microstructure of the reaction product for Region B of a JSC-1A reaction product utilizing a 19.44% Al stoichiometry is shown in Figure CLXVI, as are EDS Spectra 1, 2, and 3. Table LXV shows the chemical data obtained from analysis of Spectrum 1, 2, and 3. Spectrum 1 is located on a protrusion from a large particle surface. The chemical composition indicates significant quantities of aluminum, silicon, and oxygen. EDS data from Spectrum 1 likely indicate the region is composed primarily of reduced aluminum and silicon, with some corundum. Reduced silicon could form during oxidation-reduction reactions between silicate

minerals and aluminum. Spectrum 2 is located on a spherical particle. EDS analysis indicates roughly equal quantities of aluminum and oxygen, along with some silicon. The chemical analysis likely indicates the presence of reduced aluminum and silicon, along with corundum. Spectrum 3 is located on a sub-spherical particle. Elemental analysis indicates large concentrations of aluminum, silicon, and oxygen. The chemical analysis of Spectrum 3 likely indicates the presence of reduced aluminum, corundum, and reduced silicon. Corundum formation could occur during and oxidation-reduction reaction involving a mineral such as anorthite and aluminum. The spherical particles of iron-silicides may have been formed by phase separation from the larger particle; the spherical shape suggests a low degree of surface wetting with regards to the larger particle surface.

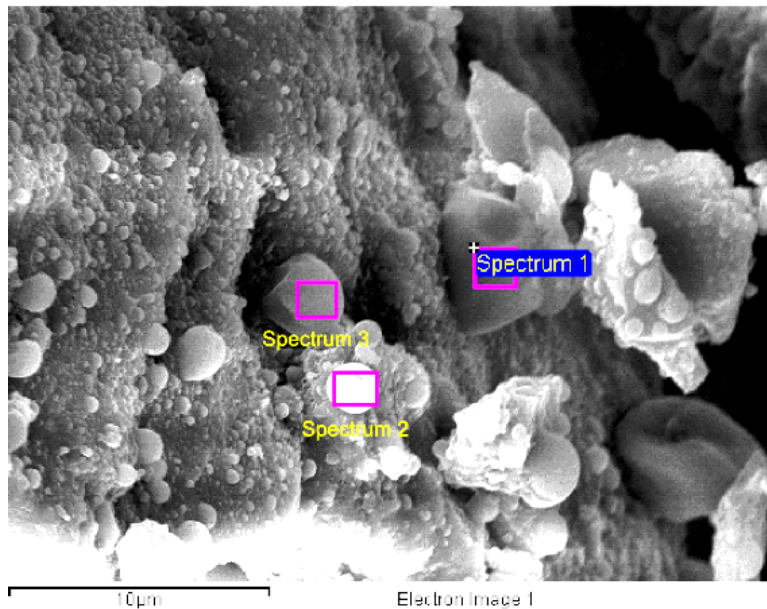


Figure CLXVI: SEM micrograph of the microstructure in Region B for the 19.44% aluminum stoichiometry with EDS regions highlighted.

Table LXV: EDS Analysis of Spectra 1, 2, and 3 shown in Figure CLXVI

Element	Spectrum 1		Spectrum 2		Spectrum 3	
	Weight%	Atomic%	Weight%	Atomic%	Weight%	Atomic%
O	12.09	19.14	32.31	45.58	19.39	29.48
Mg	-	-	1.48	1.37	0.76	0.76
Al	70.78	66.45	47.14	39.43	62.82	56.61
Si	14.49	13.07	13.99	11.25	12.97	11.23
Ca	0.82	0.52	1.76	0.99	0.76	0.46
Ti	-	-	0.66	0.31	0.42	0.21
Fe	1.83	0.83	2.65	1.08	2.89	1.26

24.45% Al by weight

Region A

The microstructure of the reaction product for Region A of a JSC-1A reaction product utilizing a 24.45% Al stoichiometry is shown in Figure CLXVII, as are EDS Spectra 1, 2, and 3. Table LXVI shows the chemical data obtained from analysis of Spectrum 1, 2, and 3. Spectrum 1 is located on a flat and smooth particle surface. The chemical composition indicates significant quantities of aluminum and oxygen. EDS data from Spectrum 1 likely indicate the region is composed primarily of spinel, grossite, and corundum. The formation of spinel, grossite, and corundum could occur during oxidation-reduction reactions involving minerals such as diopside and anorthite reacting with aluminum. Spectrum 2 is located on a spherical particle. EDS analysis indicates roughly equal quantities of iron, silicon, and aluminum. The chemical analysis likely indicates the presence of iron silicides. The formation of iron silicides could occur during a subsequent reaction incorporating the products of oxidation-reduction reactions involving minerals such as hedenbergite with aluminum. Spectrum 3 is located on a spherical particle. Elemental analysis indicates large concentrations of aluminum and oxygen, along with some silicon. The chemical analysis of Spectrum 3 likely indicates the presence of corundum, spinel, and reduced silicon. The spherical particles of iron-silicides may have been formed by phase separation from the larger particle; the spherical shape suggests a low degree of surface wetting with regards to the larger particle surface.

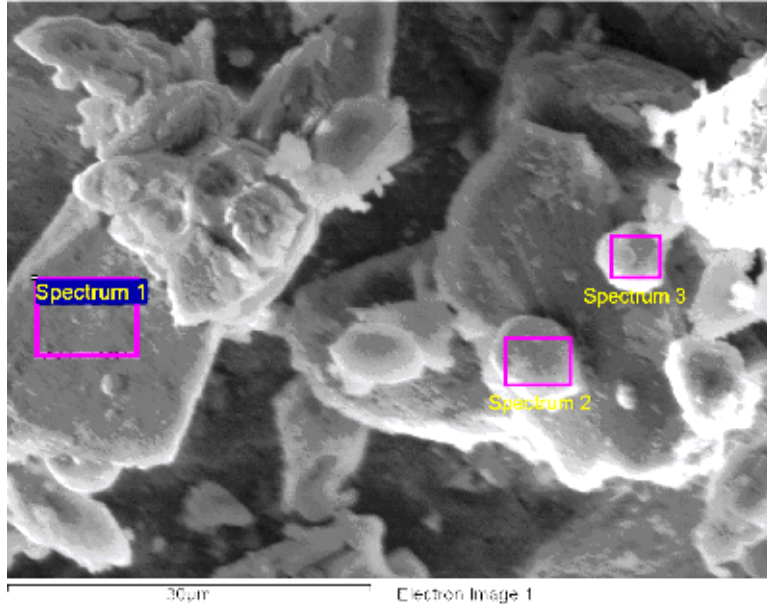


Figure CLXVII: SEM micrograph of the microstructure in Region A for the 24.45% aluminum stoichiometry with EDS regions highlighted.

Table LXVI: EDS Analysis of Spectra 1, 2, and 3 shown in Figure CLXVII

Element	Spectrum 1		Spectrum 2		Spectrum 3	
	Weight%	Atomic%	Weight%	Atomic%	Weight%	Atomic%
O	44.70	58.68	17.70	29.97	44.80	59.65
Mg	4.14	3.58	1.56	1.74	2.74	2.40
Al	40.32	31.38	29.58	29.69	32.23	25.45
Si	4.44	3.33	28.48	27.46	11.50	8.71
Ca	4.08	2.14	0.40	0.27	2.93	1.55
Ti	0.34	0.15	0.63	0.36	0.29	0.13
Cr	-	-	0.32	0.16	-	-
Fe	1.95	0.74	21.05	10.21	5.52	2.11
Ni	-	-	0.28	0.13	-	-

Region B

The microstructure of the reaction product for Region B of a JSC-1A reaction product utilizing a 24.45% Al stoichiometry is shown in Figure CLXVIII, as are EDS Spectra 1, 2, and 3. Table LXVII shows the chemical data obtained from analysis of Spectrum 1, 2, and 3. Spectrum 1 is located on a flat and smooth particle surface. The chemical composition indicates significant quantities of aluminum, magnesium, and oxygen, along with some silicon and iron. EDS data from Spectrum 1 likely indicate the region is composed primarily of spinel and iron silicides. Spinel formation could occur during an oxidation-reduction reaction involving a mineral such as

diopside reacting with aluminum. The formation of iron silicides could occur during a subsequent reaction incorporating the products of oxidation-reduction reactions involving minerals such as hedenbergite with aluminum. Spectrum 2 is located on a sub-spherical particle. EDS analysis indicates large quantities of aluminum and some silicon. The chemical analysis likely indicates that the particle is mostly aluminum and silicon. Spectrum 3 is located on an angular particle with a flat and smooth surface. Elemental analysis indicates large concentrations of aluminum and oxygen. The chemical analysis of Spectrum 3 likely indicates the presence of corundum.

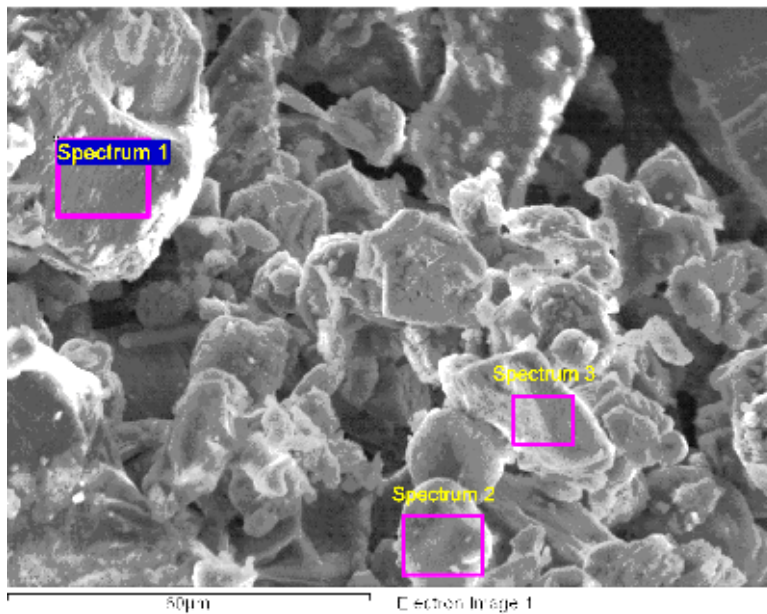


Figure CLXVIII: SEM micrograph of the microstructure in Region B for the 24.45% aluminum stoichiometry with EDS regions highlighted.

Table LXVII: EDS Analysis of Spectra 1, 2, and 3 shown in Figure CLXVIII

Element	Spectrum 1		Spectrum 2		Spectrum 3	
	Weight%	Atomic%	Weight%	Atomic%	Weight%	Atomic%
O	40.56	55.76	10.23	16.27	44.59	58.55
Mg	16.26	14.71	0.53	0.55	0.25	0.22
Al	19.33	15.75	75.49	71.22	47.43	36.92
Si	11.13	8.71	12.52	11.35	3.48	2.61
Ca	0.43	0.24	0.23	0.15	0.65	0.34
Ti	-	-	-	-	0.13	0.06
Fe	12.29	4.84	1.00	0.46	3.48	1.31

28.85% Al by weight

The microstructure of the reaction product for Region A of a JSC-1A reaction product utilizing a 28.85% Al stoichiometry is shown in Figure CLXIX, as are EDS Spectra 1, 2, and 3. Table LXVIII shows the chemical data obtained from analysis of Spectrum 1, 2, and 3. Spectrum 1 is located on a sub-spherical particle located on a large particle surface. The chemical composition indicates significant quantities of aluminum, silicon, and oxygen, along with some magnesium. EDS data from Spectrum 1 likely indicates the region is composed primarily of corundum, spinel, and reduced silicon. Corundum, spinel, and reduced silicon formation could occur during oxidation-reduction reactions involving minerals such as anorthite and diopside reacting with aluminum. Spectrum 2 is located on the surface of a large particle with many sub-spherical particles attached to it. EDS analysis indicates significant quantities of aluminum and oxygen, along with some silicon and magnesium. The chemical analysis likely indicates the presence of spinel and corundum. Spectrum 3 is located on a large and smooth particle surface, similar to the morphology of Spectrum 2. Elemental analysis indicates large concentrations of aluminum and oxygen, along with significant silicon. The chemical analysis of Spectrum 3 likely indicates the region likely has nearly the same composition as Spectrum 2.

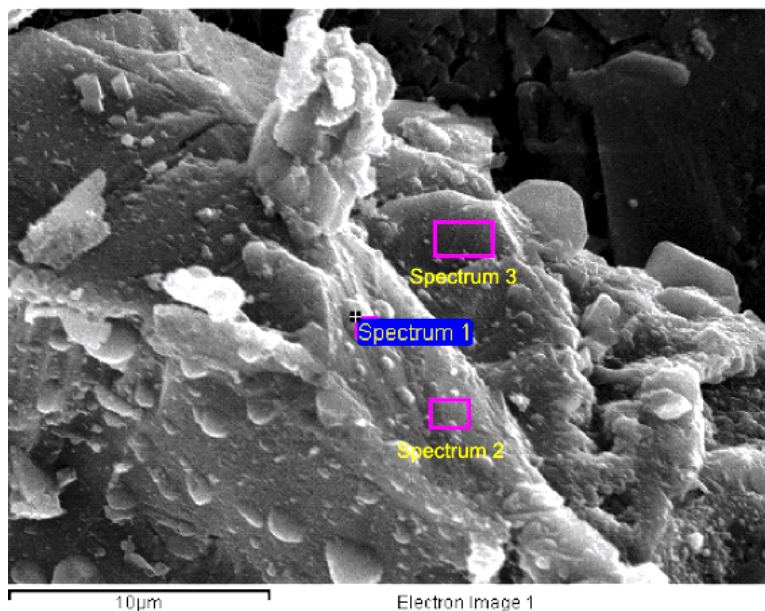


Figure CLXIX: SEM micrograph of the microstructure in Region A for the 28.85% aluminum stoichiometry with EDS regions highlighted.

Table LXVIII: EDS Analysis of Spectra 1, 2, and 3 shown in Figure CLXIX

Element	Spectrum 1		Spectrum 2		Spectrum 3	
	Weight%	Atomic%	Weight%	Atomic%	Weight%	Atomic%
O	43.37	57.35	56.24	68.61	54.27	66.46
Mg	5.18	4.52	8.19	6.59	9.61	7.75
Al	32.16	25.21	28.42	20.56	31.64	22.97
Si	14.41	10.85	4.27	2.97	3.32	2.33
Ca	1.37	0.72	2.07	1.01	0.63	0.31
Ti	0.31	0.14	-	-	-	-
Fe	3.18	1.20	0.80	0.28	0.53	0.18

Region B

The microstructure of the reaction product for Region B of a JSC-1A reaction product utilizing a 28.85% Al stoichiometry is shown in Figure CLXX, as are EDS Spectra 1, 2, and 3. Table LXIX shows the chemical data obtained from analysis of Spectrum 1, 2, and 3. Spectrum 1 is located on a spherical particle that is located on a large particle surface. The chemical composition indicates significant quantities of aluminum and oxygen, along with some silicon. EDS data from Spectrum 1 likely indicate the region is composed primarily of corundum, and possibly some reduced silicon. Formation of corundum could occur during an oxidation-reduction reaction involving a mineral such as anorthite reacting with aluminum. Spectrum 2 is located on a flat and smooth surface of a large particle. EDS analysis indicates significant quantities of aluminum and oxygen. The chemical analysis likely indicates the presence of corundum. Spectrum 3 is located on a large spherical particle. Elemental analysis indicates large concentrations of aluminum and oxygen, along with some silicon. The chemical analysis of Spectrum 3 likely indicates that corundum and reduced silicon are present. Silicon formation could occur during an oxidation-reduction reaction between a silicate mineral and aluminum.

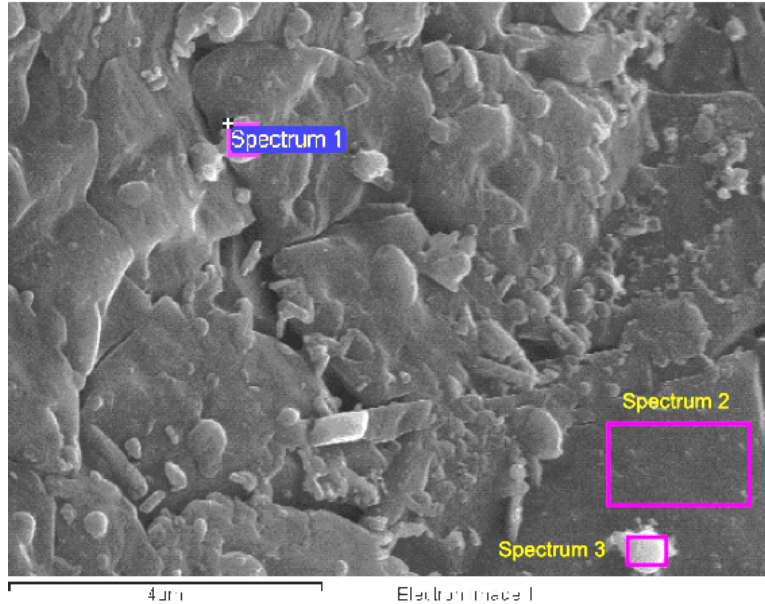


Figure CLXX: SEM micrograph of the microstructure in Region B for the 28.85% aluminum stoichiometry with EDS regions highlighted.

Table LXIX: EDS Analysis of Spectra 1, 2, and 3 shown in Figure CLXX

Element	Spectrum 1		Spectrum 2		Spectrum 3	
	Weight%	Atomic%	Weight%	Atomic%	Weight%	Atomic%
O	48.59	62.32	58.21	70.16	59.23	71.25
Mg	-	-	-	-	0.38	0.31
Al	41.24	31.36	40.42	28.89	34.81	24.83
Si	7.10	5.19	1.37	0.94	4.97	3.41
Fe	3.07	1.13	-	-	0.61	0.20

Region C

The microstructure of the reaction product for Region C of a JSC-1A reaction product utilizing a 28.85% Al stoichiometry is shown in Figure CLXXI, as are EDS Spectra 1 and 3. Table LXX shows the chemical data obtained from analysis of Spectrum 1 and 3. Spectrum 1 is located on a spherical particle. The chemical composition indicates significant quantities of silicon, aluminum and oxygen, along with some iron. EDS data from Spectrum 1 likely indicate the region is composed of reduced silicon, aluminum, corundum, and iron silicides. The formation of silicon and corundum could occur during an oxidation-reduction reaction involving a mineral such as anorthite reacting with aluminum. The formation of iron silicides could occur during a subsequent reaction incorporating the products of oxidation-reduction reactions

involving minerals such as hedenbergite with aluminum. Spectrum 3 is located on a smooth surface of a particle. Elemental analysis indicates large concentrations of silicon, aluminum, and oxygen. The chemical analysis of Spectrum 3 likely indicates that reduced silicon and aluminum, as well as corundum are present.

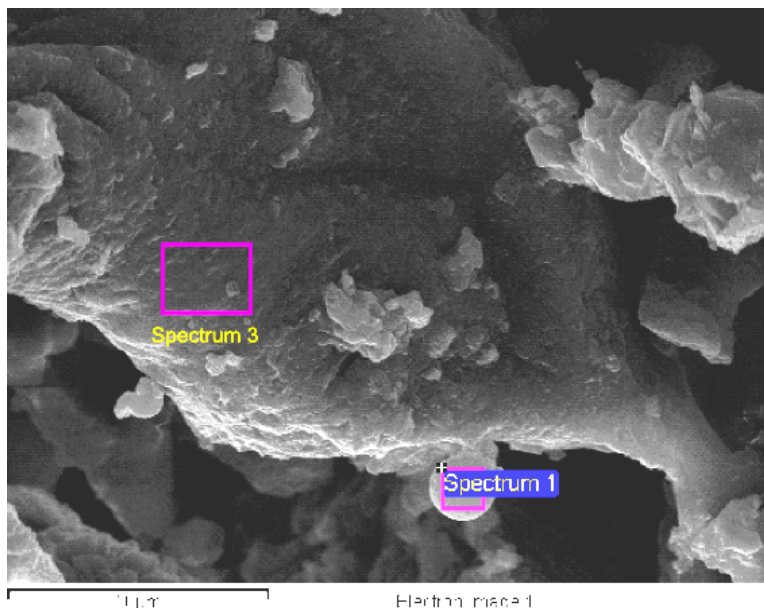


Figure CLXXI: SEM micrograph of the microstructure in Region C for the 28.85% aluminum stoichiometry with EDS region highlighted.

Table LXX: EDS Analysis of Spectra 1 and 3 shown in Figure CLXXI

Element	Spectrum 1		Spectrum 3	
	Weight%	Atomic%	Weight%	Atomic%
O	14.42	23.00	8.18	13.13
Mg	-	-	0.51	0.54
Al	52.82	49.95	74.54	70.99
Si	26.16	23.77	16.76	15.34
Ca	1.51	0.96	-	-
Fe	5.08	2.32	-	-

Region D

The microstructure of the reaction product for Region D of a JSC-1A reaction product utilizing a 28.85% Al stoichiometry is shown in Figure CLXXII, as are EDS Spectra 1 and 2. Table LXXI shows the chemical data obtained from analysis of Spectrum 1 and 2. Spectrum 1 is located on a spherical particle. The chemical composition indicates significant quantities of

silicon, aluminum and oxygen, along with some iron. EDS data from Spectrum 1 likely indicate the region is composed of reduced silicon, aluminum, corundum, and iron silicides. The formation of silicon and corundum could occur during an oxidation-reduction reaction involving a mineral such as anorthite reacting with aluminum. The formation of iron silicides could occur during a subsequent reaction incorporating the products of oxidation-reduction reactions involving minerals such as hedenbergite with aluminum. Spectrum 2 is located on a sub-spherical particle. Elemental analysis indicates large concentrations of aluminum and oxygen, along with some iron and silicon. The chemical analysis of Spectrum 2 likely indicates that corundum, aluminum, and iron silicides are present.

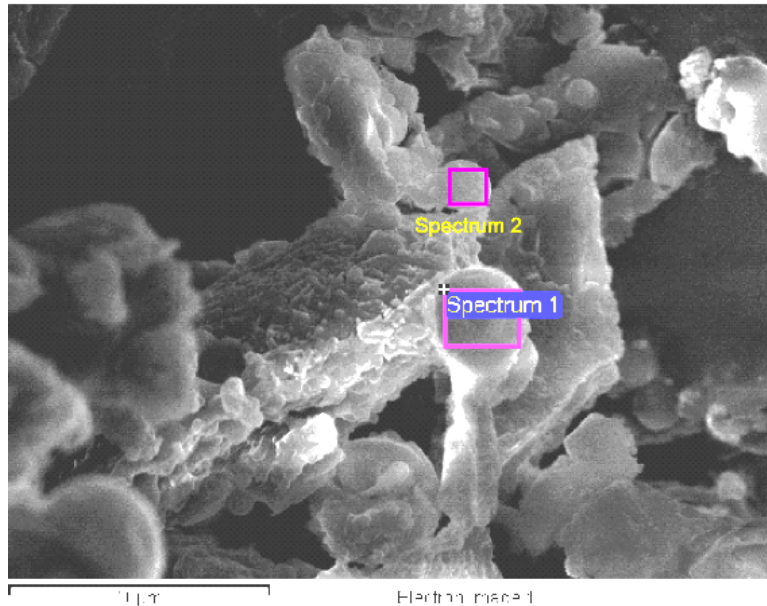


Figure CLXXII: SEM micrograph of the microstructure in Region D for the 28.85% aluminum stoichiometry with EDS regions highlighted.

Table LXXI: EDS Analysis of Spectra 1 and 2 shown in Figure CLXXII

Element	Spectrum 1		Spectrum 2	
	Weight%	Atomic%	Weight%	Atomic%
O	12.37	20.04	31.42	46.61
Al	66.84	64.19	48.15	42.35
Si	12.87	11.86	4.70	3.98
Ca	0.62	0.41	2.27	1.34
Ti	1.44	0.78	-	-
Fe	5.85	2.72	13.46	5.72

D. Density Measurements

This section covers the results of density measurements performed on reaction products synthesized in a standard atmosphere. Statistical analysis was conducted on the density datasets using t-tests in order to determine the statistical significance of density differences between reactants stoichiometries and simulant types.

Figure CLXXIII shows the mean measured density for SHS reaction products utilizing JSC-1AF and JSC-1A simulants for various reaction stoichiometries. The numbers before the colon on the label for each bar represent the weight percent of aluminum used, while the number following the colon indicates how many samples that data were obtained from. The error bars represent ± 1 standard deviation from the mean.

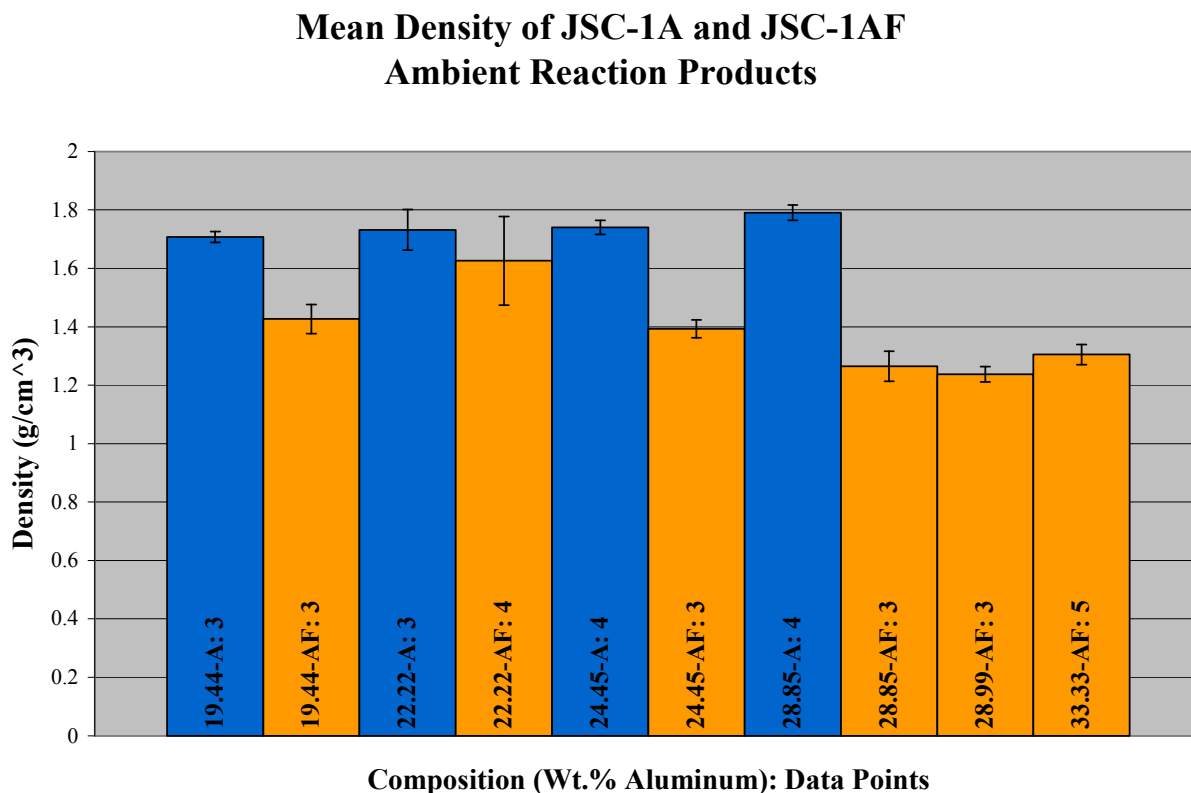


Figure CLXXIII: Mean Density of Reaction Products Utilizing JSC-1A and JSC-1AF simulants

T-tests were performed between datasets shown in Figure CLXXIII in order to determine whether variation in densities measured for reaction products synthesized using different simulants and reaction stoichiometries were statistically different. The results of the t-tests are

shown in Table LXXII and the certainty of statistical significance between each dataset is shown in the far right column. Orange color coding represents JSC-1AF stoichiometries, and blue color coding indicates JSC-1A stoichiometries.

Table LXXII: T-test Results for Mean Density Datasets shown in Figure CLXXIII

Dataset 1	Dataset 2	Certainty of Statistical Significance
19.44-AF	22.22-AF	95 %
22.22-AF	24.45-AF	97.5 %
24.45-AF	28.85-AF	97.5 %
28.85-AF	28.99-AF	75 %
28.99-AF	33.33-AF	99 %
19.44-A	22.22-A	60 %
22.22-A	24.45-A	-
24.45-A	28.85-A	97.5 %
19.44-AF	19.44-A	99.95 %
22.22-AF	22.22-A	75 %
24.45-AF	24.45-A	99.95 %
28.85-AF	28.85-A	99.95 %

The data in Figure CLXXIII indicates that the density of samples synthesized with JSC-1A simulant increased with larger aluminum quantities in the reactants. Larger quantities of aluminum would have resulted in more liquid aluminum that could fill pore spaces during the reaction process, forming a denser product. As aluminum content increased using the JSC-AF simulant, the density decreased on the whole. The 22.22% stoichiometry and 33.33% stoichiometry were exceptions to the trend. The quantity of evolved gas observed during the reaction was larger in the JSC-1AF simulant products, and appeared to increase with aluminum quantity. The evolution of gas could have resulted in higher porosities in the reaction product. Samples synthesized using JSC-1A simulant were significantly denser than those that used JSC-1AF simulant. The densities of JSC-1A samples ranged from ~20-40% larger than samples of JSC-1AF using the same stoichiometry. Data from Table LXXII indicate high statistical significance between most datasets, the main exception being the 22.22% aluminum stoichiometry using JSC-1A simulant.

E. Mechanical Strength Measurements

This section discusses the results of mechanical strength measurements performed on products of standard atmosphere reactions. Results of preliminary experiments are discussed, the method of failure is described, the ultimate compressive strengths of reactant stoichiometries and simulant types are compared, and differences elastic moduli between reactant stoichiometries and simulant types are discussed.

Preliminary Experiment Results

In initial experiments, several samples were wet cut using a diamond blade and water. An ammonia type smell was encountered after sample exposure to water. The samples were placed in ziplock bags and sealed after cutting. One of the sample bags inflated and popped open. In another instance, the sample exposed to water broke apart. From the previous observations it was hypothesized that water was chemically reacting with the reaction product, and evolving gas. Therefore, another method to machine the samples was required. The method chosen used a ceramic tile saw with a diamond blade to dry cut the samples.

Experimental Results

Sample failure was observed to occur primarily by propagation of near vertical cracks. The failure mode indicated that the specimen ends were leveled adequately to allow even load distribution across the top and bottom sample surfaces. Fracture and spallation of outer areas of the cylinders were commonly observed. It is likely that spallation was induced by tension produced perpendicular to the compressive force within the sample. It is also likely that locations of spallation were influenced by heat gradients produced by the NiCr wire and the combustion wave. Heat gradients could have been induced by variations in specific heat and thermal conductivity within different chemical species in the reaction product. Figure CLXXIV-Figure CLXXVII are images of fractured reaction products for various stoichiometries of JSC-1AF and JSC-1A simulants. The images in Figure CLXXIV-Figure CLXXVII show fracture propagation throughout the length of the specimen, indicating the sample ends were leveled adequately for the compressive strength tests.



Figure CLXXIV: Fracture of a JSC-1AF, 33.33% Al stoichiometry synthesized in a standard atmosphere.

Figure CLXXV: Fracture of a JSC-1A, 28.85% Al stoichiometry synthesized in a standard atmosphere.



Figure CLXXVI: Fracture of a JSC-1AF, 46.67% Al stoichiometry synthesized in a standard atmosphere.

Figure CLXXVII: Fracture of a JSC-1A, 28.85% Al stoichiometry synthesized in a standard atmosphere.

Figure CLXXVIII shows the ultimate mean compressive strength of various reactant stoichiometries synthesized in a standard atmosphere using JSC-1AF and JSC-1A simulants. The first number within each bar on the chart refers to the weight percent aluminum used in the reaction, the letters that follow denote whether JSC-1A simulant or JSC-1AF simulant was used, and the last number denotes how many compressive tests were run on the given stoichiometry. The error bars represent ± 1 standard deviation from the mean.

Mean Compressive Strength of JSC-1A and JSC-1AF Ambient Reaction Products

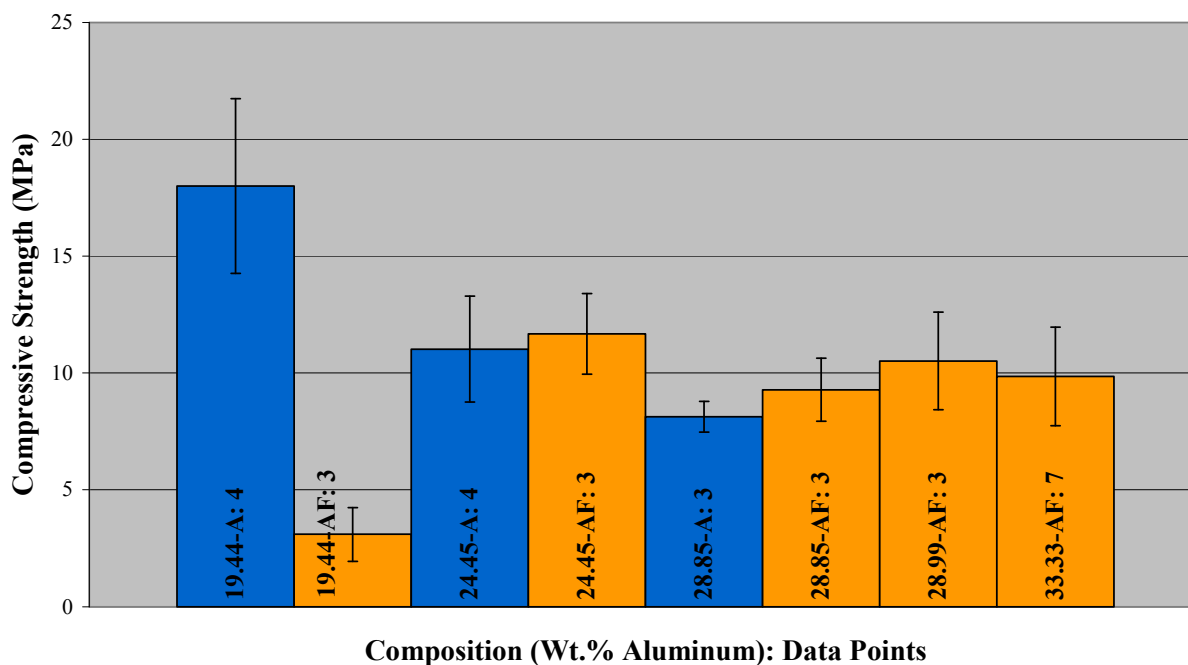


Figure CLXXVIII: Mean Compressive Strength of JSC-1A and JSC-1AF Standard Atmosphere Reaction Products

T-tests were performed between datasets shown in Figure CLXXVIII in order to determine whether the strength measured between simulants and reaction stoichiometries were statistically different. The results of the t-tests are shown in Table LXXIII, with the certainty of statistical significance between datasets shown in the far right column. Orange color coding represents JSC-1AF stoichiometries, and blue color coding represents JSC-1A stoichiometries.

Table LXXIII: T-test Results for Compressive Strength Datasets shown in Figure CLXXVIII

Dataset 1	Dataset 2	Certainty of Statistical Significance
19.44-AF	24.45-AF	99.5%
24.45-AF	28.85-AF	90%
28.85-AF	28.99-AF	75%
28.99-AF	33.33-AF	60%
19.44-A	24.45-A	99%
24.45-A	28.85-A	95%
19.44-AF	19.44-A	99.95%
24.45-AF	24.45-A	60%
28.85-AF	28.85-A	75%

Data from Figure CLXXVIII indicate that the low aluminum stoichiometries utilizing the coarse regolith simulant had the highest compressive strengths by a substantial margin. All the aluminum stoichiometries using JSC-1AF simulant except the 19.44% stoichiometry had fairly similar compressive strengths. Data from Table LXXIII indicate very high statistical significance between 19.44-AF and 24.45-AF; 19.44-A and 24.45-A; and 19.44-AF and 19.44-A datasets. A material with a larger particle size exhibiting larger strength than a material with a smaller particle size does not follow the Hall-Petch relationship. It was hypothesized that the higher strength exhibited by the coarse regolith simulant product was caused partially by chemical composition, and partially by higher densities. XRD data indicate that the lowest stoichiometries of aluminum using JSC-1A simulant had larger diffraction intensities for spinel than other reactant stoichiometries. XRD data also indicate the presence of substantially less reduced silicon within the 19.44% aluminum stoichiometries. SEM and EDS analyses indicate that dense networks of whiskers interconnect particles. Whiskers containing bound nitrogen are found in all standard atmosphere reaction products. XRD data indicate the presence of aluminum nitrides; it is therefore hypothesized that the nitrogen containing whiskers are composed of aluminum nitrides. Whiskers containing no nitrogen have also been found in the 19.44% and 24.45% aluminum stoichiometries using both types of simulant. The whiskers that contain no nitrogen may exist in all stoichiometries; however, the whiskers appear to be significantly more abundant in the 19.44% and 24.45% aluminum stoichiometries. The whiskers

containing no nitrogen have substantial aluminum and oxygen present, along with varying quantities of magnesium and silicon. It is likely that the whiskers containing no nitrogen are composed of aluminum oxide and $Mg_{0.388}Al_{2.408}O_4$. The high strengths characteristic of whiskers of aluminum nitride and aluminum oxide were likely to increase the compressive strength of the reaction product.

The coarse regolith simulant produced denser reaction products than the fine regolith simulant. It is likely that the higher sample densities of the JSC-1A simulant allowed more particle contact, promoted better sintering, and formed a stronger product. Micrographs seem to indicate a higher density of aluminum nitride whiskers within coarse regolith simulant reaction products. The diffraction intensities for aluminum nitride are significantly higher within the 19.44% and 24.45% aluminum stoichiometries using JSC-1A simulant than those using the JSC-1AF simulant. The closer packed particles may facilitate the formation of denser whisker networks and shorter whisker lengths, inducing a higher strength. The fine regolith simulant has higher porosity, which would cause longer whiskers to form between particles, and lower the total density of whiskers, thereby decreasing strength.

Figure CLXXIX and Figure CLXXX show the stress-strain curves for JSC-1AF and JSC-1A standard atmosphere reaction products, respectively. The stress-strain curves shown below are the best of all the data sets that were collected. Deformation of the reaction product prior to failure appeared to be considerably smaller in the JSC-1A simulant. The greatest deformation was observed in the largest aluminum stoichiometries using JSC-1AF simulant. Deformation increased with increasing aluminum in both JSC-1AF and JSC-1A simulant. The increase in deformation was likely due to the larger amount of metallic bonding present in the reaction products with larger quantities of aluminum present in the reactants. An increase in whisker quantities might also have allowed a greater deformation prior to failure. In the reaction products of both simulants there seemed to be a trend where as deformation increased, ultimate compressive strength decreased. The elastic moduli for the 19.44% and 28.85% stoichiometries were ~ 28 MPa. The elastic moduli for the 24.45% and 33.33% stoichiometries were 48 MPa and 18 MPa, respectively. A progressive decrease was observed in elastic moduli as aluminum increased from 24.45% to 33.33% using the JSC-AF simulant in Figure CLXXIX. Equation 8 gave the relationship between porosity and elastic modulus. The decrease in elastic moduli agrees with the trend of Equation 8, in that densities decreased from 24.45% to 33.33%.

The elastic moduli of the JSC-1A products, shown in Figure CLXXX, appear roughly equal (~ 50 MPa) for a small initial region. After the initial region, the 19.44% stoichiometry has a quasi-linear region with a significantly higher elastic modulus (~281 MPa) than the 24.45% and 28.85% stoichiometries that have quasi-linear regions that are roughly equivalent. The elastic moduli trend of the JSC-1A products does not correlate with Equation 8. It is possible that the non-correlation with the Hall-Petch relationship and Equation 8 represents an appreciable difference in chemical composition between reaction products. Overall it appears that the reaction products using the lowest aluminum stoichiometries behaved in a more brittle manner, while the higher aluminum stoichiometries were more ductile. It appeared that the JSC-1AF reaction products have more ductility than the JSC-1A reaction products.

Compressive Stress vs Strain for JSC-1AF Reaction Products

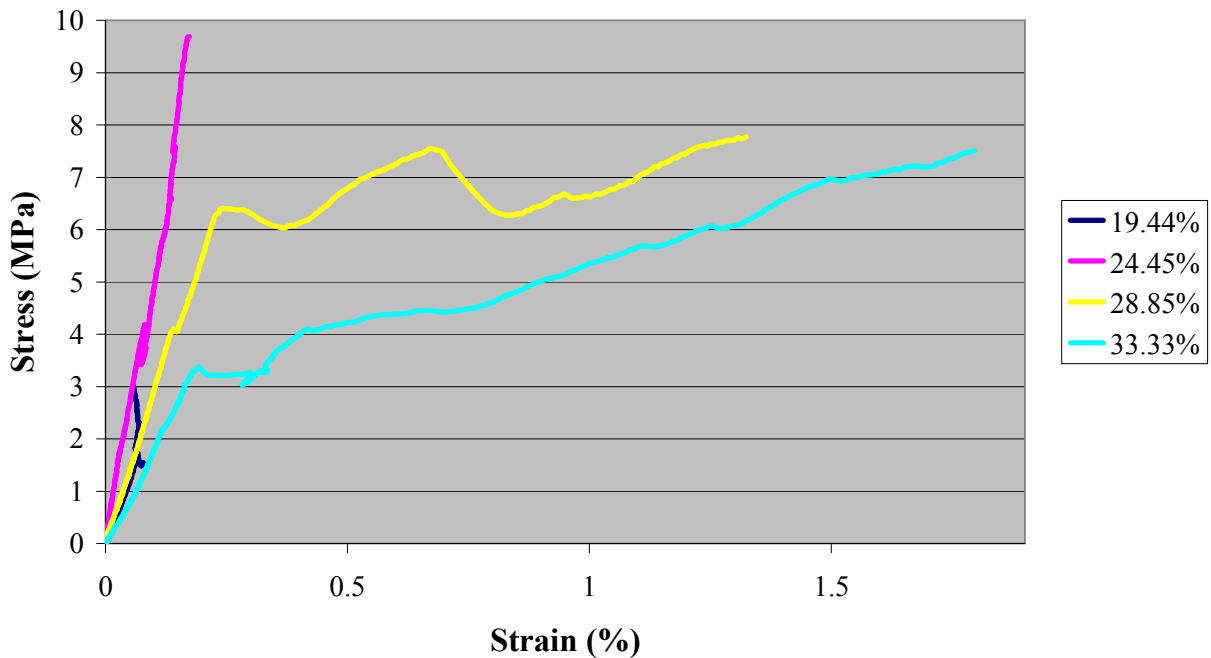


Figure CLXXIX: Stress-strain curves for standard atmosphere reaction products using JSC-1AF.

Compressive Stress vs Strain for JSC-1A Reaction Products

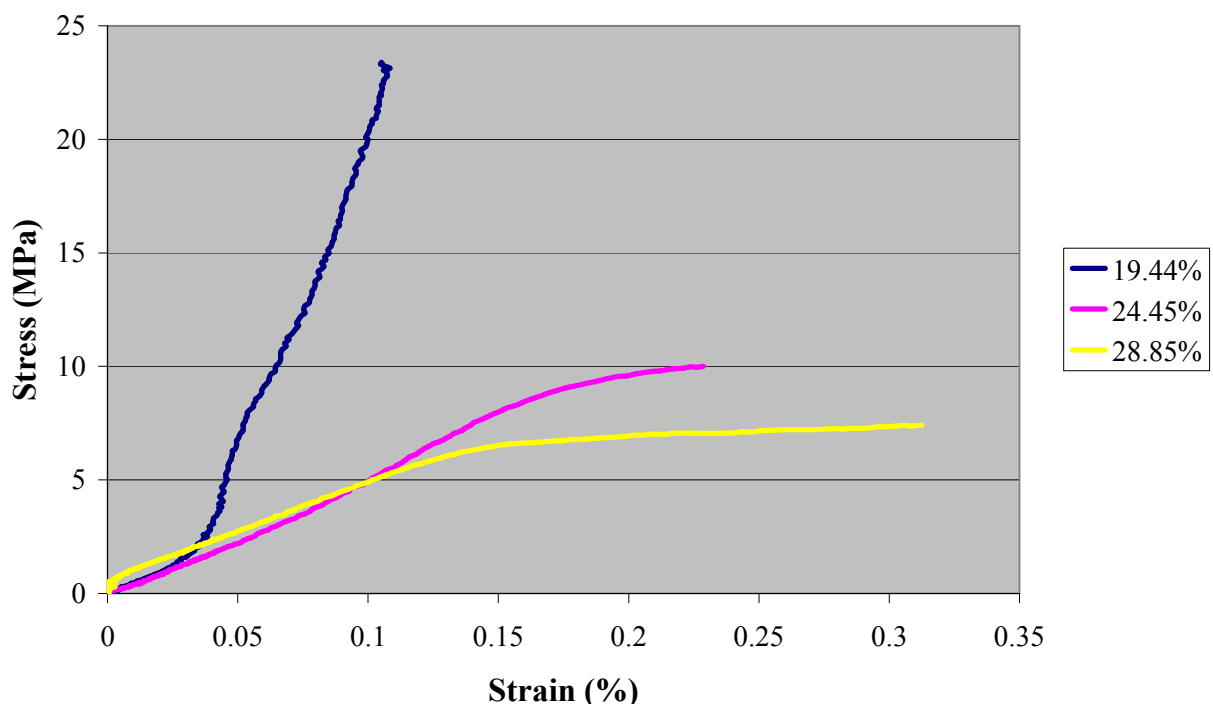


Figure CLXXX: Stress-strain curves for standard atmosphere reaction products using JSC-1A.

F. Energy Required to Initiate SHS Reactions

This section discusses the results of energy measurements required to initiate SHS reactions in a standard atmosphere using various reaction stoichiometries of JSC-1AF and JSC-1A simulants. Statistical analysis was performed on the energy datasets using t-tests in order to establish the certainty of statistical significance between differences in energy measurements obtained from each reaction stoichiometry and simulant type.

Mean Energy Required to Initiate JSC-1AF Reactions

Figure CLXXXI shows the mean energy required to initiate SHS reactions utilizing JSC-1AF simulant for various reaction stoichiometries. The number before the colon on the label for each bar represents the weight percent of aluminum used in the reactants, while the number following the colon indicates how many samples that data were obtained from. The error bars represent ± 1 standard deviation from the mean.

Mean Energy Required to Initiate Ambient JSC-1AF SHS Reactions

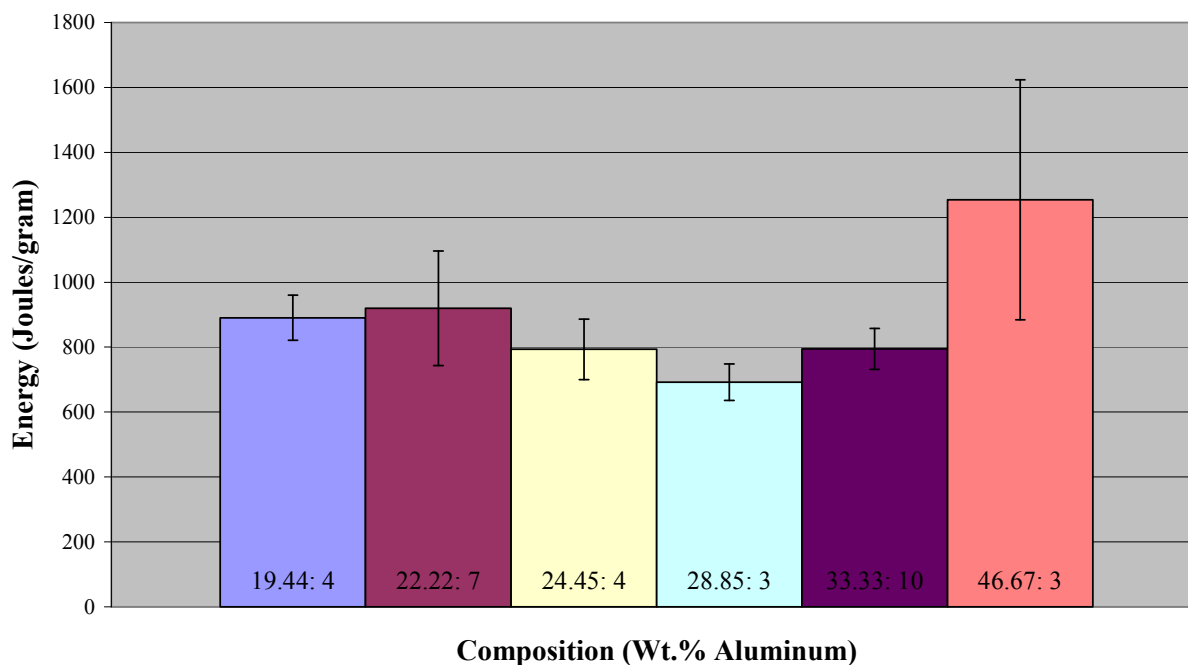


Figure CLXXXI: A graph of the mean energy required to initiate an SHS reaction vs the aluminum composition for the JSC-1AF simulant.

T-tests were performed between datasets shown in Figure CLXXXI in order to determine if the energies measured to initiate reactions for various reaction stoichiometries are statistically different. The results of the t-tests are show in Table LXXIV, with the degree of certainty of statistical significance between datasets shown in the far right column.

Table LXXIV: T-test Results for Reaction Initiation Energy Datasets shown in Figure CLXXXI

Dataset 1	Dataset 2	Certainty of Statistical Significance
19.44	22.22	60 %
22.22	24.45	90 %
24.45	28.85	90 %
28.85	28.99	99.5 %
28.99	33.33	99.95 %
33.33	46.67	95 %

Data from Figure CLXXXI indicate the minimum energy required to initiate a reaction occurred in the 28.85% aluminum composition. Data from Table LXXIV indicate that high statistical significance exists between datasets, except for the 19.44% and 22.22% stoichiometries. The 28.85% stoichiometry was calculated in order to have enough aluminum present to reduce all oxides present in the JSC-1AF bulk composition data shown in Table II. The energy required to initiate the reaction increased towards the upper and lower limits of aluminum stoichiometries. The mean energy required to initiate reactions within the JSC-1AF simulant exhibited a maximum at 46.67 wt.% aluminum. As the quantity of aluminum increased, a larger amount of energy was required in order to melt the aluminum. As aluminum decreased below a critical value, experimentally determined to be in the vicinity of 28.85 wt.%, energy required to initiate the reaction increased. Energy required to initiate the reaction likely increased in the low aluminum stoichiometries due to a lower quantity of oxidation-reduction reactions that were able to occur. Aluminum quantities less than the critical value were not able to produce as much heat during the reaction from the same volume of sample, which means that more external energy was needed to initiate self-propagation.

Mean Energy Required to Initiate JSC-1A Reactions

Figure CLXXXII shows the mean energy required to initiate SHS reactions utilizing JSC-1A simulant for various reaction stoichiometries. The number before the colon on the label for each bar represents the weight percent of aluminum used, while the number following the colon

indicates how many samples that data were obtained from. The error bars represent ± 1 standard deviation from the mean.

Mean Energy Required to Initiate Ambient JSC-1A SHS Reactions

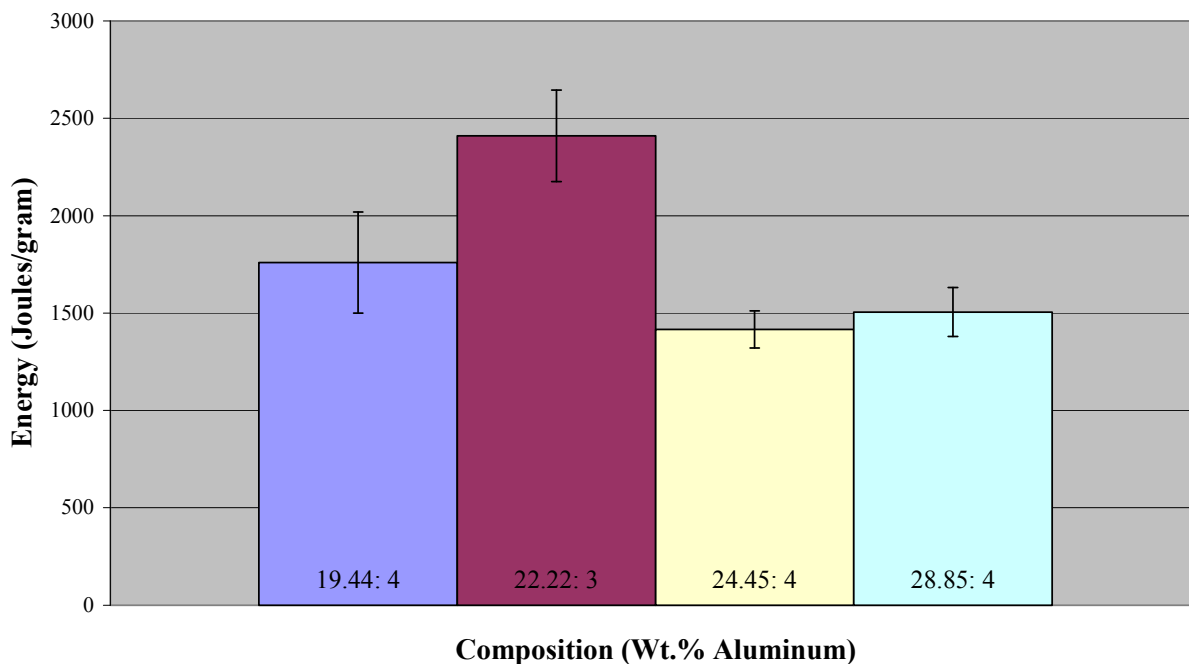


Figure CLXXXII: A graph of the mean energy required to initiate an SHS reaction vs the aluminum composition for the JSC-1A simulant.

T-tests were performed between datasets shown in Figure CLXXXII in order to determine if the energies measured to initiate reactions for various reaction stoichiometries were statistically different. The results of the t-tests are shown in Table LXXV, with the certainty of statistical significance between datasets in the far right column.

Table LXXV: T-test Results for Reaction Initiation Energy Datasets shown in Figure CLXXXII

Dataset 1	Dataset 2	Certainty of Statistical Significance
19.44	22.22	99 %
22.22	24.45	99.95 %
24.45	28.85	75 %

When the energies required to initiate the reactions utilizing JSC-1A simulant in Figure CLXXXII are examined, a similar shaped energy graph to the JSC-1AF simulant is observed. Data from Table LXXV indicate high statistical significance between the 19.44% and 22.22%; and the 22.22% and 24.45% datasets. The energies required to initiate the JSC-1A reactions, however, were substantially higher in all stoichiometries. The minimum required energy to initiate a reaction occurred in the 24.45% aluminum stoichiometry. The stoichiometry at which a minimum energy was required to initiate a reaction was likely to represent a balance between excess aluminum drawing heat away from reaction, and insufficient aluminum preventing complete reaction with the regolith simulant. The maximum energy occurred in the 22.22% aluminum stoichiometry, followed by a decrease in energy required for initiation slightly larger than a standard deviation for the 19.44% stoichiometry.

Mean Energy Required to Initiate JSC-1A & JSC-1AF Reactions

Figure CLXXXIII shows the mean energy required to initiate SHS reactions utilizing JSC-1AF and JSC-1A simulants for various reaction stoichiometries. The number before the colon on the label for each bar represents the weight percent of aluminum used, while the number following the colon indicates how many samples that data were obtained from. The error bars represent ± 1 standard deviation from the mean. The energies required to initiate the reaction in JSC-1AF and JSC-1A reactant stoichiometries are shown in orange and blue, respectively.

Mean Energy Required to Initiate Ambient Reactions

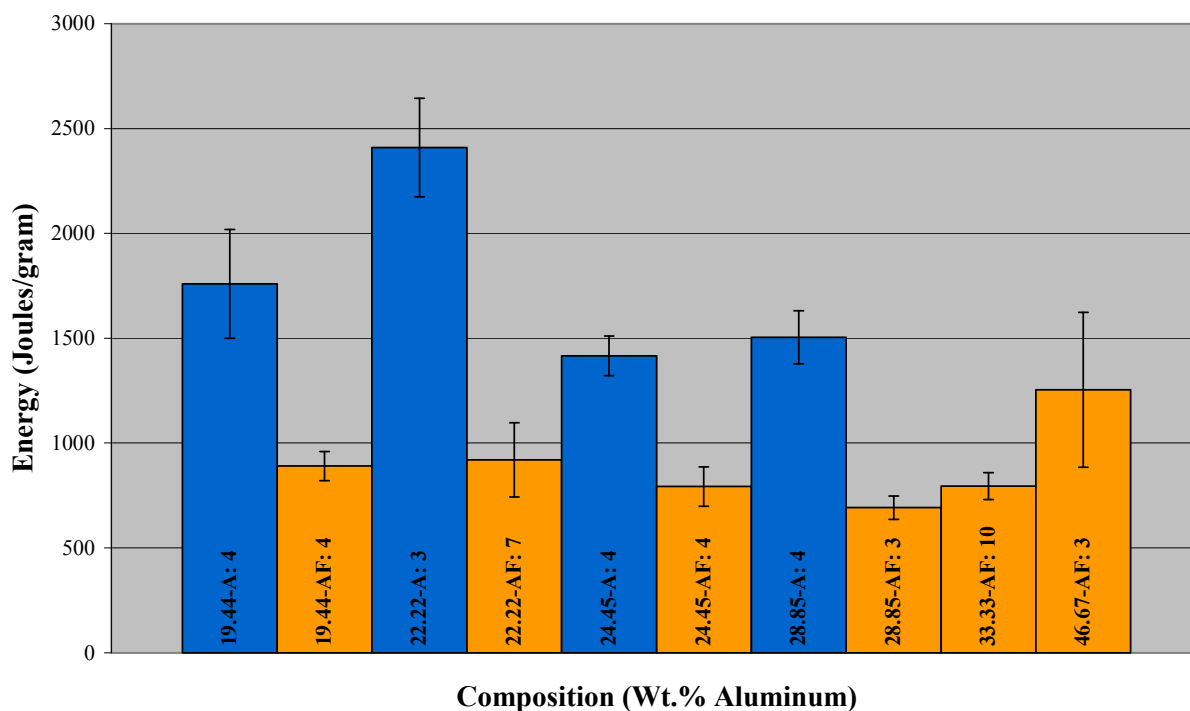


Figure CLXXXIII: A graph of the mean energy required to initiate an SHS reaction vs the aluminum composition and type of regolith simulant.

T-tests were performed between datasets shown in Figure CLXXXIII to determine if the energies measured to initiate reactions for various reaction stoichiometries were statistically different. The results of the t-tests are shown in Table LXXVI, with the certainty of statistical significance between datasets in the far right column. Orange color coding represents JSC-1AF stoichiometries, and blue color coding represents JSC-1A stoichiometries.

Table LXXVI: T-test Results for Reaction Initiation Energy Datasets shown in Figure CLXXXIII

Dataset 1	Dataset 2	Certainty of Statistical Significance
19.44-A	19.44-AF	99.95 %
22.22-A	22.22-AF	99.95 %
24.45-A	24.45-AF	99.95 %
28.85-A	28.85-AF	99.95 %

The data in Figure CLXXXIII indicate that larger energies were required to initiate reactions utilizing the JSC-1A simulant. The larger amount of energy was likely needed due to the lower surface area per unit volume of the coarse regolith simulant particles. The lower surface area reduced the quantity of oxidation-reduction reactions that could occur, which decreased the heat produced from reactions using the same quantity of external heat input. When heat was applied to aluminum it was absorbed; and when enough heat was absorbed, the aluminum melted. If the aluminum had no simulant around it to react with, no energy was released from reactions. XRD analysis indicated that there were some unreacted chemical species from the simulant in the product of the 19.44% stoichiometry using JSC-1A simulant, while none appeared in the JSC-1AF reaction product. The presence of unreacted chemical species in a reaction product observed macroscopically to be fully reacted indicated that although extensive sintering and intergranular binding through whiskers was occurring at the surfaces of particles, some of the particle interiors were left unreacted.

Energy Required to Initiate SHS Reactions in a Vacuum

It was not possible to accurately determine the time at which reactions began in vacuum due to the limited viewing area of the viewport. Therefore, energy calculations were not performed for vacuum synthesized reaction products.

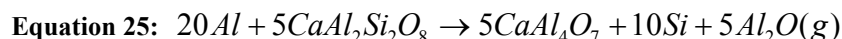
G. Reaction Thermodynamics

This section utilizes thermodynamics to propose possible chemical reactions between chemical species identified in the regolith simulants, and chemical species identified through XRD in the reaction products for standard atmosphere and vacuum reactions. Chemical reactions were input into the computer program FactSage. The resulting data were then used to create plots of enthalpy and Gibbs free energy for the chemical reaction over a proposed range of temperatures (298 K to 1998 K).

Standard Atmosphere

Figure CLXXXIV shows the ΔG and ΔH plots for a reaction between aluminum and anorthite, identified in Equation 25. The ΔG for Equation 25 turns negative around 550 K,

making the reaction thermodynamically favorable at higher temperatures. The reaction is endothermic over the proposed temperature range, except for a small region of temperatures just below 1700 K. If a reaction following Equation 25 occurred, it would consume heat over the majority of reaction temperatures and produce the gas Al_2O , which was hypothesized to react with ambient nitrogen (Equation 26) and oxygen (Equation 27). The interaction with nitrogen and oxygen was hypothesized to form the whisker networks observed in standard atmosphere reactions. Other products of Equation 25 include grossite ($CaAl_4O_7$), and silicon.



Enthalpy and Gibbs Free Energy Plot for the Standard Atmospheric Reaction:

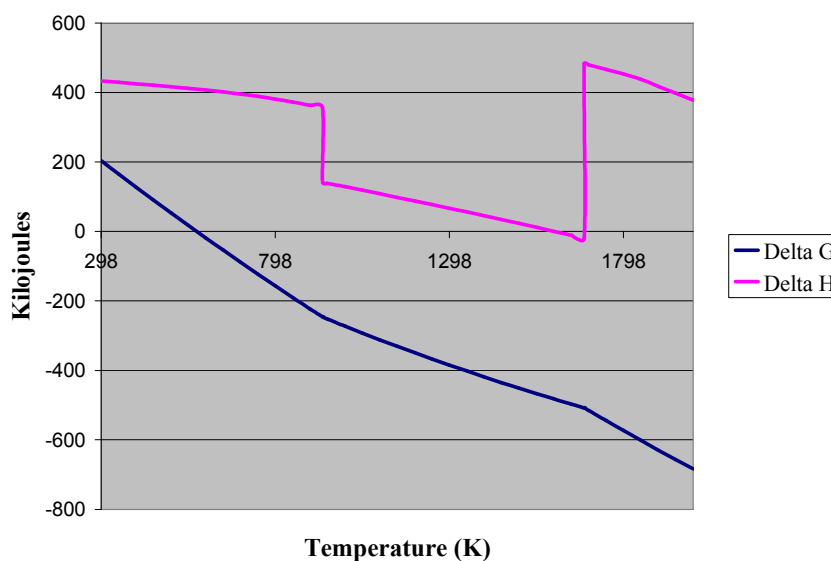
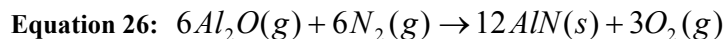


Figure CLXXXIV: Enthalpy and Gibbs Free Energy Plot for $20Al + 5CaAl_2Si_2O_8 \rightarrow 5CaAl_4O_7 + 10Si + 5Al_2O$

Figure CLXXXV shows the ΔG and ΔH plots for a reaction between Al_2O (g) and N_2 (g), identified in Equation 26, over a proposed range of temperatures. The ΔG for Equation 26 is negative until just under 1700 K, making the reaction thermodynamically favorable over a large temperature range. The reaction is highly exothermic over the proposed temperature range. In addition to the production of AlN , O_2 would also be produced by the reaction of Al_2O and N_2 .

Production of gaseous species was evidenced by evolution of gas during many of the reactions that were conducted in a standard atmosphere, particularly at larger aluminum stoichiometries.



Enthalpy and Gibbs Free Energy Plot for the Standard Atmospheric Reaction:

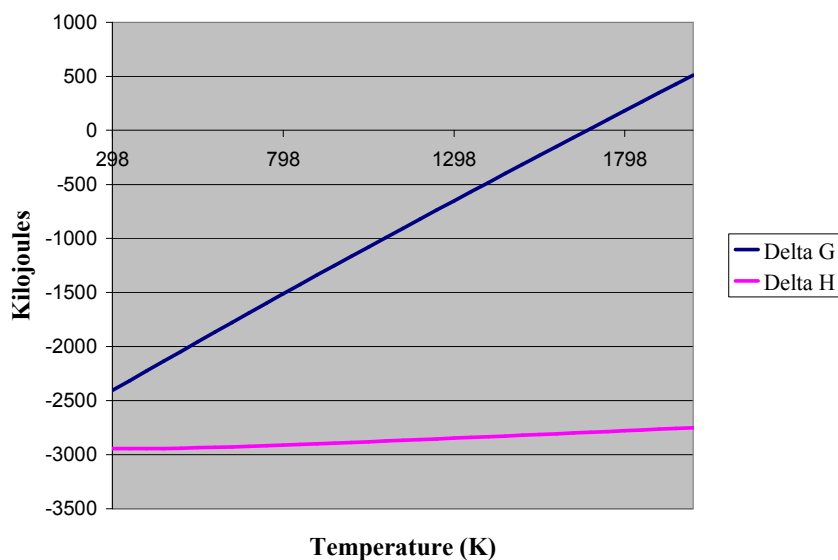
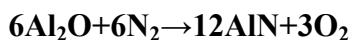
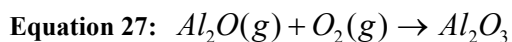


Figure CLXXXV: Enthalpy and Gibbs Free Energy Plot for $6Al_2O + 6N_2 \rightarrow 12AlN + 3O_2$

Figure CLXXXVI shows the ΔG and ΔH plots for a reaction between Al_2O (g) and O_2 (g) identified in Equation 27, over a proposed range of temperatures. The ΔG for Equation 27 is negative throughout the temperature range, making the reaction thermodynamically favorable. The reaction is also exothermic throughout the temperature range.



Enthalpy and Gibbs Free Energy Plot for the Standard Atmospheric Reaction:

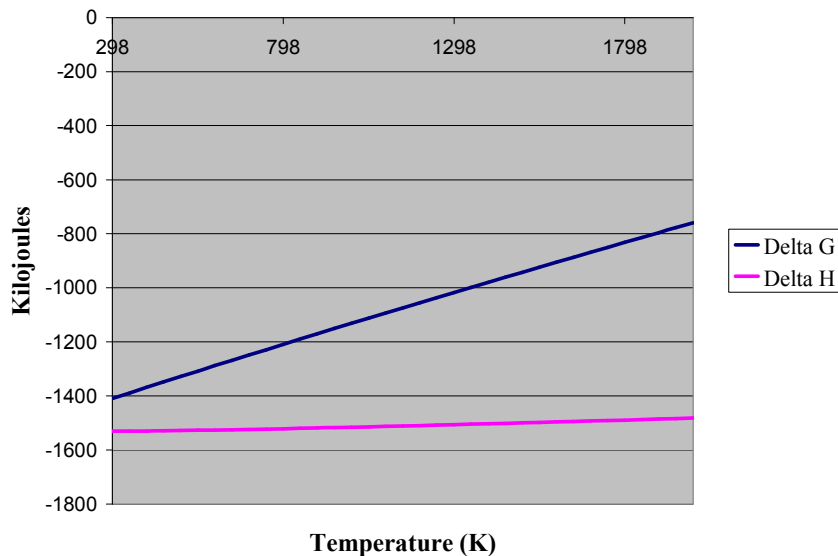
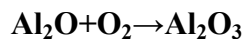
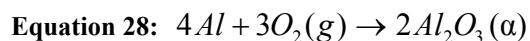


Figure CLXXXVI: Enthalpy and Gibbs Free Energy Plot for $\text{Al}_2\text{O} + \text{O}_2 \rightarrow \text{Al}_2\text{O}_3$

Figure CLXXXVII shows the ΔG and ΔH plots for a reaction between Al and O_2 (g), identified in Equation 28, over a proposed range of temperatures. The ΔG for Equation 28 is negative throughout the temperature range, making the reaction thermodynamically favorable. The reaction is also highly exothermic over the entire temperature range.



Enthalpy and Gibbs Free Energy Plot for the Standard Atmospheric Reaction:

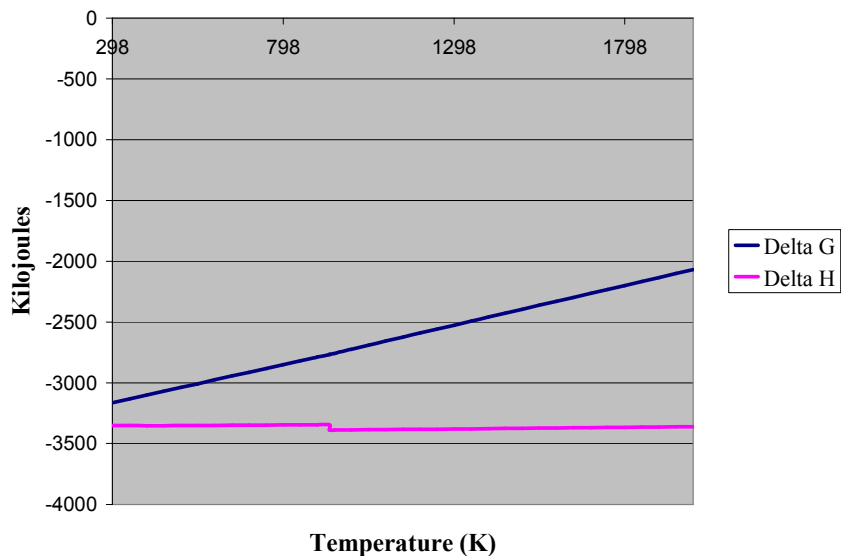
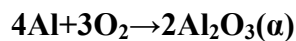
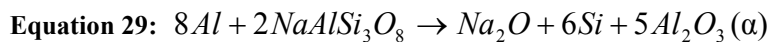
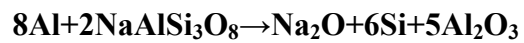


Figure CLXXXVII: Enthalpy and Gibbs Free Energy Plot for $4\text{Al} + 3\text{O}_2 \rightarrow 2\text{Al}_2\text{O}_3$

Figure CLXXXVIII shows the ΔG and ΔH plots for a reaction between aluminum and albite (low) identified in Equation 29, over a proposed range of temperatures. Figure CLXXXIX shows the same reaction as Equation 29, using another phase of albite, high-albite. The ΔG for Equation 29 is negative throughout the temperature range, making the reaction thermodynamically favorable. The reaction is also exothermic over the entire temperature range.



Enthalpy and Gibbs Free Energy Plot for the Standard Atmospheric Reaction:



(Low albite and α - Al_2O_3)

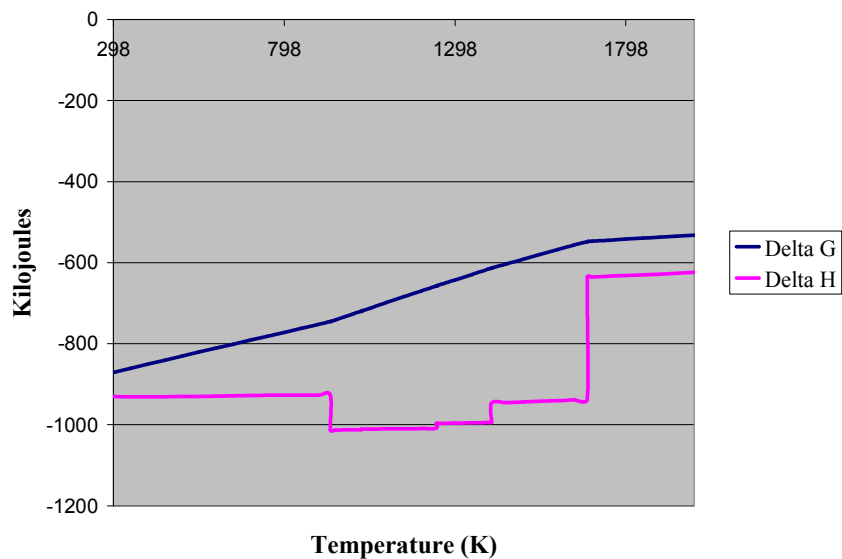


Figure CLXXXVIII: Enthalpy and Gibbs Free Energy Plot for $8\text{Al} + 2\text{NaAlSi}_3\text{O}_8 \rightarrow \text{Na}_2\text{O} + 6\text{Si} + 5\text{Al}_2\text{O}_3$

Enthalpy and Gibbs Free Energy Plot for the Standard Atmospheric Reaction:
 $8\text{Al} + 2\text{NaAlSi}_3\text{O}_8 \rightarrow \text{Na}_2\text{O} + 6\text{Si} + 5\text{Al}_2\text{O}_3$
(High Albite and $\alpha\text{-Al}_2\text{O}_3$)

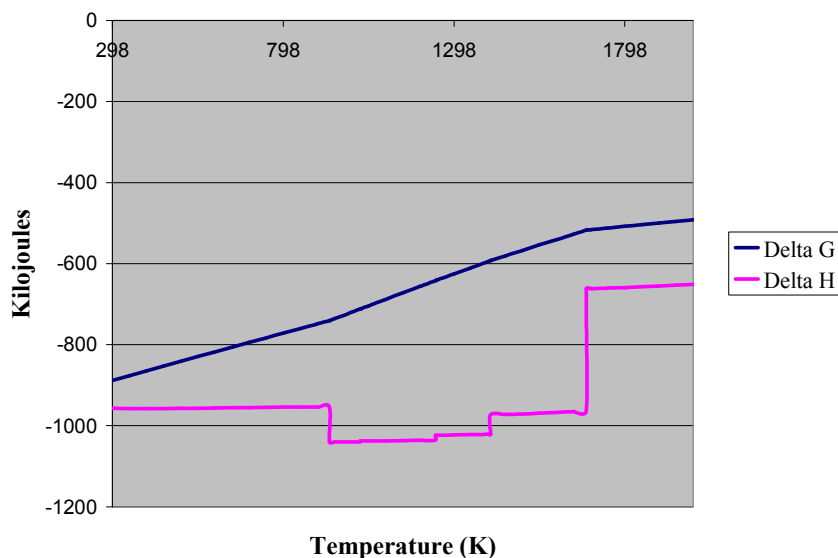


Figure CLXXXIX: Enthalpy and Gibbs Free Energy Plot for $8\text{Al} + 2\text{NaAlSi}_3\text{O}_8 \rightarrow \text{Na}_2\text{O} + 6\text{Si} + 5\text{Al}_2\text{O}_3$

Figure CXC shows the ΔG and ΔH plots for a reaction between aluminum and diopside identified in Equation 30, over a proposed range of temperatures. The ΔG for Equation 30 is negative at temperatures above ~ 400 K, making the reaction thermodynamically favorable over the vast majority of the temperature range. The reaction is endothermic over most of the temperature range, except for a region between ~ 1300 K and 1600 K, where the reaction is slightly exothermic.



Enthalpy and Gibbs Free Energy Plot for the Standard Atmospheric Reaction:

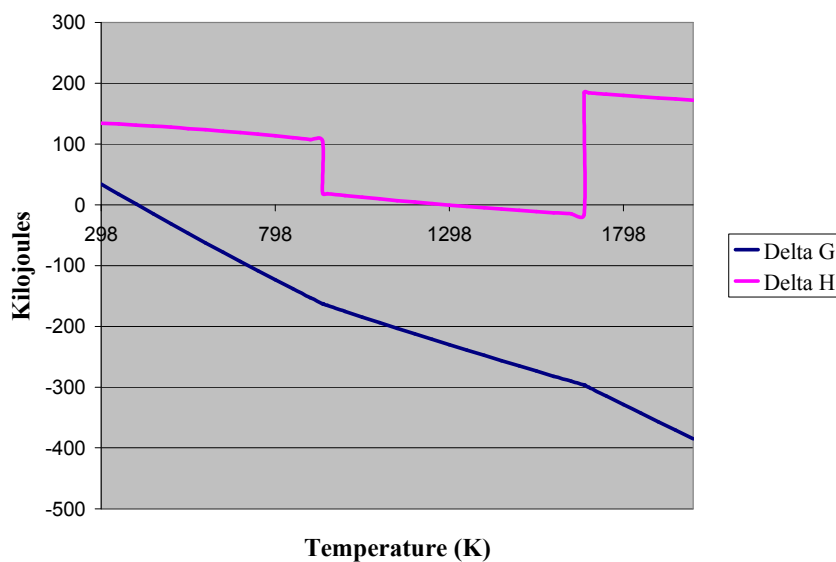
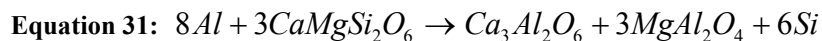


Figure CXC: Enthalpy and Gibbs Free Energy Plot for
 $8Al + 3CaMgSi_2O_6 \rightarrow Ca_3Mg(SiO_4)_2 + 2MgAl_2O_4 + 4Si + 2Al_2O_3$

Figure CXCI shows the ΔG and ΔH plots for a reaction between aluminum and diopside identified in Equation 31, over a proposed range of temperatures. The ΔG for Equation 31 is negative throughout the temperature range, making the reaction thermodynamically favorable. The reaction is also exothermic over all the temperature range.



Enthalpy and Gibbs Free Energy Plot for the Standard Atmospheric Reaction:

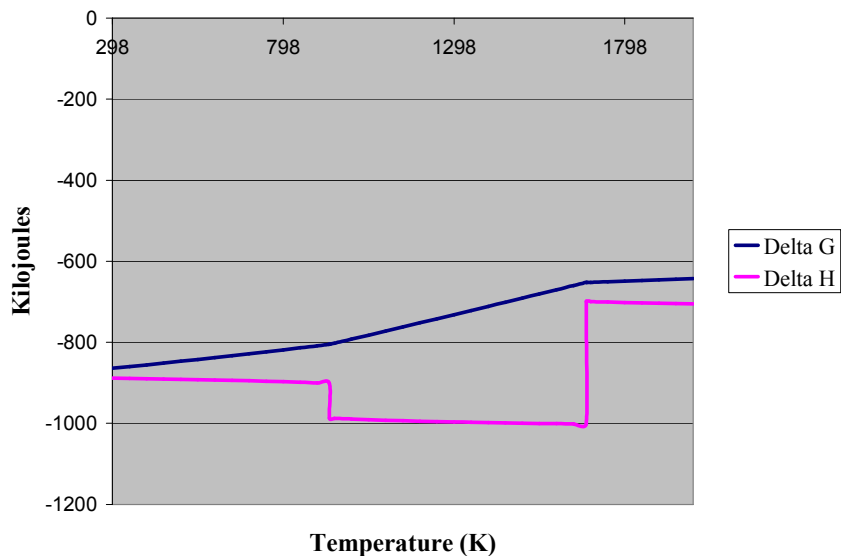
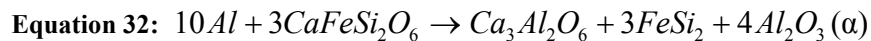


Figure CXCI: Enthalpy and Gibbs Free Energy Plot for $8Al + 3CaMgSi_2O_6 \rightarrow Ca_3Al_2O_6 + 3MgAl_2O_4 + 6Si$

Figure CXCII shows the ΔG and ΔH plots for a reaction between aluminum and hedenbergite identified in Equation 32, over a proposed range of temperatures. The ΔG for Equation 32 is negative throughout the temperature range, making the reaction thermodynamically favorable. The reaction is highly exothermic throughout the temperature range.



Enthalpy and Gibbs Free Energy Plot for the Standard Atmospheric Reaction:

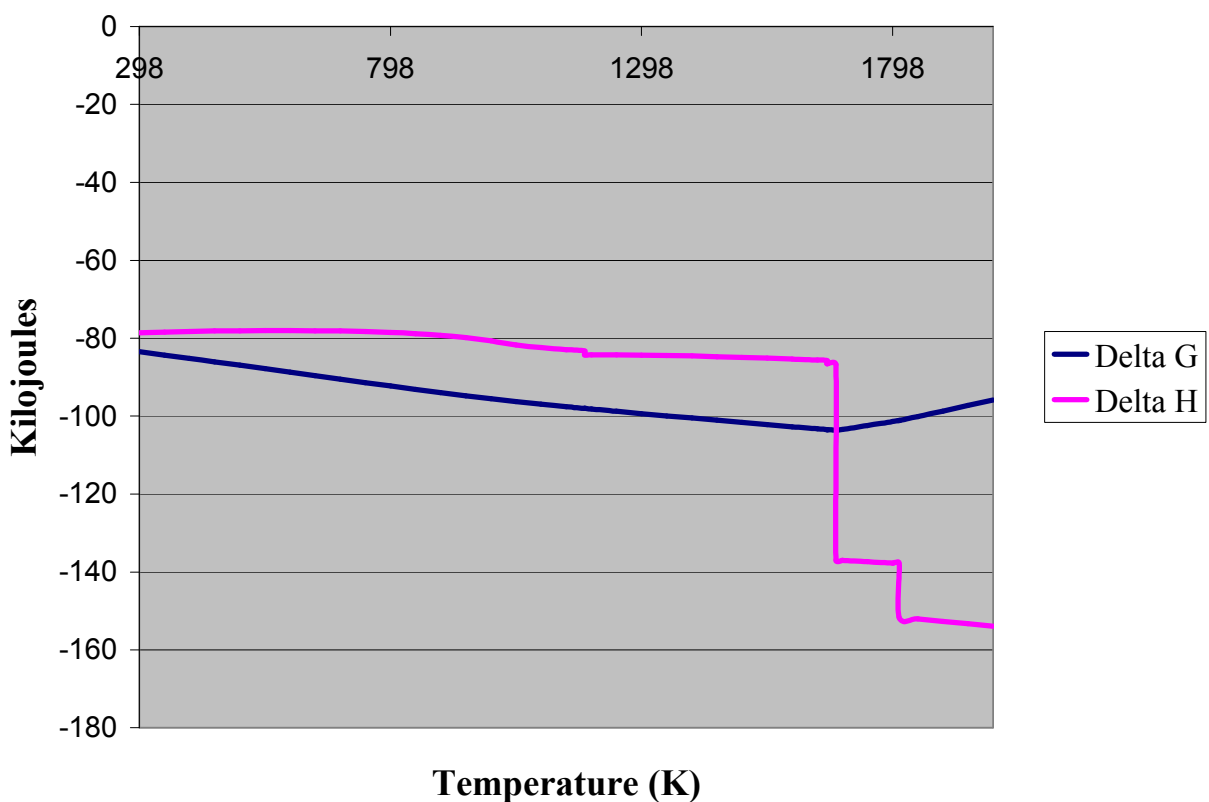
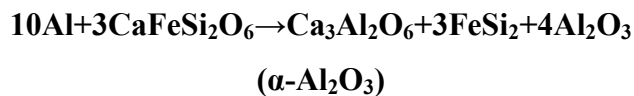


Figure CXCII: Enthalpy and Gibbs Free Energy Plot for $10\text{Al} + 3\text{CaFeSi}_2\text{O}_6 \rightarrow \text{Ca}_3\text{Al}_2\text{O}_6 + 3\text{FeSi}_2 + 4\text{Al}_2\text{O}_3$



Figure CXCI shows the ΔG and ΔH plots for a reaction between iron and silicon identified in Equation 34, over a proposed range of temperatures. The ΔG for Equation 34 is negative throughout the temperature range, making the reaction thermodynamically favorable. The reaction is also exothermic throughout the temperature range.



**Enthalpy and Gibbs Free Energy Plot for the Standard Atmospheric Reaction:
Fe+Si→FeSi**

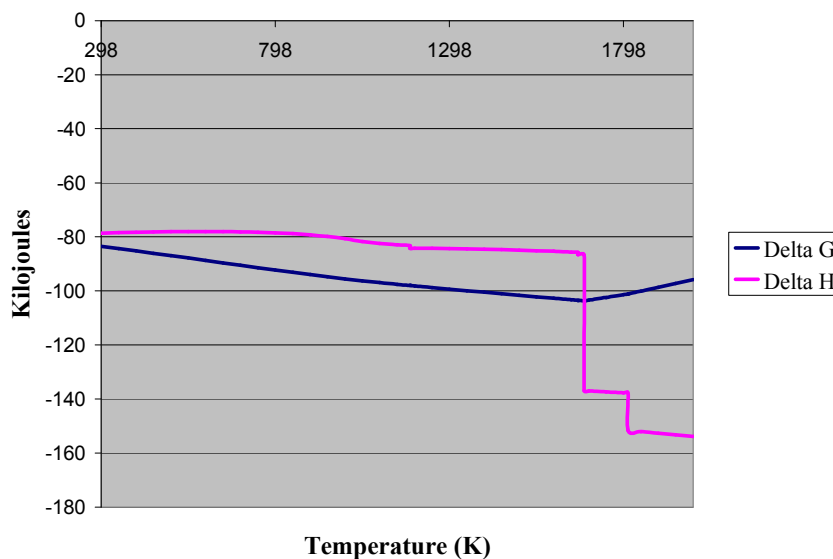


Figure CXCIII: Enthalpy and Gibbs Free Energy Plot for Fe+Si→FeSi

Figure CXCIV shows the ΔG and ΔH plots for a reaction between aluminum and hedenbergite identified in Equation 35, over a proposed range of temperatures. The ΔG for Equation 35 is negative throughout the temperature range, making the reaction thermodynamically favorable. The reaction is also exothermic throughout the temperature range.



Enthalpy and Gibbs Free Energy Plot for the Standard Atmospheric Reaction:

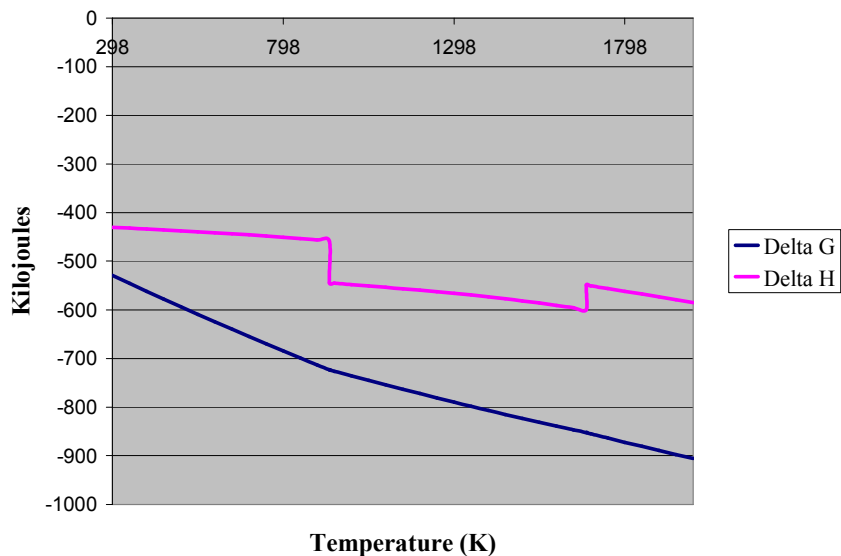
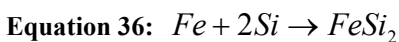


Figure CXCIV: Enthalpy and Gibbs Free Energy Plot for
 $8\text{Al} + 2\text{CaFeSi}_2\text{O}_6 \rightarrow \text{Ca}_2\text{Al}_2\text{Si}_2\text{O}_7 + \text{Al}_2\text{O}_3 + 2\text{FeSi} + \text{Si} + 2\text{Al}_2\text{O}$

Figure CXCIV shows the ΔG and ΔH plots for a reaction between iron and silicon identified in Equation 36, over a proposed range of temperatures. The ΔG for Equation 36 is negative throughout the temperature range, making the reaction thermodynamically favorable. The reaction is also exothermic throughout the temperature range.



Enthalpy and Gibbs Free Energy Plot for the Standard Atmospheric Reaction:

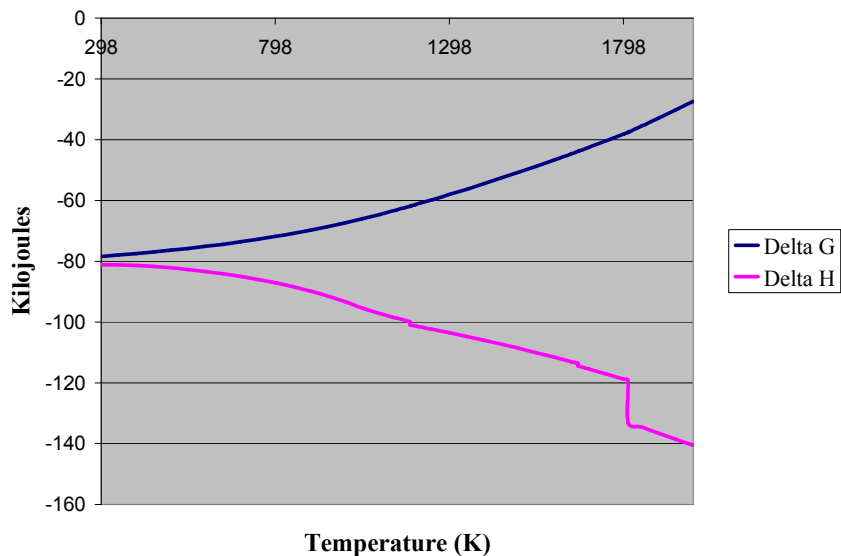
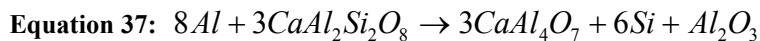


Figure CXCIV: Enthalpy and Gibbs Free Energy Plot for Fe+2Si→FeSi₂

Figure CXCVI shows the ΔG and ΔH plots for a reaction between aluminum and anorthite identified in Equation 37, over a proposed range of temperatures. The ΔG for Equation 37 is negative throughout the temperature range, making the reaction thermodynamically favorable. The reaction is also exothermic throughout the temperature range.



Enthalpy and Gibbs Free Energy Plot for the Standard Atmospheric Reaction:

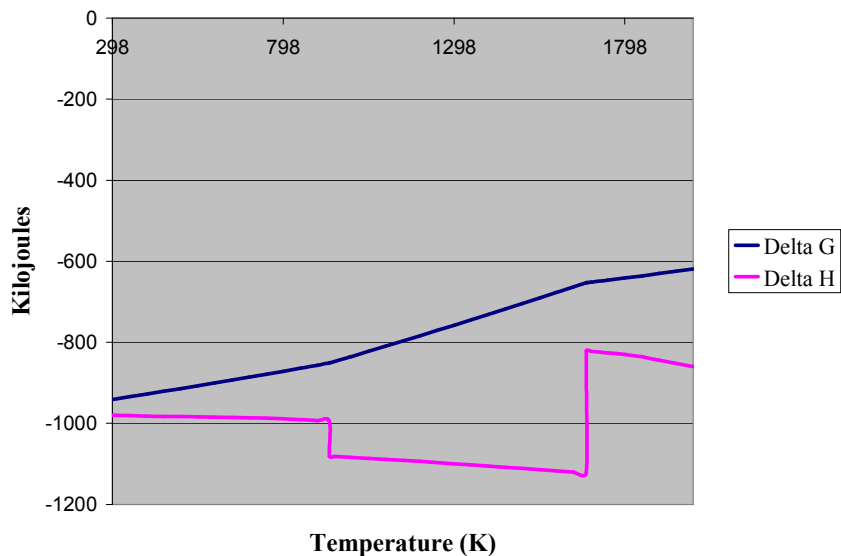
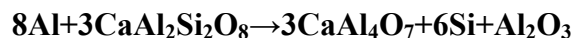


Figure CXCVI: Enthalpy and Gibbs Free Energy Plot for $8\text{Al} + 3\text{CaAl}_2\text{Si}_2\text{O}_8 \rightarrow 3\text{CaAl}_4\text{O}_7 + 6\text{Si} + \text{Al}_2\text{O}_3$

Figure CXCVII shows the ΔG and ΔH plots for a reaction between aluminum, diopside, and anorthite identified in Equation 38, over a proposed range of temperatures. The ΔG for Equation 38 is negative throughout the temperature range, making the reaction thermodynamically favorable. The reaction is also exothermic throughout the temperature range.



Enthalpy and Gibbs Free Energy Plot for the Standard Atmospheric Reaction:

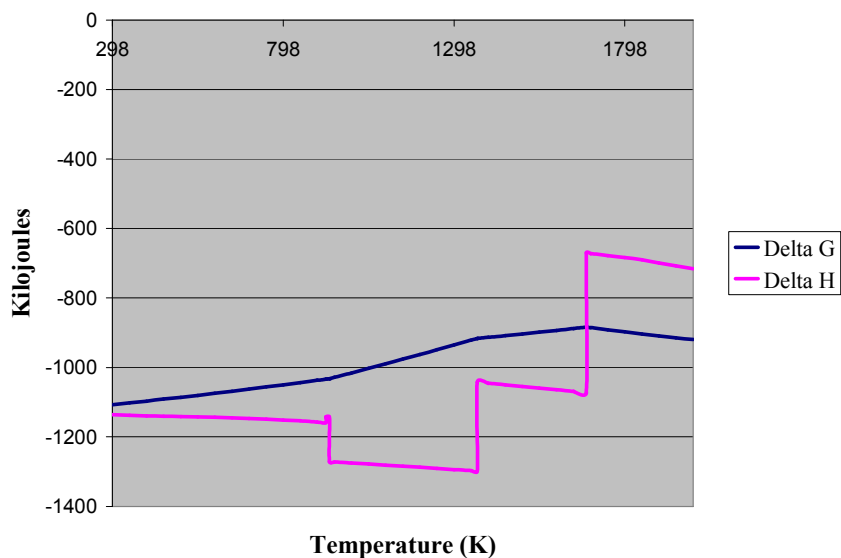
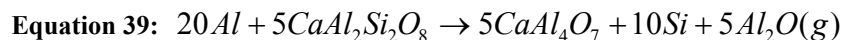


Figure CXC VII: Enthalpy and Gibbs Free Energy Plot for
 $12\text{Al} + 2\text{CaMgSi}_2\text{O}_6 + 2\text{CaAl}_2\text{Si}_2\text{O}_8 \rightarrow 4\text{CaAl}_4\text{O}_7 + 8\text{Si} + 2\text{Mg}$

Vacuum

Figure CXC VIII shows the ΔG and ΔH plots for a reaction between aluminum and anorthite identified in Equation 39, over a proposed range of temperatures. The ΔG for Equation 39 is negative above ~ 400 K, making the reaction thermodynamically favorable. The reaction is endothermic over most of the temperature range. The reaction is slightly exothermic from ~ 1625 - 1675 K, and becomes highly exothermic above 1800 K.



Enthalpy and Gibbs Free Energy Plot for the 0.600 Torr Vacuum Reaction:

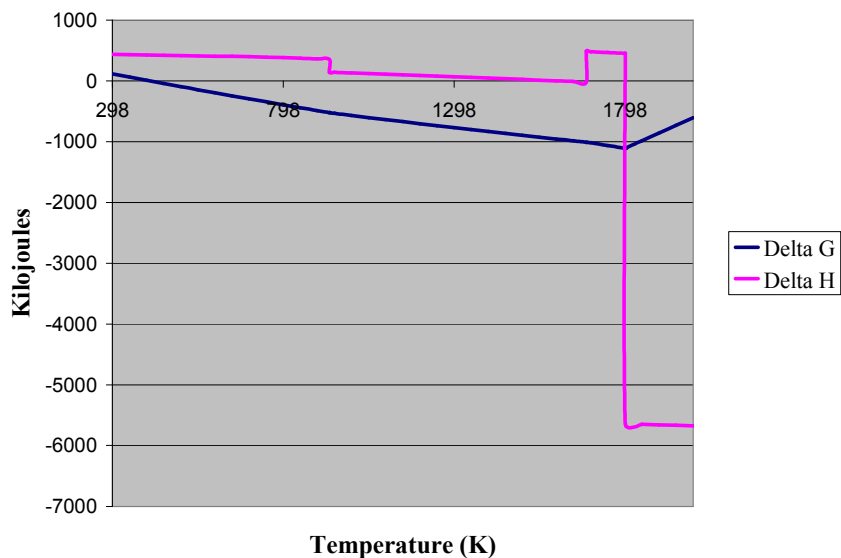
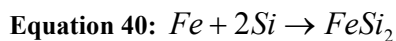


Figure CXCVIII: Enthalpy and Gibbs Free Energy Plot for $20\text{Al} + 5\text{CaAl}_2\text{Si}_2\text{O}_8 \rightarrow 5\text{CaAl}_4\text{O}_7 + 10\text{Si} + 5\text{Al}_2\text{O}$

Figure CXCIX shows the ΔG and ΔH plots for a reaction between iron and silicon identified in Equation 40, over a proposed range of temperatures. The ΔG for Equation 39 is negative throughout the temperature range, making the reaction thermodynamically favorable. The enthalpy is negative throughout the temperature range, making the reaction exothermic.



Enthalpy and Gibbs Free Energy Plot for the 0.600 Torr Vacuum Reaction:

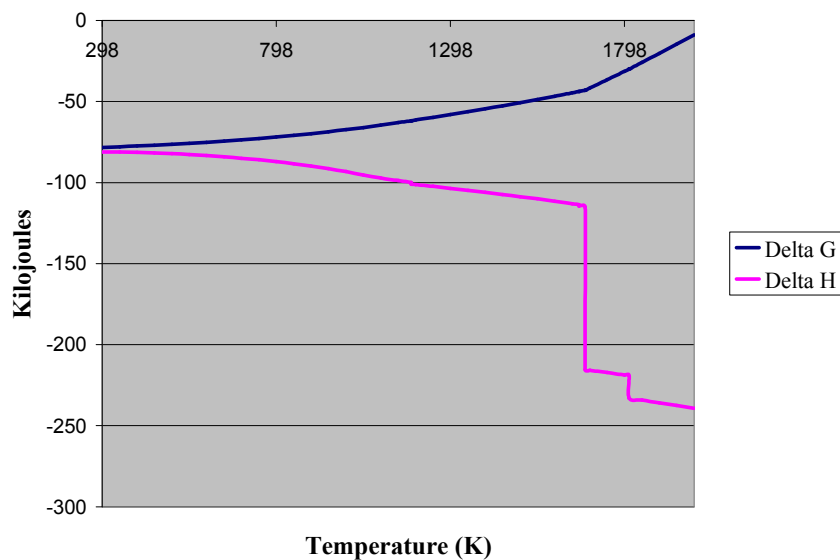


Figure CXCIX: Enthalpy and Gibbs Free Energy Plot for Fe+2Si → FeSi₂

Figure CC shows the ΔG and ΔH plots for a reaction between iron and silicon identified in Equation 41, over a proposed range of temperatures. The ΔG for Equation 41 is negative throughout the temperature range, making the reaction thermodynamically favorable. The enthalpy is negative throughout the temperature range, making the reaction exothermic.



Enthalpy and Gibbs Free Energy Plot for the 0.600 Torr Vacuum Reaction:

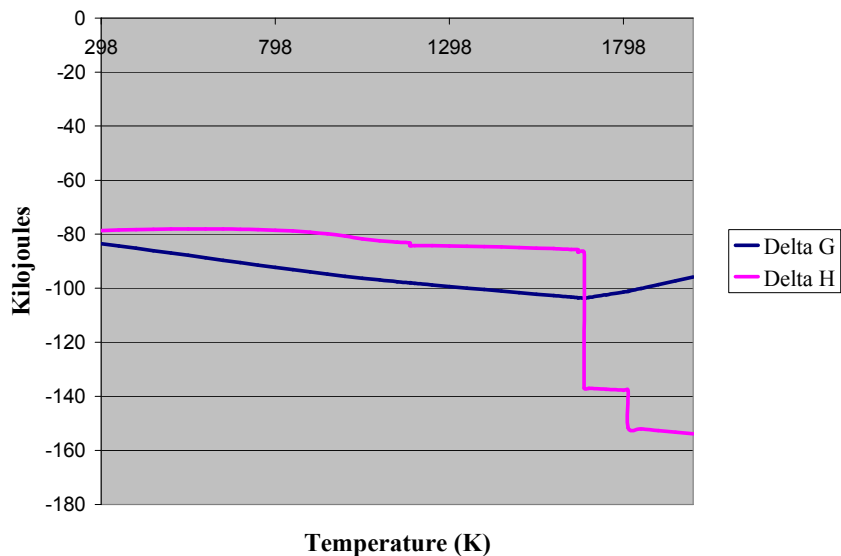
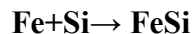


Figure CC: Enthalpy and Gibbs Free Energy Plot for Fe+Si→ FeSi

Figure CCI shows the ΔG and ΔH plots for a reaction between aluminum and hedenbergite identified in Equation 42, over a proposed range of temperatures. The ΔG for Equation 42 is negative throughout the temperature range, making the reaction thermodynamically favorable. The enthalpy is negative throughout the temperature range, making the reaction exothermic. The reaction becomes highly exothermic above 1800 K.



Enthalpy and Gibbs Free Energy Plot for the 0.600 Torr Vacuum Reaction:

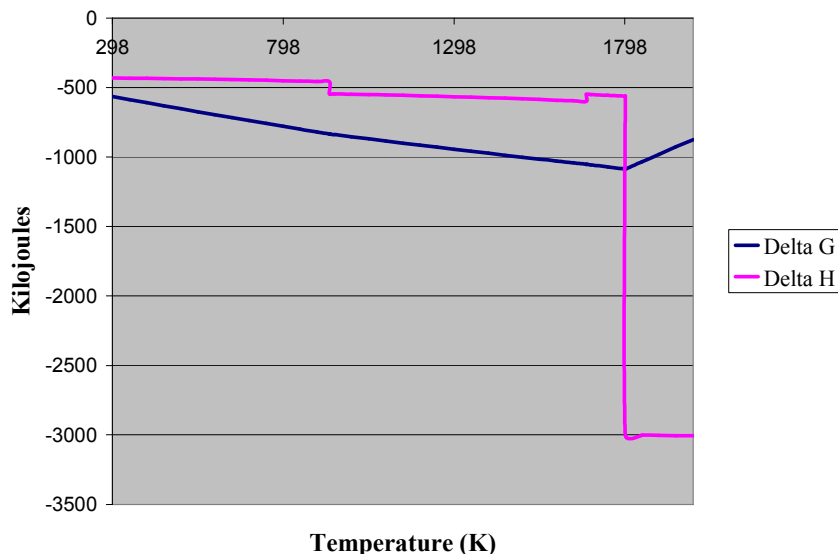
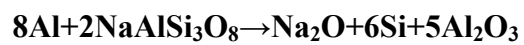


Figure CCI: Enthalpy and Gibbs Free Energy Plot for $8\text{Al} + 2\text{CaFeSi}_2\text{O}_6 \rightarrow \text{Ca}_2\text{Al}_2\text{SiO}_7 + \text{Al}_2\text{O}_3 + 2\text{FeSi} + \text{Si} + 2\text{Al}_2\text{O}$

Figure CCII shows the ΔG and ΔH plots for a reaction between aluminum and low-albite identified in Equation 43, over a proposed range of temperatures. The ΔG and ΔH plots for a reaction with high-albite are shown in Figure CCIII. The ΔG in Equation 43 for both low and high-albite is negative throughout the temperature range, making the reaction thermodynamically favorable. The enthalpy for both albite phases is negative throughout the temperature range, making the reaction exothermic. The reaction becomes highly exothermic above 1800 K.



Enthalpy and Gibbs Free Energy Plot for the 0.600 Torr Vacuum Reaction:



(low albite and α -Al₂O₃)

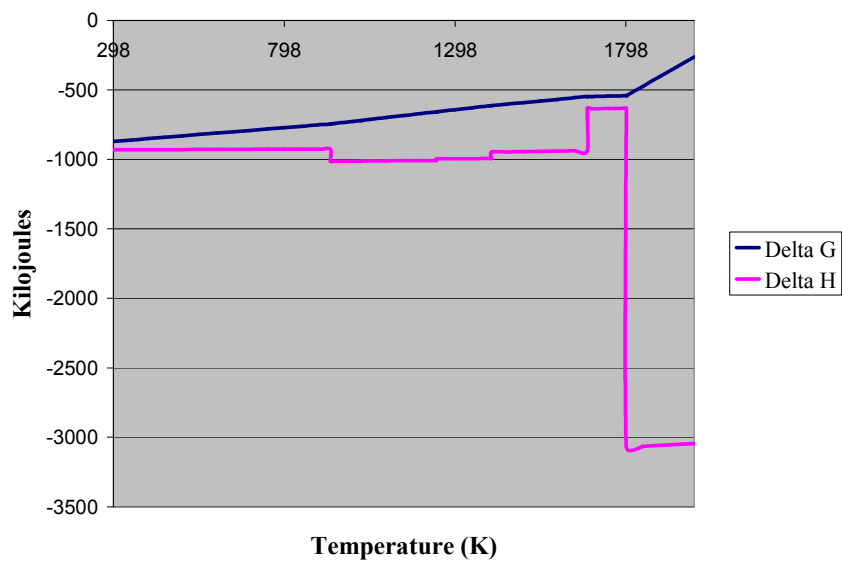
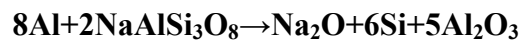


Figure CCII: Enthalpy and Gibbs Free Energy Plot for $8\text{Al} + 2\text{NaAlSi}_3\text{O}_8 \rightarrow \text{Na}_2\text{O} + 6\text{Si} + 5\text{Al}_2\text{O}_3$ using low-albite

Enthalpy and Gibbs Free Energy Plot for the 0.600 Torr Vacuum Reaction:



(high albite and $\alpha\text{-Al}_2\text{O}_3$)

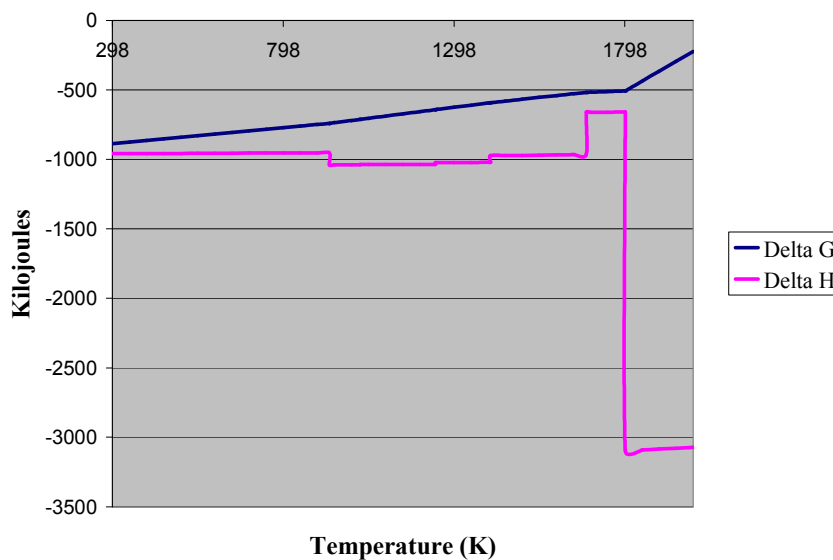


Figure CCIII: Enthalpy and Gibbs Free Energy Plot for $8\text{Al} + 2\text{NaAlSi}_3\text{O}_8 \rightarrow \text{Na}_2\text{O} + 6\text{Si} + 5\text{Al}_2\text{O}_3$ using high-albite

Figure CCIV shows the ΔG and ΔH plots for a reaction between aluminum and iron oxide identified in Equation 44, over a proposed range of temperatures. The ΔG for Equation 44 is negative throughout the temperature range, making the reaction thermodynamically favorable. The enthalpy is also negative throughout the temperature range, making the reaction exothermic. The reaction becomes highly exothermic above 1800 K.



Enthalpy and Gibbs Free Energy Plot for the 0.600 Torr Vacuum Reaction:

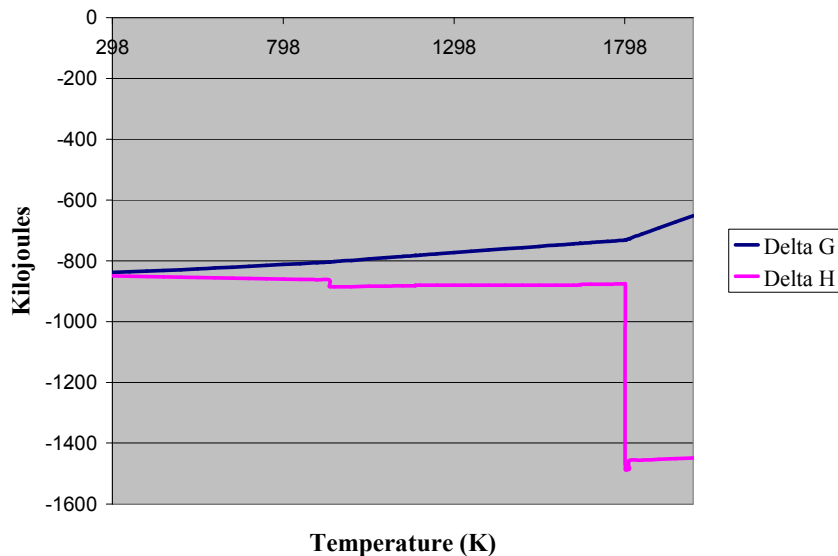
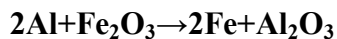
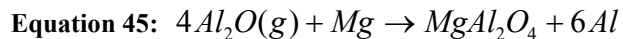


Figure CCIV: Enthalpy and Gibbs Free Energy Plot for $2\text{Al} + \text{Fe}_2\text{O}_3 \rightarrow 2\text{Fe} + \text{Al}_2\text{O}_3$

Figure CCV shows the ΔG and ΔH plots for a reaction between Al_2O (g) and magnesium identified in Equation 45, over a proposed range of temperatures. The ΔG for Equation 45 is negative below ~ 1690 K, making the reaction thermodynamically favorable over the majority of the temperature range. The enthalpy is also negative below ~ 1800 K making the reaction exothermic over the majority of the temperature range.



Enthalpy and Gibbs Free Energy Plot for the 0.600 Torr Vacuum Reaction:

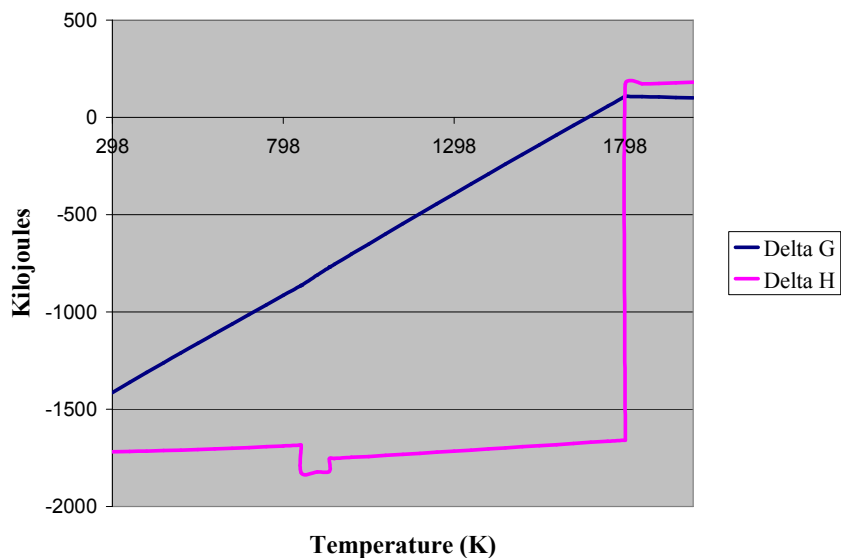
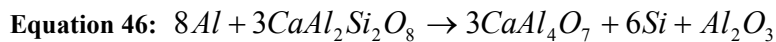


Figure CCV: Enthalpy and Gibbs Free Energy Plot for $4\text{Al}_2\text{O} + \text{Mg} \rightarrow \text{MgAl}_2\text{O}_4 + 6\text{Al}$

Figure CCVI shows the ΔG and ΔH plots for a reaction between aluminum and anorthite identified in Equation 46, over a proposed range of temperatures. The ΔG for Equation 46 is negative throughout the temperature range, making the reaction thermodynamically favorable. The enthalpy is also negative throughout the temperature range, which means the reaction is exothermic. The reaction becomes highly exothermic around ~ 1800 K.



Enthalpy and Gibbs Free Energy Plot for the 0.600 Torr Vacuum Reaction:

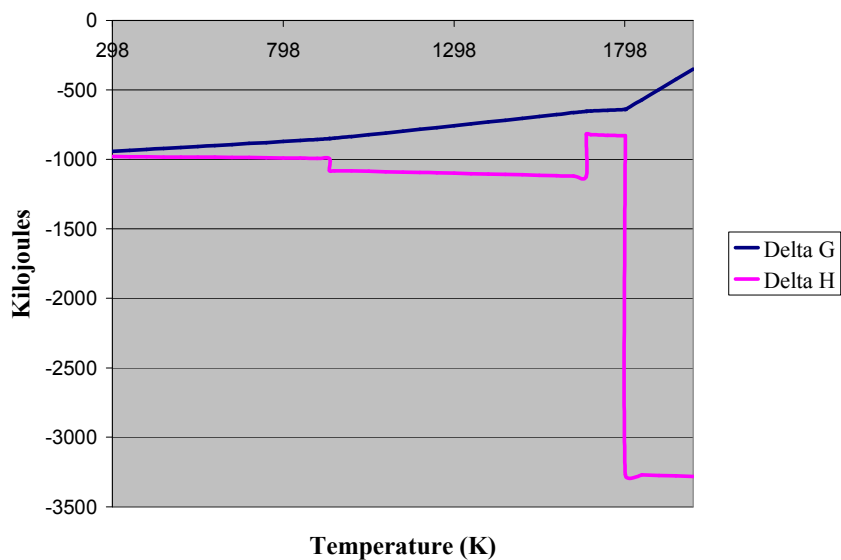
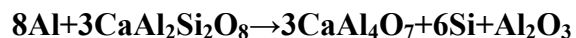


Figure CCVI: Enthalpy and Gibbs Free Energy Plot for $8\text{Al} + 3\text{CaAl}_2\text{Si}_2\text{O}_8 \rightarrow 3\text{CaAl}_4\text{O}_7 + 6\text{Si} + \text{Al}_2\text{O}_3$

Figure CCVII shows the ΔG and ΔH plots for a reaction between aluminum, diopside, and anorthite identified in Equation 47, over a proposed range of temperatures. The ΔG for Equation 47 is negative throughout the temperature range, making the reaction thermodynamically favorable. The reaction is also exothermic throughout the temperature range. Above ~ 1800 K the reaction becomes highly exothermic.



Enthalpy and Gibbs Free Energy Plot for the 0.600 Torr Vacuum Reaction:

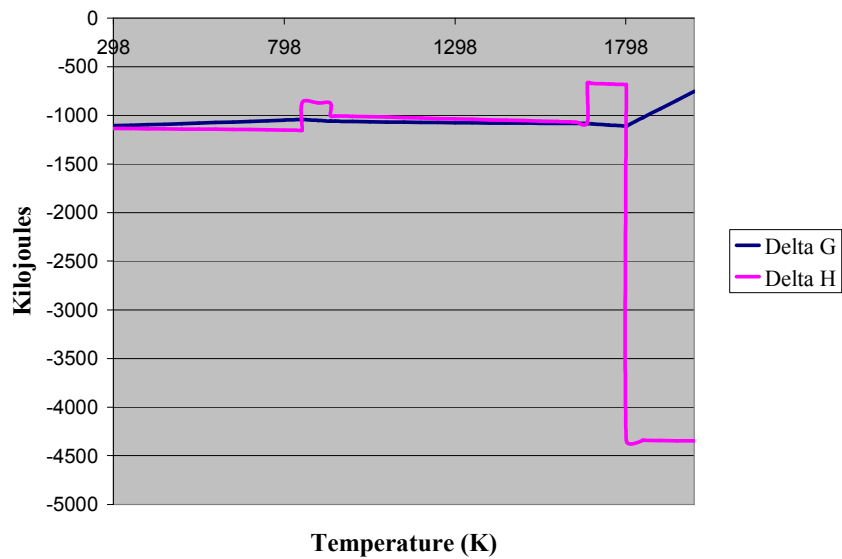


Figure CCVII: Enthalpy and Gibbs Free Energy Plot for
 $12\text{Al} + 2\text{CaMgSi}_2\text{O}_6 + 2\text{CaAl}_2\text{Si}_2\text{O}_8 \rightarrow 4\text{CaAl}_4\text{O}_7 + 8\text{Si} + 2\text{Mg}$

V. CONCLUSIONS

This section discusses conclusions drawn from the various aspects of the study. Many reaction parameters have been investigated, including: reaction environment, reactant stoichiometries, and regolith simulant particle size distributions. A great deal of knowledge regarding geothermite reactions has been obtained, particularly in relation to formation of chemical species, microstructures, and mechanical strength of reaction products fabricated under different reaction parameters.

A. Reaction Environment

The oxidation-reduction reaction investigated within this study was able to generate sufficient energy to propagate the reaction beyond the initial area of applied external heat allowing it to become a self-propagating high temperature reaction.

B. Identification of Chemical Species

Standard Atmosphere Synthesis

Within the JSC-1AF reaction products silicon (27-1402) appeared to be present in the largest quantities in reactions having the 28.85% aluminum stoichiometry. Within JSC-1A reaction products silicon (27-1402) appeared to be present in the largest quantities in reactions having the 24.45% aluminum stoichiometry. Silicon (27-1402) appeared to be present in larger quantities within JSC-1AF reaction products with the exception of reactions having the 19.44% stoichiometry.

Chemical species of aluminum nitride were characteristic of all reactions conducted in a standard atmosphere. AlN (25-1133) appeared to be present in larger quantities within reaction products synthesized using JSC-1A simulant than those synthesized using JSC-1AF simulant. In both simulants, larger quantities of AlN (25-1133) appeared to form with increased aluminum in the reactant mixture. AlN (46-1200) appeared to be present in larger quantities within JSC-1A reaction products using 19.44% and 24.45% stoichiometries than equivalent stoichiometries using JSC-1AF simulant.

Corundum (46-1212) (10-0173) and spinel (21-1152) appeared to be present in significant quantities within all JSC-1A reaction products and the low aluminum stoichiometries

of JSC-1AF reaction products. $\text{Mg}_{0.388}\text{Al}_{2.408}\text{O}_4$ (48-0528) appeared to be present within all reaction products. The largest quantity of spinel (21-1152) appeared to be present in the lowest stoichiometries using JSC-1A simulant. The largest quantities of corundum (46-1212) and (10-0173) appeared to occur in the low aluminum stoichiometries for JSC-1AF reaction products, and decreased to unmeasurable levels in the higher aluminum stoichiometries. Formation of corundum (46-1212) and (10-0173) appeared to be significantly larger in the JSC-1A reaction products than the JSC-1AF reaction products, except in the 19.44% stoichiometry. Formation of corundum appeared to be largest in the highest stoichiometry of aluminum followed by the lowest stoichiometry of aluminum within JSC-1A reaction products. Small quantities of aluminum (04-0787) appeared to be present in reaction products of all stoichiometries and both simulants. Distinctly larger quantities of aluminum (04-0787) appeared to be present in the 28.85 wt.% JSC-1A reaction product.

CaAl_4O_7 (23-1037) and (46-1475) were found within all reactant stoichiometries and both simulants. Distinctly larger quantities of CaAl_4O_7 appeared to be present in the JSC-1AF reaction products with aluminum stoichiometries above 19.44%. The significantly large quantities of CaAl_4O_7 correspond with a large decrease in corundum (46-1212) (10-0173) quantities within the high aluminum stoichiometries using JSC-1AF simulant indicating that these species may form at the expense of each other.

Diffraction peaks for FeSi (38-1397) were observed in all reactant stoichiometries using both types of simulant. Formation of FeSi_2 (35-0822) appeared to be largest in the lowest aluminum stoichiometries for both JSC-1A and JSC-1AF. The presence of FeSi_2 (35-0822) was not observed in the largest aluminum stoichiometries for JSC-1AF and JSC-1A, 33.33 wt.% and 28.85 wt.%, respectively.

Vacuum Synthesis

Chemical species commonly produced from the SHS reactions in vacuum included silicon (27-1402), corundum (10-0173), spinel (21-1152), iron silicides (35-0822) (38-1397), CaAl_4O_7 (46-1475) (23-1037), and $\text{Ca}_2\text{Al}_2\text{SiO}_7$ (35-0755).

As the quantity of aluminum in the reactants increased, the quantities of unreacted constituents from the simulant appeared to decrease within the reaction product. The 19.44% and 24.45% JSC-1A stoichiometries appeared to have larger quantities of unreacted simulant

constituents than the same stoichiometries using the JSC-1AF simulant. Quantities of unreacted simulant constituents appeared to be similar for both simulants in the 28.85% stoichiometry.

Formation of silicon (27-1402) appeared to increase as the quantity of aluminum in the reactants increased. Silicon (27-1402) formation appeared to be significantly larger in the JSC-1AF reaction products. The apparent decrease in unreacted simulant constituents and increase in reduced silicon would likely indicate that as aluminum stoichiometry increased a more reacted product was produced.

Formation of corundum (10-0173), spinel (21-1152), and CaAl_4O_7 (46-1475) (23-1037) appeared to be largest in the 33.33% aluminum stoichiometry using JSC-1AF simulant. Formation of iron silicides appeared to be largest in stoichiometries using smaller quantities of aluminum within the JSC-1AF reaction products. Formation of $\text{Mg}_{0.388}\text{Al}_{2.408}\text{O}_4$ appeared to vary from low quantities to unmeasurable quantities.

The presence of MgFeAlO_4 (11-0009) was observed in several stoichiometries for both simulants. MgFeAlO_4 (11-0009) was not observed in standard atmosphere reaction products. Aluminum nitrides were absent from vacuum reaction products.

C. Microstructural Characterization and Elemental Analysis

Networks of whiskers were characteristic of standard atmosphere reaction products, and were almost entirely absent from vacuum reaction products. Very small whiskers were observed on a few particles in vacuum, but did not compare to the quantity observed in a standard atmosphere. Most of the whiskers formed in a standard atmosphere reaction product terminated in a spherical shape, possibly indicating a vaporization process occurred. The nanoscale diameters of the whiskers also support reactions involving a vapor phase. The formation of whiskers was likely to greatly increase the interparticle bonding and overall strength within the standard atmosphere reaction product. Two types of whiskers were found using EDS analysis, referred to in this study as Type I and Type II whiskers. Small quantities of silicon appeared to be present in most Type I and Type II whiskers. EDS analysis indicated that the Type I whiskers were most prevalent, having significant bound nitrogen content, generally over 20 at.%. The whiskers also had large quantities of aluminum and oxygen present. It was hypothesized that the whiskers were primarily composed of the chemical species of aluminum nitride. The presence of oxygen likely indicated incorporation aluminum oxide into the whiskers. Formation of

aluminum oxynitride was also possible, but significant diffraction peaks were not present in XRD analysis. It is possible that the aluminum oxynitride could be amorphous. It is suggested that ambient nitrogen and oxygen combine with Al_2O gas produced during the reaction, and grow as whiskers between particle surfaces. It is possible that a VTR process is involved in the whisker growth. The process could have involved the evolution of Al_2O gas, reaction of the Al_2O gas with ambient nitrogen and oxygen, followed by nucleation and whisker growth. The termination of whiskers in a spherical shape would indicate that growth occurred by the VLS mechanism. Growth by the VLS mechanism would indicate that a liquid phase was present at the whisker tip, creating a preferential deposition surface for gas molecules. Precipitation from the super-saturated liquid phase would have caused whisker growth at the solid-liquid interface. Impurities such as silicon, magnesium, and oxygen could have been incorporated within the AlN whiskers and assisted in the growth process. Type II whiskers have no bound nitrogen; EDS analysis indicated that magnesium, aluminum, and oxygen were major constituents. It was hypothesized that Type II whiskers are composed of the chemical species aluminum oxide and $\text{Mg}_{388}\text{Al}_{2.408}\text{O}_4$, both found in the XRD patterns. The presence of silicon in most of the whiskers could indicate that silicon acts as the liquid catalyst in the VLS whisker growth process.

The reaction product utilizing a 28.85% aluminum stoichiometry and JSC-1A simulant was observed to contain whiskers that exhibited more dendritic and branched morphologies than other reactant stoichiometries. The whisker morphologies may relate to the quantity of aluminum within the sample, and aluminum saturation during whisker growth.

Evidence of partial melting was observed in several micrographs, indicating a liquid phase sintering process occurred during the reaction. The prevalence of whiskers in the microstructures concealed many aspects of the liquid phase sintering process. Reactions conducted in vacuum contained abundant spherical particles, some of which had abundant aluminum, and others had large iron and silicon content. It is likely that the spherical particles with large iron and silicon content were composed of iron silicides.

D. Density Measurements

The density of samples synthesized with JSC-1A simulant was found to increase with larger aluminum quantities in the reactants. Larger quantities of aluminum would have resulted in more liquid aluminum that could fill pore spaces during the reaction process, forming a denser

product. As aluminum content increased using the JSC-AF simulant, the density generally decreased. The quantity of evolved gas observed during the reaction was larger in the JSC-1AF simulant products, and appeared to increase with aluminum quantity. The evolution of gas could have resulted in higher porosities in the reaction product. The largest stoichiometry of aluminum was an exception, since the trend reversed. Samples synthesized using JSC-1A simulant were significantly denser than those that used JSC-1AF simulant. The densities of JSC-1A samples ranged from ~20-40% larger than samples of JSC-1AF using the same stoichiometries.

E. Mechanical Strength Measurements

Compressive strength measurements were only performed on standard atmosphere reaction products within this study. General handling of the reaction products indicated that the outer diameter of the vacuum reaction products was substantially weaker than the standard atmosphere product. The area inside the vacuum reaction product, in the vicinity of the NiCr wire was significantly stronger than the exterior areas in many instances. The difference in strength may have been due to higher temperatures, diffusion, chemical reaction of the NiCr wire with surrounding sample areas, and/or more degassing and therefore higher densification of the interior regions.

Reaction products created from the JSC-1A simulant, using the lower stoichiometries of aluminum, yielded significantly higher compressive strengths than all other samples. The results do not follow the Hall-Petch relationship which states that smaller particle sizes will give higher strengths. Higher compressive strengths are hypothesized to be a result of differences in chemical composition, and higher densities. The formation of large quantities of spinel and corundum, along with formation of lower quantities of silicon likely increased the strength of the low aluminum stoichiometries of the JSC-1A reaction product. In addition, the dense networks of Type I and Type II whiskers increased the strength of the reaction product. The Type II whiskers appeared to be present in larger quantities within low aluminum stoichiometries. It is also likely that higher sample densities promoted more particle contact, allowed better sintering, and caused the formation of a stronger product.

Reaction products using larger quantities of aluminum were observed to deform more before failure. An increase in metallic bonding caused by the larger quantities of aluminum was likely to allow the larger deformation. An increase in whisker quantity could also have allowed

greater deformation prior to failure. Substantially higher deformation was observed in the JSC-1AF simulant. Overall, as deformation increased, compressive strength was observed to decrease. The modulus of elasticity was observed to decrease as aluminum increased from 24.45% to 33.33% in the JSC-1AF reaction products. The decrease in modulus of elasticity correlated with the relationship between porosity and elastic modulus given in Equation 8, which stated that as porosity increased, elastic modulus decreased. A distinctly larger modulus of elasticity was observed in the 19.44% JSC-1A reaction product.

F. Measurements of Energy Required to Initiate Reactions

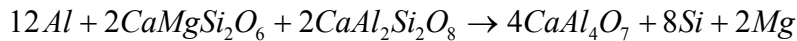
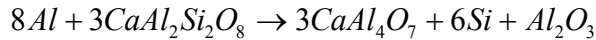
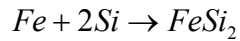
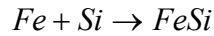
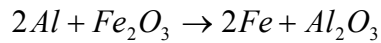
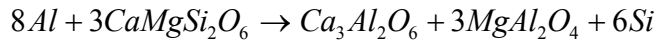
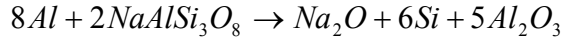
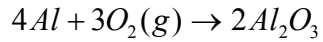
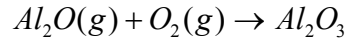
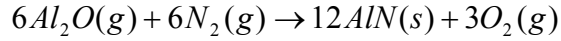
It was found that reactions performed in a standard atmosphere using JSC-1A simulant required substantially more energy to initiate than those of equivalent stoichiometries using JSC-1AF simulant. The increase in energy required to initiate reactions using JSC-1A simulant was likely due to the lower surface area available for reaction with aluminum. The minimum energy required to initiate JSC-1AF reactions occurred in the 28.85% stoichiometry, at a 90% confidence level compared to the stoichiometry showing the next lowest energy. The 28.85% aluminum stoichiometry also appeared to have the largest quantity of silicon present within the reaction product. For reactions conducted using JSC-1A simulant the minimum energy to initiate the reaction occurred at 24.45% aluminum, with a 75% confidence level compared to the stoichiometry showing the next lowest energy (28.85%). The stoichiometry at which a minimum energy is required to initiate a reaction is likely to represent a balance between excess aluminum drawing heat away from reaction, and insufficient aluminum preventing complete reaction with the regolith simulant. The correlation of minimum initiation energy and maximum silicon formation may indicate that the oxidation-reduction process proceeds furthest in the reduction of silicates within the 28.85% and 24.45% aluminum stoichiometries, utilizing JSC-1AF and JSC-1A simulants, respectively.

G. Reaction Thermodynamics

Standard Atmosphere

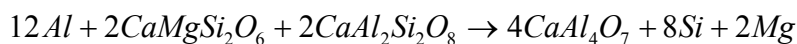
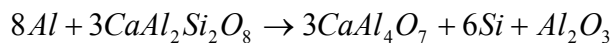
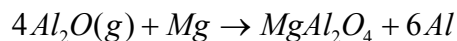
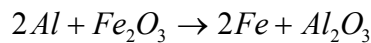
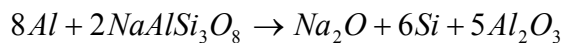
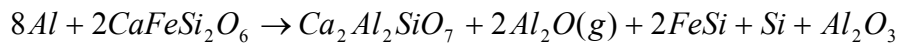
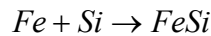
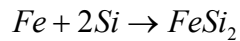
It was determined that the following reactions were thermodynamically favorable over a proposed temperature range (298 K to 1998 K) in a standard atmosphere reaction:





Vacuum

It was determined that the following reactions were thermodynamically favorable over a proposed temperature range (298 K to 1998 K) in a reaction conducted in a 0.600 Torr vacuum:



VI. FUTURE WORK

The future work section discusses potential areas that can be investigated to advance knowledge of geothermite reactions. Alternate methods of reaction initiation, utilization of different reducing mediums, and modifications to reactants are discussed. Methods to further advance geothermite reactions in a vacuum environment are discussed, as are potential ISRU applications on Mars.

One area of interest for future work would be to investigate better methods to initiate the SHS reaction. Two methods that appear promising to investigate would be the use of microwaves and the use of concentrated solar flux. An enormous area of research is possible through investigating geothermite reactions using indigenous materials from around the world. A thorough investigation of radiation transmission characteristics of the reaction product would be highly useful. Preliminary characterizations of neutron transmission were conducted by the author, the results of which are not included in this work. The material was found to provide reasonable shielding from neutron transmission. Potential may exist for the reaction product to be used on a large scale to encase radioactive material in a manner similar to the way concrete is used. In addition, it may be possible to mix radioactive material into the reactant mixture, and mitigate radiation by binding radioactive atoms into the structure of the reaction product. Another potential area of research could relate to the use of geothermite reactant mixtures as propellants, particularly using nano-particles of aluminum. The feasibility of performing geothermite reactions with other reducing agents such as carbon could also be studied. In addition, it would be desirable to obtain temperature profiles for the various reaction stoichiometries, simulant types, and reaction environments.

Further work is needed in the investigation of vacuum reactions. It would be beneficial to drive off volatile species prior to initiating the geothermite reaction. It may be useful to investigate a process to use excess reaction heat to drive off easily volatilized species, in order to reduce porosity and degassing, which degrades the structure of the vacuum synthesized reaction product. Alternate methods of reaction initiation would be very desirable in vacuum, since the use of NiCr wire is undesirable. Pressing the reactant mixture after driving off volatiles is another avenue worth investigating. Pressing would be particularly useful in a vacuum environment to assure maximum particle contact during the reaction.

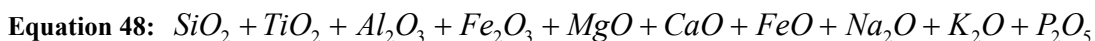
Research can also be extended to ISRU on Mars. The chemical composition of Mars regolith obtained from Viking Lander 1, Viking Lander 2 , and the Pathfinder missions are shown in Table LXXVII.⁵⁸ As with the lunar regolith compositions, the quantities in Table LXXVII reflect bulk composition, not actual compounds found in the regolith. The high content of iron oxides would create higher energy release during the geothermite reaction. In addition, since aluminum oxides tend to stifle the reaction, the lower quantities of aluminum oxides present in the Mars regolith would likely increase the reaction wave propagation velocities. The composition of the Mars regolith suggests that it would be able to produce more energy in a geothermite reaction than lunar regolith.

Table LXXVII: Bulk Composition of Mars Regolith (Values in Wt.%)⁵⁸

	VL-1	VL-2	Pathfinder
SiO ₂	43	43	44.0
Fe ₂ O ₃	18.5	17.8	16.5
Al ₂ O ₃	7.3	7	7.5
MgO	6	6	7.0
CaO	5.9	5.7	5.6
SO ₃	6.6	8.1	4.9
TiO ₂	0.66	0.56	1.1

Appendix 1: Calculations for Reactant Stoichiometries

This section deals with the calculation of reactant stoichiometries. The values obtained for weight percent composition of the regolith simulant were added together to obtain the total value of components accounted for, since not all trace components are accounted for in the bulk analysis. The summation is shown in Equation 48 and Equation 49.



Equation 49: $47.1 + 1.87 + 17.1 + 3.41 + 6.9 + 10.3 + 7.57 + 3.3 + 0.86 + 0.76 = 99.17$

Each of the above values was divided by 99.17 and multiplied by 100 to obtain a new standardized weight percent for components accounted for in the simulant, shown in Table LXXVIII.

Table LXXVIII: Standardized Wt.% for Bulk Components in JSC-1AF

SiO ₂	TiO ₂	Al ₂ O ₃	Fe ₂ O ₃	MgO	CaO	FeO	Na ₂ O	K ₂ O	P ₂ O ₅
47.5	1.89	17.2	3.44	7.0	10.4	7.63	3.3	0.87	0.77

The number of grams per mole in each of the above compounds was calculated, and is listed in Table LXXIX.

Table LXXIX: Grams per Mole for Bulk Components in JSC-1AF

SiO ₂	TiO ₂	Al ₂ O ₃	Fe ₂ O ₃	MgO	CaO	FeO	Na ₂ O	K ₂ O	P ₂ O ₅
60.084	79.866	101.961	159.688	40.304	56.077	71.844	61.979	94.196	109.945

The number of moles for each bulk component in a 100 g sample were calculated and are listed in Table LXXX.

Table LXXX: Moles of Each Bulk Component Present in a 100 g sample of JSC-1AF

SiO ₂	TiO ₂	Al ₂ O ₃	Fe ₂ O ₃	MgO	CaO	FeO	Na ₂ O	K ₂ O	P ₂ O ₅
0.79	0.02	0.17	0.02	0.17	0.19	0.11	0.05	0.01	0.01

The number of moles of aluminum necessary to reduce one mole of each of the above compounds was calculated, and is listed in Table LXXXI. Moles of aluminum required were determined using the chemical reactions shown previously in Equation 15-Equation 20. Thermodynamic feasibility was not relevant for the purposes of the calculations.

Table LXXXI: Moles of Aluminum Required to Reduce One Mole of the Respective Bulk Components

SiO ₂	TiO ₂	Al ₂ O ₃	Fe ₂ O ₃	MgO	CaO	FeO	Na ₂ O	K ₂ O	P ₂ O ₅
1.333	1.333	-	2	0.666	0.666	0.666	0.666	0.666	3.333

The number of moles of aluminum needed to reduce one mole of each of the compounds making up the bulk composition of the regolith simulant was then multiplied by the number of moles in a 100 g regolith sample.

Table LXXXII: Moles of Aluminum Required to Reduce Total Moles of Each Bulk Component present in a 100g Sample of Regolith

SiO ₂	TiO ₂	Al ₂ O ₃	Fe ₂ O ₃	MgO	CaO	FeO	Na ₂ O	K ₂ O	P ₂ O ₅
1.05	0.03	-	0.04	0.12	0.12	0.07	0.04	0.01	0.02

The sum of the molar aluminum quantities calculated in Table LXXXII gives the total number of moles of aluminum necessary to reduce all the oxides in a 100 g sample of regolith. The total moles of aluminum required to reduce all compounds given from bulk composition analysis of regolith simulant is 1.50 moles. There are 26.98154 g/mol of aluminum, which means that 40.556 g of aluminum would be needed to reduce all the compounds in a 100 g regolith sample. The percent weight of aluminum required in a regolith-aluminum mixture is determined by Equation 50.

$$\text{Equation 50: } \frac{40.556}{(40.556 + 100)} \cdot 100 = 28.854\%$$

Using the above percentage, a stoichiometric 80 g mixture of regolith and aluminum would require 23.083 g aluminum and 56.917 g regolith.

The same methodology was then used to obtain the proportions of aluminum necessary to reduce all thermodynamically favorable oxides present within the regolith simulant. The moles of aluminum required to reduce the thermodynamically favorable compounds within the regolith simulant are shown in Table LXXXIII.

Table LXXXIII: Moles of Aluminum Required to Reduce Total Moles of Each Thermodynamically Favorable Bulk Component present in a 100g Sample of Regolith

SiO ₂	TiO ₂	Fe ₂ O ₃	FeO
1.05	0.03	0.04	0.07

The total amount of aluminum required to reduce thermodynamically favorable compounds within 100 g of the regolith simulant is 1.20 moles. The mass of aluminum required is 32.359 g.

The percent weight of aluminum required in a regolith-aluminum mixture is determined by Equation 51.

$$\text{Equation 51: } \frac{32.359}{(32.359 + 100)} \cdot 100 = 24.448\%$$

Using the above percentage, an 80 g mixture of regolith and aluminum would require 19.558 g of aluminum to reduce all the thermodynamically favorable regolith compounds.

Appendix 2: Images of Standard Atmosphere Reaction Products



Figure CCVIII: Image of a reaction product using JSC-1AF simulant and 19.44% aluminum.



Figure CCIX: Image of a reaction product using JSC-1AF simulant and 24.45% aluminum.



Figure CCX: Image of a reaction product using JSC-1AF simulant and 28.85% aluminum.



Figure CCXI: Image of a reaction product using JSC-1AF simulant and 33.33% aluminum.



Figure CCXII: Image of a reaction product using JSC-1A simulant and 19.44% aluminum.



Figure CCXIII: Image of a reaction product using JSC-1A simulant and 24.45% aluminum.



Figure CCXIV: Image of a reaction product using JSC-1A simulant and 28.85% aluminum.

Appendix 3: Images of Vacuum Reaction Products



Figure CCXV: Image of a reaction product using JSC-1AF simulant and 19.44% aluminum.



Figure CCXVI: Image of a reaction product using JSC-1AF simulant and 24.45% aluminum.



Figure CCXVII: Image of a reaction product using JSC-1AF simulant and 28.85% aluminum.



Figure CCXVIII: Image of a reaction product using JSC-1AF simulant and 33.33% aluminum.



Figure CCXIX: Image of a reaction product using JSC-1A simulant and 19.44% aluminum.



Figure CCXX: Image of a reaction product using JSC-1A simulant and 24.45% aluminum.



Figure CCXXI: Image of a reaction product using JSC-1A simulant and 28.85% aluminum.

VII. REFERENCES

1. Mei, J.; Halldearn, R. D.; Xiao, P., Mechanisms of the Aluminum-Iron Oxide Thermite Reaction. *Scripta Materialia* **1999**, 41, (5), 541-548.
2. Aldridge, E. C., Report of the President's Commission on Implementation of United States Space Exploration Policy. **2004**, 1-64.
3. Zumdahl, S. S., *Chemical Principles*. Houghton Mifflin Company: New York, 1998; p 1040.
4. Cutler, R. A.; Rigtrup, K. M.; Virkar, A. V., Synthesis, Sintering, Microstructure, and Mechanical Properties of Ceramics Made by Exothermic Reactions. *Journal of the American Ceramic Society* **1992**, 75, (1), 36-43.
5. Mossino, P., Some Aspects in Self-propagating High-temperature Synthesis. *Ceramics International* **2004**, 30, 311-332.
6. Tubalov, N. P.; Lebedeva, O. A.; Vereshchagin, V. I., Porous Composite Ceramic Materials Produced by a Self-propagating High-temperature Synthesis in the $\text{Fe}_2\text{O}_3\text{-Al}_2\text{O}_3\text{-Al}$ system. *Refractories and Industrial Ceramics* **2003**, 44, (5), 343-345.
7. Karpukhin, I. A.; Vladimirov, V. S.; Moizis, S. E., Phase and Structural Transformations in Refractory SHS-Materials. *Refractories and Industrial Ceramics* **2005**, 46, (4), 284-286.
8. Horvitz, D.; Gotman, I., Pressure-assisted SHS synthesis of $\text{MgAl}_2\text{O}_4\text{-TiAl}$ in situ composites with interpenetrating networks. *Acta Materialia* **2002**, 50, (8), 1961-1971.
9. West, A. R., *Solid State Chemistry and its Applications*. John Wiley and Sons: 1991; p 742.
10. Schaffer, J. P.; Saxena, A.; Antolovich, S. D.; Sanders, T. H.; Warner, S. B., *The Science and Design of Engineering Materials*. Irwin: Chicago, 1995; p 842.
11. Callister, W. D., *Fundamentals of Materials Science and Engineering*. 2 ed.; John Wiley & Sons: 2005; p 712.
12. Gaskell, D. R., *Introduction to the Thermodynamics of Materials*. Taylor & Francis: New York, 1995; p 561.
13. Serway, R. A.; Jewett, J. R. J., *Physics for Scientists and Engineers*. 6 ed.; Thomson-Brooks/Cole: 2004.
14. Budinski, K. G.; Budinski, M. K., *Engineering Materials: Properties and Selection*. 8th ed.; Pearson-Prentice Hall: Upper Saddle River, 2005; p 855.
15. German, R. M., *Liquid Phase Sintering*. Plenum Press: New York, 1985; p 240.
16. McMillan, P. W., *Glass-Ceramics*. 2 ed.; Academic Press: London, 1979; p 285.
17. Dowling, N. E., *Mechanical Behavior of Materials*. Prentice-Hall: Upper Saddle River, 1999; p 830.
18. Beer, F. P.; Johnston, E. R. J.; DeWolf, J. T., *Mechanics of Materials*. 3 ed.; McGraw-Hill: New York, 2002; p 774.
19. ASTM, Standard Test Method for Monotonic Compressive Strength of Advanced Ceramics at Ambient Temperature. In 1999; Vol. C 1424-99.
20. Logan, K. V.; Walton, J. D., TiB_2 Formation Using Thermite Ignition. In *Ceramic Engineering and Science Proceedings*, 1984; Vol. 5.
21. Payyapilly, J. J.; Logan, P. P., Diffusion of Aluminum into Aluminum Oxide. In *32nd International Conference on Advanced Ceramics and Composites*, Daytona Beach, FL, 2008.

22. Duraes, L.; Costa, B. F.; Santos, R.; Correia, A.; Campos, J.; Portugal, A., Fe₂O₃/Aluminum Thermite Reaction Intermediate and Final Products Characterization. *Materials Science and Engineering A* **2007**, 465, 199-210.
23. Ping, L. R.; Azad, A.; Dung, T. W., Magnesium Aluminate (MgAl₂O₄) Spinel Produced via Self-heat-sustained (SHS) Technique. *Materials Research Bulletin* **2001**, 36, 1417-1430.
24. Gromov, A.; Vereshchagin, V., Study of Aluminum Nitride Formation by Superfine Aluminum Powder Combustion in Air. *Journal of the European Ceramic Society* **2004**, 24, 2879-2884.
25. Zakorzhevskii, V. V.; Borovinskaya, I. P.; Sachkova, N. V., Combustion Synthesis of Aluminum Nitride. *Inorganic Materials* **2002**, 38, (11), 1131-1140.
26. Guojian, J.; Hanrui, Z.; Jiong, Z.; Meiling, R.; Wenlan, L.; Fengying, W.; Baolin, Z., Morphologies and Growth Mechanisms of Aluminum Nitride Whiskers by SHS Method-Part I. *Journal of Materials Science* **2000**, 35, 57-62.
27. Guojian, J.; Hanrui, Z.; Jiong, Z.; Meiling, R.; Wenlan, L.; Fengying, W.; Baolin, Z., Morphologies and Growth Mechanisms of Aluminum Nitride Whiskers by SHS Method-Part 2. *Journal of Materials Science* **2000**, 35, 63-69.
28. Maltsev, V. M.; Gafiyatulina, G. P.; Tavrov, A. V. In *Spreading of the Combustion Wave in SiO₂-Al Systems*, Optical Technology in Fluid, Thermal, and Combustion Flow III, San Diego, CA, 1997; SPIE: San Diego, CA, 1997; pp 726-729.
29. Urakaev, F. K.; Shevchenko, V. S.; Nartikoev, V. D. In *Self-Propagating Reactions of Burning of the Thermite Compositions (MT, SHS, MSR) with Use of Mineral Raw Material*, Experimental Mineralogy, Petrology, and Geochemistry Annual Seminar, Moscow, Russia, April 16-17, 2002; Moscow, Russia, 2002.
30. Prentice, D.; Pantoya, M. L.; Clapsaddle, B. J., Effect of Nanocomposite Synthesis on the Combustion Performance of a Ternary Thermite. *Journal of Physical Chemistry B* **2005**, 109, (43), 20180-20185.
31. Chernyshev, V. N., Production of Materials with Controlled Porosity Using the Combination of the SHS Process and Hot Rolling in Vacuum. *Refractories and Industrial Ceramics* **1997**, 38, (9-10), 371-373.
32. Shabalin, I. L.; Luchka, M. V.; Shabalin, L. I., Vacuum SHS in systems with group IV transition metals for production of ceramic compositions. *Physics and Chemistry of Solid State* **2007**, 8, (1), 159-175.
33. Taylor, L. A. In *Resources for a Lunar Base: Rocks, Minerals, and Soil of the Moon*, 2nd Conference on Lunar Bases and Space Activities, 1992; 1992; pp 361-377.
34. Taylor, L. A.; Schmitt, H. H.; Carrier, W. D.; Nakagawa, M., The Lunar Dust Problem: From Liability to Asset. In *1st Space Exploration Conference: Continuing the Voyage of Discovery*, AIAA: Orlando, FL, 2005.
35. Robens, E.; Bischoff, A.; Schreiber, A.; Dabrowski, A.; Unger, K. K., Investigation of surface properties of lunar regolith: Part I. *Applied Surface Science* **2007**, 253, 5709-5714.
36. Klein, C., *Mineral Science*. 22nd ed.; John Wiley & Sons: New York, 2002.
37. Fabes, B.; Poisl, W.; Beck, A.; Raymond, L., Processing and Properties of Lunar Ceramics. In *AIAA Space Programs and Technology Conferences*, Huntsville, AL, 1992.
38. Ito, M.; Morioka, M., Growth of Diopside (CaMgSi₂O₆) Single Crystal by the Czochralski Technique. *Geochemical Journal* **2006**, 40, (6), 625-629.

39. Aleksandrov, S. M., *Geochemistry of Skarn and Ore Formation in Dolomites*. VSP: 1998; p 300.
40. Palmer, G., Petrographic Examination of Refractory Damage to a Burner Pipe. *World Cement* **1989**, 266-270.
41. Best, M. G., *Igneous and Metamorphic Petrology*. Blackwell Publishing: 2003.
42. Magoffin, M.; Garvey, J., Lunar Glass Production Using Concentrated Solar Energy. In *AIAA Space Programs and Technologies Conference*, Huntsville, AL, 1990.
43. Tucker, D.; Ethridge, E.; Toutanji, H. In *Production of Glass Fibers for Reinforcing Lunar Concrete*, 44th AIAA Aerospace Sciences Meeting and Exhibit, Reno, NV, Jan. 9-12, 2006; Reno, NV, 2006.
44. Allen, C. C.; Graf, J. C.; McKay, D. S., Sintering Bricks on the Moon. In *Engineering, Construction, and Operations in Space IV*, 1994; pp 1220-1229.
45. Characterization Summary of JSC-1AF Lunar Mare Regolith Simulant. In 1.6.2 ed.; NASA Marshall Space Flight Center: 2006.
46. Characterization Summary of JSC-1A Bulk Lunar Mare Regolith Simulant. In B.1 ed.; NASA Marshall Space Flight Center: 2007.
47. Sen, S.; Ray, C. S.; Reddy, R. G., Processing of Lunar Soil Simulant for Space Exploration Applications. *Materials Science and Engineering A* **2005**, 413-414, 592-597.
48. Faierson, E.; Logan, K.; Hunt, M.; Stewart, B., Lunar Habitat Construction Utilizing In-Situ Resources and an SHS Reaction. In *AIAA Space 2008 Conference and Exposition*, San Diego, 2008.
49. Yu, Y.; Hewins, R. H. In *Evaporation of Potassium and Sodium Under Vacuum Conditions - Did Chondrules Really Form at Low Pressure?*, 28th Annual Lunar and Planetary Science Conference, Houston, TX, 1997; Houston, TX, 1997.
50. Matovic, B.; Boskovic, S.; Logar, M., Preparation of basalt-based glass ceramics. *Journal of the Serbian Chemical Society* **2003**, 68, (6), 505-510.
51. Honig, R. E.; Kramer, D. A., Vapor Pressure Data for the Solid and Liquid Elements. *RCA Review* **1969**, 30.
52. Cullity, B. D.; Stock, S. R., *Elements of X-Ray Diffraction*. Prentice Hall: Upper Saddle River, 2001; p 664.
53. Tas, A. C., Chemical Preparation of the Binary Compounds in the Calcia-Alumina System by Self-Propagating Combustion Synthesis. *Journal of the American Ceramic Society* **1998**, 81, (11), 2853-2863.
54. Kumashiro, Y., *Electric Refractory Materials*. 2nd ed.; CRC Press: 2000; p 760.
55. Mitchell, B. S., *An Introduction to Materials Engineering and Science for Chemical and Materials Engineers: For Chemical and Materials Engineers*. Wiley-IEEE: 2004; p 954.
56. Sickafus, K. E.; Larson, A. C.; Yu, N.; Nastasi, M.; Hollenberg, G. W.; Garner, F. A.; Bradt, R. C., Cation Disorder in High-Dose Neutron-Irradiated Spinel. *Journal of Nuclear Materials* **1995**, 219, 128-134.
57. Keppel, G.; Saufley, W. H.; Tokunaga, H., *Introduction to design and analysis: a student's handbook*. 2 ed.; Macmillan: 1992; p 626.
58. Allen, C. C.; Morris, R. V.; Jager, K. M.; Golden, D. C.; Lindstrom, D. J.; Lindstrom, M. M.; Lockwood, J. P., MARTIAN REGOLITH SIMULANT JSC MARS-1. In *Lunar and Planetary Science XXIX*, Houston, TX, 1998.

